

THE PROPERTIES AND PERFORMANCE OF LEDE STONE IN CULTURAL HERITAGE: NEW INSIGHTS FOR ITS PRESERVATION AND REPLACEMENT

Tim De Kock



Promotor: Prof. Dr. Veerle Cnudde

Thesis submitted in fulfillment of the requirements for the
degree of Doctor of Science: Geology



Universiteit Gent
Faculteit Wetenschappen
Vakgroep Geologie

De eigenschappen en het gedrag van Ledesteen in cultureel erfgoed:
nieuwe inzichten voor zijn bescherming en vervanging

Promotor: Prof. Dr. Veerle Cnudde

Examencommissie: Prof. Dr. Stephen Louwye (voorzitter)
Dr. Hannelore Derluyn (secretaris)
Prof. Dr. Johan De Grave
Prof. Dr. Gilles Fronteau
Prof. Dr. Ákos Török
Dr. Timo G. Nijland
Prof. Dr. Veerle Cnudde (promotor)

Universiteit Gent
Faculteit Wetenschappen

Vakgroep Geologie
Krijgslaan 281, S8, B-9000 Gent, België

Tel.: +32-9-264.46.47
Fax.: +32-9-264.47.85



Proefschrift tot het behalen van de graad van
Doctor in de Wetenschappen:
Geologie
Academiejaar 2015-2016

© Tim De Kock, 2016.

Alle rechten voorbehouden. Niets uit deze uitgave mag worden vermenigvuldigd en/of openbaar gemaakt worden door middel van druk, fotokopie, microfilm, elektronisch of op welke andere wijze ook, zonder voorafgaande schriftelijke toestemming van de uitgever.

All rights reserved. No part of this publication may be reproduced in any form by print, photo print, microfilm or any other means without written permission from the author.

Dankwoord

De eigenschappen van steen hebben mij altijd geïnteresseerd. Ik vond het ook geweldig hoe die groeve in Balegem, waar je zo mooie haaiantanden kunt vinden, de laatste exponent is van een eeuwenlange geschiedenis waarin onze lokale natuursteen zo waardevol is. Het is moeilijk te vatten dat enkele versteende horizonten zo volumineus hebben bijgedragen aan ons patrimonium. Ik heb dan ook met veel plezier aan dit onderwerp gewerkt en ik heb enorm veel bijgeleerd de voorbij zes jaar.

De keuze voor dit onderwerp is zeker en vast een gevolg van de goede begeleiding en de inspirerende woorden en daden van mijn promotor Prof. Dr. Veerle Cnudde tijdens mijn masterthesis. Ook tijdens de afgelopen zes jaar heeft ze mij uitstekend begeleid. Ik kreeg alle kansen en de nodige vrijheid, maar ook ideeën, steun en uitdagingen. Veerle, zowel op academisch, professioneel en menselijk vlak heb ik veel van jou kunnen bijleren, waarvoor mijn oprechte dank.

Het team dat Veerle de afgelopen jaren bij elkaar gekregen heeft, bestaat uit fantastische collega's. Samen hebben we heel wat *progress* gemaakt, op en naast het werk. Marijn, na meer dan tien jaar samen studeren en werken is een bureau-afscheid misschien wel nakend. Bedankt voor alle ideeën, goede raad en de kuisvrouw. Jan, Wesley, Jeroen, Tom, Hannelore en Delphine, bedankt voor de leuke congressen en onderzoekstripjes naar het buitenland. En samen met Victor, Aurélie, Jolien, Karen, Danielle, Neil en Patric bedankt voor de leuke samenwerking en de hulp, en alle mooie momenten op het bureau en in het lab. Jeroen, ik neem graag ongeslagen afscheid van het tabletoptennis. Misschien meer succes met de volgende collega's. Op dezelfde manier wil ik alle collega's van het UGCT team bedanken voor de leuke tijd in de bunkers en -gelukkig- aan een bepaalde tafel met een aantal roze peetjes. Vooral hulplijn 6628, Matthieu, Thomas en Pieter, waarop je terecht kan voor advies over (echt wel alle) problemen, maar even goed ook Prof. Dr. Luc Van Hoorebeke,

Manu, Amélie, Loes, Elin, Jelle 1, Jelle 2, Denis, Bert, Prof. Dr. Joris Van Acker en Jan en iedereen in het atelier.

Verder wil ik ook alle collega's van de vakgroep bedanken waarmee ik de voorbije jaren aangenaam heb samen gewerkt. Hierbij in het speciaal toch wel de Alpen en Kartering A -ploeg: Prof. Dr. Marc De Batist, Prof. Dr. Johan De Grave, Elien, Stan, Nore, Pieter, Philipp en Willem; ook Prof. Dr. Jacques Verniers en Prof. Dr. Frank Mostaert voor de overige excursies; mijn nog niet genoemde mede-assistenten Thomas en Mathijs; Wim, Kurt en Lieven; laboranten Jan, Veerle, Ann-Eline en Jill; en zeker ook de bachelorproef- en thesisstudenten waarmee ik samen gewerkt heb.

Ook dank ik de collega's van de universiteit die mij verder geholpen hebben met specifieke proeven of toelating hebben gegeven tot hun materiaal, in het bijzonder de medewerkers van Labo Mangel met onder meer Prof. Dr. Ir. Geert De Schutter, Dr. Ir. Peter De Pauw, Ing. Tommy De Ghein en Nicolas Coppieters, en de collega's waarmee ik heb mogen samenwerken waaronder Prof. Dr. Philippe Crombé, Prof. Dr. Wim De Clercq en Sibrecht Reniere. Daarnaast heb ik de kans gekregen om met vele goede wetenschappers samen te werken buiten de UGent, van de Belgisch Geologische Dienst Marleen en Michiel, van het KIK Hilde, Roald, Roel, Sebastiaan en Laurent, van KU Leuven Prof. Dr. Jan Elsen en ook Prof. Dr. Els Verstrynge, van de Universiteit van Mons Prof. Dr. Jean-Marc Baele en Dr. Fabrice Dagrain, en van het committee van de Vlaams-Nederlandse Natuursteendag ook nog Roland, Wido, Timo, David, Hendrik, Jan en Prof. Dr. Rob Van Hees; allen bedankt voor de fijne samenwerking en de leerrijke ervaringen. Ook in de professionele wereld ben ik geholpen, bedankt Philippe, Maarten en Ignace van Architectenbureau Bressers, Hendrik Vergote voor de toegang tot Balegro en het materiaal, Tine Schotte van Monument en Stefanie Bergez van Denys en hun collega's voor het proefmateriaal en/of de toegang tot werfbezoeken, Freddy De Schacht voor betrokkenheid bij de voorstudie in Dudzele, Kristof Callebaut voor toegang tot de voorstudie van het Huis van de Vrije Schippers, en de verschillende groeves in België, Duitsland, Frankrijk en Spanje waar ik verwelkomd ben of die mij stenen hebben toegestuurd.

I would also like to thank many foreign colleagues, especially from the Université de Reims Champagne-Ardenne and Universidad Politécnica de Cartagena for hosting me; Prof. Dr. Gilles Fronteau, Dr. Stéphanie Eyssautier, Aurélie, Soizic and all colleagues from Reims;

Prof. Dr. Marcos Lanzón and the colleagues from the SAIT lab in Cartagena and Juan-Antonio; Dr. Timothy Palmer and many others. I would also like to thank the entire jury for critically reading this text and for all the useful comments to improve this work and to improve future research, amongst them not mentioned so far Prof. Dr. Stephen Louwye and Prof. Dr. Ákos Török.

Verder wil ik mijn vrienden bedanken voor de nodige afleiding wanneer nodig en de vele sportieve momenten bij KMTC, Het Plan en de WE05 voetbalmiddagen; mijn ouders voor de nodige steun om te kunnen doen wat ik graag doe, en de rest van mijn (schoon)familie voor alle leuke momenten en (gespeelde) interesse in steen. Als laatste wil ik de belangrijkste persoon in mijn leven bedanken. Ook zij heeft elke dag te maken met steen, boren en restauraties, zij het in de mond. Silke, bedankt om de beste vriendin te zijn die ik kan wensen en voor alle inspiratie die je mij geeft omdat je de dingen zo perfect kan doen.

Bedankt! ... En veel leesplezier.

Gent, 2016

Tim De Kock

English summary

Natural stone is one of the Earth's most pure natural resources. As such, it has been used since prehistoric times. Natural stone in our cultural heritage is invariably connected to local geology, cultural and architectural developments and several socio-economic factors. Flanders is relatively poor in extractable natural stone. Nevertheless, some stone horizons with remarkable properties occur at several stratigraphic levels near the surface. Amongst them are the sandy limestones of the Eocene deposits. Ypresian stone, Brussels stone and Lede stone are forthcoming of different quarries and today represent an important part of our heritage. This research focuses on the material characteristics of Lede stone, which is dominant in the city of Ghent and important in the cultural built heritage of Flanders and The Netherlands.

Some previous studies already focused on Lede stone: on its resources, its properties and weathering, its historic use and on restoration strategies. Yet so far, no study has focused profoundly on the natural variability of the Lede stone and its influence on the material's properties. Here, the different properties and the weathering of Lede stone are investigated in the context of monument restoration and the preservation of our cultural heritage.

Chapter 1 to 3 establish the context and provide the geological background and previous studies on Lede stone and other closely related limestones. This is supplemented by some illustrations of its sources and use in the cultural heritage.

Chapter 4 explores the perception on natural stone and restoration. It presents some cases where knowledge of the stone is applicable for the sustainable and economical restoration of our cultural heritage. By means of a survey, the opinion was checked of both professionals and the broader public, who are not professionally involved but admire our heritage daily. This study indicated that the perception of damage is mainly related to structural damage of the stone. Soiling and other aesthetic aspects are less

perceived as damage. It is clear that the more a stone is considered as damaged, the more an intervention is required. Such interventions can be done in several ways, but for most of the respondents, it only succeeded when the historical aspect of a building is put in the picture and/or when the intervention looks aged.

Chapter 5 illustrates the large natural variability of Lede stone. A Visual Estimation Chart gives different kinds of Lede stone with increasing porosity. These are further characterized, based on petrography, porosity, petrophysical properties and strength properties, which can be used by professionals in the building and heritage sector. Therefore, Lede stone samples were divided in three groups: a low porous, a medium porous and a high porous group. The results show a significant difference in the water absorption, vapour diffusion and water retention of the different groups, all related to the pore network. Yet all have a good durability, notwithstanding that the most porous variant should be applied with reservation in moist or wet applications.

Chapters 6 and 7 explore the two most noticed damage phenomena on Lede stone: the formation of black crusts and frost damage. Chapter 6 focuses on the general characterization of a black crust and a dynamic weathering experiment on the pore-scale using μ CT. The latter shows that aside from chemical alteration, also a structural damage occurs as cracks which were initiated by the crystallization pressure. Rather than the intrinsic frost susceptibility of Lede stone, these cracks could enhance the frost susceptibility by modifying the water absorption of Lede stone. In chapter 7, the dynamics of the freeze-thaw process in stone were studied on a pore scale level. Therefore, a stone with similar components, but higher porosity and lower strength was used: the French Noyant limestone. The time-resolving aspect of continuous μ CT showed that the damage occurring during freeze-thaw cycling is related to the ice crystallization pressure. Moreover, the spatial information allows to link the damage with the texture and pore size distribution of the stone. Similar experiments were performed on Lede stone, but rather than image acquisition with μ CT, the length change of the specimen was registered. This also allowed to interpret the process, based on the knowledge gained with the μ CT experiments on Noyant limestone.

Achieving a successful intervention can be done by stripping the original stone from its weathered skin, by treating it or by replacing it with a new stone. The study of conservation and restoration treatments is not part of

this research, but future work can be supported by the insights made on the properties of Lede stone, in chapter 5. In the case of stone replacement, one should take notice of the historical, aesthetical and technical compatibility. This is illustrated in chapter 8. The historic compatibility always requires a case-study, whilst for the aesthetical and technical compatibility some guidelines can be formulated, again related to the material properties themselves. In addition, the ageing aspects of the different materials should be thoroughly explored. Over the last two centuries, mainly French limestones were used to replace Lede stone in Belgium. As this did not always give the desired result, some more exotic stone types have recently been applied in the aim for finding a better alternative. Yet still, the replacement of Lede stone remains a delicate topic, with no straightforward solution so far. Of course, the best practice is to use Lede stone from the current quarry in Balegem as replacement stone, although it should be used wisely and sustainably.

Finally, chapter 9 is a reflection of the before mentioned principles and methods that they apply to all natural stones in historic monuments. The identification of a formerly unknown limestone as Caen stone, and the characterization of the damage aids in the thoughtful and sustainable restoration of the tower ruin in Dudzele. Unlike the previous restorations, where this natural stone with a unique historical value was simply replaced by commercial alternatives, whilst the same stone type was easily available.

The results of this research contribute to the fundamental knowledge on natural stone. They illustrate that the petrophysical properties are closely related to the pore network and that this pore network can best be characterized by a combination of techniques. Furthermore, the results can be directly applied in the design of restoration strategies for the conservation and preservation of our cultural heritage. In addition, the weathering of Lede stone was investigated on the pore-scale. The results show that a pore-scale approach can provide new fundamental insights in weathering processes.

Nederlandse samenvatting

Natuursteen is één van de puurste natuurlijke rijkdommen van de Aarde. Daarom is ze ook al gebruikt sinds de prehistorie. De natuursteen in ons erfgoed is onlosmakelijk verbonden met de lokale geologie, culturele en architecturale ontwikkelingen en diverse socio-economische factoren. Vlaanderen is relatief arm aan ontginbare natuursteen. Toch komen er op verschillende stratigrafische niveau's steenbanken met een opmerkelijke kwaliteit aan het oppervlak. Onder hen bevinden zich een aantal kalksteenbanken, voornamelijk in de Eocene afzettingen. Hieruit zijn onder meer Ieperiaanse steen, Brusselse steen en Ledesteen gewonnen, die vandaag een belangrijk deel uitmaken van ons patrimonium. Dit onderzoek focust zich op de materiaalkarakteristieke aspecten van de Ledesteen, die dominant is in het erfgoed van de stad Gent, maar ook een belangrijke plaats heeft in het erfgoed van Vlaanderen en Nederland.

Verschillende studies hebben zich al toegelegd op het onderzoek van Ledesteen; op zijn ontginningsplaatsen, op zijn eigenschappen en verwerking, op zijn historisch gebruik en op strategieën voor restauratie. Toch heeft er nog geen enkele studie diepgaand de invloed van zijn natuurlijke variabiliteit op zijn eigenschappen onderzocht. In deze scriptie worden de eigenschappen en verwerking van verschillende variaties Ledesteen onderzocht in de context van monument restauratie en het behoud van cultureel erfgoed.

Hoofdstukken 1 tot en met 3 schetsen de context, de geologische achtergrond en gekende informatie over de Ledesteen en nauw verwante stenen. Dit wordt aangevuld met enkele illustraties van ontginning en gebruik.

Hoofdstuk 4 gaat dieper in op de percepties over natuursteen en restauratie. Hier worden voorbeelden aangehaald waarbij de kennis van de steen van toepassing is met het oog op een duurzaam en economisch onderhoud van ons erfgoed. Door middel van een enquête werd deze

context getoetst aan de visie van professionelen en de toeschouwer, of de mensen die niet professioneel betrokken zijn, maar wel elke dag ons erfgoed bewonderen. Hieruit bleek dat de perceptie van beschadigde steen vooral voortkomt uit structurele schade en minder uit vervuiling van de steen die geen rechtstreekse structurele schade vertoont. Het is wel duidelijk dat naarmate men de steen meer en meer als beschadigd gaat bestempelen, het algemene gevoel ook is dat er een ingreep nodig is. Een daaropvolgende interventie kan op verschillende manieren opgevat worden, maar voor het grote publiek is ze pas geslaagd wanneer het historische aspect van een gebouw uit de verf komt en/of wanneer de interventie er ook al verouderd uitziet.

Hoofdstuk 5 toont aan dat er wel degelijk een grote variabiliteit zit op de Ledesteen. Een Visuele Referentiekaart geeft verschillende illustraties van Ledesteen met een toenemende porositeit. Deze zijn verder gekarakteriseerd op basis van petrografie, porosimetrie en het bepalen van de petrofysische en mechanische eigenschappen. Hiervoor werden de proefstukken Ledesteen opgedeeld in drie groepen: een laag poreuze, medium poreuze en een hoog poreuze groep. Deze groepen tonen een duidelijk verschil in wateropname, dampdoorlatendheid en droging, wat gerelateerd kan worden aan hun poriestructuur. Toch kan gezegd worden dat ze allen duurzaam zijn, enkel voor de meest poreuze stenen is enig voorbehoud noodzakelijk in zeer natte en blootgestelde toepassingen.

Hoofdstuk 6 en 7 gaan dieper in op de twee meest besproken schadepatronen van de Ledesteen: korstvorming door vervuilde atmosfeer en vorstschade. Hoofdstuk 6 focust op een algemene karakterisatie van een zwarte gipskorst en een dynamisch verwerkingsexperiment op de porieschaal met behulp van μ CT. Hier wordt aangetoond dat de inwerking van SO_2 niet enkel oplossing en kristallisatie in de hand werkt, maar dat er ook structurele schade optreedt in de vorm van breuken, door de geïnduceerde kristallisatiedruk. Eerder dan intrinsieke vorstgevoeligheid, zouden deze breuken de vorstgevoeligheid van de Ledesteen kunnen verhogen, door de wijzigingen in het waterabsorberend gedrag die ze kunnen teweeg brengen. In hoofdstuk 7 wordt de dynamiek van vorstschade op porieschaal experimenteel onderzocht, zij het op een zachtere kalksteen met gelijkaardige componenten: de Franse Noyant kalksteen. De dynamische tijdsgebonden resolutie van deze experimenten toont aan dat de schade enkel gerelateerd is aan de ijskristallisatiedruk. Bovendien kan de schade duidelijk gelinkt worden aan de textuur van het

gesteente. Op Ledesteen werden gelijkaardige experimenten uitgevoerd, maar in plaats van beeldvorming werd de lengteregistratie gemeten. Ook hier kan het proces geïnterpreteerd worden, maar het is niet mogelijk om dit rechtstreeks te koppelen aan texturele componenten van de steen.

Om tot een geslaagde interventie te komen, kan men de steen ofwel ontdoen van zijn verweerde laag, of kan men hem behandelen of vervangen door een andere steensoort. De studie van behandelingen behoort niet tot dit werk, maar kan wel steunen op de inzichten die verkregen zijn in de materiaalkarakterisatie van hoofdstuk 5. In het geval van vervanging, moet er rekening gehouden worden met de historische, esthetische en technische compatibiliteit. Dit wordt besproken in hoofdstuk 8. De historische compatibiliteit vergt altijd een case-studie, terwijl voor esthetische en technische compatibiliteit wel zekere richtlijnen kunnen gegeven worden, opnieuw met betrekking tot de materiaalkarakteristieken zelf. Daarbij moet zeker ook rekening gehouden worden met de veroudering van de mogelijke alternatieven. De voorbije eeuwen heeft men in noordwest-België vooral gebruik gemaakt van Franse kalkstenen. In de zoektocht naar steeds betere alternatieven worden er tegenwoordig ook meer exotische vervangstenen gebruikt. Hierbij rijst wel de vraag hoe deze verouderen en hoe deze zich gedragen in het Belgische klimaat. Alleszins blijft de vervanging van Ledesteen een moeilijk punt dat nog verder onderzoek vraagt in de toekomst. Er zijn bovendien nog reserves aanwezig met de normale kwaliteit in de huidige groeve in Balegem. Het lijkt wel aangewezen om deze oordeelkundig aan te wenden in ons erfgoed.

Hoofdstuk 9, tot slot, bevat een reflectie waarom de algemene principes die besproken zijn in de voorgaande hoofdstukken op elke natuursteen in een historisch gebouw van toepassing kunnen zijn. De identificatie van een tot dan toe onbekende witte kalksteen als Pierre de Caen, en het benoemen van de schadefenomenen kan helpen in een doordachte en duurzame restauratie van een als monument geklasseerde torenruïne. Op deze manier kan vermeden worden dat deze unieke steensoort met historische waarde zonder meer vervangen wordt door alternatieven, terwijl hetzelfde gesteentetype voorhanden is, zoals het geval was bij de voorgaande restauraties.

De resultaten van dit onderzoek dragen bij aan de fundamentele kennis van natuursteen. Ze tonen aan dat de petrofysische eigenschappen verklaard kunnen worden door een grondige karakterisatie van de porieruimte en dat

de combinatie van porosimetrische technieken een meerwaarde biedt voor het begrijpen van het porienetwerk. Bovendien hebben de resultaten ook praktisch nut en kunnen ze gebruikt worden in het opstellen van strategieën voor de restauratie en het behoud van ons cultureel erfgoed. Ook werd de verwerking van Ledesteen in ons erfgoed diepgaander onderzocht. Een benadering van de verwerking op de porieschaal is belangrijk voor het verkrijgen van nieuwe inzichten in deze processen.

List of abbreviations

BTS	Brazilian tensile strength
EN	European Standard
Fm	Formation
ICP-MS	Inductively coupled plasma - mass spectrometry
Lf1	Lede stone - microfacies with lowest porosity
Lf2	Lede stone - microfacies with intermediate porosity
Lf3	Lede stone - microfacies with highest porosity
Ma	Million year
Mbr	Member
MIP	Mercury Intrusion Porosimetry
Nc	Number of cycles
RH	Relative humidity
SEM	Scanning electron microscopy
UCS	Uniaxial compressive strength
US	Ultrasound velocity
VEC	Visual estimation chart
μ CT	X-ray computed microtomography
μ XRF	micro X-ray fluorescence
XRD	X-ray diffraction

Contents

Dankwoord	i
English summary	v
Nederlandse samenvatting	ix
List of abbreviations	xiii
Preface	1
1 General introduction	1-1
1.1 Natural building stones	1-2
1.2 Natural stone in cultural heritage	1-3
1.3 Aims and scope	1-5
2 Eocene white limestone resources in northern Belgium	2-1
2.1 Geological setting	2-2
2.2 Ypresian stone	2-8
2.3 Brussels stone	2-9
2.3.1 Diegem stone	2-10
2.3.2 Gobertange stone	2-11
2.4 Nomenclature of the white limestones	2-11
3 Lede stone	3-1
3.1 Lede Formation	3-2
3.2 Historic production and use	3-2
3.3 Appearance	3-7
3.4 Performance	3-10
3.5 Contemporary availability and issues	3-12
3.6 Previous technical studies	3-13

4	Natural stone damage and interventions: a human perception	4-1
4.1	Introduction	4-2
4.2	Methods	4-3
4.3	Results part 1: damage	4-13
4.3.1	Structural damage is less appreciated	4-13
4.3.2	Damage and the need for intervention	4-14
4.3.3	Specific considerations on damage	4-15
4.4	Results part 2: intervention	4-16
4.4.1	Ageing is appreciated	4-16
4.4.2	Interventions: integration versus distinguishability	4-18
4.5	Conclusions	4-19
5	Integrated characterization of the natural variability of Lede stone	5-1
5.1	Lede stone samples & Visual estimation chart	5-2
5.2	Petrography	5-3
5.2.1	Lf1: low porosity	5-4
5.2.2	Lf2: medium porosity	5-6
5.2.3	Lf3: high porosity	5-9
5.2.4	Petrographic variation	5-10
5.3	Porosity	5-11
5.3.1	Vacuum saturation	5-11
5.3.2	Pycnometry	5-13
5.3.3	Mercury Intrusion Porosimetry	5-14
5.3.4	X-ray computed microtomography	5-18
5.3.5	Characterizing the pore system	5-22
5.4	Water transport properties	5-24
5.4.1	Water absorption by total immersion	5-24
5.4.2	Capillary water absorption	5-26
5.4.3	Moisture adsorption	5-29
5.4.4	Water vapour diffusion	5-31
5.4.5	Gas permeability	5-32
5.4.6	Drying	5-34
5.5	Strength properties and sound speed propagation	5-36
5.5.1	Uniaxial compressive strength	5-36
5.5.2	Brazilian tensile strength	5-38
5.5.3	Ultrasound velocity	5-40
5.6	On-site methods for water absorption	5-41
5.6.1	Karsten tube	5-42

5.6.2	Contact sponge	5-44
5.7	Salt weathering test	5-45
5.8	Freeze-thaw weathering test	5-51
5.9	Comparison with technical sheet	5-52
5.10	Performance in use	5-53
5.11	Discussion and Conclusion	5-56
6	Laminar black crusts on Lede stone	6-1
6.1	Introduction	6-2
6.2	Microstructure, composition and petrophysical properties of the laminar gypsum crust	6-3
6.2.1	Materials and methods	6-3
6.2.2	Results	6-5
6.2.3	Discussion	6-14
6.3	Acid weathering: evolution of the stone with black crust	6-19
6.3.1	Materials and Methods	6-19
6.3.2	Results	6-20
6.3.3	Discussion	6-25
6.4	Glauconite weathering: explorative experiments	6-26
6.4.1	Materials and methods	6-27
6.4.2	Results and discussion	6-27
6.5	Conclusion	6-29
7	A pore-scale study of freeze-thaw processes in Lede stone and Noyant limestone	7-1
7.1	Introduction	7-2
7.2	Pore-scale freeze-thaw experiments with EMCT on Noyant limestone	7-4
7.2.1	Material	7-4
7.2.2	Methods	7-5
7.2.3	Petrophysical properties	7-8
7.2.4	Capillary water absorption with μ CT	7-9
7.2.5	Pore-scale freeze-thaw cycling	7-10
7.2.6	Discussion	7-15
7.3	Freezing induced dilatation of Lede stone	7-18
7.3.1	Material and methods	7-18
7.3.2	Results	7-20
7.3.3	Discussion	7-24
7.4	Discussion and conclusion	7-26

8	Replacement stones for Lede stone	8-1
8.1	Historical replacement of Lede stone in northwestern Belgium	8-2
8.1.1	19 th and early 20 th century	8-2
8.1.2	Late 20 th and 21 th century	8-4
8.2	The tower of St Bavo's cathedral in Ghent as textbook example	8-5
8.2.1	Ghent and St Bavo's Cathedral	8-5
8.2.2	White stones and historical reconstruction	8-7
8.2.3	Decision-making factors	8-10
8.3	Compatibility of traditional and new replacement stones	8-12
8.3.1	Description of replacement stones	8-13
8.3.2	Petrophysical properties of replacement stones	8-19
8.3.3	Discussion	8-24
8.4	Conclusion	8-26
9	The identification and characterization of white limestone in the 12th century tower of Dudzele: a reflection	9-1
9.1	Introduction	9-2
9.2	Methods	9-4
9.3	Materials	9-6
9.4	Results and discussion	9-7
9.4.1	Stone and architecture	9-7
9.4.2	Identifying the buff-coloured limestone	9-9
9.4.3	Deterioration and performance	9-12
9.5	Conclusion	9-18
10	Conclusions and future outlook	10-1

List of Figures

- 2.1 Geological map of Flanders (based on Databank Ondergrond Vlaanderen). Colour legend of the discussed formations in Fig. 2.2. 2-2
- 2.2 Chronostratigraphic cartoon of the early and middle Eocene deposits in Flanders (inspired on Vandenberghe et al. (1998)), with colour legend for Fig. 2.1 and Fig. 2.4. 2-4
- 2.3 Eocene palaeogeographical map of northwestern Europe with an indication of the depot centre of Lede sands (arrow), adopted from Ziegler (1990). 2-5
- 2.4 E-W cross-section of southern Flanders, with indication of the occurrence of Lede, Brussels and Ypresian stone (based on Databank Ondergrond Vlaanderen). Colour legend similar to Fig. 2.2. 2-7
- 2.5 Macroscopic example of A) Ypresian stone perpendicular to bedding, with green colour and exfoliation; B) Ypresian stone perpendicular to bedding with *Nummulite* concentrations; C) Brussels stone and D) Gobertange stone; all in the same scale. 2-9
- 2.6 Map from the area in between Ghent and Brussels, with indication of the most prominent locations in this chapter and Chapter 3. 2-13
- 2.7 Map from the area in around and east of Brussels, with indication of the most prominent locations in this chapter and Chapter 3. 2-14
- 3.1 Cover page of *Oryctographie de Bruxelles* (Burtin et al., 1784), showing an open air quarry (left) and a subsurface mine (right) in Brussels. 3-4

3.2	Photos of (ancient) Lede stone quarries. A) topographical relicts of historical quarrying at <i>De Wolfsputen</i> in Dilbeek; B) pond with some piled residual Lede stone as quarry relict at <i>De Steenberg</i> in Bambrugge; C) Balegro quarry anno 2012 with stone layer (white arrow) at the sharp erosive base of the Lede Fm, with a basal gravel.	3-5
3.3	Examples of Lede stone. A) accumulation of <i>Nummulites variolarius</i> and <i>Ditrupa strangulata</i> ; B) dispersed occurrence of <i>Nummulites variolarius</i> and <i>Ditrupa strangulata</i> ; C) layering; D) stratification, pronounced by <i>Nummulites variolarius</i> , E) coarse, porous shell bed, F) orange-brown patina, with contour scaling.	3-8
3.4	Examples of Lede stone. A and B) subhorizontal bioturbation; C) liesegang structures (central); D) elongated stone; E) casts of <i>Turritella</i> ; F) detail of <i>Turritella</i> casts.	3-9
3.5	Deterioration processes; A: Blistering of masonry; B: Flaking at stone frame; C: Black crust on sheltered blocks; D: Alveolization and biological colonization (green algae) in a near coastal setting; E: Biological colonization (algae, lichens and mosses); F: Scaling originating along joints; G: Rounding of corner blocks along joints.	3-11
3.6	Extract from TV80 Belgian Building Research Institute (1970) with properties of Lede stone, translated to English.	3-14
3.7	New blocks of Lede stone. A) with a porous shell layer central, thickness ± 40 cm; B) detail of A; C) compact block with liesegang structures, thickness ± 40 cm; D) cut to size for finishing, height ± 20 cm.	3-15
3.8	Extract and detail from Camerman (1951): classification of rocks according to their hardness, with <i>UCS</i> (kg/cm^2) in ordinate and density (kg/m^3) in abscissa.	3-16
4.1	Results for photos 1–11.	4-6
4.2	Results for photos 12–21.	4-7
4.3	Photos 1–3 related to damage of white limestone.	4-8
4.4	Photos 4–6 related to damage of white limestone.	4-9
4.5	Photos 7–11 related to damage of white limestone.	4-10
4.6	Photos 12–16 related to interventions on white limestone.	4-11
4.7	Photos 17–21 related to interventions on white limestone.	4-12
4.8	Average appreciation for photos 1–11.	4-13

4.9	Link between appreciation and statement for photos 1–11.	4-14
4.10	Average appreciation for photos 12–21.	4-17
4.11	Link between appreciation and statement for photos 12–21.	4-18
4.12	Opinion on the interventions for photos 12–21.	4-19
5.1	Visual estimation chart to estimate the porosity of Ledestone. Binary images represent the porosity (black). Field of view approximately 12 cm × 18 cm for each sample. . .	5-4
5.2	Macroscopic photograph of the three microfacies; A) Lf1; B) Lf2 and C) Lf3.	5-5
5.3	Micrographs of the different microfacies, in the left column under plane polarised light (PPL) and in the right column under crossed polars (XPL). A and B) Lf1 with quartz grains (white in PPL), <i>Nummulites</i> (central), <i>Miliolina</i> (brown tests), glauconite (yellow-green in PPL), micrite and microsparite (fine grained and dark in PPL). C and D) Lf2 with quartz grains (white in PPL), <i>Nummulites</i> (left), <i>Miliolina</i> (brown tests left and right), glauconite (yellow-green in PPL), <i>Ditrupa sp.</i> (top) with sparite crystals inside. E and F) quartz grains (white in PPL), <i>Nummulites</i> (left) with dog tooth cement, glauconite (yellow-green in PPL), micrite and microsparite, and moldic porosity (top and bottom) (fine grained and dark in PPL). The scale bar is 1000 μm.	5-7
5.4	Micrographs of different features. A) <i>Ditrupa sp.</i> with infilling of dog tooth cement; B) <i>Ditrupa sp.</i> with sediment infilling; C) Moldic porosity with dog tooth cement lining the porosity; D) <i>Nummulite</i> with dog tooth cement and iron oxides, E) K-ferricyanide staining of dog tooth cement on <i>Nummulites</i> and microsparite indicating the carbonate is ferroan calcite (blue), the tests of <i>Nummulites</i> are not ferroan; F) K-ferricyanide staining of microsparite and parts of <i>Ditrupa</i>	5-8
5.5	Results of density plotted vs. porosity for each sample (bullets) and linear regression between the samples.	5-13
5.6	Differential mercury intrusion volume in function of the pore radius.	5-17
5.7	Cumulative absolute porosity measured by MIP in function of the pore radius.	5-18

5.8	Cumulative absolute porosity for μ CT analysis in function of the pore radius.	5-21
5.9	Comparison of the partial and total porosity obtained by vacuum saturation (black arrow), MIP and μ CT (white arrows) over the specific measurement range	5-23
5.10	Relation between the water absorption in wt% and the porosity.	5-26
5.11	Relation between the saturation coefficient and the porosity.	5-26
5.12	Capillary rise in function of time for a representative sample for each microfacies, with the measurements indicated by bullet points. C was approximated by a non-linear regression function for Lf1 and Lf2 and a linear regression function for Lf3.	5-28
5.13	Relation between the coefficient of capillarity and the total porosity.	5-30
5.14	Relation between the breakthrough radius and the coefficient of capillarity.	5-30
5.15	Decrease in water content in function of time for a representative sample for each microfacies, with the measurements indicated as bullet points. The graph is cut off at 100 h.	5-36
5.16	Values for the uniaxial compressive strength in relation to the total porosity.	5-38
5.17	Values for the tensile strength in relation to the theoretical uniaxial compressive strength according to Figure 5.16. . .	5-39
5.18	Values for the sound speed propagation in relation to the total porosity.	5-41
5.19	Values for the sound speed propagation in relation to the uniaxial compressive strength.	5-42
5.20	Average water absorption with Karsten tube in function of time for the different microfacies.	5-44
5.21	Visualization of a salt weathering cycle.	5-46
5.22	Normalized weight evolution during 15 cycles of the salt test for the different microfacies.	5-47
5.23	Visual evolution of the samples from Lf1 after 0, 5, 10 and 15 salt cycles.	5-48
5.24	Visual evolution of the samples from Lf2 after 0, 5, 10 and 15 salt cycles.	5-49

5.25	Visual evolution of the samples from Lf3 after 0, 5, 10 and 15 salt cycles.	5-50
5.26	Normalized weight evolution after 14, 56 and 100 freeze-thaw cycles for two samples of each microfacies.	5-52
5.27	Photograph of the samples after 100 freeze-thaw cycles, with detail of the damage of sample 3.1 (bottom). From left to right: Lf1.1, Lf1.2; Lf2.1, Lf2.2, Lf3.1, Lf3.2. . . .	5-53
5.28	Performance diagram with plot of the different microfacies. Zone 1: all exterior applications; zone 2, all exterior applications except for flooring or gargoyles; zone 3 exterior except for very exposed parts; zone 4: only exterior masonry.	5-55
6.1	Image of the Lede stone sample with gypsum crust from the Sint-Salvator church in Wieze.	6-4
6.2	Cross-section photograph of Lede stone with gypsum crust from the Sint-Salvator church in Wieze.	6-6
6.3	A) thin sections micrograph of gypsum crust; B) fluorescent image of the same view as A, illustrating the porosity and fractures in green; C) indication of opaque upper layer (zone 1), gypsum crystallization layer (zone 2) and sound stone with fractures (zone 3); D) <i>Nummulites variolarius</i> with partial dissolution of the outer shell, indicated by arrow. Scale bars are 500 μm	6-7
6.4	A) SEM-BSE image of gypsum crust oriented to the left with indication of zones 1, 2 and 3; B) detailed SEM-BSE image of the crust with particulate matter in the outer layer and intertwined gypsum crystals underneath; C-E) SEM-EDX mapping of Si, S, Ca with the same field of view as A.	6-8
6.5	μXRF mapping of cross section of 5.1 mm \times 9.1 mm, crustal surface oriented on the left side and marked by rectangle, with relative concentrations of the elements Al, P, Si, K, Ca, Fe and Zn.	6-10
6.6	Sagittal slice obtained with μCT and correlated Partial Grey Volume and Partial Porosity graphs of the total volume in function of depth beneath the crustal surface. . .	6-10

-
- 6.7 Frontal slices obtained by μ CT through each zone. Zone 1 consists of fine grained accretionary material. Zone 2 consists of dark grey quartz grains in a matrix with higher grey value (gypsum). Zone 3 consists of similar quartz grains in a lighter matrix (calcite) and fractures. Grains with higher grey value represent glauconite, calcite and accessory dense mineral phases; black zones are porosity. 6-11
- 6.8 3D rendering of μ CT samples (left) represented as a semi-transparent volume, while fractures are depicted in green (right); stereoplot of fracture orientation and distribution of the fracture size based on Maximum Opening (right). . . . 6-12
- 6.9 A) sagittal sample for scratch test and gas permeability measurements with position of drilling test; B) scratch test tomography fitted to sample outline; C) gas permeability mapping fitted to sample outline. 6-15
- 6.10 Depth logs of the drilling strength measurements. Average weight on bit around 20 N corresponds to average initial rock strength, while lower average weight on bit corresponds to the decayed zone near the surface. The decayed zone is thinnest in profile 4 (± 5 mm) and thickest in profile 1 and 3 (± 25 mm). The large drop in weight on bit at 8 mm depth in profile 6 correlates to the fracture observed in Fig. 6.9A and B. 6-16
- 6.11 A) 6 mm diameter sample for acid weathering experiment sleeved with heat-shrink tubing; B) climatic cell set-up on HECTOR; C) GenRH humidity generator. 6-20
- 6.12 Sagittal cross section of μ CT with the crust on top of the initial state (left) and the final state (right). Arrow 1 indicates the depth of the original gypsum crust. Arrow 2 indicates superficial gypsum crystallization crust after 21 days acid exposure. Arrow 3 indicates a zone with a development of cracks. Relative grey scale given in the histogram of Fig. 6.13. 6-21
- 6.13 Histogram of the grey values (relating to the attenuation) obtained with μ CT of the initial state and final state. First peak represents porosity, second peak represents the bulk with quartz for the lower grey values, calcite for the higher and gypsum in between both. 6-22

-
- 6.14 Plot of voxel volume in function of depth for the initial and final state. 6-22
- 6.15 Plot of the partial porosity in function of depth for the initial and final state. The partial porosity in the final state increased in the top part and decreased deeper in the sample. 6-23
- 6.16 Detail of Figure 6.12 showing the top of the sample in the final state together with a zonal model. A superficial gypsum crystallization can be observed, with the development of a crack network underneath. 6-24
- 6.17 Slice through the crust of the initial and final state together with a zonal model. Arrows indicate the growth direction of the crust, which is observed by tracking the encircled dense grains on top (left) and beneath (right) the original crust. Both become incorporated in the final crust, illustrating crystallization on top and below the original crust. The view on the crack network is subparallel to the surface. Two dense grains used for tracking are encircled. . 6-25
- 6.18 Leached Fe in ppb after 1, 5 and 10 cycles of wetting 200 mg of glauconite at room temperature, heating in water to 60 °C, heating in air to 85 °C and immersion in an aqueous 10 % H₂SO₄ solution. 6-28
- 7.1 Photo of the custom designed cooling stage for μCT (De Schryver et al., 2014). 7-6
- 7.2 Visual representation of the freeze-thaw cycles and the moments of scanning. 7-7
- 7.3 SEM images of *O. complanatus* foram indicated by the arrow with large cavities, surrounded by a microporous lime mud matrix (close up 1). The test of the foram consists of calcite microcrystals (close up 2) and is nanoporous. 7-10
- 7.4 Left: graph with temporal evolution (in minutes, indicated in legend) of the partial grey value (ordinate) during capillary uptake. The increase in grey value is the result of water progressively saturating the pore system in time and height. Right: visualization of water uptake through preferential flow paths within the rock; the rock rendering has been partially cut, showing the location of water in blue at a specific time. 7-11

- 7.5 Chronological renderings of the scans: sample volume transparent, 2D slice in gray-scale and fracture volume in blue showing the opening and closing of the fractures during subsequent freeze-thaw cycles. The first fracture can be segmented in scan 3, which was performed during the freezing period of the 2nd cycle. Its growth and the development of new fractures is visible in subsequent freezing periods. 7-12

- 7.6 Equivalent diameter of objects in the lower fracture zone for a given scan. Even scan numbers represent the thawing stage, odd scan numbers the freezing stage. Different lines represent co-existing fracture planes, separated by apertures below the Hessian detection limit or by partial closure. The fracture opens and grows during freezing stages and (partially) closes during subsequent thawing stages. The initiating fracture in scan 3 was analyzed with different parameters. 7-13

- 7.7 Readout of the temperature sensor in function of time, with set point $-5\text{ }^{\circ}\text{C}$ (a) and $-15\text{ }^{\circ}\text{C}$ (b). A small undershoot is visible after reaching the set point temperature. Note the sudden increase in (b) at $t = 547\text{ s}$ after the start of the cooling stage, caused by the release of latent heat upon ice crystallization at a temperature of $-9.7\text{ }^{\circ}\text{C}$. This is not observed in (a), suggesting no crystallization takes place and the water is only supercooled within the pores. Below, the reference slice is reconstructed for the situation just before and just after crystallization, showing the opening of the existing fracture. Graphical insets of FWHM have the same scale. 7-14

- 7.8 Custom dilatometric setup in invar, with an indication of the sample position. 7-19

- 7.9 Temperature evolution of the Lf2 sample (ordinate) for 0 %, atmospheric and 100 % water saturation in relation to the chamber temperature (abscissa) during a freeze-thaw cycle. The start point is indicated by the black arrow. 7-20

7.10	Length change (ordinate) of Lf1 (top), Lf2 (middle) and Lf 3 (bottom) for 0 %, atmospheric and 100 % water saturation in relation to the chamber temperature (abscissa) during a freeze-thaw cycle. The starting point is indicated by the black arrow.	7-22
8.1	Replacement of Lede stone at St Martinus Basilica in Halle. A) Use of new Lede stone to replace Lede stone; B) the use of Massangis to replace Massangis that formerly replaced Lede stone; C1) old replacement of Lede stone in Savonnières; C2) replacement of Savonnières that formerly replaced Lede stone by Savonnières.	8-3
8.2	Wall dormers in the Caermers monastery in Ghent. Left: the bottom of the water dormer is retained in Brussels stone (masonry) and Lede stone (corners), whilst the top of the wall dormer is replaced with Gobertange stone (masonry) and San Louis (corners). Right: wall dormer originally in Lede stone which is now completely replaced by San Louis.	8-5
8.3	Lithological map indicated on plan in frontal view (left) and in a sagittal section (right) of the St Bavo tower (property of Architectenbureau Bressers bvba).	8-8
8.4	Frontal view of the tower, pictures taken in between 1866–1885 (left; Ghent University Library, topographical collection, BRKZ.TOPO.558.A.02) and in 2011 (right; photo Visit Gent). Arrow points out Gobertange stone, which were already present by the time the left photograph was taken. These are also indicated on Fig. 8.3.	8-10
8.5	Macroscopical and microscopical photograph of Lede stone.	8-13
8.6	Macroscopical and microscopical photograph of A: Brussels stone; B: Euville stone; C: Savonnières stone; D: Massangis <i>roche jaune</i>	8-16
8.7	Macroscopical and microscopical photograph of A: San Louis stone; B: Azul Bateig stone; C: Coulmier-le-Sec stone; D: Reffroy stone.	8-18
8.8	Macroscopical and microscopical photograph of A: St Pierre-Aigle stone; B: St Maximin stone; C: Portland stone; D: Larochette stone.	8-20
8.9	Source locations of the different replacement stones mentioned in Section 8.3.1.	8-21

8.10	Performance diagram (see Figure 5.28) with a plot of the replacement stones based on the properties of Table 8.1. . . .	8-22
9.1	Tower ruin in Dudzele as seen from the northwest. The lower façade is mainly built with buff-coloured limestone, the upper masonry with Fieldstone and parts in brick. . . .	9-3
9.2	Location map of Dudzele with respect to Bruges, the North Sea and The Zwin. The present-day extent of The Zwin is shaded, while its extent in the 12 th century (adapted from Wintein (1967) is represented by the dashed line.	9-5
9.3	Floor plan of the tower ruins. Dashed lines indicate where the lower ashlar masonry is composed out of buff-coloured limestone and where cartography was performed.	9-8
9.4	Cartography of the different walls as indicated on Figure 9.3, with three colours for the buff-coloured limestone. Intact stones (category A) are coloured in green; stones with cracks or partial loss of volume (category B) in orange; stones with surface retreat (category C) in red. Replacement stones are given in blue (Lede stone) and white (Luxembourg sandstone).	9-8
9.5	Macroscopical image of the buff-coloured limestone from Dudzele, identified as Caen stone.	9-10
9.6	A) Thin section micrographs of buff-coloured limestone illustrating the packstone texture with dominant pelloidal components; B) discolouration in the crust section; C and D) growth of saxicolous lichens; E) detail of lichens with individual cells.	9-11
9.7	SEM-EDX images with A) Si-map; B) Ca-map; C) SEM-BSI image of mapped area; D) SEM-BSI image with pyrite particles indicated by arrows.	9-12
9.8	Macroscopic view (field of view approximately 1.5×1.5 m ²) of lower ashlar masonry of buff-coloured limestone with fissures and cracks, spalling, sanding, alveolization, soiling and red discolouration with large scaling.	9-13
9.9	μCT rendering of the crust with lichens (scale bar for both images). Left: top view with puzzle pattern of lichens. Right: sagittal section through stone with lichens in green showing limited lichen penetration.	9-15

- 9.10 A) Salt efflorescence after capillary rise tests; B) sample with the most severe damage after freeze-thaw tests; C) decay pattern after salt weathering tests; all samples retrieved from the tower ruin of Dudzele. 9-16
- 9.11 Average normalized dry weights of samples in function of the salt weathering cycles. The samples from the tower ruin of Dudzele show the least susceptibility to salt weathering. 9-18

List of Tables

3.1	Reported density, porosity and UCS of Lede stone.	3-13
3.2	Properties of Lede stone, measured by the author in command of Balegro BVBA in 2012.	3-14
5.1	Density and total porosity of the three microfacies, measured with vacuum saturation (EN 1936), pycnometry, MIP and μ CT.	5-12
5.2	Total MIP porosity, critical radius and breakthrough radius for each microfacies	5-17
5.3	Water absorption and saturation after 48 and 72 hours immersion under atmospheric pressure.	5-25
5.4	Average coefficient of capillarity and maximum and minimum measured value for each microfacies.	5-29
5.5	Moisture adsorption at 95 % RH and 30 °C.	5-31
5.6	Average water vapour resistance for each microfacies.	5-32
5.7	Average TP value and corresponding gas permeability for each microfacies.	5-33
5.8	Average values for the drying characteristics of the different microfacies at 85 % RH and 25 °C. The critical moisture content is given in % of the initial water content.	5-35
5.9	Average values of uniaxial compressive strength and Brazilian tensile strength for the different microfacies.	5-37
5.10	Average values of sound speed propagation for the prismatic and cylindrical samples of the different microfacies.	5-41
5.11	Average values of water uptake by Karsten tube and contact sponge for the different microfacies.	5-43

7.1	Results for bulk density, effective porosity, atmospheric absorption, saturation degree, capillary coefficient, ultrasound velocity, uniaxial compressive strength, flexural strength, Brazilian tensile strength of Noyant limestone for a minimum of six samples with exception of MIP measured on one sample.	7-9
8.1	The properties of Lede stone (see Chapter 5) and different discussed replacement stones for Lede stone. The properties were measured by the author except where otherwise indicated.	8-23
9.1	Physical properties of buff-coloured limestone samples from the tower ruin of Dudzele (tested) and Caen stone (technical information of the Cintheaux quarry).	9-12
9.2	Percentage of categories A (intact stone), B (cracks, partial loss of volume) and C (strong surface retreat) blocks and orientation of the wall as can be seen in Figure 9.4.	9-14
9.3	XRD analysis of salt efflorescence after capillary rise tests.	9-16
9.4	Results of laboratory induced freeze-thaw and salt weathering tests on the samples from the tower ruin of Dudzele.	9-17

Preface

The Earth's own building material -rock- has provided an excellent raw material for construction purposes from the very beginning of civilization.

Prikryl and Török (2010)

Quotes do not always have to be very old to be written in stone. The citation of Prikryl and Török at the beginning of this chapter perfectly captures the value of natural stone. Not only does it reflect the remarkable qualities of the material and the role it plays in our society, it also highlights the unconditional connection of many constructions in natural stone with geology.

Natural stones are one of the Earth's most pure natural resources. From the first use of ancient stone tools in the Palaeolithic to modern constructions and artwork, natural stone has been intertwined with the evolution and development of our society. They make up great part of our cultural heritage. Making a city tour suffices to get an idea of local geology, as raw materials from the vicinity mostly have a high abundance in the historic buildings. Yet stones sometimes traveled long distances. Hunter-gatherer societies took their stone tools during migrations. Egyptians, Greeks and Romans transported stone for their well-known monuments. They favoured the use of traditional quarries and well-known material such as travertine or tuff. Economic development during the postclassical ages favoured the rise of natural stone trading. Improved transport possibilities and globalisation in modern time resulted in the world-wide distribution of commercialised stone. But despite this evolution and all factors that could come into play, the use of a specific stone type in a specific place is often time bound.

Flanders is not particularly rich in natural stone resources, at least in terms of quantity and diversity. Nevertheless, the built heritage of Flanders counts many natural stone types. The few natural stone resources Flanders

is rich of, are of good quality, have some remarkable properties and were intensively exploited and distributed in the past. In addition, many diverse stone types were imported, not the least from Wallonia, which has more natural stone resources. Also adjacent regions such as northern France, Luxemburg, Germany, The Netherlands, and the UK have provided natural stone to our areas. And over the last decades, this diversity only increased with the globalisation of the stone market.

Ghent is one of the oldest and most important cities of Flanders. In the Middle Ages it was even one of the largest cities in northwestern Europe. As such, some of the built heritage in Ghent spreads back in time over centuries. Moreover, Ghent was easily accessible for some of the most used historical stones in the region. Upstream, the river Scheldt provided easy access to Tournai limestone in the early Middle Ages and to some northern French resources such as Avesnes stone later in times. Downstream, the connection of the Scheldt with the Dyle and Senne rivers provided access to the agglomeration of Brussels and the white limestone, such as the Brussels stone and Lede stone, excavated there. Finally, the direct neighbourhood, the Scheldt-Dender interfluvium southeast of Ghent, yielded large amounts of Lede stone exploitations. The natural stone assemblage identifies Ghent the same way it does in other cities; it perfectly reflects how the building history relates to geology, geopolitics, economic development, transport possibilities and architectural trends. Especially Lede stone is strongly associated with the face of Ghent. A profound knowledge on this local resources is important for the conservation of the built cultural heritage in Ghent, northern Belgium and The Netherlands.

1

General introduction

This thesis deals with the properties of natural building stones, Lede stone in particular, in a cultural and historical context. To sketch this context, this chapter gives a non exhaustive introduction on natural building stones in general and more specifically in cultural heritage. The thesis covers the geological background, the petrophysical properties and the replacement of Lede stone and puts its weathering in perspective to its properties. The results provide a basis for case studies involving the preservation or replacement of Lede stone.

1.1 Natural building stones

Large quantities of rock are quarried as natural stone for construction and decoration. In 2011, 1.265 billion m² natural stone (m² is based on stone slabs of 2 cm thick) was used in construction and decoration, a number that shows a yearly increase (Montani, 2012). China is the largest supplier of natural stone from quarries, followed by India, Turkey, Iran, Italy, Brazil and Spain. Together these countries produce 77 % of the total volume of commercial natural stone.

Whereas the volume fraction of natural stone used in Belgium compared to the world consumption is marginal, Belgium takes the lead in the volumetric demand of natural stone per person, before Switzerland, Taiwan, South Korea, Italy and Portugal. This puts the affinity of Belgium with natural stone in the picture. In Belgium, the building sector segment Natural stone, granite, marble employed 5.911 people in 2013, good for a sales volume of 1.020.191.790 euro (Knack, 2015). This sector includes natural stone quarries, importers, specialized contractors and sculptors. The total Belgian production of natural stone is 850 10³ ton; compared to the import of 286 10³ ton of raw material and 1039 10³ ton of finished stone (Montani, 2012). The total production is dominated by Wallonia, where mainly Palaeozoic limestones and sandstones are extracted.

Sedimentary rocks

In general, rocks are classified in three groups: igneous rocks, sedimentary rocks and metamorphic rocks. Further classification exists within each group; for natural building stones this classification is standardised under EN 12670 (2001) and specifically in Belgium also PTV 844 (2005). Each type of rock has distinct characteristics and properties compared to others. Most rocks in Belgium are sedimentary rocks. Only few have an igneous (e.g. Quenast) or low grade metamorphic (e.g. in the Stavelot Massif) origin. The sedimentary rocks used as natural building stone in Belgium are dominantly limestone, sandstone and shale. The most famous is probably the Blue stone from the lower Carboniferous. Locally, also conglomerates (e.g. Burnot) or Quaternary tufas (e.g. Hoyoux valley) are used as building stone. Northern Belgium is mainly built by Mesozoic and Cenozoic sediments that cover the Palaeozoic basement of the Brabant Massif, and gently dip to the north-northeast. Hardrock of the Brabant massif outcrops upstream in the river valleys in the south of Flanders and

the north of Wallonia. The Cenozoic cover is mainly composed of alternating sand-clay packages, some of them continental, but most of them (shallow) marine. Aside from other resources, such as clay, the natural building stone resources from the Cenozoic cover are relatively sparse. They can be classified in three groups: sandy white limestones, sandstones and silicifications, ferruginous sandstones.

In Ghent, the sandy white limestones are the most dominant in the cultural heritage, together with imported stone, mainly from Wallonia and France.

Properties and durability

The specific properties of natural stone significantly contribute to their use and appreciation (e.g. Winkler, 1997). The intrinsic properties can be divided in aesthetical and technical (physico-mechanical) properties. The aesthetical properties mainly involve the amenity and appreciation of a stone, and will play a role in its selection and its use for applications that catch the eye. Technical properties include mass, dimension, strength and water transfer, which relate to the rock composition and fabric. They can be measured in several ways under several conditions, mainly depending on the application. They must satisfy the constructional requirements. Durability on the other hand is depending on the interaction between a rock's intrinsic properties and the extrinsic conditions, such as application and ambient environment.

1.2 Natural stone in cultural heritage

Ever since rocks have been used as raw material for constructions, natural building stone has become a long lasting material in architecture due to its excellent technical and aesthetic properties. It is pervasive in our daily life and our historic monuments. Natural stone in historic monuments is an expression of the local terrain, cultural evolution and socio-economic history of a region (Gomez-Heras et al., 2010; Devos et al., 2010; Ventola et al., 2012). Therefore, natural stone is an important part of the cultural heritage to which special attention is, or should be, paid during restoration works. However, the conservation of natural stone in monuments often encounters practical difficulties which are well described by Török and Prikryl (2010), mainly concerning their present-day availability. As such, there is a growing interest of, amongst other specialists, geologists in the

scientific studies for the conservation and preservation of our cultural heritage. This includes the identification and characterization of historic materials (Fronteau et al., 2010).

Stone damage

The weathering and deterioration of building stone are intensely studied (e.g. Schaffer, 2004), both under laboratory conditions and by in situ monitoring (e.g. Al-Omari et al., 2014, 2015). Damage can be conceived as integral loss of aesthetic value and/or decrease in technical performance (ICOMOS-ICS, 2008). It is governed by a combination of extrinsic factors and the intrinsic properties and can be gradual or catastrophic (McCabe et al., 2010). The possible ways of deterioration are too extensive and diverse to discuss here exhaustively, but they are typically grouped as chemical deterioration (e.g. dissolution-precipitation), physical deterioration (e.g. crystallization stress; temperature or humidity induced stress) and biomodification (e.g. fouling). More details can be found in Chapter 4 – 'Weathering and Deterioration' by Steiger and Charola (2011) and illustrations in ICOMOS-ICS (2008).

Conservation, restoration and the use of replacement stones

When a stone is damaged, an intervention is eventually forthcoming. The main principles of interventions on historic monuments are defined in the Venice Charter (ICOMOS, 1966) and other charters, resolutions and declarations adopted by ICOMOS. This also applies to natural stone in our cultural heritage. Building stone conservation allows the application of protective elements and possible treatments (e.g. desalinisation, consolidation, use of water repellents), either remedial or preventive, to preserve the stone. Restoration is a more profound intervention, with the aim to recover some lost stone characteristics. This can apply to situations where the structural integrity of a stone is compromised, or where there is harassing aesthetic damage. In this case, the stone can be repaired, e.g. repointing with repair mortars, or the stone can be partly or fully replaced. The choice for repair or replacement depends mainly on the state of the stone and economical considerations.

When a damaged stone is replaced, it should ideally be replaced by the same stone type from the original quarry. The use of original historic materials for replacement is, however, often restricted by the exhaustion or cessation of the exploitation. Sometimes, the origin of the original materials remains unknown. And economic factors also play a role in the

selection of replacement stones due to the emergence of cheap alien stones (Prikryl and Török, 2010). If for any case, it is not possible to use the original stone, it is important to consider which alternatives are most appropriate. In order to conserve the architectural value of a historical monument, the aesthetic and technical properties as well as the ageing characteristics of the newly implemented stones should fit the original stone as close as possible. In addition, badly chosen or inappropriate replacement materials can accelerate the original stone weathering (Gomez-Heras et al., 2010). The compatibility of the original stone type with its replacement material has therefore been assessed by several researchers (e.g. Beck and Al-Mukhtar, 2010; Nijland et al., 2010; Graue et al., 2011; Turmel et al., 2014).

The question of availability and alternative resources also applies to the Lede stone, used in historical monuments in Belgium and The Netherlands. In northern Belgium, restoration projects concerning Lede stone are continuously on-going. Despite of time bound availability of the original Lede stone, restoration works have used several replacement stones over the past century. Quist (2011) extensively listed several restoration philosophies during the 20th century with respect to the Lede stone in The Netherlands.

1.3 Aims and scope

In the very beginning of the 20th century, the Dutch architect Van Nieuwerkerke visited Ghent to study Reffroy stone (France) for the restoration of the Our-Lady-Cathedral in Breda (The Netherlands) (Van Nieuwerkerken, 1904). According to his notes, Lede stone was considered as a lower quality stone compared to its competitors and more specifically compared to Reffroy, notwithstanding he also mentioned the induration of Lede stone in the atmosphere. At that time, Lede stone was used for restoration works. Van Nieuwerkerke said that Reffroy stone had better properties, but nevertheless Lede stone was selected because it was cheaper. Today we observe the opposite, but the decision is based on the same criterion: Lede stone is often replaced by cheaper foreign limestone.

A decade before, architect Mortier, charged with the restoration of the House of the Free Boatmen in Ghent, praised Lede stone for its amenity and apparently did not share the concern of Van Nieuwerkerken. *'Il est permis*

de dire que, c'est à ces diverses circonstances et particularités ... pierres posées en délit présentent leur partie coquillière à front de la façade ... mis en oeuvre sans même prendre la précaution d'en enlever tout le bousin ... , que la plupart de ces monuments doivent une partie de leur irrégularité de patina, qui nest pas exempté d'un certain charme pittoresque' (Mortier, 1898). The observations and concerns of Van Nieuckerken and Mortier are still up-to-date and lead to the following question: **What is the spread in petrophysical properties between different Lede stone types, compact and fossiliferous, and how do they influence the durability?**

The replacement of Lede stone with different foreign stone types has definitely influenced the appearance and authenticity of our cultural heritage. The choice for appropriate replacement stone balances between aesthetic properties and technical compatibility. In practice, economic considerations also play a (large) role. Quist (2011) has performed a profound study of historical replacement material on selected historic buildings in The Netherlands, where Belgian white stone was used. He has put in evidence the replacement stones used, the selection criteria and the timeframe during which specific materials were used. This work addresses a complimentary research question: **What are the petrophysical considerations for the selection of replacement stones and how do they vary for the variety in Lede stone which is compact or porous and fossiliferous?**

When Lede stone is replaced according to good practice, this means that the stone was severely damaged. Field methods or sampling or laboratory research can be used to quantitatively assess a technical decrease in performance. However, the initiation of such research or of an intervention is often based on a visual assessment. Therefore, a survey was conducted to investigate the question: **How is damage perceived in the first place?** And if damage is determined by means of any assessment method, such as thin sectioning, then **what are the most diagnostic factors initiating damage to Lede stone?**

In summary, this work focuses on the characterization and performance of Lede stone as a contribution to the preservation and restoration of cultural heritage in Belgium and The Netherlands in general. Chapter 2 starts with a geological background on the Eocene deposits of Flanders and its white stone resources. Chapter 3 gives a geological setting and background on Lede stone. Chapter 4 provides a survey on the perception of damage and

the appreciation of natural stone and natural stone interventions. Chapter 5 presents an integral characterization study of the natural variability of Lede stone. These properties can be used to interpret the quality and durability of Lede stone. Chapter 6 and 7 provide new further insights in the deterioration phenomena on Lede stone. Here, fundamental contributions are made in the combination of techniques for characterization and in the study of weathering, especially in the study of weathering with time-lapse and continuous μ CT. Chapter 8 gives an overview on the most frequently used replacement stones in Ghent and northern Belgium, on the different aspects of stone compatibility, the decision-making factors and the complexity of finding an appropriate replacement stone, aside from using Lede stone itself. Chapter 9 presents a case study on a formerly unknown white stone in the historic tower ruin in Dudzele. It illustrates the need for identification of the natural stone and its preservation state, according to the principles investigated in the previous chapter. A final overview and future outlook is provided in Chapter 10.

References

- A Al-Omari, X Brunetaud, K Beck, and M Al-Mukhtar. Effect of thermal stress, condensation and freezing-thawing action on the degradation of stones on the Castle of Chambord, France. *Environmental Earth Sciences*, 71(9):3977–3989, 2014. doi: 10.1007/s12665-013-2782-4.
- A Al-Omari, K Beck, X Brunetaud, Á Török, and M Al-Mukhtar. Critical degree of saturation: A control factor of freeze-thaw damage of porous limestones at Castle of Chambord, France. *Engineering Geology*, 185: 71–80, 2015. doi: 10.1016/j.enggeo.2014.11.018.
- K Beck and M Al-Mukhtar. Evaluation of the compatibility of building limestones from salt crystallization experiments. *Geological Society, London, Special Publications*, 333(1):111–118, jan 2010. ISSN 0305-8719. doi: 10.1144/SP333.11.
- A Devos, G Fronteau, O Lejeune, C Sosson, E Chopin, and V Barbin. Influence of geomorphological constraints and exploitation techniques on stone quarry spatial organisation Example of Lutetian underground quarries in Rheims, Laon and Soissons areas. *Engineering Geology*, 115 (3-4):268–275, 2010. doi: 10.1016/j.enggeo.2010.05.004.
- EN 12670. Natural stone - Terminology, 2001.
- G Fronteau, C Moreau, C Thomachot-Schneider, and V Barbin. Variability of some Lutetian building stones from the Paris Basin, from characterisation to conservation. *Engineering Geology*, 115(3-4):158–166, 2010. doi: 10.1016/j.enggeo.2009.08.001.
- M Gomez-Heras, B J Smith, and H A Viles. Oxford stone revisited: causes and consequences of diversity in building limestone used in the historic centre of Oxford, England. *Geological Society, London, Special Publications*, 333(1):101–110, jan 2010. ISSN 0305-8719. doi: 10.1144/SP333.10.

- B Graue, S Siegesmund, and B Middendorf. Quality assessment of replacement stones for the Cologne Cathedral: mineralogical and petrophysical requirements. *Environmental Earth Sciences*, 63(7-8): 1799–1822, 2011. doi: 10.1007/s12665-011-1077-x.
- ICOMOS. The Venice Charter - International Charter for the conservation and Restoration of Monuments and sites. Approved by the 2nd International Congress of Architects and Technicians of Historic Monuments. Technical report, Venice, 1964, 1966.
- ICOMOS-ICS. Illustrated glossary on stone deterioration pattern, 2008. URL http://international.icomos.org/publications/monuments{_}and{_}sites/15/pdf/Monuments{_}and{_}Sites{_}15{_}ISCS{_}Glossary{_}Stone.pdf.
- Knack. Knack Trendstop - sectorindex, 2015. URL <http://trendstop.knack.be/nl/home.aspx>.
- S McCabe, B J Smith, P A Warke, and Geological Society. A legacy of mistreatment: conceptualizing the decay of medieval sandstones in NE Ireland. In R Prikryl and Á Török, editors, *Natural Stone Resources for Historical Monuments*, volume 333, pages 87–100, London, 2010. Geological Society.
- C Montani. Marble and stones in the world XXIII Report. Technical report, Aldus Casa do Edizioni, Carrara, 2012.
- S Mortier. Communications sur les recherches faites dans les anciennes carrières de Baelegem., 1898.
- T G Nijland, R P J Van Hees, and L Bolondi. Evaluation of three Italian tuffs (Neapolitan Yellow Tuff, Tufo Romano and Tufo Etrusco) as compatible replacement stone for Romer tuff in Dutch built cultural heritage. *Geological Society, London, Special Publications*, 333(1):119–127, jan 2010. ISSN 0305-8719. doi: 10.1144/SP333.12.
- R Prikryl and Á Török. Natural stones for monuments: their availability for restoration and evaluation. *Geological Society, London, Special Publications*, 333(1):1–9, jan 2010. ISSN 0305-8719. doi: 10.1144/SP333.1.
- PTV 844. Classificatie van gesteenten, 2005.

- W J Quist. *Vervanging van witte Belgische steen: Materiaalkeuze bij restauratie*. PhD thesis, TU Delft, Delft, 2011.
- R J Schaffer. *The weathering of natural building stones*. Donhead Publishing Ltd, London, 2004.
- M Steiger and A E Charola. Weathering and Deterioration. In S Siegesmund and R Snethlage, editors, *Stone in Architecture - Properties, Durability*, chapter Chapter 4, page 552. Springer, Berlin Heidelberg, 4th edition, 2011.
- Á Török and R Prikryl. Current methods and future trends in testing, durability analyses and provenance studies of natural stones used in historical monuments. *Engineering Geology*, 115(3-4):139–142, 2010. doi: 10.1016/j.enggeo.2010.07.003.
- A Turmel, G Fronteau, C Thomachot-Schneider, C Moreau, L Chalumeau, and V Barbin. Stone uses in Reims Cathedral: provenance, physical properties and restoration phases. *Geological Society, London, Special Publications*, 391(1):17–30, mar 2014. ISSN 0305-8719. doi: 10.1144/SP391.7.
- J J Van Nieuwerkerken. Verslag over het onderzoek ingesteld naar de kwaliteit van eenige natuurlijke steensoort, ten behoeve van de Restauratie van de Groote of Onze Lieve Vrouwe Kerk te Breda. Technical report, 's Gravenhage, 1904.
- L Ventola, P Giraldez, and M Vendrell. Selective use of stones in the medieval cathedral of Tarragona, Spain: construction and historical reasons. *International Journal of Architectural Heritage*, 6(5):478–488, 2012. doi: 10.1080/15583058.2011.585276.
- Erhard M Winkler. *Stone in Architecture*. Springer, Berlin, Heidelberg, 1997. ISBN 978-3-662-10072-1. doi: 10.1007/978-3-662-10070-7.

2

Eocene white limestone resources in northern Belgium

Northern Belgium possesses a large WNW-ESE striking outcrop of Eocene sediments (56.0 – 33.9 Ma). Central in this outcrop is the line Bruges - Ghent - Leuven. This thick Eocene sequence was deposited on southern North Sea bight. For Flanders and The Netherlands, where the local natural stone resources are mainly restricted to Cretaceous deposits and discrete lithifications in the Cenozoic cover, this Eocene outcrop is an important resource area for the production of natural stone. At different stratigraphic levels three types of sandy white limestones (Ypresian stone, Brussels stone and Lede stone) and a greenish-grey glauconiferous sandstone can be found. This chapter gives a brief overview on the geology of the three types of sandy white limestone, with an overview of Ypresian stone and Brussels stone at the end. Lede stone will be discussed in Chapter 3. This chapter is based on De Kock et al. (2015). Marleen De Ceukelaire contributed to the description of Ypresian stone, Prof. Dr. Jan Elsen contributed to the description of Brussels stone.

2.1 Geological setting

On the passive continental margin, in a southern bight of the North Sea, the deposits pass from continental and shallow marine deposits in the Paleogene Thanetian to marine deposits of the Eocene Ypresian after a hiatus related to a tectonic pulse at the end of the Thanetian. The lowermost Eocene sediments make up the Kortrijk Formation. In detail, this Formation is composed of four transgression-regression cycles, which do not perfectly coincide with the four defined stratigraphic Members (Vandenberghe et al., 1998). In general, it is assumed that sedimentation took place in a subsiding basin in an open marine environment. This gave rise to the famous deposits of Ypresian clay, that dominates the subsoil in West- and partly East-Flanders and to which also the above Kortemark Member (Tielt Formation) is accounted (Jacobs et al., 2000). In the south of East-Flanders and the adjacent part of Flemish-Brabant, the top part of the Kortrijk Formation consists of alternating silty clay to clayey silt, defined as the Moen Member or as Roubaix Member. It is in this top part that lithified horizons of Ypresian stone occur within the silty layers. These were deposited above storm wave base, on a continental margin rich in benthic *Nummulites planulatus*, resulting often in cross-layered accumulations of the latter.

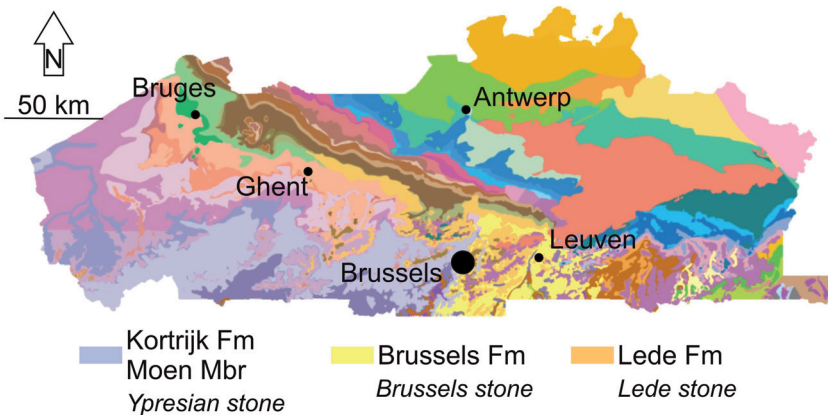


Figure 2.1: Geological map of Flanders (based on Databank Ondergrond Vlaanderen). Colour legend of the discussed formations in Fig. 2.2.

West of the Senne river, the deposits of the Ypresian clay were followed by alternating sand and clay deposits (Steurbaut, 1998): the Tielt Formation (Egem Member), Gentbrugge Formation (Merelbeke, Pittem and Vlierzele Member) and Aalter Formation. The base corresponds to an erosive surface and the infilling deposition of the Egem Member corresponds to a lowstand system tract, followed by transgressive deposits that evolve into highstand system tract deposits of the Pittem Member (Jacobs and De Batist, 1996). The following sequence starts with the Vlierzele Member which is a lowstand system tract, infilling large erosive surfaces progressively from the west to the east (Vandenberghe et al., 1998). On top, the glauconite-rich sands of the Aalter Formation represent transgressive to highstand system tract deposits (Vandenberghe et al., 1998). Notwithstanding that a greenish-grey glauconiferous sandstone can be found at different levels, these deposits are of low importance in the context of white limestone.

East of the Senne river, however, this sequence was absent and the progressive infill of the erosive surface boundaries from west to east took place subsequently during the transition from Ypresian to Lutetian (Houthuys, 2011). This sedimentary infill, known as the Brussels Formation, was deposited above an erosive surface after a global sea level drop. This low sea level allowed the erosion of large north-south trending valleys in the Brabant area, from the Senne river in the west to the Haute Mehaigne and Grote Gete in the east. This erosive surface was first flattened by wave action during the following transgression, when the sea entered these valleys forming a stretched sea bay or estuary. Sedimentation of the Brussels Formation possibly started during this transgression, but took mainly place during the subsequent highstand system tract, progressively filling the bay with sediment from the west. The Brussels Formation, or Brussels Sands, are quite heterogeneous and have an alternating high and low carbonate content and a fluctuating glauconitic content. Amongst other fauna, these sands contain *Nummulites laevigatus*. Near the border of the bay or estuary, several sandy limestone horizons were formed, having a typical thickness of 20 cm, in the eastern border defined as Gobertange stone and as Diegem stone in the west. These are separated by sand bodies of 50 cm to more than a meter. Except white sandy limestone, also ferruginous sandstone and tube shaped silicifications can be found in this Formation. Currently, the Brussels Formation defines parts of the topography along the Senne and Dyle.

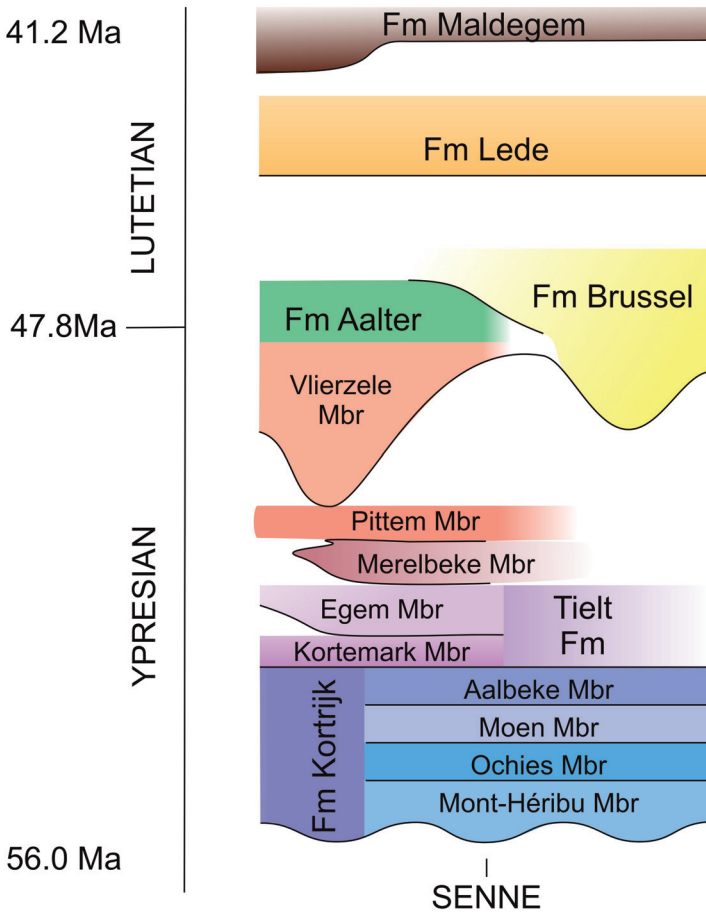


Figure 2.2: Chronostratigraphic cartoon of the early and middle Eocene deposits in Flanders (inspired on Vandenberghe et al. (1998)), with colour legend for Fig. 2.1 and Fig. 2.4.

After a hiatus of 2 Ma ('NP15a hiatus'), during which the top of the Aalter Fm and Brussels Fm were eroded, a new transgression initiated the deposition of the Lede Formation (Jacobs and Sevens, 1993). This hiatus could have been the result of (the onset of) an epirogenetic movement of the Brabant Massif (Herman et al., 2000) and the Weald-Artois ridge (Fig. 2.3). This hiatus is characterised by a sedimentation stop more distal; the Lede Fm lies para- or disconform on top of the Aalter Fm in the north

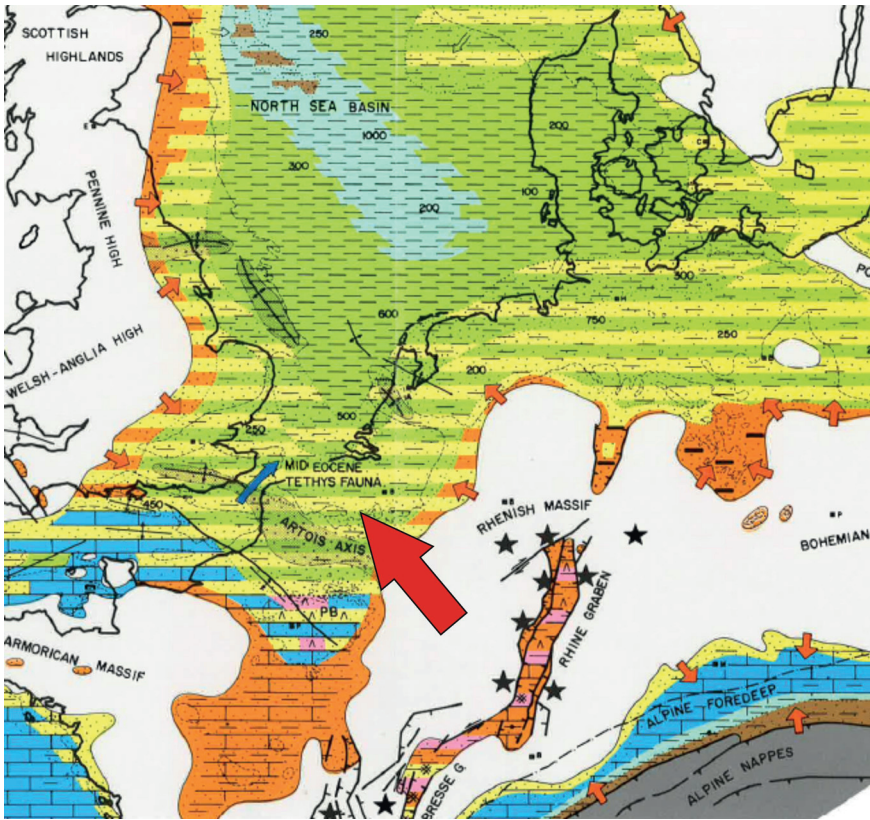


Figure 2.3: Eocene palaeogeographical map of northwestern Europe with an indication of the depot centre of Lede sands (arrow), adopted from Ziegler (1990).

(currently offshore) and on top of the Brussels Formation to the south (in Cassel, France) and east (Fig. 2.2). In the more proximal part of the southern North Sea bight (e.g. Balegem), the Lede Fm cuts through these Formations on to the Vlierzele Member. In this part, the hiatus is represented by a remaining basal conglomerate that correlates with the Formations more distal. The Lede Fm contains a rich foraminiferal assemblage, amongst them planktonic *Miliolina* and benthic *Rotaliina* (*Nummulites variolarius*), which indicates a shallow marine environment. Several concentrated shell layers, so-called lumachelles, are attributed to the action of storm waves. These deposits wedge out to the south and southwest, against a rising Weald-Artoid ridge. Near Ronse, close to its southernmost outcrops, Fobe and Spiers (1992) described a beach facies. In general, the Lede Fm has a high carbonate content due to bioclastic

material, and lithified layers occur at several levels. In general, three stone layers are described in the Scheldt-Dender interfluvium. Near Brussels, up to five (Gulinck, 1949) or even fifteen (Camerman, 1955) stone layers have been described. The Lede Fm is topped by the Maldegem Fm, which continues into the Bartonian.

During the Ypresian to Lutetian, the North Sea Basin was located in the north-northeast of Flanders, today resulting in an outcrop band perpendicular to this direction. In the current landscape, which is cut by river erosion, the lithified horizons outcrop at different locations. They were often exploited in open air quarries, but in the region of Brussels, also superficial mining was common practice.

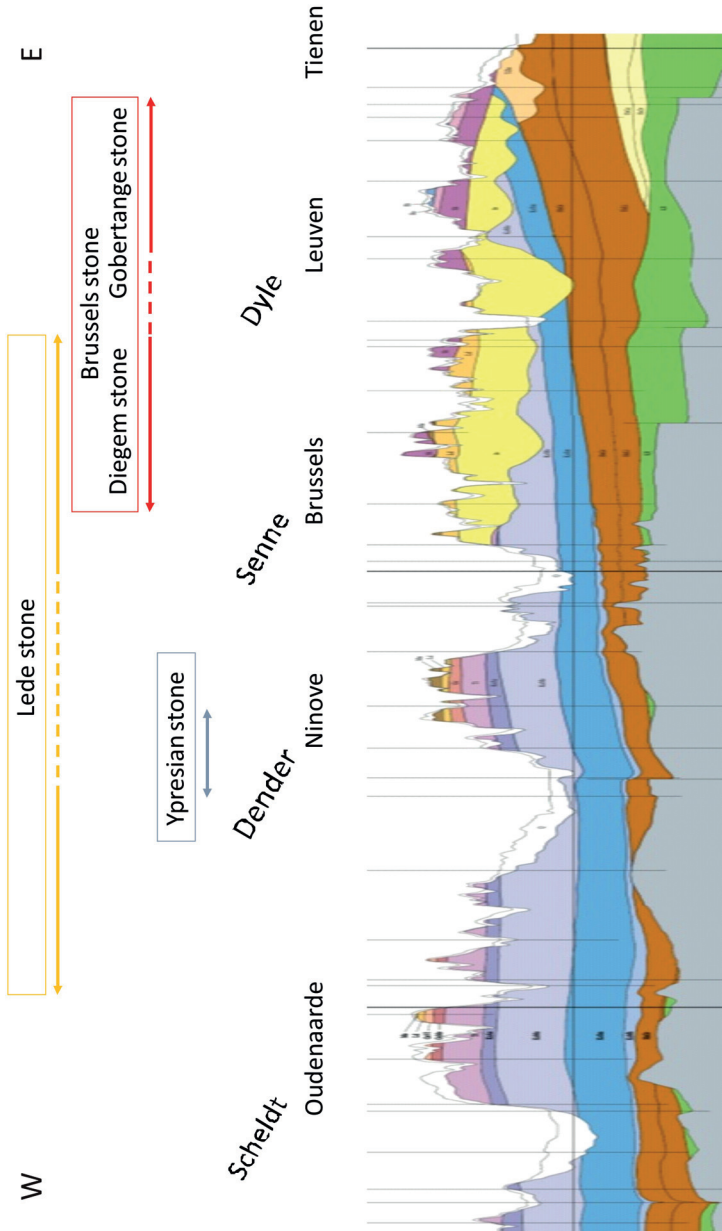


Figure 2.4: E-W cross-section of southern Flanders, with indication of the occurrence of Lede, Brussels and Ypresian stone (based on Databank Ondergrond Vlaanderen). Colour legend similar to Fig. 2.2.

2.2 Ypresian stone

Ypresian stone can easily be identified by the presence of *Nummulites planulatus*, which grow to a centimetre in size. This differs with Ledestone where the average size of *Nummulites variolarius* is typically 1–2 millimetre. In Ypresian stone, the *Nummulites* are often aligned and accumulated in cross-bedding. Other macrofossils are sparse; occasionally some bivalves or gastropods (*Turritella*) can be found. From thin section, this limestone contains a fine to very fine quartz fraction (10–30 vol.%), with a relative high amount of glauconite (up to 10 vol.%). It is mainly cemented with an ferroan calcite (micro-)sparite and epitaxial growth on the *Nummulites*. Depending on the amount of *Nummulites*, it can be classified as a grainstone to rudstone (Dunham, 1962).

In buildings, most Ypresian stones develop an intense brown rust-coloured patina, while stones which are exposed to exfoliation or scaling show a more greenish colour (Fig. 2.5A and B). When the stone is almost purely built out of *Nummulite* concentrations, the appearance can be white. Cross bedding, whether or not indicated by *Nummulite* concentrations, can be very distinctive for the rock, but is not always visible. The stone shows scaling and exfoliation when it is used perpendicular to its bedding. In these cases, the original greenish tint of the stone is often visible.

The block size can vary; a thickness larger than 15 cm is not uncommon, but often restricted to a maximum of 30 cm. Some blocks can be very long, such as the 1.8 m long Ypresian stone in the St Bartholomeuskerk in Geraardsbergen, without exceeding the normal stone height.

The quarrying of Ypresian stone has left few traces in the landscape. The stone was intensively quarried along the valley flanks of the Dender river (Fig. 2.4), in the south of East-Flanders and in the west of Flemish-Brabant. One of the few references leads to the *Geitenbos* in Zandbergen (Cosyns, 1986) (Fig. 2.6). At this location, stone was extracted for the finalisation of the Our-Lady-Assumption church (a.o. the tower) of Ninove at the beginning of the 18th century.

Ypresian stone is mainly used proximate to its source area: Ninove, Geraardsbergen, Oudenaarde, Ronse, Flobecq in the south of East-Flanders and also in Aalst, close by and easily accessible downstream the Dender river (Fig. 2.6). Further away, the stone can be found in Antwerp, Ghent, Bruges and even in The Netherlands (e.g.

Scheveningen). In these cases, it often concerns a couple of individual Ypresian stones, which are blended with other white limestone. Ypresian stone is mainly found in ashlar in the masonry of buildings that date back to the 17th and 18th century, but it can also be found as window and door frames, ground sill and occasionally as floor tiles.

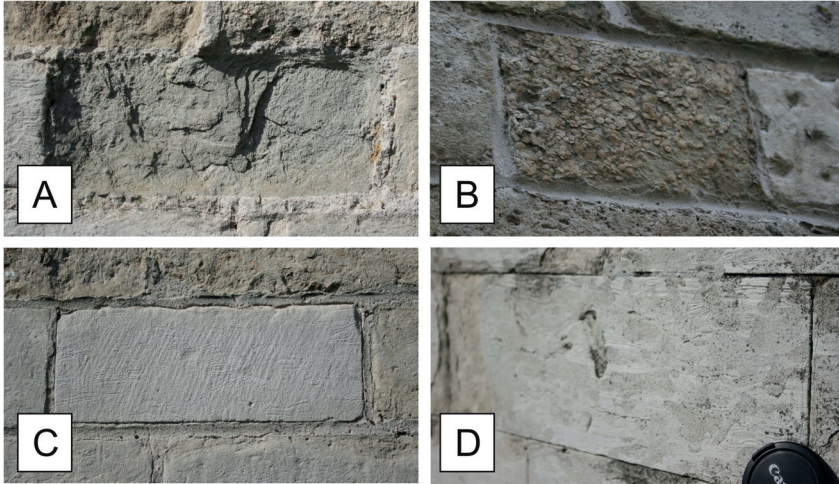


Figure 2.5: Macroscopic example of A) Ypresian stone perpendicular to bedding, with green colour and exfoliation; B) Ypresian stone perpendicular to bedding with Nummulite concentrations; C) Brussels stone and D) Gobertange stone; all in the same scale.

2.3 Brussels stone

Brussels stone is typically paler than Ypresian stone or Lede stone. Also the size of Brussels stone is typically smaller than that of Ypresian stone or Lede stone, especially in height. By consequence, Brussels stone and Lede stone are often easily distinguishable in masonry. Brussels stone is also more compact and rather homogeneous (except for bioturbation), with the absence of macroporosity or macrofossils, whilst Lede stone is much more heterogeneous, with the regular occurrence of macrofossils and -porosity.

Brussels stone was quarried in the area east of Brussels and in the northwest of Jodoigne (Fig. 2.7). To distinguish between both production centres, the name Diegem stone is used for stone coming from the Brussels area and Gobertange stone for those coming from the region of Jodoigne (Fig.

2.4). Near Brussels, Diegem stone was quarried in Diegem, Zaventem, St Pieters Woluwe, Oudergem and Ukkel, in open air quarries (Fig. 2.7). Gobertange stone was mainly quarried subsurface in Mélin - Lathuy and Saint-Remy-Geest in small mines, up to 30 m depth (ASBL Gobertange, 2000) (Fig. 2.7). Today, one open air quarry is active, extracting around 10 horizontal stone layers in Mélin - Jodoigne (Carrière de Gobertange, Entreprise Bernard Pierrot et Fils S.A.).

Brussels stone is used in several historical buildings in Flanders and The Netherlands. At the beginning of the Middle Ages, it seems subordinate to Lede stone, but before the end of the Middle Ages, Brussels stone - Diegem variety is also a common building stone. Examples can be found in the 15th century City Hall of Leuven and the 16th century highrise masonry of St Bavo's cathedral in Ghent. In both cases, Diegem stone is used aside Lede stone. From the end of the 18th century, Gobertange stone comes to the fore, and becomes important in new constructions, such as the neogothic castle in Meldert, and restorations, such as the 19th century restoration of the City Hall in Leuven or the restoration of the Cathedral of Our Lady in Antwerp, where Gobertange was used to replace Lede stone. Also in The Netherlands, e.g. in the City Hall of Gouda (Quist, 2011), Gobertange was used during the 20th century as replacement stone for Lede stone.

In addition, Diegem stone and in less quantity Gobertange were also used as pavement or as levees and embankments (Goudriaan, 1833; Slinger et al., 1982).

2.3.1 Diegem stone

Diegem stone is a white to grey sandy limestone, much less coloured than Lede stone, but also often less white than Gobertange stone (Fig. 2.5C). Some lamination can be found but this is far less pronounced than in Gobertange stone. On the other hand, more homogeneous stones can rather resemble Lede stone. Examples of macroscopic bioclasts are sparse but exist and are mainly shell ghosts. Some stones can show Liesegang structures. In general, the petrography and petrophysics of this stone are not very exhaustively studied, as no active quarries remain. However, a profound study would be welcome to map the possible variability of this stone, its similarities and differences with other limestones and to know its properties for stone conservation.

2.3.2 Gobertange stone

Gobertange stone has a very typical texture with a pronounced lamination and sometimes intense burrowing (Fig. 2.5D). The wavy to lenticular lamination represents an alternation of fine, white, carbonate rich with more grey and sandy lamina. Differential weathering pronounces this lamination, contributing to the rock's amenity. Intense bioturbation, burrows with branching chambers with circular to elongated cross-sections, is often present. The resulting texture is often by comparison described as an oak texture. The microscopic texture is a laminated wackestone (white lamina) to packstone (grey lamina) ??, with a matrix of iron-poor microsparite, micritic patches and locally some silicifications. The main detritic components are fine grained quartz (20–30 %; < 250 µm), feldspars (ca. 5 %), glauconite and accessory minerals. Shell fragments can be present, but in general the macrofossil content is sparse. Typical microfossils are foraminifera (e.g. *Cibicides*), bryozoa and echinoderm fragments.

2.4 Nomenclature of the white limestones

The name of natural stone often refers to its origin, its texture or its geological context, whether or not supplemented with an additive that refers to its colour. The nomenclature of the Belgian Eocene white stones used in this work can use some clarification, as different synonyms or historical names exist for the same rock or even for the different rocks.

Ypresian stone refers to the old lithostratigraphy to which the deposits belong. Today, the Ypresian is an official stage in the IUGS-ICS stratigraphy (Steurbaut, 2006) and the name can be retained. The often used name Nummulitic limestone refers to the abundancy of large eye-catching *Nummulites*.

The name Brussels stone is more confusing. In the first place it refers to the Brussels Fm (or Brussels Sands), not to Brussel as main production centre. Nevertheless, a lot of Brussels stone was quarried in Brussel and historical references in this context do exist. However, in such cases, Brussels stone can also refer to Lede stone that was quarried in or around Brussels. Brussels stone as a reference to its production centre can thus best be avoided. The common term Brusselia(a)n(se) stone refers to its old

Belgian lithostratigraphy, and more specifically to the variety that was quarried in the area of Brussels, although that theoretically Gobertange also belongs to the Brusselian (or Bruxellian). Today, Brusselia(a)n is disused as a stage (De Geyter et al., 2006) and only has an informal status. In The Netherlands, on the other hand, it is more common to use Gobertange stone for all stones from the Brussels Fm. In this work, Brussels stone is used as overall term for stones from the Brussels Fm, and Diegem stone and Gobertange stone is used for the macroscopic distinguishable varieties that were quarried near Brussels and near Jodoigne respectively.

Lede stone is currently the most common name for what is also known as Balegem(se) stone. Here as well, the name Lede needs to be understood as a reference to the Lede Fm in which the stone occurs. Lede is thus not a reference to the town of Lede, where the stone was historically quarried. Balegem(se) stone, on the other hand, does refer the village in which the quarry is located. However, as at this point it is not possible to link every stone back to its exact exploitation, the reference to its Formation is most suited.

Existing synonyms or old nomenclature used for Lede stone:

Ledia(a)n(se) stone, Balegem(se) stone, Diegem(se) stone (also used for Brussels stone; see above), Affligem/Hafflichen stone, Houtem(se) stone, Dender stone, Grimbergen(/se) stone, *witten ordu(y)n(e)* (white hardstone), Dieleghem(se) stone, Brussels stone, Dilbeek(se)/Dilbecq stone, Meldert(se) stone.

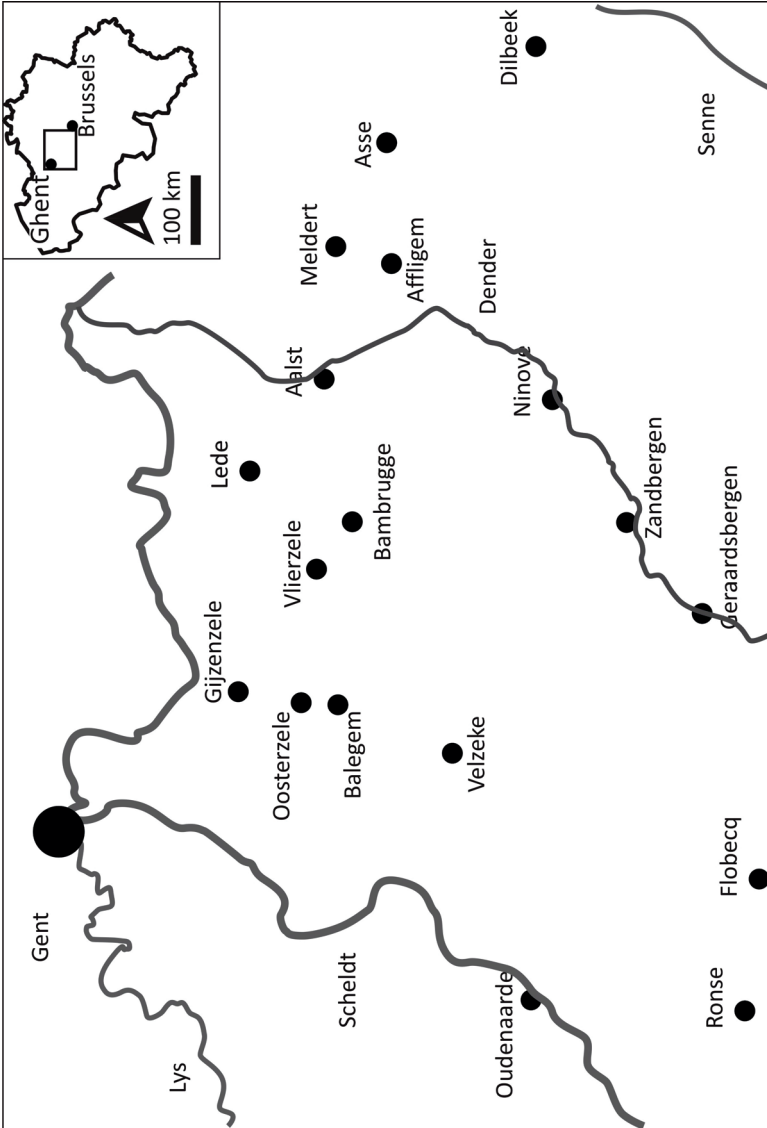


Figure 2.6: Map from the area in between Ghent and Brussels, with indication of the most prominent locations in this chapter and Chapter 3.

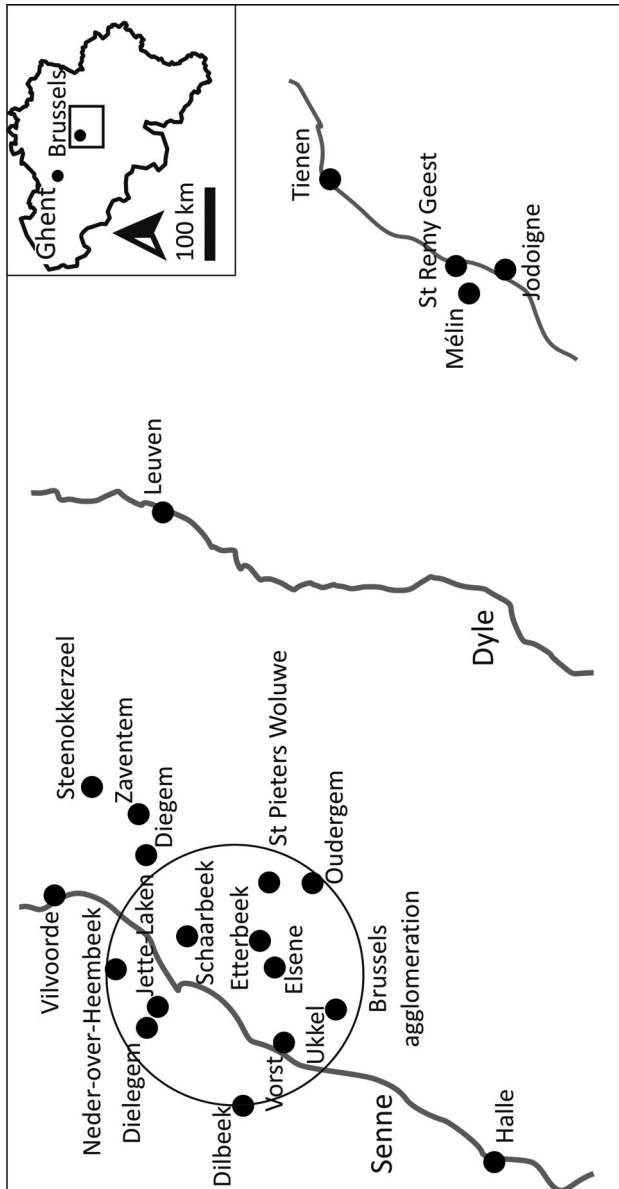


Figure 2.7: Map from the area in around and east of Brussels, with indication of the most prominent locations in this chapter and Chapter 3.

References

- ASBL Gobertange. *La Gobertange: une pierre, des hommes*. Editions Rencontres A.S.B.L., Glimes, 2000.
- C Camerman. Le sous-sol de Bruxelles et ses anciennes carrières souterraines. *Annales des travaux publics de Belgique*, 2-3:5–28, 1955.
- E Cosyns. *Het Geitebos (Zandbergen, Oo.-Vl.): een historisch ecologische studie*. Ghent University, Ghent, 1986.
- G De Geyter, E De Man, J Herman, P Jacobs, T Moorkens, E Steurbaut, and N Vandenberghe. Disused Paleogene regional stages from Belgium: Montian, Heersian, Landenian, Paniselian, Bruxellian, Laekenian, Ledian, Wemmelian and Tongrian. *Geologica Belgica*, 9(1-2):203–213, 2006.
- T De Kock, M De Ceukelaire, J Elsen, and V Cnudde. De Eocene witte stenen van Noord-België. *Grondboor & Hamer*2, 69(5/6):84–91, 2015.
- R J Dunham. Classification of carbonate rocks according to depositional texture. . In W E Ham, editor, *Classification of carbonate rocks*, volume Memoir. 1, pages 108–121. American Association of Petroleum Geologists, 1962.
- B Fobe and V Spiers. Sedimentology and facies distribution of the Lede Formation (Eocene) in Belgium and northern France. *Contr. Tert. Quatern. Geol.*, 29(1-2):9–20, 1992.
- B H Goudriaan. Rapport van de hoofd-ingenieur bij den Waterstaat, B.H. Goudriaan, wegens een gedaan plaatselijk onderzoek, omtrent het gebruik van sommige in Duitschland voorhandene steensoorten, tot vervanging van de Escosijnsche, Doorniksche en Vilvoorsche stenen. Technical report, 1833.

- M Gulinck. Oude Natuurlijke Bouwmaterialen in Laag- en Midden-België. *Technisch-Wetenschappelijk Tijdschrift*, 18(2):25–32, 1949.
- J Herman, E Steurbaut, and N Vandenberghe. The boundary between the middle Eocene Brussel sand and the Lede sand Formations in the Zaventem-Nederokkerzeel area (Northeast of Brussels, Belgium). *Geologica Belgica*2, 3(3/4):231–255, 2000.
- R Houthuys. A sedimentary model of the Brussels sands, Eocene, Belgium. *Geologica Belgica*, 14(1-2):55–74, 2011.
- P Jacobs and M De Batist. Sequence stratigraphy and architecture on a ramp-type continental shelf: the Belgian Palaeogene. *Geology of Siliciclastic Shelf Seas*, 117:23–48, 1996.
- P Jacobs and E Sevens. Middle Eocene sequence stratigraphy in the Balegem quarry (western Belgium, southern bight North Sea). *Bulletin de la Société belge de Géologie*, 102(1-2):203–213, 1993.
- P Jacobs, M De Batist, B Van Bavinckhove, and E Sevens. Sedimentary environments and depositional history in the Belgian Basin during Ypresian times (Lower Eocene, Southern Bight North Sea). *Zentralblatt für Geologie und Paläontologie*, 1999(3):419–440, 2000.
- W J Quist. *Vervanging van witte Belgische steen: Materiaalkeuze bij restauratie*. PhD thesis, TU Delft, Delft, 2011.
- A Slinger, H Janse, and G Berends. *Natuursteen in monumenten*. Bosch & Keuning / Rijksdienst voor de Monumentenzorg, Zeist, 1982.
- E Steurbaut. High-resolution holostratigraphy of Middle Paleocene to Early Eocene strata of Belgium and adjacent areas. *Palaeontographica, Abt. A*, 247:91–156, 1998.
- E Steurbaut. Ypresian. *Geologica Belgica*, 9(1):73–93, 2006.
- N Vandenberghe, P Laga, E Steurbaut, J Hardenbol, and PR Vail. Tertiary sequence stratigraphy at the southern border of the North Sea Basin in Belgium. *SEPM Special Publication*, 60:118–154, 1998.
- P A Ziegler. *Geological atlas of western and central Europe*. Shell International Petroleum Maatschappij, 1990.

3

Lede stone

Lede stone is the youngest white limestone found in the Belgian Eocene deposits (Chapter 2). This chapter gives a general overview of the occurrence, appearance, and historical use of Lede stone, based on literature and in-house testing. Chapter 5 presents a more detailed study on the natural variability and intrinsic properties of Lede stone. Chapter 6 and 7 give more details in the aspects of weathering and Lede stone replacement. This chapter contains information from De Kock et al. (2014) and De Kock et al. (2015) where the co-authors assisted in the discussion.

3.1 Lede Formation

Lede stone is found in the Lede Formation. The shallow marine sands from this Formation were deposited during the Lutetian (Eocene) (Fig. 2.2) in a southern North Sea bight (Jacobs and Sevens, 1993; Jacobs and De Batist, 1996). These sands are interpreted as a stepwise transgressive deposit with correlative unconformities overlying a ravinement surface. Some lithified layers within these sands gave rise to natural building stone resources. West of the Senne, three more or less continuous stone layers can be found. East of the Senne, their thickness and continuity decreases, and Camerman (1955) has described 9–11, sometimes up to 15 different stone levels. Three lateral facies have been described by Fobe and Spiers (1992); the Einsdale facies, the Meldert facies and the Mont des Récollets facies. They describe the most important Meldert facies as a shallow marine facies with storm deposits. This facies includes the principal building stone resource. The Mont des Récollets facies is a deeper marine facies without storm beds, found to the north, where these NNE-dipping layers are buried by younger Cenozoic sediments, and to the west, where outcrops can be found in the hill flanks of some outliers, near Heuveland and Cassel (France). The third facies from the southernmost outcrop near Ronse represents more near shore deposits. The latter two facies are less relevant as a stone resource.

3.2 Historic production and use

Lede stone is abundantly used in the region where it outcrops (Fig. 2.4). Beside this, it is also traded and transported to the corners of Flanders and up north to The Netherlands (Hurx, 2012), as far north as Texel (oral communication Dr. Timo Nijland). It is mainly used as freestone, for masonry, door and window frames, sill pavement or sculptures. The outer façade of buildings could either be constructed entirely in Lede stone, either in combination with other materials, such as Brussels stone and brick. In such combinations, Lede stone was often reserved for corner blocks and frames.

The oldest evidence of quarrying and use of Lede Stone dates back to Roman times. Archeological finds prove the mining and use of Lede Stone around Balegem during the 2nd and 3rd century. Such records are

exhibited at the Provincial Archeological Museum (PAM) in Velzeke (Nijs, 1990) (Fig. 2.6). However, up to the 11th century, the use of Lede stone remained marginal. Together with the emergence of Gothic architecture, the production of Lede stone commenced and developed as commercial activity. From the 12th century and especially during the 14th and 15th century Lede stone is one of the most, if not most, important building material in northern Belgium. It was used in rural architecture, but it is more notable in prestigious buildings such as churches, city halls and guild houses in the medieval Belgian cities.

The Abbey of Affligem governed one of the first known commercial quarries in Meldert, near Aalst, and the region of Asse in the 12th and 13th century (Fig. 2.6). They extracted Lede stone first for constructions under its own management, later for export to different areas in Flanders and The Netherlands (Groessens, 2011). Soon, others would follow their example. The Abbey of Dielegem was probably the most important producers in Brussels with quarries in the northwest of Brussels, a.o. in Neder-over-Heembeek. Stone from the latter was respected as good in quality and large in size (Camerman, 1955). In the area of Brussels, Lede stone was mainly quarried on the southern part (e.g. Oudergem, Elsene, Vorst, Ukkel) and the western part (e.g. Dilbeek, Neder-over-Heembeek) (Fig. 2.7). Stones were sometimes extracted in open air quarries, but mainly by underground mining, sometimes up to 15 m deep (Camerman, 1955). The exact locations of these ancient underground quarries are not entirely known, but Camerman (1955), after his study, grouped them in six different areas: Etterbeek-Oudergem, Elsene-Boendaal, Ukkel-Vorst, Linthout (Etterbeek), Ketelberg (Etterbeek), Laken-Jette (Fig. 2.7).

Architectural developments coincide with the further development of exploitation sites and stone trading. By the 14th and 15th century, the stone business would evolve into a modern structure (Hurx, 2012). Especially in the area of Brussels, several private stone suppliers emerged, leasing ground and exploiting it on independent base. Stone masons and architects mutually benefited from each other. Vilvoorde, on the border of the Senne, north of Brussels, acted as the commercial centre where stone from around Brussel was gathered and further distributed to the north. Southeast of Ghent quarries were also operated in private property during the 13th and 14th century (De Smet et al., 2003; Cnudde et al., 2009), with important quarries in Oosterzele and especially Vlierzele (Fig. 2.6). Here, stone was quarried in open air. But whereas the shipping from stone

around Brussels is well documented, transport from the area southeast of Ghent has left fewer traces. The export of stone from Brussels had a large coverage in Flanders, also to Ghent, and The Netherlands, while the export of stone from southeast of Ghent was probably more restricted to the area of Ghent itself.



Figure 3.1: Cover page of *Oryctographie de Bruxelles* (Burtin et al., 1784), showing an open air quarry (left) and a subsurface mine (right) in Brussels.

Socio-economic factors governed the rise and fall of Lede stone exploitations. Events as the Hundred Years War in the 14th century had a negative impact on economics and could have restricted use and distribution of Lede stone, which was to revive by the end of the 14th century. Under the Burgundy sovereignty of the 15th century, the wealth in Flanders re-established. This is certainly the era par excellence of Lede stone, reflected in the amount of historical buildings for which the Lede stone serves great purpose in their appearance. One of the oldest examples is the 13th century *Schepenhuis* in Aalst, now part of the Belfry. In the 14th century Lede stone was used by prominent architects for prestigious buildings. Architect Jan van Haelst ordered the stone from Vlierzele for the building of the Clothmakers' Hall and St Michael's Church in Ghent (Van der Kelen, 1996; De Smet et al., 2003) and architect Peter Appelmans, working on the Cathedral of Our Lady in Antwerp visited the quarries owned by the Abbey of Affligem (Groessens, 2011). Amongst the prominent 15th century examples can be considered: the City Hall of Bruges, St Bavo's Cathedral and the Gothic wing of the City Hall in

Ghent, the Our Lady Church in Breda (The Netherlands) and the St Bavo Church in Harlem (The Netherlands) (Quist, 2012) where stone was supplied from the area of Dilbeek and Affligem (Slinger et al., 1982). At the St Jan's Cathedral in 's-Hertogenbosch (The Netherlands), Lede stone was supplied from Dilbeek at the end of the 15th century and from Dielegem at the beginning of the 16th century (Peeters, 1985) (Fig. 2.7).

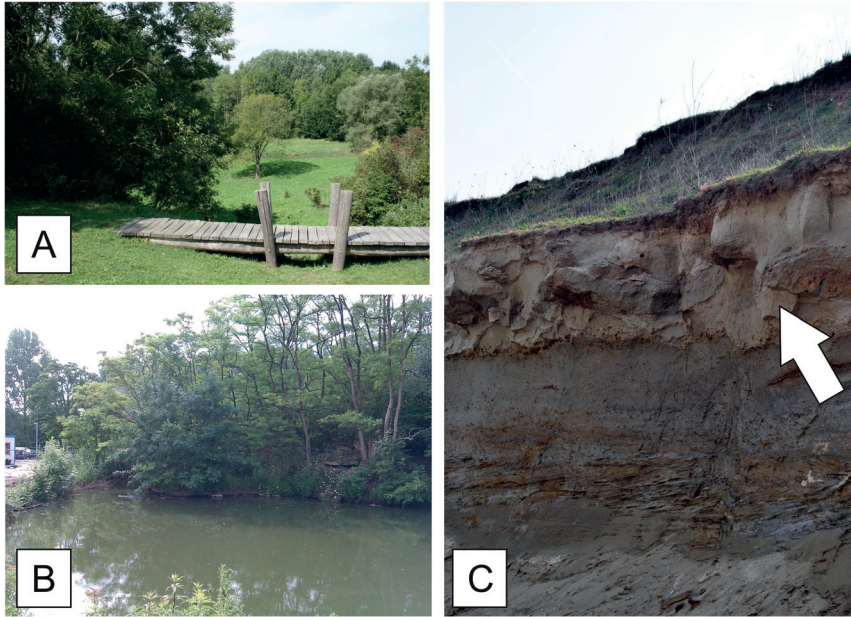


Figure 3.2: Photos of (ancient) Lede stone quarries. A) topographical relicts of historical quarrying at De Wolfspuiten in Dilbeek; B) pond with some piled residual Lede stone as quarry relict at De Steenberg in Bambrugge; C) Balegro quarry anno 2012 with stone layer (white arrow) at the sharp erosive base of the Lede Fm, with a basal gravel.

During the 16th century, the production centre of gravity southeast of Ghent shifted from Vlierzele towards Balegem (De Smet et al., 2003) (Fig. 2.6). The House of the Free Boatmen and the Guildhouse of the Bricklayers in Ghent are magnificent examples of late Gothic constructions in stone from Balegem. The Renaissance wing from the City Hall of Ghent was built during the end of the 16th and the beginning of the 17th century. Since the 17th century, Lede Stone was increasingly used as a decorative element in combination with brick masonry. Quarries in the area of Brussels remained important during the 17th and 18th century, but stopped by the end of the 19th century (Gulinck, 1949). The Neogothic St

Servaas church in Schaarbeek is one of the last monuments built integrally in Lede stone in 1876 (Fig. 2.7). The stone was supplied from Steenokkerzeel. After this date, with a very few exceptions, Lede stone was mainly integrated as elements, e.g. in the St Peters railway station in Ghent in 1913. In between 1866 and 1905, some quarries were opened in Balegem, Oosterzele, Gijzenzele, Lede and Bambrugge and stone was retrieved from the railroad construction between Ghent and Brussels. Bambrugge was the last quarry to close in 1942. In 1966, a new quarry opened in Balegem that remains active until today. In 2010, this quarry was taken over by Groep Verhelst and exploited under Balegro BVBA. Anno 2012, there was a stock of 10 661 m³ stone and more to be exploited (van der Horst, 2012).

The production of such large volumes of Lede Stone was and remains dependent on quarrying at many locations with only limited volumes of stone being sourced from the subsurface. This contrasts with many other natural resources, where quarries produce large volumes from one location.

It is impossible to determine the production rate or total volume. The total volume of Lede Stone for constructing the 15th century St Walburga Church in Oudenaarde amounted 1108 m³ (Van der Kelen, 1996). A small recalculation demonstrates that this is equivalent to a quarry pit with a surface area of more than 1000 m², assuming a useable total thickness of 1 m for the typical occurrence of three stone layers. The total surface over which stone has been quarried over the centuries must therefore be reasonably high.

Another illustration on the concept of production volume can be found in Slinger et al. (1982). They mention the excavation of 750 ton Lede stone with the construction of the highway between Ghent and Brussels. After removing the thin blocks and the soft outer layers, 100 ton of useable rock remained, which could result in 60 ton of finished product or less than 1/10 of the original volume. This batch was tested to be used at the restoration of the *Nieuwe kerk* in Amsterdam (The Netherlands), but eventually, this was discarded because the cost-benefit was too low as the entire 750 ton had to be bought.

3.3 Appearance

Lede Stone is a mixed siliciclastic-carbonate rock, consisting of a quartz fraction together with other detrital grains of glauconite and carbonate allochems with a calcite matrix/cement. Therefore it has been classified either as sandy limestone or as calcareous sandstone. Since the amount of carbonate exceeds 50 vol.% of the rock, this rock can be preferably classified within carbonate rock classifications. In general, it can be determined as a sandy sparry packstone (Dunham, 1962), a poorly washed sandy biosparite (Folk, 1959) or as a sandy allochem limestone (Mount, 1985). Given the natural variability in the stone, more precise denomination is best provided to individually assessed stone blocks.

The nature of the bioclasts indicates a shallow marine fauna. The most diagnostic fossils are the foraminifera *Nummulites variolarius* and the serpulid *Ditrupa strangulata*. Bivalves, gastropods, echinoderms and shark teeth are the most common macrofossils, which are commonly deposited as shell beds. Especially casts of *Turritella* gastropod can be striking, but are far from common. The microfauna are predominantly foraminifera, mainly miliolids and ostracods. The siliclastic composition is dominated by a bimodal quartz population (up to 40 vol.%) of subangular very fine sand supplemented with rounded medium sized sand. Nijs (1980) studied the grain size distribution of several samples in detail after decalcification, and concluded that this sand fraction is finer compared to other local building stones, such as fieldstone or Gobertange. He also measured that 10 % of the siliclastic residu is smaller than 50 µm. Glauconite is commonly present in 2–3 vol.%. Accessory minerals are feldspars, zircon, tourmaline, micas and opaque minerals (e.g. pyrite).

Matrix may be present, but is sometimes washed away. Cement is most commonly present, from fine grained microsparite to coarse grained sparite in some cases, and is mostly ferroan calcite. Epitaxial overgrowth can occur around echinoderm fragments and doog tooth cement can be present around *Nummulites variolarius* and *Ditrupa strangulata*. Silicification does not occur, in contrast to Brussels stone. The porosity is mainly defined by intergranular and intragranular porosity; however moldic porosity can considerably contribute to porosity and appearance.

The light tint and the workability of the Lede stone favoured its use for gothic architecture. Fresh fracture surfaces appear soft grey with a yellow

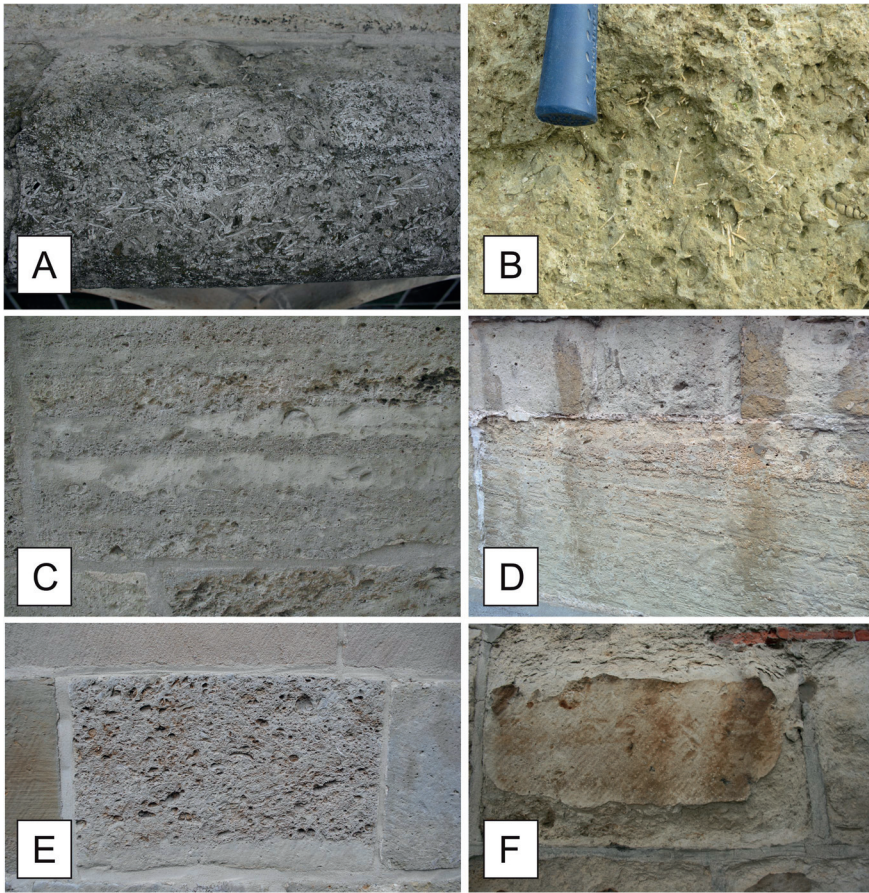


Figure 3.3: Examples of Lede stone. A) accumulation of *Nummulites variolarius* and *Ditrupea strangulata*; B) dispersed occurrence of *Nummulites variolarius* and *Ditrupea strangulata*; C) layering; D) stratification, pronounced by *Nummulites variolarius*, E) coarse, porous shell bed, F) orange-brown patina, with contour scaling.

to green tint. Typical for this stone, however, is the yellow to brown natural patina that develops on exposed surfaces (Fig. 3.3F). ICOMOS-ICS (2008) defines a patina as a *chromatic modification of the material, generally resulting from natural or artificial ageing and not involving in most cases visible surface deterioration*. An iron rich patina is defined as a *natural black to brown thin layer enriched in iron/clay minerals, which can be found on iron containing sandstones. This kind of patina is generally observed in outdoors environment, and develops quite*

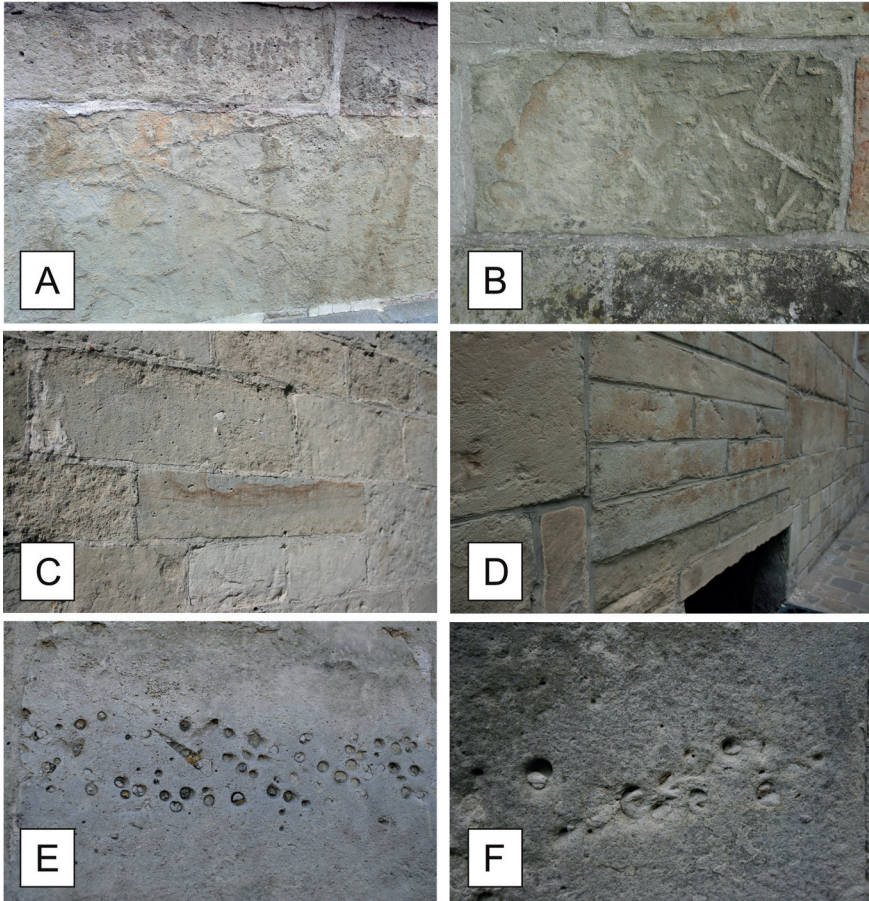


Figure 3.4: Examples of Lede stone. A and B) subhorizontal bioturbation; C) liesegang structures (central); D) elongated stone; E) casts of Turritella; F) detail of Turritella casts.

uniformly on the stone surface. Lede stone shows subtle variations in this patina, with a green or yellow overtone. It is the variability in its fresh state colour and patina development together with its heterogeneous texture which gives a significant identity to the Lede stone. The patina formation is attributed to mineral-released iron oxidation and subsequent superficial iron oxy-hydroxide precipitation. This can result in case hardening and subsequent scaling, flaking or blistering of the surface in combination with moisture or salts. This natural patina is nevertheless not a prognosis of forthcoming deterioration, nor is it deterioration on itself.

The patina is present on every aged façade and is mostly not related to any signs of deterioration or decay. Moreover, it is an intrinsic part of the architectural expression of these buildings.

The typical size for masonry blocks ranges from 15 to 30 cm thickness and 20 to 40 cm in length. Exceptionally, stones of 1 m in length and more can be found. Differences in texture are related to local sedimentation conditions and subsequent diagenesis. These differences are expressed by a natural range from compact to porous stone and from fossil poor to fossil rich zones. Shells can be concentrated in layers, so-called lumachelles. Sedimentary structures are often absent or not visible, but sometimes, bioturbation and also bedding can be recognized. Hence, neighbouring blocks can have a different aspect, which grants a vigorous aspect to façades and reflects the heterogeneity of this stone. In rural churches it can sometimes be observed that the most regular, uniform blocks are used on the western entrance façade, while more random sized blocks with a greater diversity are used on the other sides of the church.

3.4 Performance

With all the monuments of several centuries old still standing, it can be said that Lede stone overall shows a good performance and has a good durability in the Belgian and Dutch climate. In central Belgium (Ukkel), the absolute yearly maximum is 30–32 °C and the absolute minimum is –15 °C. In average, there are 200 rainy days (> 0.1 mm/day) with a total rainfall 750–800 mm water per year (www.meteo.be). In the period 1981–2010, there was an average of 46 frost days (www.frankdeboosere.be). Of course, the climate has fluctuated over the last centuries and as such, the stones have been exposed to changing conditions. This and other factors are inherited by the stone and should be considered when assessing its performance McCabe et al. (2010).

The formation of black gypsum crusts (Fig. 3.5C) was recognised as the main threat during the 20th century (Camerman, 1951; De Witte, 1990; Nijs, 1990). Black crusts started to grow on stone surfaces as a result of increased atmospheric sulphur content due to the industrial revolution during the 19th century. Atmospheric sulphur dissolves in wet conditions to form sulphurous acid, that in turn reacts with carbonates to form salt minerals such as gypsum. Therefore, this is a common problem for all

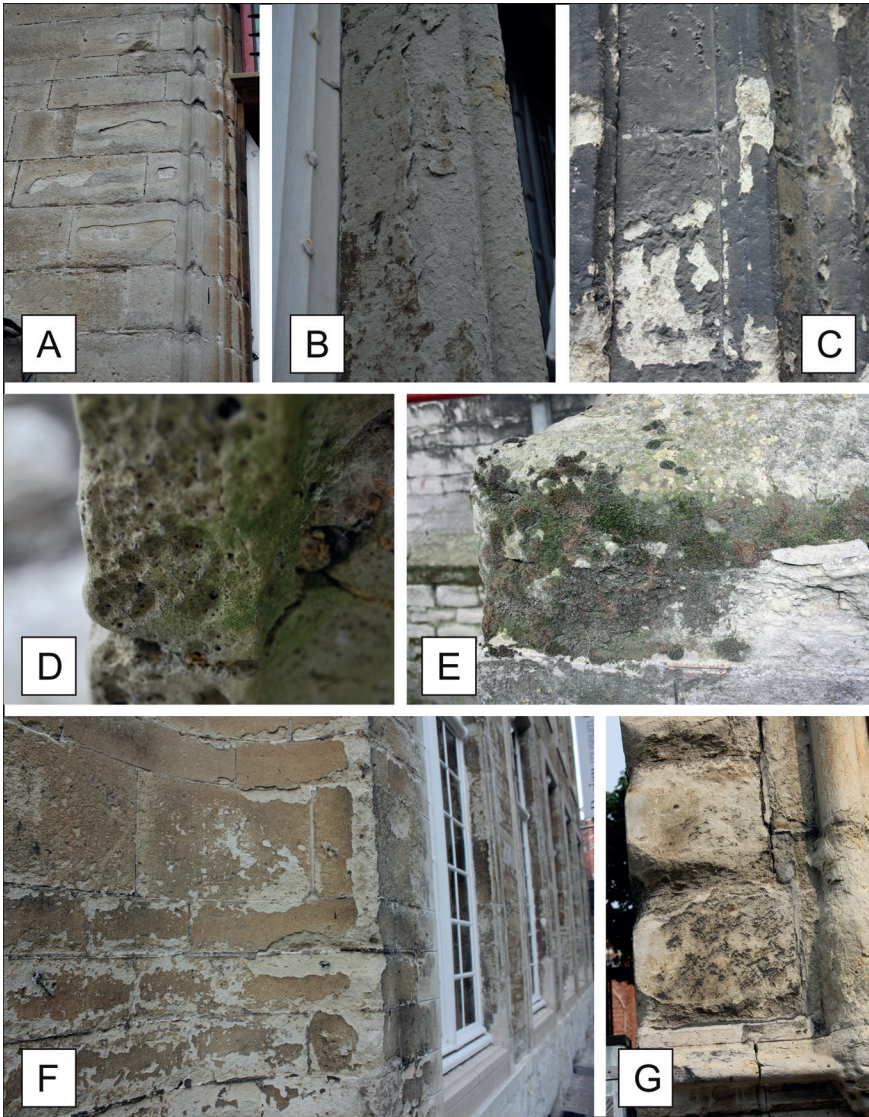


Figure 3.5: Deterioration processes; A: Blistering of masonry; B: Flaking at stone frame; C: Black crust on sheltered blocks; D: Alveolization and biological colonization (green algae) in a near coastal setting; E: Biological colonization (algae, lichens and mosses); F: Scaling originating along joints; G: Rounding of corner blocks along joints.

limestones (Török and Rozgonyi, 2004; Charola et al., 2007; Fronteau et al., 2010) , and is thus also recognised for the Lede stone (Larbi et al.,

2003; Dreesen and Nielsen, 2009). Larbi et al. (2003) distinguished a superficial black layer and a subsurface gypsum alteration zone in thin sections of black crust on Lede stone. Gypsum crystallization below the surface of the stone is preferentially found inside the microporous tests of cryptocrystalline foraminifera (*Miliolina*) and on the borders of dissolved shell fragments (Dewanckele et al., 2012, 2013). Dreesen and Nielsen (2009) have recognised that glauconite potentially triggers the sulphation process.

Where stones are exposed to frequent rain impact, or water drainage over the surface, black crusts can be washed (Fig. 3.5B and G). Here, the stone can show partially or thinly developed crusts, or a weakened surface with sugaring quartz grains. In such cases, the stone profile is often rounded (Fig. 3.5G). The formation of a patina can result in some case hardening, which can peel by blistering, scaling or contour scaling (Fig. 3.5A and F). In humid, sun-sheltered areas, biological colonization can dominate over black crusts (Fig. 3.5E). Alveolization due to moist and salts is rare, but sometimes observed in both coastal and inland setting (Fig. 3.5D).

3.5 Contemporary availability and issues

In 1966, Verlee BVBA started to produce Lede Stone as by-product from a sandpit in Balegem. In 2011, Balegro BVBA took over the sand pit and the associated stock of Lede stone. Production continues today and Lede stone remains available for restoration works. However, because of the low available quantity, diverse stones have been imported as replacement material for Lede Stone, both in Belgium (De Kock et al., 2014) and in the Netherlands (Quist et al., 2013). This was already an issue more than hundred years ago, as a consequence of the actions of architects Mortier in Belgium and Van der Veen in The Netherlands (Quist and Nijland, 2013). Mortier, charged with the restoration of the House of the Free Boatsmen, investigated the resources in an abandoned quarry wall in Balegem (Mortier, 1898). Van der Veen often traveled to Belgium to purchase Lede Stone from the remaining quarry in Bambrugge or utilised stone recovered from the demolition of buildings in Belgium for restoration in the Netherlands (Quist and Nijland, 2013). By the end of the 20th century, replacement of Lede Stone in monuments was so drastic, that architect Breda described the use of dissimilar foreign stones in a metaphor as a

disease (Breda, 2005). This awareness suggested that the use of authentic materials was not only beneficial for aesthetic purposes, but also for stone compatibility and durability.

3.6 Previous technical studies

The petrophysical properties of Lede stone were not yet intensely studied. Camerman (1951) did not even incorporate Lede stone in a summarizing graph in for that time a leading publication on the use of limestone in Belgium, while he did incorporate Gobertange limestone (Fig. 3.8).

	Density kg/m ³	Porosity vol. %	UCS MPa
Gulinck (1949)	/	/	28–68
Camerman (1951)	2358 ± 158	12.62 ± 5.88	52.6 ± 15.4
BBRI (1970)	2305–2400–2513	5.7–10.9–13.2	55.7–82.6–122.5
Slinger et al. (1982)	2400	7–22.4	82.5
BBRI (1997)	2305–2400–2513	5.7–10.9–13.2	55.7–82.6–122.5

Table 3.1: Reported density, porosity and UCS of Lede stone.

Historical studies are limited to the basic technical properties, necessary for the construction industry. Mainly density, porosity and uniaxial compressive strength (*UCS*) were reported (Table 3.1). The technical sheet on white stone (TV 80) (Fig. 3.6) of the Belgian Building Research Institute (BBRI) from 1970 also reported ultrasound velocity, saturation coefficient, thermal conductivity and an MIP parameter (Belgian Building Research Institute, 1970). In 1997, the same values were reported (Belgian Building Research Institute, 1997). Although the order of magnitude of the porosity, density and *UCS* is similar, it can be seen that there is a significant spread on the measurements. Porosities range from as low as 5.7 vol.% to as high as 22.4 vol.% in different studies. So does the *UCS* vary from 28 to 122.5 MPa. More than porosity, the *UCS* values can be influenced by the way they were tested. Yet, the spread on both properties indicates that there must have been a reasonable heterogeneity in the samples, from relatively compact to relatively porous. In general, however, the mean porosity seems to be 7–10 vol.% and the typical *UCS* around 50–80 MPa. This is in accordance with the values of the latest tests for

Balegro BVBA at Ghent University in 2012, under supervision of the author (Table 3.2). The results were listed in a technical sheet provided to Balegro BVBA and were also incorporated in De Kock et al. (2015).

		7. Technical properties										8. Possibility for external use					
		compressive strength (kg/cm ²)	apparent density (kg/m ³)		ultrasound velocity (m/s)	scratch width (mm)	porositeit (%)	thermal conductivity (kcal/mh °C)	10% quantile pore diameter at MIP	10% quantile pore diameter at MIP	performance during frost action	AFNOR classification	plinths, pedestals, substructure	stairs, door steps, flooring	masonry, ashlar	unprotected elements (cornice, capstone,...)	fine framework, sculpture
Balegem	Min.	557	2305	3895	(*)	5.7		0.61	8.7								
	Av.	826	2400	4073		10.9	1.8	0.66	9.3			+	+	+	+	+	
	Max.	1225	2513	4472		13.2		0.73	9.92								
(*) test not performed on crumbling specimen												(**) ashlar					

Figure 3.6: Extract from TV80 Belgian Building Research Institute (1970) with properties of Lede stone, translated to English.

One of the common misconceptions is that Lede stone layers are more fossiliferous on its top and bottom parts and that the centre is the most compact. It is often mentioned that stone banks need to be stripped of their porous or shell layers on top and bottom to obtain stone with enough quality (Slinger et al., 1982; Duser et al., 2009). This seems relevant to get rid of the jagged boundary layer. However, there is no direct relation with biodiversity and associated porosity in such that a fossil rich layer is by definition an inferior boundary layer. Fossiliferous and porous zones can or cannot occur at the edges of the centre of a stone layer (Fig. 3.7).

Physical properties (mean)

Apparent density (EN 1936, 2006)	$2448 \pm 29 \text{ kg/m}^3$
Open Porosity (EN 1936, 2006)	$8.27 \pm 1.09 \text{ vol.}\%$
Capillary absorption coefficient (EN 1925, 1999)	$11.98 \pm 4.07 \text{ g}/(\text{m}^2 \sqrt{\text{s}})$
Compressive strength (EN 1926, 2006)	$48.4 \pm 12.6 \text{ MPa}$
Flexural strength (EN 12372, 2006)	$17.6 \pm 3.9 \text{ MPa}$
Ultrasound velocity (14579, 2004)	$4359 \pm 41 \text{ m/s}$
Abrasion resistance (EN 14157, 2004)	$19.00 \pm 1.19 \text{ mm}$
Frost resistance (EN 12371, 2010)	Nc 168 (frost resistant)

Table 3.2: Properties of Lede stone, measured by the author in command of Balegro BVBA in 2012.

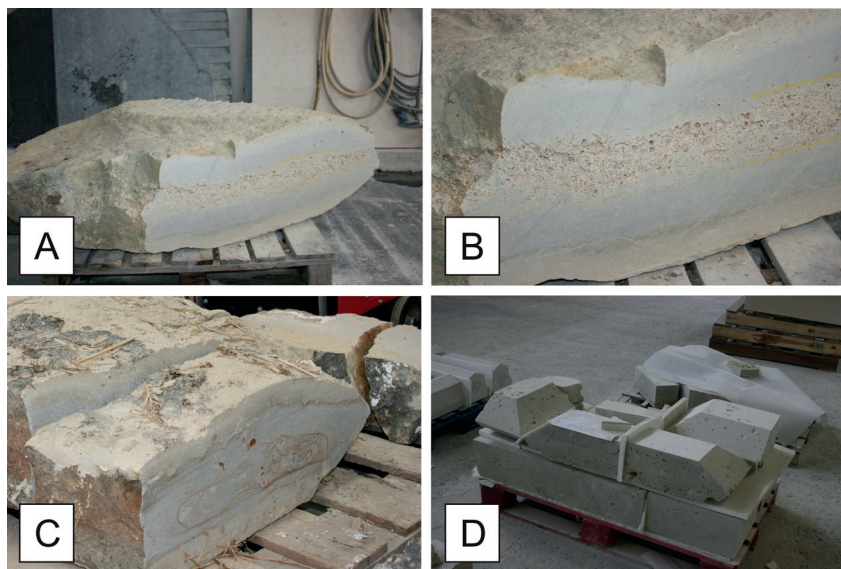


Figure 3.7: New blocks of Lede stone. A) with a porous shell layer central, thickness ± 40 cm; B) detail of A; C) compact block with liesegang structures, thickness ± 40 cm; D) cut to size for finishing, height ± 20 cm.

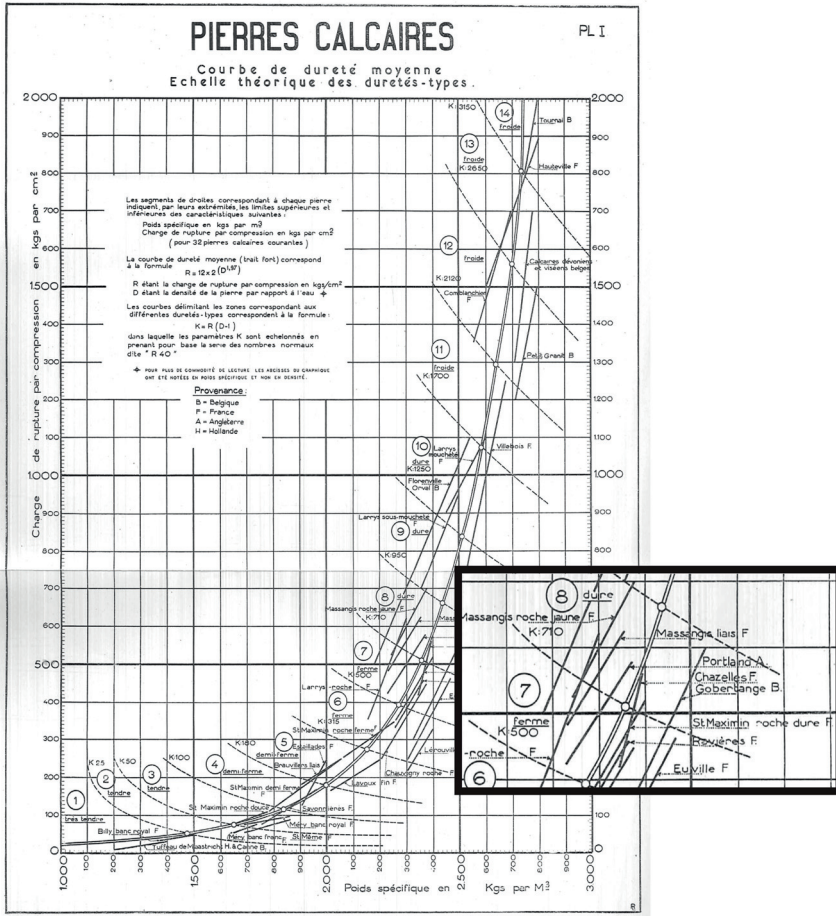


Figure 3.8: Extract and detail from Camerman (1951): classification of rocks according to their hardness, with UCS (kg/cm²) in ordinate and density (kg/m³) in abscissa.

References

- EN 14579. Natural stone test methods - Determination of sound speed propagation, 2004.
- Belgian Building Research Institute. TV 80 Witte steen - Balegem. Technical report, 1970.
- Belgian Building Research Institute. TV 205 Natuursteen. Technical report, 1997.
- K Breda. De 'carrière' van een architect. In *ICOMOS contact*, volume 18, pages 20–24, Leuven, 2005.
- F X Burtin, M J Speeckaert, J A Balconi, and A Pris. *Oryctographie de Bruxelles ou description des fossiles tant naturels qu'accidentels découverts jusqu'à ce jour dans les environs de cette ville*. Le Maire, Brussels, 1784.
- C Camerman. Les pierres de taille calcaires. Leur comportement sous l'action des fumées. *Annales des travaux publics de Belgique*, 52:509–532, 1951.
- C Camerman. Le sous-sol de Bruxelles et ses anciennes carrières souterraines. *Annales des travaux publics de Belgique*, 2-3:5–28, 1955.
- A Elena Charola, Josef Pühringer, and Michael Steiger. Gypsum: a review of its role in the deterioration of building materials. *Environmental Geology*, 52(2):339–352, mar 2007. ISSN 0943-0105. doi: 10.1007/s00254-006-0566-9.
- V Cnudde, J Dewanckele, M De Ceukelaire, G Everaert, P Jacobs, and M C Laleman. *Gent...Steengoed!* Academia Press, Ghent, 2009.
- T De Kock, J Dewanckele, M. Boone, G De Schutter, P Jacobs, and V Cnudde. Replacement stones for Lede stone in Belgian historical

- monuments. *Geological Society, London, Special Publications*, 391(1): 31–46, mar 2014. ISSN 0305-8719. doi: 10.1144/SP391.9.
- T De Kock, M Boone, J Dewanckele, M De Ceukelaire, and V Cnudde. Lede stone: a potential "Global Heritage Stone Resource" from Belgium. *Episodes*, 38(2):91–96, 2015.
- L De Smet, P Devos, W Eeckhout, and R Nijs. *Balegemse steen - vier aspecten*. Provinciebestuur Oost-Vlaanderen, Gent, 2003. doi: D/2003/1933/4.
- E De Witte. Natuursteen in de monumentenzorg: vervangen of conserveren? *Bulletin de la Société belge de Géologie*, 99(2):197–205, 1990.
- J Dewanckele, T De Kock, M A Boone, V Cnudde, L Brabant, M N Boone, G Fronteau, L Van Hoorebeke, and P Jacobs. 4D imaging and quantification of pore structure modifications inside natural building stones by means of high resolution X-ray CT. *Science of the Total Environment*, 416:436–448, 2012. doi: 10.1016/j.scitotenv.2011.11.018.
- J Dewanckele, M A Boone, T De Kock, W De Boever, L Brabant, M N Boone, G Fronteau, J Dils, L Van Hoorebeke, P Jacobs, and V Cnudde. Holistic approach of pre-existing flaws on the decay of two limestones. *Science of the Total Environment*, 447:403–414, 2013. doi: 10.1016/j.scitotenv.2012.12.094.
- R Dreesen and P Nielsen. On the triggering role of glauconite in the sulphate attack of sandy limestones, based on a study of historical building stones in Flanders, Belgium. In *12th Euroseminar on Microscopy Applied to Building Materials*, pages 13–19, Dortmund, 2009. Technische Universität Dortmund.
- R J Dunham. Classification of carbonate rocks according to depositional texture. . In W E Ham, editor, *Classification of carbonate rocks*, volume Memoir. 1, pages 108–121. American Association of Petroleum Geologists, 1962.
- M Duser, R Dreesen, and A De Naeyer. *Natuursteen in Vlaanderen - Versteend verleden*. Kluwer-Wolters Belgie nv, Mechelen, 2009.
- EN 12371. Natural stone test methods - Determination of frost resistance, 2010.

- EN 12372. Natural stone test methods - Determination of flexural strength under concentrated load, 2006.
- EN 14157. Natural stone test methods - Determination of the abrasion resistance. Technical report, European Committee for Standardization, 2004.
- EN 1925. Natural stone test methods - Determination of water absorption coefficient by capillarity. Technical report, European Committee for Standardization, 1999.
- EN 1926. Natural stone test methods - Determination of uniaxial compressive strength, 2006.
- EN 1936. Natural stone test methods - Determination of real density and apparent density, and of total and open porosity, 2006.
- B Fobe and V Spiers. Sedimentology and facies distribution of the Lede Formation (Eocene) in Belgium and northern France. *Contr. Tert. Quatern. Geol.*, 29(1-2):9–20, 1992.
- R L Folk. Practical petrographic classification of limestones. *American Association of Petroleum Geologists Bulletin*, 43:1–38, 1959.
- G Fronteau, C Thomachot-Schneider, E Chopin, V Barbin, D Mouze, and A Pascal. Black-crust growth and interaction with underlying limestone microfacies, 2010.
- E Groessens. Some white stones in the Land of Blue Stones (Belgium). In J.-P. Gély and J Lorenz, editors, *Carrieres et batisseurs de la periode preindustrielle - Europe et regions limitrophes*, pages 165–176, Paris, 2011. Editions du CTHS.
- M Gulinck. Oude Natuurlijke Bouwmaterialen in Laag- en Midden-België. *Technisch-Wetenschappelijk Tijdschrift*, 18(2):25–32, 1949.
- M Hurx. *Architect en aannemer - De opkomst van de bouwmarkt in de Nederlanden 1350-1530*. Vantilt, Nijmegen, 2012.
- ICOMOS-ICS. Illustrated glossary on stone deterioration pattern, 2008. URL http://international.icomos.org/publications/monuments{_}and{_}sites/15/pdf/Monuments{_}and{_}Sites{_}15{_}ISCS{_}Glossary{_}Stone.pdf.

- P Jacobs and M De Batist. Sequence stratigraphy and architecture on a ramp-type continental shelf: the Belgian Palaeogene. *Geology of Siliciclastic Shelf Seas*, 117:23–48, 1996.
- P Jacobs and E Sevens. Middle Eocene sequence stratigraphy in the Balegem quarry (western Belgium, southern bight North Sea). *Bulletin de la Société belge de Géologie*, 102(1-2):203–213, 1993.
- J A Larbi, R P J van Hees, and S Naldini. Microscopic study of weathering of white Flemish stone from the monumental Church of Our Lady in Breda, The Netherlands. *Heron*, 48(3):13, 2003.
- S McCabe, B J Smith, P A Warke, and Geological Society. A legacy of mistreatment: conceptualizing the decay of medieval sandstones in NE Ireland. In R Prikryl and Á Török, editors, *Natural Stone Resources for Historical Monuments*, volume 333, pages 87–100, London, 2010. Geological Society.
- S Mortier. Communications sur les recherches faites dans les anciennes carrières de Balegem., 1898.
- J Mount. Mixed siliciclastic and carbonate sediments: a proposed first-order textural and compositional classification. *Sedimentology*, 32(3): 435–442, jun 1985. ISSN 0037-0746. doi: 10.1111/j.1365-3091.1985.tb00522.x.
- R Nijs. Identificatie van Balegemse steen door middel van de korrelgrootteverdeling van de zandfractie. *Vlaanderens Erfgoed*, 55:8–13, 1980.
- R Nijs. Tertiaire kalksteen en Franse witte steen als natuurlijke bouwsteen voor onze historische monumenten. *Bulletin de la Société belge de Géologie*, 99(2):115–121, 1990.
- C J A C Peeters. *De Sint Janskathedraal te 's-Hertogenbosch*. SDU, Den Haag, 1985.
- W J Quist. Steenkeuze voor restauratie: 150 jaar ontwikkeling in Nederland en Vlaanderen, 2012.
- W J Quist and T G Nijland. A.L.W.E. Van der Veen - Een Delfts mijningenieur in monumentenland. *Bulletin KNOB*, 112(4):204–224, 2013.

- W J Quist, T G Nijland, and R P J van Hees. Replacement of Eocene white sandy limestone in historical buildings: over 100 years of practice in the Netherlands. *Quarterly Journal of Engineering Geology and Hydrogeology*, 46(4):431–438, 2013. doi: 10.1144/qjegh2013-023.
- A Slinger, H Janse, and G Berends. *Natuursteen in monumenten*. Bosch & Keuning / Rijksdienst voor de Monumentenzorg, Zeist, 1982.
- Á Török and N Rozgonyi. Morphology and mineralogy of weathering crusts on highly porous oolitic limestones, a case study from Budapest. *Environmental Geology*, 46(3):333–349, 2004. doi: 10.1007/s00254-004-1036-x.
- S van der Horst. Balegemse steen leeft nog altijd. *Natuursteen*, 6:2, 2012.
- I Van der Kelen. *Steengroeven te Houtem - De Houtemse steen*, 1996.

4

Natural stone damage and interventions: a human perception

The need for intervention and the kind of intervention are things that are not quantitatively defined. Interventions can take place for aesthetic reasons, because of safety precautions or because of structural adjustments. This chapter is dedicated to the decision-making process of interventions, to place the aims and scope (Section 1.3) in a broader context. By means of a survey, it was tested firstly how people feel about damage on natural stone and how this influenced their opinion on the need for an intervention. Secondly, it was tested how people appreciate performed interventions, in order to evaluate the criteria of good practice. All cases were dedicated to white stone, mostly Lede stone. The survey was performed as a cooperation between the author, Dr. Wido Quist (TU Delft) and Dr. Timo Nijland (TNO). In this chapter, the results interpreted by the author are discussed from the material's perspective and some cases of specific interest are explored more thoroughly. Other results of this survey, which focus on differences in perception related to nationality or profession can be consulted in Quist et al. (2014a) and Quist et al. (2014b). There, it was shown that differences in response were more related to profession rather than to nationality (Belgium - The

Netherlands), notwithstanding the different historical approach on natural stone restoration.

4.1 Introduction

Aside from its commercial value, natural stone also has a high cultural, historic and aesthetic value. Especially the aesthetic value is subjective to the perception of humans. This value is prevailing in the choice of natural stone for new constructions, as for external cladding, flooring or for applications in the kitchen or bathroom. Similarly, it is a very important factor in the conservation and restoration of our cultural heritage. The conservation and restoration guidelines of The Venice Charter (ICOMOS, 1966) aim to preserve the integral value of historic monuments, safeguarding it as historical evidence and as work of art. Considering natural stone as a material in historic monuments, this implies that any act of conservation or restoration should respect the intrinsic historic and aesthetic value of the stone in itself, as well as its blending into the architecture. Consequently, this implies that some expressions of weathering are not necessarily to be undone. Andrew (2002) showed, also based on a survey, that e.g. soiling adds a historical dimension to building façades as in specific cases in his study the majority of participants thought cleaning could be detrimental to the look of a building. Quist et al. (2008) illustrated that intervention is not always considered to be necessary for cases where the natural stone is perceived as damaged.

Damage

The loss of value in human perception due to decay -chemical or physical modification of the intrinsic stone properties- is called damage (ICOMOS-ICS, 2008). The process of becoming worse or lower in value is called deterioration (ICOMOS-ICS, 2008). Damage is often a reason for interventions such as conservation treatments (Doehne and Price, 2010) or restoration and possibly material replacement. It was the idea to evaluate the human perception on cases which are in theory damage and to relate this with the personal conception of possible interventions.

Interventions

The aim of an intervention is the preservation of the monument. One reason could be the structural safety or stability. Another could be the damage of the material, leading to a decrease in value in human

perception. Interventions can upgrade the value of natural stone, but the question whether or not this is true depends on the perception of humans. This perception was tested in relation to the opinion on the situation and on the intervention.

4.2 Methods

The survey was performed in cooperation with TU Delft and TNO (The Netherlands) and was drafted in Dutch. The survey was created and distributed online with Collector software from Survalyzer AG licensed to TU Delft. It existed out of 21 photos that represented cases on damage and interventions of white limestones. The inquiry was thematically divided in two parts: photos 1–11 related to damage, photos 12–21 related to interventions. For each of the 21 photos, the appreciation was questioned in a scale from 1 (ugly) to 5 (attractive). For both themes one or two additional thematic questions were formulated. For photo 1–11 (damage) this was the selection of the most appropriate statement amongst: no intervention needed; the stone needs to be cleaned; the stone needs to be repaired; the stone needs to be replaced. For photos 12–21 (interventions) this was the selection of the most appropriate statement amongst: the stone looks well looked after; the stone looks shabby; the stone looks damaged; the stone is (too) obvious treated/cured; none of the above. In addition; respondents were asked to give their opinion on the intervention as one of the following three: unnoticed; clearly visible but not distracting; clearly visible and distracting (unbalanced).

The population was characterized based on their country of employment: Belgium (Flanders) or The Netherlands; their professional occupation in relation to natural stone: monument or restoration specialist, art, building or architectural historian, stonemason, geologist, student, not-professionally involved; and on their age: < 25, 25–45, 45–65, > 65 years. In total, 151 respondents filled in the survey completely, of which 82 respondents are working in The Netherlands and 69 in Belgium (Flanders). The results for the total population are summarized in Figure 4.1 and 4.2.

Photos 1–11: damage

The photos 1–11 (Fig. 4.3, 4.4 and 4.5) relate to damage with the aim to investigate the human perception of loss of value. All photographs show Lede stone, with the exception of photo 2 which is dominantly Brussels

stone and photo 11 which is northern French limestone. All photos with the exception of photo 10 show damage to a greater or lesser extent. According to the ICOMOS-ICS (2008), the damage could be described as follows:

Photo 1: bursting at the joints

Photo 2: scaling

Photo 3: none to poorly developed loss of matrix (differential erosion)

Photo 4: peeling of the patina crust

Photo 5: blistering

Photo 6: scratches (mechanical damage) and soiling

Photo 7: biological colonization (lichen)

Photo 8: discolouration (moisture area)

Photo 9: black crust and soiling

Photo 10: none

Photo 11: impact damage of bullets (mechanical damage) and soiling

The presence of a patina (see Section 3.3) can be detected in several photos. This is not interpreted as damage on itself, but rather as alteration. According to ICOMOS-ICS (2008), alteration is a *modification of the material that does not necessary imply a worsening of its characteristics from the point of conservation.*

Photos 12–21: interventions

The photos 12–21 (Fig. 4.6 and 4.7) relate to interventions on white stone. The interventions and the point of interest (POI) which should draw the attention could be described as follows:

Photo 12: Lede stone replacement in trachyte; POI: differences in colour and shaping

Photo 13: Lede stone treated with linseed oil (orange-brown) and half replaced with Euville limestone (yellow-white); POI: colour difference

Photo 14: Lede stone replacement by limestone from Burgundy (France); POI: differences in colour and shaping (straight lines for replacement stones)

Photo 15: Reconstruction (in Lede stone) of a crow-stepped gable on a façade in Brussels stone; POI: architectural reconstruction

Photo 16: Replacement Brussels stone by Gobertange and Brussels stone; POI: age aspect

Photo 17: Repointing; POI: colour and texture

Photo 18: Patchwork of Lede stone and Brussels stone, considered as

historic intervention except for the window frame; POI: all stones in the masonry have aged

Photo 19: Replacement in Lede stone; POI: surface finishing for integration

Photo 20: Replacement in similar stone type; POI: the structure of the replacement and state of replacement stones

Photo 21: Replacement in Lede stone; POI: shape of the replacement stones and surface finishing for integration

Appreciation	Statement	Photo												
		1	2	3	4	5	6	7	8	9	10	11		
1	no intervention needed	0	0	0	0	1	2	1	0	1	0	0	0	0
	... needs cleaning	1	0	1	0	1	4	6	7	2	0	0	7	7
	... needs repointing	2	0	0	3	3	0	0	1	8	0	0	7	7
	... needs replacement	1	3	0	0	2	0	0	0	15	0	0	14	14
2	no intervention needed	6	2	5	9	3	7	5	4	0	1	4	4	
	... needs cleaning	1	2	0	9	7	3	9	22	10	2	10	10	
	... needs repointing	28	5	3	7	32	0	2	0	21	2	20	20	
	... needs replacement	6	2	2	4	5	0	0	0	17	2	6	6	
3	no intervention needed	17	29	31	26	24	12	12	19	2	15	9	9	
	... needs cleaning	7	4	4	12	1	8	22	31	13	8	17	17	
	... needs repointing	33	5	6	16	25	1	0	1	32	6	9	9	
	... needs replacement	3	6	0	0	1	0	0	0	8	0	3	3	
4	no intervention needed	24	62	46	43	21	55	39	36	2	62	17	17	
	... needs cleaning	3	3	2	5	7	8	13	18	3	5	14	14	
	... needs repointing	16	1	6	3	8	0	2	0	6	2	5	5	
	... needs replacement	0	0	0	1	1	0	1	0	3	0	1	1	
5	no intervention needed	3	25	45	13	8	50	37	10	3	46	7	7	
	... needs cleaning	0	0	0	0	0	1	2	2	0	0	1	1	
	... needs repointing	0	2	0	0	1	0	0	0	2	0	0	0	
	... needs replacement	0	0	0	0	0	0	0	0	3	0	0	0	

Figure 4.1: Results for photos 1–11.

Appreciation	Statement	Photo																				
		12	13	14	15	16	17	18	19	20	21	12	13	14	15	16	17	18	19	20	21	
1	... looks neat	0	0	0	2	0	0	1	0	0	0	0	0	2	0	0	1	0	0	0	0	
	... looks unkempt	2	0	1	0	1	7	0	0	0	1	0	0	0	1	7	0	0	0	0	1	
	... looks damaged	3	0	0	0	1	3	0	0	0	1	0	0	0	1	3	0	0	0	0	2	
	... (too) obvious treated	1	6	20	9	13	21	2	24	4	13	21	2	24	4	22	2	24	4	22		
	none of the above	0	0	1	0	0	0	0	0	0	0	0	1	0	0	0	0	0	0	0	4	
2	... looks neat	0	3	0	4	3	0	1	3	2	3	0	0	4	3	0	1	3	2	2	1	
	... looks unkempt	7	0	5	1	2	8	2	2	2	2	8	2	2	2	8	2	2	2	2	3	
	... looks damaged	6	1	2	0	0	2	1	2	0	0	2	1	2	0	2	1	2	0	0	3	
	... (too) obvious treated	15	32	42	28	30	38	6	32	19	30	38	6	32	19	30	6	32	19	30		
	none of the above	1	7	3	4	1	4	1	2	4	1	4	1	4	1	2	4	1	2	4	6	
3	... looks neat	4	20	7	23	14	2	7	22	19	14	2	7	23	14	2	7	22	19	16		
	... looks unkempt	7	1	4	1	6	4	1	0	0	6	4	1	0	6	4	1	0	0	0	0	
	... looks damaged	10	1	6	1	0	11	0	1	1	0	11	0	1	0	11	0	1	1	1	1	
	... (too) obvious treated	22	20	29	23	29	18	12	20	21	29	18	12	20	21	29	18	12	20	21	29	
	none of the above	14	10	11	5	13	10	12	10	7	13	10	12	10	12	10	7	10	12	10	7	4
4	... looks neat	5	24	5	23	18	6	44	23	35	18	6	44	23	18	6	44	23	35	16		
	... looks unkempt	9	0	2	0	3	0	3	0	1	0	3	0	3	0	3	0	1	0	0	0	
	... looks damaged	7	0	2	0	0	4	2	0	0	0	4	2	0	0	4	2	0	0	0	0	
	... (too) obvious treated	12	8	7	9	8	3	9	5	18	8	3	9	5	18	8	3	9	5	18	6	
	none of the above	14	7	3	3	5	7	11	2	7	3	5	7	11	2	7	11	2	7	3	3	
5	... looks neat	4	10	1	12	2	1	33	3	11	2	1	33	3	11	2	1	33	3	11	4	
	... looks unkempt	0	0	0	0	0	0	0	0	0	0	0	0	0	0	0	0	0	0	0	0	
	... looks damaged	2	0	0	0	0	0	0	0	0	0	0	0	0	0	0	0	0	0	0	0	
	... (too) obvious treated	3	0	0	2	1	2	0	0	0	2	1	2	0	0	2	1	2	0	0	0	
	none of the above	3	1	0	1	1	1	0	3	0	1	1	0	3	0	1	1	0	3	0	0	

Figure 4.2: Results for photos 12–21.

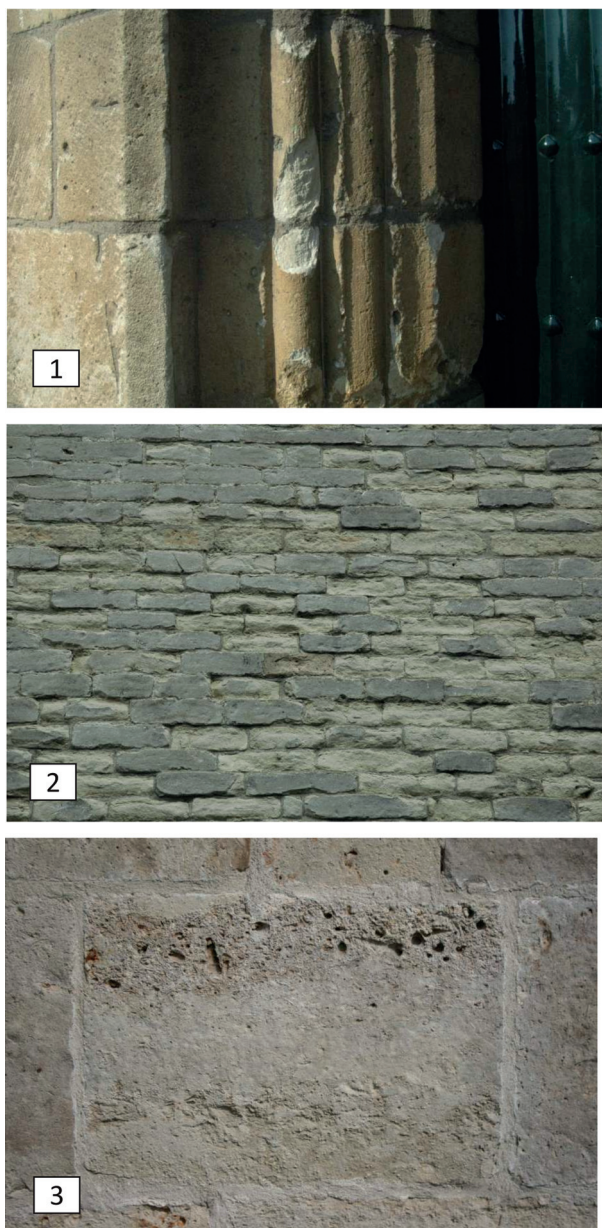


Figure 4.3: Photos 1–3 related to damage of white limestone.



Figure 4.4: Photos 4–6 related to damage of white limestone.



Figure 4.5: Photos 7–11 related to damage of white limestone.

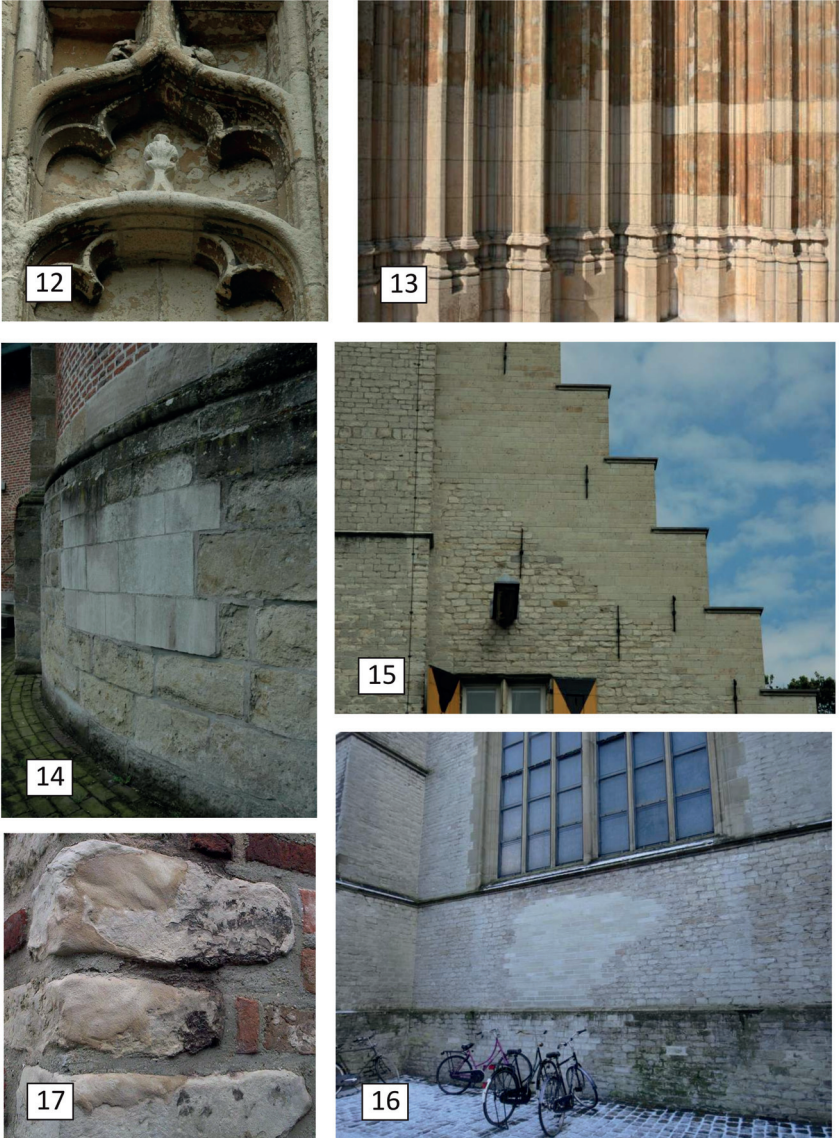


Figure 4.6: Photos 12–16 related to interventions on white limestone.

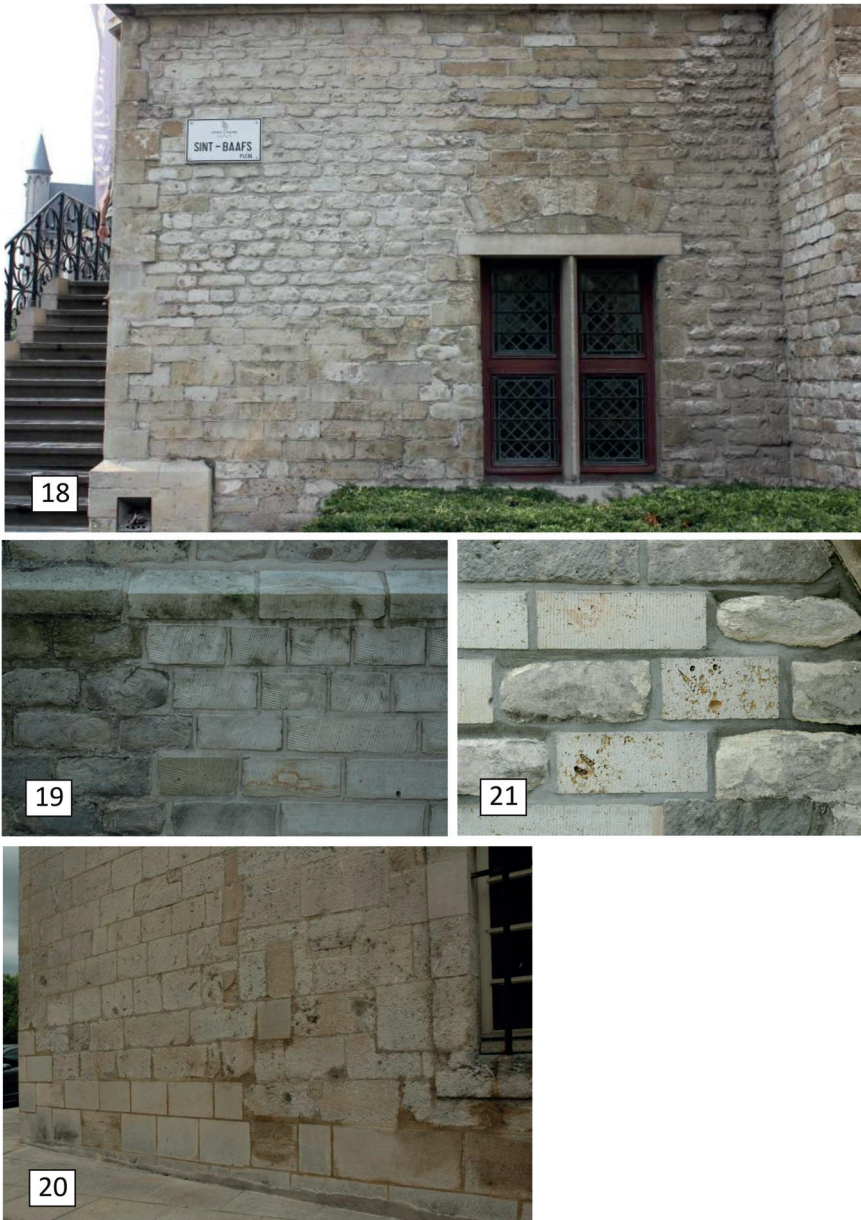


Figure 4.7: Photos 17–21 related to interventions on white limestone.

4.3 Results part 1: damage

4.3.1 Structural damage is less appreciated

The appreciation is used here as a relative amenity value for the stones in question. As damage is related to the human perception of loss of value, this is difficult to measure on itself, as it should be referenced to the original value. Nevertheless, some conclusions can be drawn from the appreciation.

Figure 4.8 shows the average appreciation for each photo. On a scale of 0 to 5, the lowest average appreciation is 2.5, meaning that the general feeling of these cases is them being attractive, even though being illustrations of damage. Photo 10, considered as not showing real damage, received the highest appreciation with a score of 4. If this is used as a sort of reference, the lower appreciation of the other photos can be considered as lower in value and thus they were perceived as having some sort of damage.

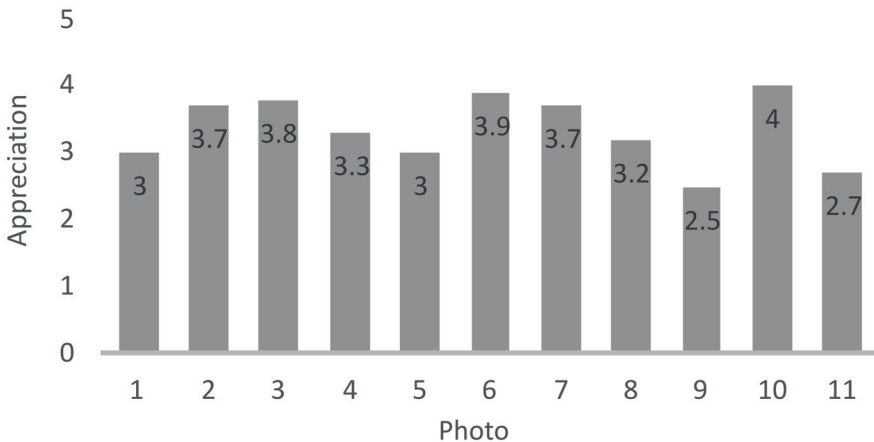


Figure 4.8: Average appreciation for photos 1–11.

Photos 1, 5, 9 and 11 clearly have the lowest appreciation. Compared to the other photos, except photo 2, these are the cases where structural damage is the most obvious; the shape of the blocks is clearly affected. Photos 6, 7 and 8 score higher in appreciation. These cases show respectively soiling, lichen growth and discolouration, but the shape of the block was not affected. It seems that natural stone is much less appreciated when it shows clear structural damage than when it is only fouled. The reason could

be that structural damage is perceived as more difficult to repair or even that it compromises the stone's structural integrity.

The difference in appreciation between Belgian and Dutch respondents is low (< 0.2) except for photo 5, which scored higher for Belgian participants (3.2 vs. 2.8) and photo 11 which scored higher for Dutch participants (2.9 vs. 2.5).

4.3.2 Damage and the need for intervention

Figure 4.9 shows the link between the participants appreciation and the statement he or she found most appropriate with the photo. The higher the score a participant gave, the more he or she was confident that no intervention was needed. On the other side, the lower the appreciation score, the more was the participant convinced that an intervention was necessary. The need for replacement increases with decreasing appreciation. No specific conclusions could be drawn for cleaning or repointing. Both can be considered as an option, especially in the case of lower appreciation. It depends, however, on the specific case rather than on appreciation.

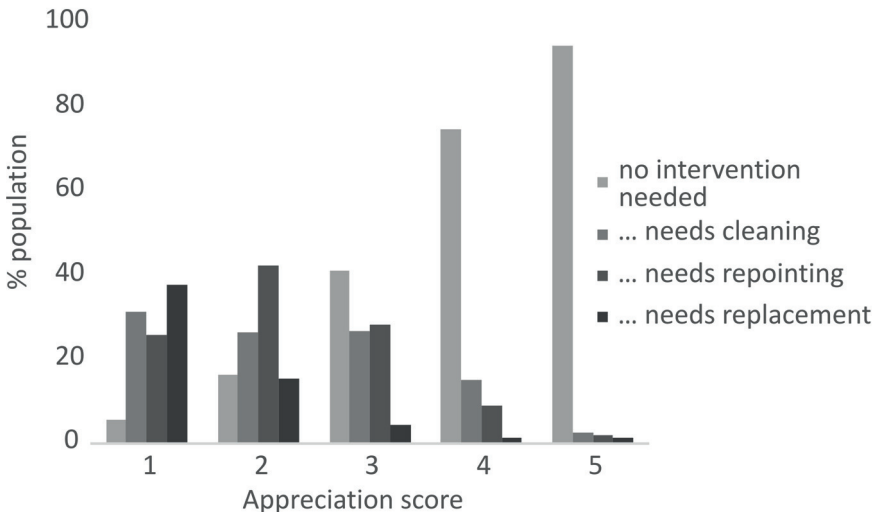


Figure 4.9: Link between appreciation and statement for photos 1–11.

From the detail of Figure 4.1, a majority of 82 % agrees that no intervention

is needed for photo 10. 10 % feels like the stone needs to be cleaned and 7 % feels like it should be repointed. From its high score in appreciation, it was deducted that there was a general feeling of no or little damage. This corresponds to the feeling that no intervention is needed.

Photos 1, 5, 9 and 11, which scored low on appreciation, score high on the need for intervention. For photos 1, 5 and 9, repointing is the most appropriate intervention according to the participants. Only photo 9 scores high on the need for cleaning as well. The opinions on photo 11 are divided between cleaning, repointing, replacement or even no intervention at all. It seems that soiling (deposition of exogenous particles giving a dirty appearance to the stone surface) is perceived equally unattractive as the mechanical damage.

The opinion on photos 6, 7 and 8 are clear. Either the participants believe no intervention is needed, either they feel cleaning is appropriate. Less than 4 % indicates repointing or replacement as an appropriate intervention, illustrating these cases are perceived as having no structural damage. With feedback to the appreciation, this confirms that the perception of the loss of value is more bound to structural loss of stone rather than alterations, where no structural changes are clearly visible to the naked eye, such as discolouration, soiling and biological colonization.

4.3.3 Specific considerations on damage

Photo 2 shows a façade with differential erosion of similar stones. Notwithstanding parts of the stones clearly show structural loss of volume, the average appreciation of this photo was relatively high (3.7) and 76 % of the participants judged that no intervention is needed. This might illustrate a scale-effect, where the historical appearance of the entire façade is greatly valued.

Photo 3 shows only little differential weathering and could also be interpreted as its natural state with little or no damage. However, the stone itself is quite heterogeneous, with the presence of a porous shell layer. This seems not to have negatively influenced the appreciation, as its score is relatively high (3.8). 84 % of the participants agree that no intervention is needed and do not seem to bother about this porous zone.

In photo 11, it is remarkable that repointing scores high. This indicates that at least part of the participants prefers a straight façade over the historical

signs of bullet impact. In many examples in different countries, repointing is exactly what has been done with such damage.

4.4 Results part 2: intervention

4.4.1 Ageing is appreciated

Figure 4.10 shows the average appreciation for each photo. Photo 18 clearly got the highest appreciation with an average score of 3.8. Different white stones, mainly Brussels and Lede stone, were used here in between each other. This results in different block sizes and colours in the façade. On the other hand, all stones are aged. It seems that the latter is decisive in the appreciation. People like the historical view of the façade. They are not distracted by the mingling of different stones. This contrasts very much with photos 19 and 21. Here, there is an obvious use of replacement stones; for both photos 99 % finds that the intervention is clearly visible. These cases score relatively low, 2.6 and 2.5 respectively. Nevertheless, it was aimed to use the same material for replacement, but they do not show much signs of ageing. The low scores can thus not be related to the choice of material. Rather, the intervention is clearly visible because the replacement stones have straight edges, corners and faces, which contrasts to the rounded shape of the old neighbouring stones. In this way, their appreciation is very similar to photo 14 (2.5), where different material is used as replacement stone. This contrasts with the rest of the wall in colour and block shape. The conclusion is that a similar level of ageing is a very important factor in the appreciation of interventions. More in detail, the chiseled surface finishing of the new stones in photo 19 and 21 probably aimed to effectuate the age aspect artificially. Where the different chiseling directions in photo 19 create more dimensions, the vertical chiseling in photo 21 emphasizes the straight lines. In addition, the macroporosity of the new stones in photo 21 is also striking. Almost 80 % of the participants finds the intervention in photo 21 obvious and distracting, with almost 60 % of participants who feel the same about photo 19. Hence, the idea to create a more aged appearance yields some appreciation. The same goes for photo 16, where part of the façade was replaced by the same material, but which has not yet gained the same ageing as the surrounding material. This case also has a relative low appreciation (2.8).

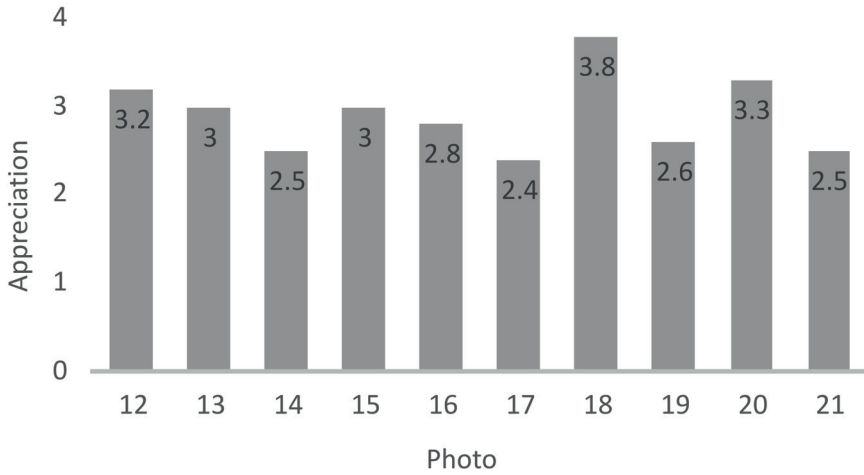


Figure 4.10: Average appreciation for photos 12–21.

Photo 17 also has a relative low appreciation. In this case, it concerns the use of repair mortar. The mortar is clearly distinguishable from the stone and 65 % of the participants find it distracting. In this case, the colour of the mortar was not well chosen neither was great attention paid to the application. The mortar is not well aligned with the surface of the stone, and the rough stone texture contradicts with the smooth rounded mortar.

Figure 4.11 shows the relation between appreciation and the most applicable statement. Not surprisingly, there is a clear correlation between the appreciation and the perception of a well looked after stone. Photo 18, with the highest score on appreciation, is perceived as a well looked after stone according to most participants (57 %). Also photos 13, 15 and 19 score high on this statement. It seems that the perception of a well looked after stone is that of a stone which resolves the (historical?) architectural details.

Similarly, there is a negative correlation between the appreciation and the obviousness of stone treatment. Lower appreciation scores were granted when the participant feels that the intervention was too obvious. No conclusions can be drawn for the other statements, looking shabby or damaged as the response on these was low and without a trend.

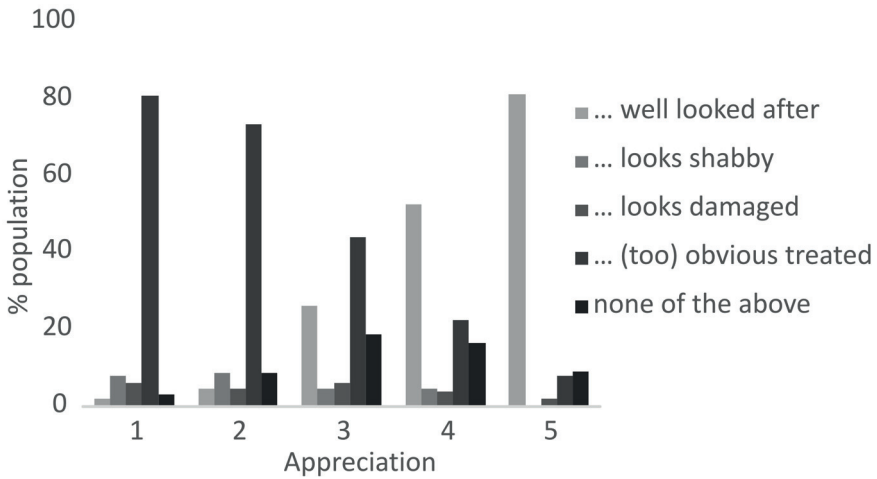


Figure 4.11: Link between appreciation and statement for photos 12–21.

4.4.2 Interventions: integration versus distinguishability

Article 12 of the Venice Charter states: *Replacements of missing parts must integrate harmoniously with the whole, but at the same time must be distinguishable from the original so that restoration does not falsify the artistic or historic evidence.*

This can be applied for the replacement of natural stone. The use of replacement stones should integrate harmoniously with the original material. At the same time they should be distinguishable from it, so that it is clear where interventions on the original material have taken place. To facilitate the harmonious integration, replacement stones can be made distinguishable by a small stone mark and good documentation. As such, an intervention could be considered successful if it is unnoticed or if it is not distracting. Figure 4.12 shows the opinion on the interventions for each photo.

Photo 18 scores the best; only 11 % found the intervention visible and distracting. It is even possible that part of this response relates to the window frame. Nevertheless, this case scores good on integration which is most likely the result of the ageing, even with different stone types used among each other.

In the case of photos 12, 15 and 20, more participants think that the

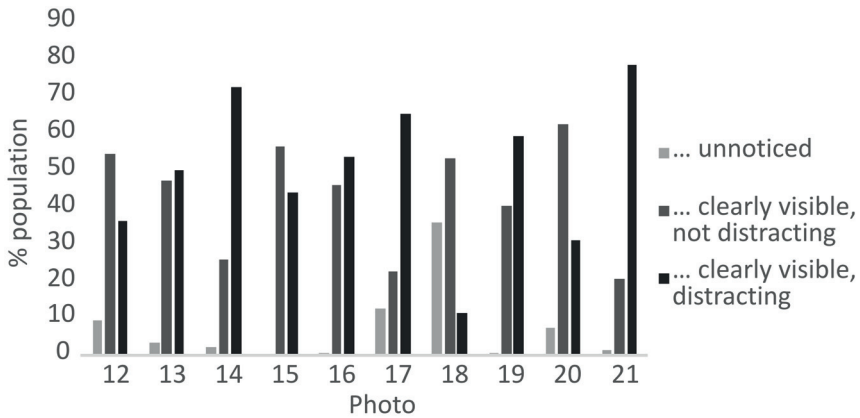


Figure 4.12: Opinion on the interventions for photos 12–21.

intervention is not distracting. This is especially striking for the (aim of) historical reconstruction in photo 15. As such, the results could indicate a positive notion in the eye of most participants on distinguishability and integration. However, a relatively large group remains to think it is distracting. Here, the question remains whether a less distinguishable reconstruction could resolve this.

4.5 Conclusions

The appreciation of natural stone could be an indication for the need for intervention. With increasing appreciation, the apparent need for intervention decreases. As such, damage is defined by the appreciation. Structural damage is less appreciated than fouling. However, in contrast to structural damage, textural heterogeneity in the stone, such as macroporosity, is not perceived negatively.

The appreciation of natural stone is also influenced by human intervention. Mainly the historical or authentic appearance is important. An assemblage of different natural stones is more appreciated when all stones are aged. Opposite, clearly new stones which do not show this ageing decrease the appreciation, even if the material is the same or has similar historical value.

References

- C Andrew. Perception and aesthetics of weathered stone façades. In R Prikryl and H A Viles, editors, *Understanding and managing stone decay*, pages 331–339, Prague, 2002. Karolinum Press.
- E Doehne and C Price. *Stone Conservation - An overview of current research*. The Getty Conservation Institute, Los Angeles, 2010.
- ICOMOS. The Venice Charter - International Charter for the conservation and Restoration of Monuments and sites. Approved by the 2nd International Congress of Architects and Technicians of Historic Monuments. Technical report, Venice, 1964, 1966.
- ICOMOS-ICS. Illustrated glossary on stone deterioration pattern, 2008. URL http://international.icomos.org/publications/monuments{_}and{_}sites/15/pdf/Monuments{_}and{_}Sites{_}15{_}ISCS{_}Glossary{_}Stone.pdf.
- W Quist, T De Kock, T G Nijland, R P J Van Hees, and V Cnudde. Conserving van witte steen: verbetering of verspilde moeite? De beleving van interventies in Vlaanderen en Nederland. In H De Clercq and W Quist, editors, *5e Vlaams-Nederlandse Natuursteendag*, volume 316, pages 5–14, Brussels, Belgium, 2014a. Geological Survey of Belgium Professional Paper.
- W Quist, T G Nijland, R P J Van Hees, and V Cnudde. Verbetering of verspilde moeite? Conserving van witte steen. *Natuursteen*, (Nummer 9):4, 2014b.
- W J Quist, R P J Van Hees, S Naldini, and T G Nijland. The perception of small scale damage and repairs of natural stone. In *I1DBMC International Conference on Durability of Building Materials and Components*, page 9, Istanbul, 2008.

5

Integrated characterization of the natural variability of Lede stone

Different individual chemical, (petro-)physical and mechanical properties can be defined for natural building stones. Such properties can relate to chemical reactivity (e.g. dissolution-precipitation), mechanical strength (e.g. exposure to stress), and petrophysical behaviour (e.g. water transfer). The physico-chemical properties of limestone are at least partly related to the microfacies (Flügel, 2010) i.e. to the sedimentary and diagenetic history. Thus an integrated approach contains a multi-perspective characterization, based on petrographical and chemical analysis, mechanical and petrophysical studies. The study of the physico-chemical properties is important to understand the natural variability in resources (e.g. Fronteau et al., 2010; Bednarik et al., 2014), to establish quality criteria, to understand alteration, deterioration and ageing (e.g. Benavente et al., 2007; Vazquez et al., 2013, 2015), and to establish criteria for replacement stones (e.g. Graue et al., 2011; Urosevic et al., 2011).

As discussed in Chapter 3, the petrological heterogeneity in Lede stone is relatively large. The stone, however, is always discussed under one name, *Balegemse steen*, as which it is included in the reference list of EN 12440 (2008). Hence, only one technical sheet is required, and it has always been

composed on the most average and reproducible samples. In old buildings, one can find the entire natural variability from compact to more fossiliferous and/or porous stones. In general, professionals are not too enthusiastic when they have to deal with the very porous variant. It relates to the general misconception that a higher porosity irrefutably means lower quality and lower durability. Rather than the total porosity, however, specialists agree that pore size and pore size distribution, pore connectivity and rock texture are critical for its durability. This chapter will deal more detailed with the natural variability in petrophysical properties of Lede stone, and the implications for durability.

5.1 Lede stone samples & Visual estimation chart

To illustrate the natural variability in Lede stone, six reference specimen from the Balegro quarry in Balegem with sizes of approximate 12.5 cm × 20 cm were selected. These cover the macroscopic variability from compact to very porous. They were photographed using a flatbed scanner to reproduce standard conditions. The images were thresholded using ImageJ/Fiji based on their Hue-Saturation-Brightness values to segment the porosity. Thresholding values were Saturation (46–255) and Brightness (0–167/169). The porosity was calculated from the binary images and the binary images were saved to create a visual porosity estimation chart (VEC), similar to visual estimation charts for mineral abundance in microscopy (Fig. 5.1). The six different reference specimen were ordered from low porosity or compact (type 1–2), over medium porosity (type 3–4) to high porosity (type 5–6). As the VEC is usable for industrial purposes, the denomination of the different kinds as type rather than as class is chosen to avoid the misconception that type 1 (compact) would be the best quality and type 6 (very porous) would be the lowest quality. Therefore also, in the visual estimation chart, the samples are referred to only by the numbers 1–6 (Fig. 5.1).

Even for these relative large samples, there is a large spread on the visual estimations of porosity, going from less than 2 % to estimations of 25 %. As only the visual porosity (or macroporosity, see section 5.3) is incorporated here, the true porosity of the samples will always be higher. It is absolutely possible that building stones consist of different types, and that porous zones pass into compact stones in the same stone.

The compact samples contain very few macrofossils, and seem macroscopically well sorted. Moreover, they often contain liesegang rings. The macroscopic fossil content increases with porosity in the samples with medium porosity. Their fabric goes from dispersed to loosely packed and their sorting evolves into a bimodal distribution. The samples with high porosity show a densely packed, poorly sorted bioclastic content, with macrofossils or fossil casts that give rise to moldic porosity. The difference between the six types can be small and gradual to abrupt. In practice, for example type 1 and 2 or type 3 and 4 will be very difficult to distinguish. Therefore, these classes were regrouped into three arbitrarily defined microfacies based on the visual estimated porosity: low porosity (< 7 %, type 1–2), medium porosity (7–15 %, type 3, 4, 5) and high porosity (> 15 %, type 6). These microfacies are abbreviated as Lf1, Lf2 and Lf3 respectively and samples from each group were achieved from Balegro quarry (Balegem, Lambert72 XY 110960 178760) (Fig. 2.6 and 5.2). Several subsamples were drilled or sawn with appropriate dimensions for a detailed characterization. The samples were always oven dried at 40 °C, unless specified otherwise. The characterization was performed on the smallest possible stone volume. Therefore, non-destructive tests were repeatedly performed on the same samples. Karsten tube and contact sponge measurements were done on the large samples before subsampling. From each microfacies (Lf1, Lf2, Lf3) six cylindrical specimen with nominal diameter 36.50 mm and a nominal length of 44–52 mm were cored to measure subsequently open porosity, water absorption under atmospheric pressure, capillary rise, drying rate, ultrasound velocity and uniaxial compressive strength; six specimen with nominal diameter 36.50 mm and nominal length of 15 mm were cored to measure subsequently open porosity, water vapour diffusion and tensile strength.

5.2 Petrography

Optical microscopy was performed with a Zeiss Axioscope A.1 equipped with an Axiocam camera and Axiovision software. 30 µm thin sections were partly stained with K-ferricyanide to distinguish ferroan carbonate phases. The abundancy of the different components was measured by point counting using JMicrovision freeware.





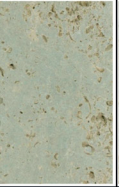
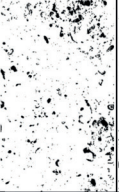
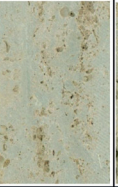
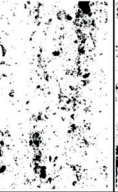
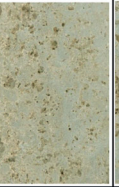
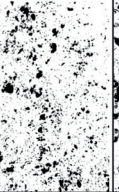
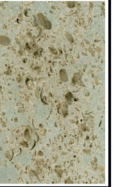
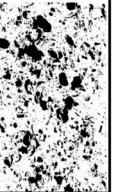
Lede stone			
Photo	Visual Porosity		Typical structures & fabric
	estimation chart	area-%	
		< 2	Compact Liesegang rings (red colored)
		~ 3,2	Compact with bioclasts
		~ 6,9	Local fossil concentrations Similar to 4
		~ 9,5	Local fossil concentrations Similar to 3
		~ 12	High Nummulid & Ditrupa content
		~ 25	Bioclastic molds > 1 cm ³

Figure 5.1: Visual estimation chart to estimate the porosity of Lede stone. Binary images represent the porosity (black). Field of view approximately 12 cm × 18 cm for each sample.

5.2.1 Lf1: low porosity

Lf1 is the microfacies with the lowest visible porosity. It can be determined as a quartz-rich packstone to grainstone (Fig. 5.3 A and B).

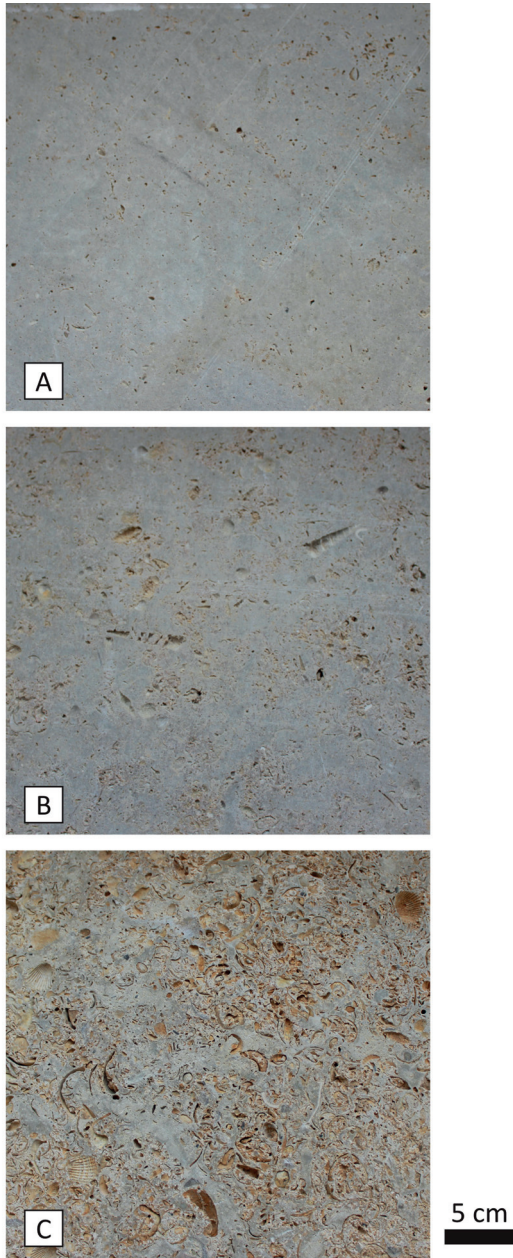


Figure 5.2: Macroscopic photograph of the three microfacies; A) Lf1; B) Lf2 and C) Lf3.

Macroscopically, it is (greenish) grey, with locally some orange-brown shine, especially around the porous zones. The porosity is dispersed and mainly moldic related to small bioclasts. Layering is not obvious in the sample.

This microfacies is composed out of sand fraction (43.8 %), matrix/cement (43 %), bioclasts (6.6 %), glauconite (2 %), porosity (3.6 %) and others (1 %). The sand fraction dominantly consists out of quartz, with some feldspars (mainly K-feldspar) estimated below 10 % of the total sand fraction. The sand fraction is bimodal distributed with a dominant population of very fine to fine sand grains (63–250 μm), with a positive skewness, being an excess of fine grains. They have a dominantly angular to sometimes subrounded texture. A subordinate population of medium to coarse quartz (250–1000 μm) is dispersed in the rock and is subrounded to rounded. The texture is grain supported with point contacts between the quartz grains. Other detritic components are heavy minerals and muscovite. The glauconite grains are oval, not very lobate, and generally green and not weathered. Sizes range from dominantly 60–100 μm to exceptionally 250 μm .

The bioclasts are dominated by smaller *Miliolina* forams (sizes up to 200 μm) and larger *Nummulites variolarius* (sizes up to 1500 μm). Some *Ditrupa sp.* are present, filled either with sediment either with sparite dog tooth crystals. Some bioclasts are broken by reworking. Echinoderm fragments and shell ghosts are occasionally found.

The matrix/cement is mainly intergranular microsparite, alternated locally by micrite lamina or bands. A first cement phase is dog tooth cement on *Nummulites* and echinoderms. Staining with K-ferricyanide shows that this first cement phase, and the intergranular microsparite and micrite are all ferroan calcite (Fig. 5.4 E). The calcite tests of the bioclasts are not ferroan.

5.2.2 Lf2: medium porosity

The texture of Lf2 is more heterogeneous compared to Lf1, but it can also be classified as a quartz-rich packstone to grainstone (Fig. 5.3 C and D). Macroscopically, the porosity is estimated larger than that of Lf1, also larger moldic features are more common, e.g. *Turritella sp.*. The colour is very similar, except for the larger pores, which have more clearly an orange-brown lining. Layering is not obvious in textural variation, but can

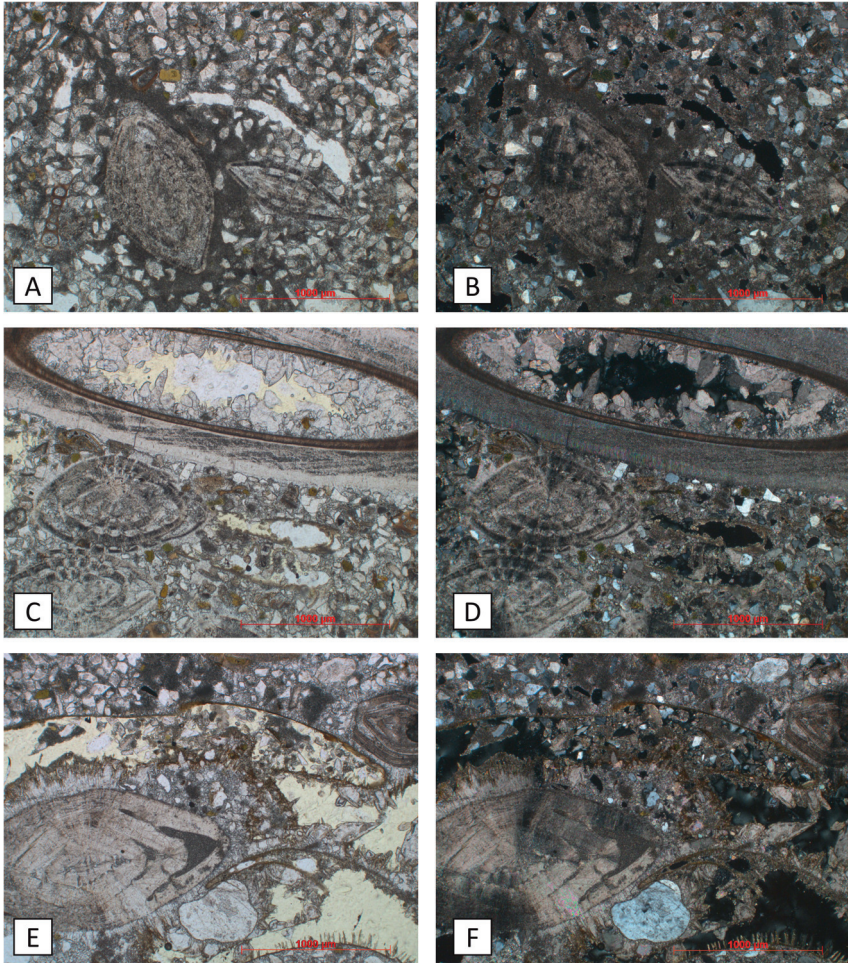


Figure 5.3: Micrographs of the different microfacies, in the left column under plane polarised light (PPL) and in the right column under crossed polars (XPL). A and B) Lf1 with quartz grains (white in PPL), Nummulites (central), Miliolina (brown tests), glauconite (yellow-green in PPL), micrite and microsparite (fine grained and dark in PPL). C and D) Lf2 with quartz grains (white in PPL), Nummulites (left), Miliolina (brown tests left and right), glauconite (yellow-green in PPL), *Ditrupa* sp. (top) with sparite crystals inside. E and F) quartz grains (white in PPL), Nummulites (left) with dog tooth cement, glauconite (yellow-green in PPL), micrite and microsparite, and moldic porosity (top and bottom) (fine grained and dark in PPL). The scale bar is 1000 μm .

be deduced by the orientation of elongated components such as *Turritella* sp. casts, of which the elongated direction is (sub)parallel to the bedding

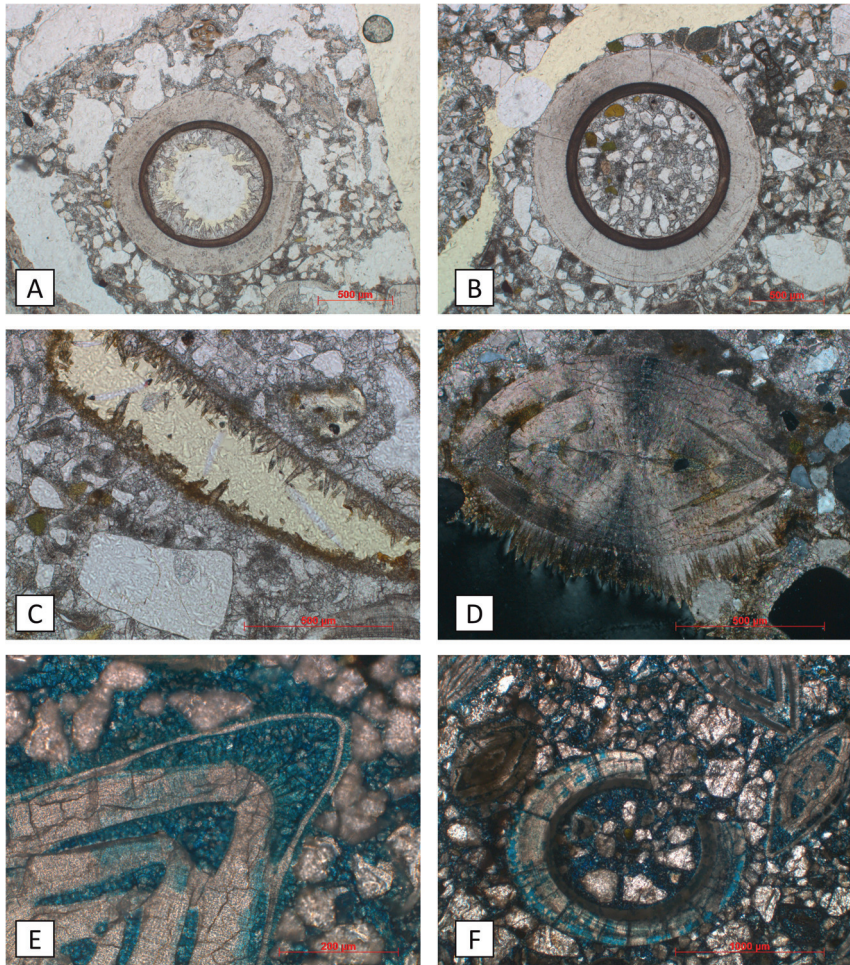


Figure 5.4: Micrographs of different features. A) *Ditrupa* sp. with infilling of dog tooth cement; B) *Ditrupa* sp. with sediment infilling; C) Moldic porosity with dog tooth cement lining the porosity; D) Nummulite with dog tooth cement and iron oxides, E) K-ferricyanide staining of dog tooth cement on Nummulites and microsparite indicating the carbonate is ferroan calcite (blue), the tests of Nummulites are not ferroan; F) K-ferricyanide staining of microsparite and parts of *Ditrupa*.

plane.

Relative more bioclasts and pores are present at the expense of the sand fraction (quartz with some feldspars). This microfacies has 26.4 % sand fraction and 17 % bioclasts. The matrix and cement fraction is similar to

Lf1, 43.7 %, as is the others fraction (heavy minerals and muscovite) with 1 %. Lf2 contains somewhat more glauconite (3.4 %) and more porosity (8.1 %). Areas with texture and composition similar to Lf1 frequently alternate with more coarse textures. These consist out of higher concentrations of packed *Nummulites variolarius*, *Ditrupa sp.*, coarse rounded quartz and shell ghosts. Relative more *Ditrupa sp.* and larger Miliolina forams are fragmented, indicating reworking before sedimentation. The larger pores mainly have a moldic or shelter character, the smaller pores are mainly interparticular and intraparticular. Dog tooth cement is pronounced around *Nummulites*, whilst the main phase is microsparite. Both are ferroan calcite. *Ditrupa sp.* have partially ferroan and non-ferroan calcite zones, suggesting partial recrystallization (Fig. 5.4 F).

5.2.3 Lf3: high porosity

Lf3 has the coarsest and most porous texture of all three defined microfacies. It can be classified as a packstone to grainstone or as a rudstone (Fig. 5.3 E and F). As these classifications are based on depositional texture, rudstone is the most appropriate classification, since more than 10 % of the grains is larger than 2 mm. Many of those initially deposited grains (in fact bioclasts) are now partially or completely dissolved, resulting in an obvious moldic porosity. The colour of the compact zones is similar to Lf1 and Lf2, but the overall colour is more dominated by the orange-brown lining of macroscopic porosity. The moldic features can mainly be attributed to bivalves, although gastropods are also present. Also shark teeth can be present. This facies can be described as a shell bed, or lumachelle, with a concordant to oblique stacking, mostly interpreted as storm lags (Kidwell, 1991).

Microscopically, Lf3 shows a coarse texture with the presence of larger (> 1000 μm) shell relicts, a packing of *Nummulites* and relative high abundance of coarse rounded quartz compared to the other microfacies. The rock is composed of 14 % sand fraction (quartz with some feldspars), 2.2 % glauconite, 24 % bioclasts, 64 % matrix and cement, 1% others and 12.8 % porosity. The coarse fragments irregularly alternate with areas of fine grained texture similar to Lf1. In most cases, shell relicts give rise to a high moldic porosity, contributing largely the high total porosity of the sample. The moldic porosity is often lined with dog tooth cement and a diffuse layer of iron oxides (Fig. 5.4 C), giving rise to the brownish colour

of the shell ghosts in macroscopic view. Some of the *Nummulites* have dog tooth cement overgrowth where they are adjacent to (moldic) pores. This cement is also ferroan calcite.

5.2.4 Petrographic variation

The three microfacies, Lf1, Lf2 and Lf3, have some similarities as well as some differences. The texture of Lf1 is compact, with a large fraction of small angular quartz, a small fraction of glauconite, diverse microfossils and dispersed throughout the stone *Nummulites*, *Ditrupa* and larger rounded quartz. This facies has the lowest porosity and is mostly quartz grain-supported. A relict micrite matrix is present, whilst around some bioclasts dog tooth cement and syntaxial overgrowth is slightly developed and also microsparitic regions are common.

In Lf2 and Lf3, regions with a similar texture can be found. However, these are irregularly alternated with coarser and more porous zones. In Lf2, regions with a higher abundance of *Nummulites*, *Ditrupa* and coarse quartz are frequent. In addition to this, Lf3 also shows the packing of larger bioclasts such as bivalve shells, which gave rise to a high shelter and later moldic porosity which is responsible for the high porosity.

Lf3 contains larger clasts relative to Lf1. Where in Lf1 *Miliolina* are abundant, relative more *Nummulites*, coarse quartz and larger bioclasts such as bivalves are present. Mainly the packing of the large bioclasts and moldic structures are responsible for an increased porosity. Lf3, in contrast to the others, also has iron oxide precipitation on the edges of large moldic pores.

The glauconite content varies between 2 and 4 %, but no significant differences in amount could be found between the different microfacies. In Lf3, however, glauconite is occasionally observed in the tests of forams. The first cement phase dog tooth cement on *Nummulites* and syntaxial overgrowth on echinoderms is more pronounced in the porous microfacies Lf3, likely because the cementing fluids were preferentially conducted in this facies. This phenomenon could also have enhanced the dissolution of (aragonite?) mollusc shells, heaving a positive feedback on the fluid flow in this facies. Some recrystallization of the matrix to microsparite must have occurred subsequently. During or after this phase, sparry dog tooth cement developed on the border of moldic pores.

5.3 Porosity

Porosity is defined as the volume of pores with respect to the bulk volume of the stone. Its shape and dimensions affect properties such as strength and water transfer, which in turn affect durability (Beck et al., 2003). There is a difference in total porosity and effective or open porosity, the latter being the total volume of interconnected pores. In limestone, the pore geometry is generally related to its genesis and is best classified as such (Choquette and Pray, 1970). They could be classified based on their time of formation (primary or secondary pores) and on their relation to rock fabric (fabric selective or non-fabric selective pores) (Flügel, 2010). Choquette and Pray (1970) suggest size classes of microporosity ($< 63 \mu\text{m}$) and macroporosity ($> 63 \mu\text{m}$). Other authors have used different size classes depending on the method they used or the process they studied, for example Di Benedetto et al. (2015) define mesoporosity as $0.002\text{--}0.05 \mu\text{m}$ and macroporosity $> 0.05 \mu\text{m}$. Here, micropores are defined as $< 1 \mu\text{m}$, mesopores as $1\text{--}63 \mu\text{m}$ and macropores as $> 63 \mu\text{m}$; in this definition, macropores should generally be visible for the naked eye. Overlapping this, is the use of capillary pores as the range from $0.1\text{--}1000 \mu\text{m}$ (Siegesmund and Dürrast, 2011) and subcapillary pores as the range $< 0.1 \mu\text{m}$. The use of micro-, meso- and macropores or of capillary and subcapillary pores in this text will depend on the context.

5.3.1 Vacuum saturation

Method

The open porosity (P_o) and apparent density (ρ) were measured on six samples of each microfacies according to EN 1936 (2006) with cylindrical sample dimensions of 36.50 mm diameter and a height between 44 and 52 mm. The dry samples ($P1$) were kept in an evacuation vessel under a lowered pressure of approximately 2 kPa for 2 h, after which they were gradually immersed in water under the same conditions. After immersion, air pressure was recovered and the samples were left to equilibrate for 24 h. Subsequently, the samples were weighted under air ($P2$) and under water ($P3$). P_o and ρ are then determined based on the Archimedes principle with ρ_w as density of water (Eq. 5.1 and 5.2).

	ρ kg/m ³	ρ_{pc} kg/m ³	P_o vol.%	P_{pc} vol.%	MIP vol.%	μCT vol.%
Lf1	2531 ± 26	2531	6.30 ± 0.95	6.29	6.18	2.2
Lf2	2416 ± 46	2397	10.95 ± 1.82	11.81	8.57	8.1
Lf3	2184 ± 57	2212	19.57 ± 2.13	19.16	11.65	5.5

Table 5.1: Density and total porosity of the three microfacies, measured with vacuum saturation (EN 1936), pycnometry, MIP and μCT .

$$\rho = \frac{P1}{P2 - P3} \times \rho_w \quad (5.1)$$

$$P_o = \frac{P2 - P1}{P2 - P3} \times 100 \quad (5.2)$$

Results and discussion

The determination of the open porosity gives a more complete result with respect to the visual estimation (Table 5.1). Nevertheless, it confirms the classification of three groups of microfacies based on low, medium and high porosity. The average porosity of Lf1 is 6.30 ± 0.95 vol.%, with the lowest value 5.23 vol.% and the highest 7.62 vol.%. For Lf2 this is 10.95 ± 1.82 vol.%, 8.93 vol.% and 14.50 vol.% respectively, and for Lf3 19.57 ± 2.13 vol.%, 15.84 vol. % and 23.19 vol.%.

The absolute standard deviation increases with porosity, but it is more or less the same percentage. It reflects the natural heterogeneity. Figure 5.5 shows ρ with respect to P_o . Samples with higher porosity have a slightly higher real density (i.e. the density of the material without its voids). Lf1 has a real density of 2706 ± 4 kg/m³, Lf2 has a real density of 2713 ± 6 kg/m³ and Lf3 has a real density of 2715 ± 2.7 kg/m³. This could be explained by a small difference in composition. For example, the porous samples could contain relatively more calcite (specific gravity 2.71) with respect to quartz (general specific gravity 2.65) compared to the compact samples. This was also observed by point counting.

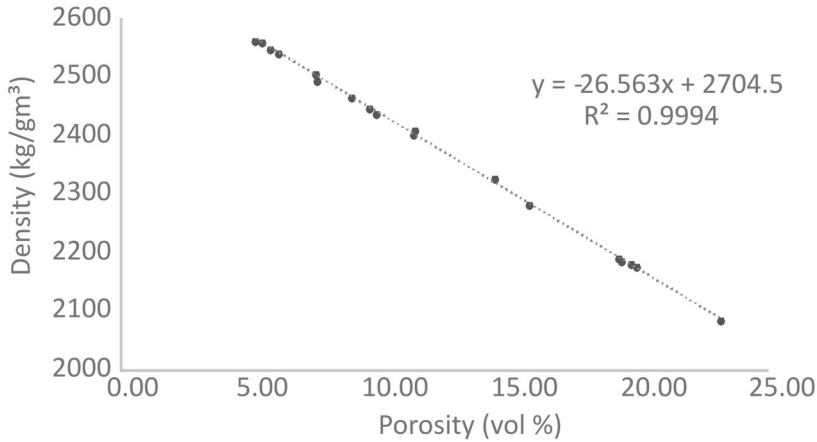


Figure 5.5: Results of density plotted vs. porosity for each sample (bullets) and linear regression between the samples.

5.3.2 Pycnometry

Method

Pycnometry is based on measuring the absolute volume of a material. For example a specific volume of gas, preferentially helium for its low viscosity and minimal adsorption on surfaces (Hall and Hoff, 2002), is entered in a probe of known volume containing a sample. The volume change of the gas is estimated by the pressure difference and equalizes the real volume of the material.

Here, pycnometry was used to validate the results of the vacuum saturation method. Open porosity and apparent density by means of pycnometry were measured at the University of Mons on 2 cylindrical samples of each microfacies with diameter of approximately 25 mm and a height of approximately 50 mm. A Micromeritics GeoPyc 1360 was used to measure the sample volume. The apparent density (ρ_{pc}) was calculated from the dry mass and the sample volume. A Micromeritics AccuPyc II 1340 gas pycnometer was used to determine the real density (ρ_r) by measuring the skeletal volume. Open porosity (P_{pc}) was then calculated using the apparent and real density according to Eq. 5.3. The samples were derived from the same material as the samples for the vacuum saturation method, but were not exactly the same for practical issues

concerning the dimensions. Therefore, results can only be compared indirectly.

$$P_{pc} = 1 - \frac{\rho_{pc}}{\rho_r} \times 1000 \quad (5.3)$$

Results and discussion

The open porosity P_{pc} and apparent density ρ_{pc} by means of pycnometry correspond in a good extent to the results of vacuum saturation (Table 5.1). The method is somewhat more labour intensive, the equipment is more expensive and in this case the sample size is more restricted compared to the vacuum saturation method. However, the results tend to be very accurate. The vacuum saturation has the disadvantage that it can not be determined whether the saturation state is completely attained or not, and that larger pores on the sample surface lose their water upon weighing in the air. Here, the results show a good agreement with the porosity variation in between the different microfacies.

5.3.3 Mercury Intrusion Porosimetry

Method

Mercury Intrusion Porosimetry (MIP) is a way to measure total porosity and pore size distribution of a porous material by imbibition with mercury. Mercury is a non-wetting fluid, so that imbibition of the pores only occurs by applying a capillary pressure. The smaller the capillary, the larger the pressure that needs to be applied. This is expressed by the Washburn equation (Eq. 5.4), where P_c is the capillary pressure, γ stands for surface tension, θ is the contact angle of the liquid and r is the radius of the capillary (Abell et al., 1999).

$$P_c = \frac{2\gamma}{r} \cos\theta \quad (5.4)$$

As such, the capillary pressure corresponds to a pore radius and a pressure range results in a pore size distribution. The volume intruded at a specific pressure stands for the volume of the corresponding pore radius. However, some assumptions and limitation should be taken into considerations (Diamond, 2000; Giesche, 2006). The Washburn equation holds for ideal, i.e. cylindrical, capillary pores and a theoretically defined contact angle.

In reality, pore geometries are much more complex. Certain geometries can for example create the so-called ink bottle effect. Here, a larger pore can only be accessed by a smaller bottleneck. In this case, the volume of the larger pore can only be measured after applying pressure to protrude the bottleneck and the corresponding pore size will be that of the size of the bottleneck. Therefore, MIP will overestimate the volume of small pores. Rather than a pore size distribution, MIP measures the pore throat or pore access size distribution. In other words, MIP measures the largest connection from the sample surface towards a pore.

From this perspective, two parameters are formulated (Boel, 2007). The critical radius (R_{cr}) is defined as the inflection point on the cumulative porosity curve, or the largest volume of mercury intrusion on the differential pore size distribution. It represents the most frequent radius for maximum percolation of the sample. The breakthrough radius (R_{br}) corresponds to the largest radius which gives access to the percolation of the pore network. Below this radius, an important increase in mercury intrusion is observed.

Typically, pressures over 400 MPa can be applied, resulting in pore (throat) size measurements up to 4 nm. Exerting such pressure, not all rocks are capable withstanding it, thereby potentially creating error in the measurement. Samples sizes are small, and because of the residual mercury after the test, this technique can be seen as destructive. MIP was performed at the Université de Reims-Champagne Ardenne (France) with a Micromeritics Autopore IV 9500.

Results and discussion

The results can be presented as total porosity or as a pore size distribution. Table 5.1 shows that the porosity results are lower compared to the porosity by vacuum saturation and helium pycnometry. Lf1 has an MIP porosity of 6.18 vol.%. This is still in relative good agreement with the porosity by vacuum saturation (6.30 vol.%) and helium pycnometry (6.28 vol.%). The sample is about 5^3 times smaller than the samples for vacuum saturation, but the value for porosity is largely within the margin of error for the mean porosity. This is because Lf1 lacks larger (moldic) pores as described in 5.2. The pore size distribution as measured here can be seen as representative for the entire sample.

Lf2 has an MIP porosity of 8.57 vol.%. This falls outside of the margin of error for the mean porosity of this microfacies measured by vacuum saturation. It is also lower than the lowest measured value (8.93 vol.%).

This is a question of representative elementary volume. In this microfacies, larger moldic pores as described in section 5.2 have a significant influence of the total porosity. The recurrence of such larger moldic pores is too low in the sample volume suited for MIP. Therefore, these pores and thus the total porosity is underestimated.

This effect becomes very pronounced in the analysis of Lf3. The MIP porosity is 11.68 vol.%, compared to a mean of 19.57 vol.% and a lowest value of 15.84 vol.% for vacuum saturation. This microfacies was dominated by the presence of larger moldic porosity, often larger than 2 mm in cross section. This moldic porosity has a major influence on porosity and the recurrence of such porosity is not high enough in the sample dimensions for MIP. This is also a sampling effect: cores of 10 mm diameter could only be drilled on more compact surfaces, between the larger pores, because of the precondition that they would fall apart if a larger pore crosscuts the sample. Also, pores with a large radius connected to the surface could already be partially filled with mercury before applying pressure.

Pore (throat) size distributions could be measured in the range of pores with radius of 175 μm to 0.005 μm . For Lf1, the pore size distribution can be seen as representative for the microfacies. For Lf2 and especially Lf3, it has been discussed above that it lacks the measurement of pores larger than 175 μm to create an accurate total pore (throat) size distribution. Figure 5.6 shows the differential pore size distribution for the three samples. Figure 5.7 gives the cumulative intrusion curve, recalculated to the measured total MIP porosity. Table 5.2 shows the R_{cr} and R_{br} together with the total MIP porosity.

Lf1 shows a bimodal distribution, with a subordinate volume of larger pores between 10 and 175 μm , and a main distribution of pores smaller than 1 μm . The cumulative distribution shows that more than 4 vol.% porosity is attributed to microporosity. R_{cr} is 0.032 μm , but a secondary peak is observed at 0.055 μm . R_{br} is 0.37 μm . Lf2 has multiple intrusion peaks, at 19.72, 6.49, 2.06 and 1.02 μm and a broad distribution around R_{cr} of 0.055 μm . Because of this, the pore (throat) size seems relatively continuous distributed above R_{br} , which is 0.58 μm . Visual observations and petrography allowed to identify reasonable amount of macroporosity, however, whilst pores with a radius corresponding to the observed intrusion peaks in the mesoporosity range are difficult to assign to the fabric. It is likely that the intrusion peaks in the mesoporosity are actual

	MIP total porosity vol. %	R_{cr} μm	R_{br} μm
Lf1	6.18	0.032	0.37
Lf2	8.57	0.055	0.58
Lf3	11.65	0.15	1.03

Table 5.2: Total MIP porosity, critical radius and breakthrough radius for each microfacies

the largest connection of macropores to the outer surface (i.e. ink bottle effects). At pressures where these pore throats are overcome, the macropores rapidly fill with mercury. Thus, more likely than a relative continuous pore network, it seems that the macroporosity is connected by pores on the meso- and microporosity range. Lf3 shows a distribution similar to Lf1, but with a larger differential intrusion volume, thus higher porosities. The shape of the differential pore size distribution shows that the macroporosity is likely well connected by larger pore throats, in contrast to Lf2. R_{cr} is 0.15 μm and R_{br} is 1.03 μm . Ink bottle effects are much less pronounced for Lf1 and Lf3, as the former microfacies has less macropores and the latter has macropores that are very well connected, especially on the scale of the sample size for MIP.

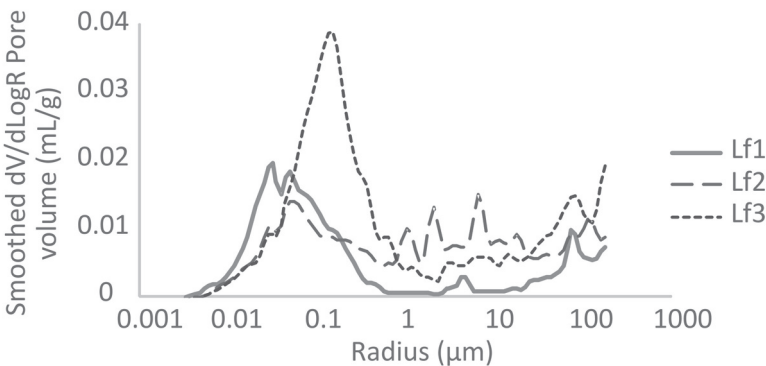


Figure 5.6: Differential mercury intrusion volume in function of the pore radius.

The absolute volume of micropores in Lf3 is the largest of all three, but the relative proportion of pores below 1 μm is larger for Lf1 (76.6 % of the total pore volume) than for Lf3 (66.7 %). For Lf2, only 46.8 % of the

total pore volume has access smaller than 1 μm . This can also be observed on the differential pore size distribution, where Lf1 has the largest fraction of small pores ($< 0.055 \mu\text{m}$). However, such interpretation should be taken with care. The higher total porosity and the higher amount of meso- and macroporosity in Lf2 and Lf3 increase the probability than an inner pore is connected with the surface through a larger connection. This is reflected by R_{cr} and R_{br} , which increase with increasing total porosity from Lf1 to Lf3.

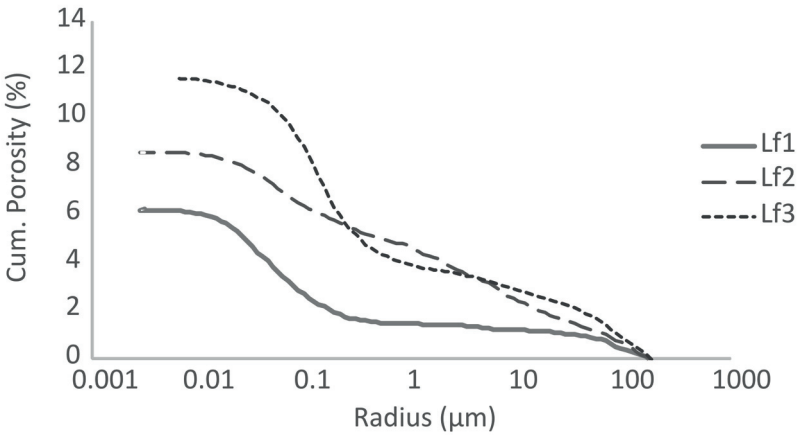


Figure 5.7: Cumulative absolute porosity measured by MIP in function of the pore radius.

In terms of capillary pores measured in the range 0.1–175 μm , Lf1 clearly has a lower relative proportion ($\pm 42.0 \%$), compared to Lf 2 and Lf3 ($\pm 73.5 \%$ and 73.7% respectively). This means that Lf1 has a high absolute volume of subcapillary pores, 3.58 vol. %. For Lf2 and Lf3, the absolute volume of subcapillary pores is only 2.27 vol.% and 3.06 vol.% respectively for the MIP samples.

5.3.4 X-ray computed microtomography

Method

X-ray computed microtomography (μCT) allows to visualize the internal structure of materials in 3D, in a non-destructive way and on the micrometer scale. A typical laboratory μCT system is composed of an

X-ray source, an X-ray detector and a motorized sample stage that provides rotational and translational movement of the sample relative to the source and detector. The principle is based on the attenuation of X-rays when they pass through the sample. When a monochromatic X-ray beam passes through a homogeneous material with thickness (T), the incident intensity (I_0) will attenuate to a transmitted intensity (I) as defined by the Lambert-Beer equation:

$$I = I_0 e^{-\mu T} \quad (5.5)$$

where μ is the linear attenuation coefficient. At a specific radiation energy, μ is a function of the material's density and chemical composition. As a stone is composed of different mineral phases and pores, the attenuation should be integrated over the entire path length (s) and a local linear attenuation coefficient for the specific phase ($\mu(s)$).

$$I = I_0 e^{-\int_T \mu^s ds} \quad (5.6)$$

This is valid for monochromatic X-ray beams. However, laboratory based μ CT have polychromatic X-ray sources, and eventually this can induce artefacts after reconstruction. Laboratory based systems also typically produce cone beams. This way, the sample is geometrically magnified by reducing the source object distance and increasing the object detector distance. The lower resolution limit is mainly determined by the focal spot size of the X-ray source.

μ CT was performed at the Centre for X-ray Tomography of the Ghent University (UGCT) using HECTOR, a high energy μ CT scanner (Masschaele et al., 2013) on samples of 10 mm diameter for each microfacies. The in-house protocol for stone sample was followed: 1 mm Al was applied as an X-ray filter to reduce beam hardening; the tube was operated at 130 kV and 10 W and 2001 projections with an exposure time of 1 s were taken. The scanning geometry allowed a reconstructed voxel size of 6.13 μ m. During scanning, the sample is rotated and several 2D radiographs are obtained under different angle. A stack of 2D slices through the object that create the 3D volume is obtained from a series of projections by a filtered backprojection algorithm. The reconstructions are performed with Octopus Reconstruction software (Vlassenbroeck et al., 2007). Images analysis as in traditional 2D porosimetry on optical

microscopy or scanning electron microscope images can be performed on a stack of slices, resulting in 3D measurements of the porosity (Brabant et al., 2011). The advantage is that the porosity and connectivity can be determined in 3D, and that shape parameters as well as other spatial information can be obtained. The limitations of μ CT are the lower resolution limits, here taken as three times the voxel resolution. Drawbacks that should be taken into consideration or that should be dealt with during reconstruction are possible artefacts, amongst others noise, beam hardening, ring artefacts and cone beam artefacts. There are largely reduced by the scanner hardware, as well during reconstruction.

Porosities were calculated after segmentation of the porosity using Octopus Analysis (Vlassenbroeck et al., 2007). The values can be represented as a total μ CT porosity value and as a pore size distribution based on the Equivalent Diameter (ED). This is the diameter of a sphere that has the same volume as a separated object, i.e. a pore. Other than MIP which measures the largest entrance to a pore, μ CT measures the total volume of the pore. To make a better comparison with MIP, the values of ED are presented in Figure 5.8 as Equivalent Radius, being ED/2. In theory, the largest possible measurable volume of a pore equals the sample volume. In practice, however, samples could only be prepared under the presumption that no pores with a dimension larger than the sample dimensions in the same direction could occur. The theoretical smallest pore sizes without manipulation equals the voxel resolution, if a pore has the same dimension and location of a voxel. In practice, only objects with an ED larger or equal to three times the voxel size, i.e. ED 18.39 μm were retained. The images were rendered using VG StudioMax.

Results and discussion

Table 5.1 shows the total porosity by means of μ CT image analysis. This results in 2.2 vol.% porosity for Lf1, 8.11 vol.% for Lf2 and 5.52 vol.% for Lf3. The porosities of all microfacies are underestimated with respect to the porosities measured by vacuum saturation and pycnometry. This is not surprising, as MIP revealed that a representative fraction of the porosity is microporosity, which is well below the analysis resolution. μ CT provides essential information on the pore sizes with an Equivalent Radius larger than 9.2 μm . Hence, the measured total μ CT porosity represents a fraction of the mesoporosity and the macroporosity.

Thus, Lf1 has a relative low volume fraction of meso- and macropores measured by μ CT. This agrees with the visual and petrographic

description where not many macropores were observed. Lf2 has a high volume fraction of pores in the mesoporosity and macroporosity range; this corresponds to the visual observations. Lf3, however, has a lower μ CT porosity than Lf2, whilst visual and petrographic observation clearly show that the amount of macroporosity is the largest for this facies. This again is a result of the sample size and sample preparation which did not allow to measure the largest moldic pores (i.e. $> 2000 \mu\text{m}$). On the other hand, Lf3 contains the highest volume fraction of pores with an Equivalent Radius $> 300 \mu\text{m}$ (Fig. 5.8), indicating the importance of larger pores for this sample.

The cumulative porosity is stepwise for the larger pore radii (Fig. 5.8). This is the result of the nature of the pores themselves: the larger a pore, the more influence it has on the total porosity. Moreover, with increasing pore size, the probability of encountering a large pore decreases with decreasing sample size. In other words, only a limited amount of pores with e.g. an equivalent radius of $1000 \mu\text{m}$ can be present in a sample with a diameter of 10 mm .

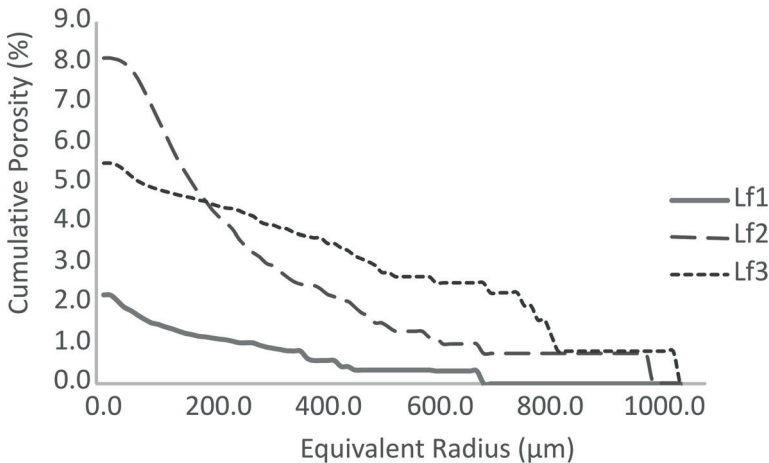


Figure 5.8: Cumulative absolute porosity for μ CT analysis in function of the pore radius.

5.3.5 Characterizing the pore system

The information of MIP and μ CT can be combined to get more complete information on the pore system (Cnudde et al., 2009; Andriani and Walsh, 2002). μ CT provides information on the larger pore sizes, where MIP provides information on the lower pore sizes or the pore throats. There is an overlap in the measuring range between both, depending on the resolution of μ CT. This overlap can be increased by using differential imaging (Boone et al., 2014). In this case, there is an overlap in the size range between 9.2 μm to 175 μm (Fig. 5.9). For the porosity or the pore network which is connected by pore throats lower than 9.2 μm , the MIP data can be consulted. On individual pores larger than 175 μm , the μ CT data provide information. In the range of overlap, both yield complementary information. μ CT gives more information on the absolute volume of the pores and pore throats in the meso- and macroporosity, whilst MIP gives information on the pore throats of any larger pore.

In general, Lf1 has the lowest porosity, in average 6.3 vol.%. The pore network shows a bimodal distribution, with a subordinate population of macropores (± 2 vol.%) and a major population of micropores (± 4 vol.%). The micropore network is accessed by a pore radius of 0.37 μm and connected by a pore radius of 0.032 μm . The macropores are related to intraparticle porosity and a very low fraction of moldic or shelter porosity. The microporosity is mainly related to interparticle porosity in the micrite phase or in between the microsparite cement.

The pore network of Lf2 is the most difficult to analyse. MIP shows several peaks in the mesoporous range. This is probably because the larger macropores are not well connected by a macropore network and the respective mesopore radii give access to more isolated macropores. In this case, also approximately 4 vol.% is attributed to micropores. From an average total porosity of 10.95 vol.% this means that approximately 7 vol.% can be related to macropores. This corresponds closely to the observation with μ CT.

The pore network of Lf3 also shows a bimodal distribution, but the total porosity is much higher, in average 19.57 vol.% compared to the Lf1 and Lf2. This is mainly related to the present of large moldic pores that relate to the dissolution of larger mollusc shells. However, an absolute volume of almost 8 vol.% can be attributed to micropores, which corresponds to 66.7 % of the pore fraction measured with MIP. In relation to the total

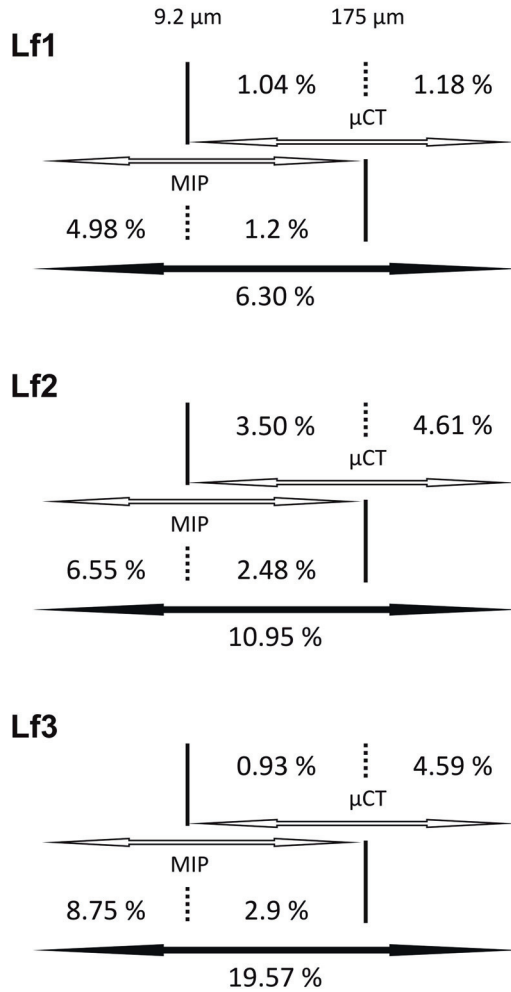


Figure 5.9: Comparison of the partial and total porosity obtained by vacuum saturation (black arrow), MIP and μCT (white arrows) over the specific measurement range

(average) porosity, this number is reduced to 40 % of the total porosity. This micropore network, however is accessed and connected with larger radii, 1.03 and 0.15 μm respectively, than the micropore network of Lf1. The network of micropores is well connected compared to Lf2.

5.4 Water transport properties

Water is an important medium for many deterioration processes in porous natural stone. It contributes to physical weathering, e.g. ice and salt crystallization (Ruedrich and Siegesmund, 2007), hydric and hygric expansion (Ruedrich et al., 2011). It can mediate chemical weathering (Rodríguez-Navarro and Sebastian, 1996), patina formation (Beck and Al-Mukhtar, 2014), biomodification (Smith et al., 2011) and it modifies the strength properties of stone (Török and Vasarhelyi, 2010). The uptake, retention and release depends on the pore structure and the ambient conditions. The rock tendency to the different processes of uptake, retention and release can be characterized and related to the pore structure.

5.4.1 Water absorption by total immersion

The water absorption by total immersion represents the weight of the absorbed water after 48 h in relation to the dry sample weight. This is the water which is freely absorbed under atmospheric pressure. From this the water saturation coefficient can be calculated as volume fraction of pores which is filled under atmospheric pressure. Historically, this has been used as a parameter to evaluate the frost susceptibility (Camerman, 1961), established by Hirschwald in 1912. A saturation coefficient > 0.9 was related to frost susceptible rocks, $0.8-0.9$ to possible frost susceptible rocks and < 0.8 to frost resistant rocks. As the water will be absorbed by capillary pores, the saturation coefficient depends on the pore size distribution and connectivity, while the water absorption also depends on total porosity and bulk density.

Method

The water absorption by total immersion was measured on six specimen of each microfacies according to EN 13755 (2008). The porosity by means of vacuum saturation was measured on the same samples. The dry samples (m_d) were placed in a container with a water level up to halfway the specimen. After 1 h, the water level was increased up to three quarters of the specimens height and after 2 h the specimen were totally immersed. After 48 h, the samples were weighted (m_w). The water absorption by total immersion (W_{atm}) was calculated according to Eq. 5.7. After weighing, the samples were immersed again for weighing after 72h. The difference between the successive weighing was less than 0.1 %. The

	W_{48} wt%	S_{48}	W_{72} wt%	S_{72}
Lf1	1.39 ± 0.17	0.54 ± 0.02	1.40 ± 0.17	0.55 ± 0.02
Lf2	2.57 ± 0.54	0.55 ± 0.02	2.57 ± 0.55	0.55 ± 0.02
Lf3	5.29 ± 0.86	0.58 ± 0.03	5.26 ± 0.88	0.57 ± 0.04

Table 5.3: Water absorption and saturation after 48 and 72 hours immersion under atmospheric pressure.

water saturation coefficient (S) is calculated as the relation of W_{atm48} to the water absorption under vacuum (W_{vac}) according to equation 5.8. W_{atm48} and S_{48} , and W_{atm72} and S_{72} are the water absorption and water saturation coefficients after 48 h and 72 h respectively.

$$W_{atm} = \frac{m_w - m_d}{m_d} \times 100 \quad (5.7)$$

$$S = \frac{W_{atm}}{W_{vac}} \quad (5.8)$$

Results and Discussion

The results are expressed in Table 5.3 with the water absorption after both 48 h and 72 h. The values for W_{atm48} are comparable to those of carbonate rocks and sandstones as listed by Mosch (2008). S_{48} , however, is relatively low, indicating that for most samples less than 60 % of the pores is filled with water after 48 h immersion.

Lf1 absorbs little more water in the 24h between 48h and 72h, whilst Lf2 does not absorb significant amounts and Lf3 seems to loose water. The latter is probably a measuring error because the macropores drain when the sample is taken out of the water. The water absorption is the lowest for Lf1, the highest for Lf3, and intermediate between both for Lf2. This is not surprising, as the total porosity increases equally. Figure 5.10 shows that there is a linear relation between W_{atm48} and the total porosity. Such a correlation is not present for S_{48} (Fig. 5.11), which is also strongly related to pore size and connectivity. From MIP it was clear that Lf3 has the best connectivity of the capillary pore network. This is reflected in a slightly higher water absorption.

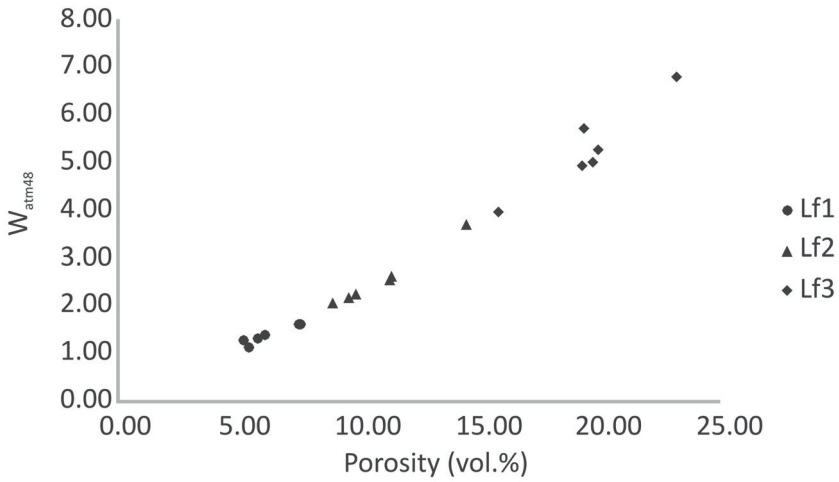


Figure 5.10: Relation between the water absorption in wt% and the porosity.

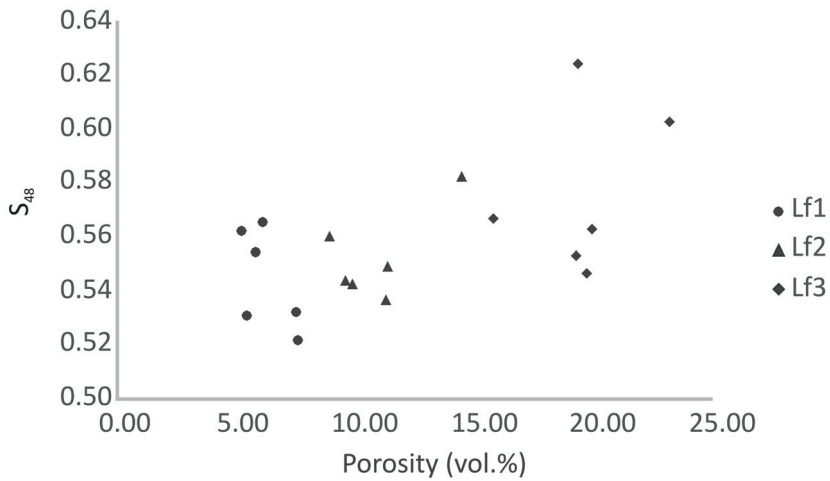


Figure 5.11: Relation between the saturation coefficient and the porosity.

5.4.2 Capillary water absorption

Capillary water absorption is the most important process for water absorption of building stones in contact with ground water or exposed to runoff or direct rain impact. In contact with a porous rock substrate, water, being a wetting liquid, will tend to spread out on the surface and enter the

pores. This phenomenon drives capillary absorption. This is determined by the capillary pressure inside a pore with radius r . For a cylindrical capillary tube, analogues to equation 5.4 and considered $\theta = 0^\circ$, the pressure gradient (ΔP) that forces capillary water uptake in a pore is governed by Laplace's equation (Beck et al., 2003):

$$\Delta P = \frac{2\gamma}{r} \quad (5.9)$$

The driving force, or the suction power, will be higher in smaller capillaries. The capillary rise in rocks is not only dependent on the size of the pores, but also on the shape (i.e. pore throats) and connectivity. The process of capillary water uptake is mainly important in the pore size range of 0.1 μm to 1 mm (Benavente et al., 2015). Smaller pores will have larger suction power (Eq. 5.9), i.e. the deepest water penetration. Larger pores, however, can have a higher suction velocity (Beck et al., 2006).

Method

Capillary water absorption was measured on six samples of each microfacies according to EN 1925 (1999). The porosity under vacuum saturation was also measured on these samples. Dry samples were placed on a support in a closed box and the bottom was filled with H_2O until the samples were approximately 3 mm immersed. Initially, samples were weighted after 4, 10, 20, 35, 60 and 180 minutes and subsequently at daily or weekly time intervals. The test was performed for 10 weeks and 1 day. The specimen were kept in a closed box and were not sealed. The results are plotted as a graph with the mass of absorbed water in grams divided by the absorption surface in m^2 in ordinate and the \sqrt{s} in abscissa. Generally, this graph can be approximated by two straight lines. The first line represents the initial absorption phase, filling the larger pores by capillary rise. The second line is a plateau that represents the further filling with water of the smaller pores by diffusion. If the linear regression of the measuring points in the first line is greater than 0.90 for five measuring points, or greater than 0.95 for four measuring points, the coefficient of water absorption is equal to the slope of this linear regression function (EN 1925, 1999):

$$C = \frac{m_i - m_d}{A\sqrt{t_i}} \quad (5.10)$$

In more complex pore systems, such a linear regression function cannot be satisfactorily. In this case, the measuring points can be better approximated by a non-linear regression function (EN 1925, 1999):

$$y_i = a(1 - e^{-b\sqrt{t_i}}) \quad (5.11)$$

Where y_i is the mass of absorbed water related to the surface area at time t_i . The coefficient of water absorption C is (EN 1925, 1999):

$$C = ab \quad (5.12)$$

Results and discussion

Each sample was evaluated individually to see if the capillary water absorption as mass divided by the surface in function of the square root of time can be approximated by a linear regression function or by a non-linear regression function. All samples of Lf1 and Lf2 were approximated by a non-linear regression function (Fig. 5.12). In Lf3, 5 samples were analysed with a linear regression function and 1 with a non-linear regression function (Fig. 5.12).

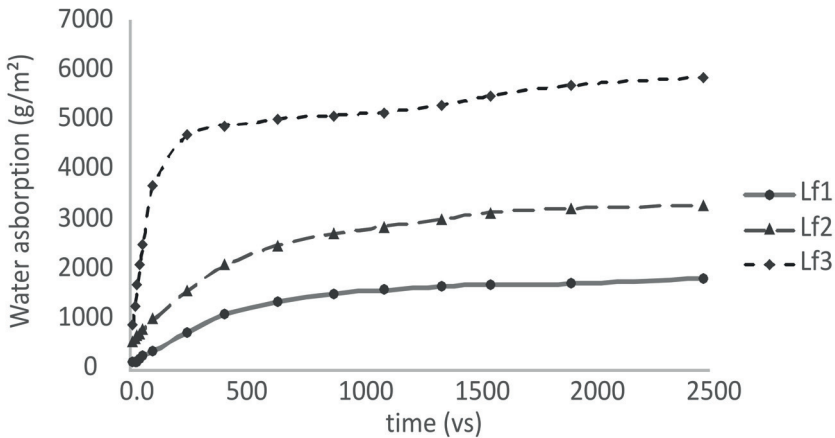


Figure 5.12: Capillary rise in function of time for a representative sample for each microfacies, with the measurements indicated by bullet points. C was approximated by a non-linear regression function for Lf1 and Lf2 and a linear regression function for Lf3.

	$C_{average}$ $\text{g m}^{-2} \text{s}^{-1/2}$	C_{min} $\text{g m}^{-2} \text{s}^{-1/2}$	C_{max} $\text{g m}^{-2} \text{s}^{-1/2}$
Lf1	4.73 ± 0.37	4.04	5.87
Lf2	15.76 ± 8.62	4.72	31.75
Lf3	33.55 ± 19.76	14.6	74.83

Table 5.4: Average coefficient of capillarity and maximum and minimum measured value for each microfacies.

Table 5.4 shows the average, minimal and maximal coefficient of capillarity for all three microfacies. There is both a large spread in average values as well as on the standard deviation. Depending on the coefficient in capillarity, rocks could be divided in three classes: low capillary absorption ($C < 8.33 \text{ g m}^{-2} \text{ s}^{-1/2}$), medium capillary absorption ($C = 8.33 - 50 \text{ g m}^{-2} \text{ s}^{-1/2}$) or high capillary absorption ($C > 50 \text{ g m}^{-2} \text{ s}^{-1/2}$).

The samples of Lf1 clearly have a low capillary absorption and a low variability. Most Lf2 samples have a medium capillary absorption, with some samples that have low capillary absorption. The samples of Lf3 have a medium capillary absorption with one sample having a high capillary absorption. This relates to the characteristics of the pore network (Fig. 5.13 and 5.14). In general, C increases with porosity and with better pore connectivity. The pore network of Lf3 is characterized by a breakthrough radius of $1.03 \mu\text{m}$, within the range of capillary pores. R_{br} of Lf1 and Lf2 are 0.37 and $0.58 \mu\text{m}$ respectively, which are more close to the lower boundary of capillary pores. In addition, Lf1 and Lf2 have a critical radius (most frequent radius) of 0.032 and $0.055 \mu\text{m}$ respectively, in the range of subcapillary pores, whilst R_{cr} of Lf3 is $0.15 \mu\text{m}$ and falls within the capillary pore range. Furthermore, the macroscopic pore network of Lf3 is better connected than that of Lf2 and Lf3 also has the highest amount of macroscopic pores. This results in a larger suction velocity for Lf3, compared to Lf2 and Lf1.

5.4.3 Moisture adsorption

Moisture adsorption in a stone occurs in equilibrium with the relative humidity of the surrounding air. At elevated relative humidity, capillary condensation occurs in the smallest pores (Franzen and Mirwald, 2004).

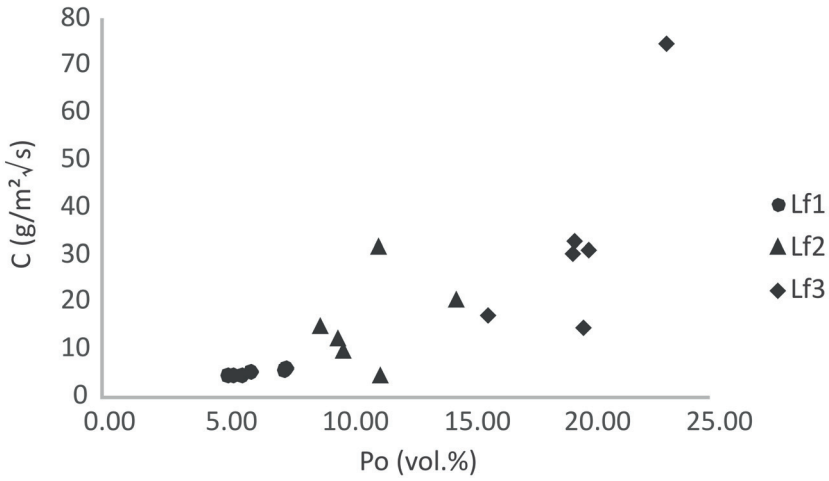


Figure 5.13: Relation between the coefficient of capillarity and the total porosity.

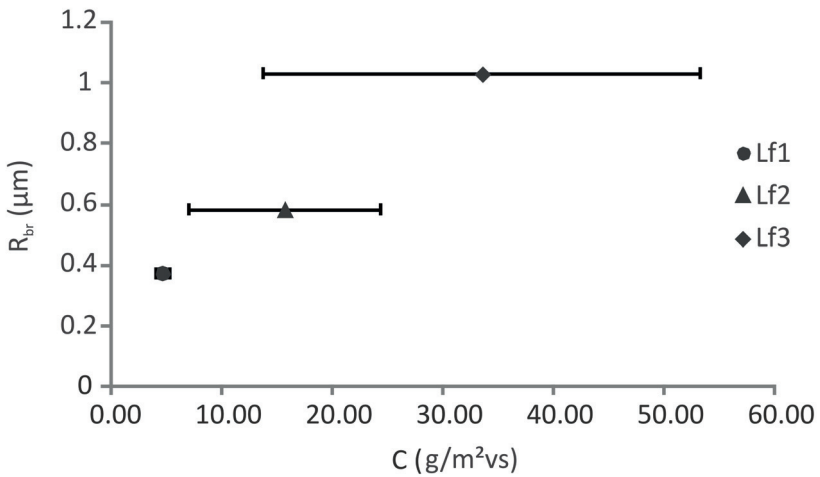


Figure 5.14: Relation between the breakthrough radius and the coefficient of capillarity.

This process is effective for pores with a radius up to some 0.1 μm, or in other words, more or less the subcapillary pores.

Moisture adsorption (wt%)	
Lf1	0.22
Lf2	0.20
Lf3	0.27

Table 5.5: Moisture adsorption at 95 % RH and 30 °C.

Method

Two cylindrical samples of each microfacies, with diameter 25.4 mm and a length of approximately 40 mm, were dried and subsequently conditioned in a climatic chamber at a constant temperature of 30 °C and 95 % RH. At such high relative humidity, capillary condensation occurs in the subcapillary pores (Stück et al., 2013). The samples were left to equilibrate for 21 days and were measured subsequently. The moisture absorption M was measured as wt% with respect to the dry weight. The porosity of the samples was measured with pycnometry (see section 5.3.2).

Results and discussion

The moisture adsorption of the samples at 95 % RH is very low (Table 5.5). This is related to the specific combination of total porosity and subcapillary pores. Lf2, which has the lowest moisture adsorption, has a low amount of subcapillary pores and an intermediate porosity. Lf1 has a low porosity, but has a higher relative amount of subcapillary pores, which results in a higher moisture adsorption. Lf3 has the highest moisture adsorption. It has a lower relative volume of subcapillary pores than Lf1, the higher moisture adsorption is the result of the overall much higher total porosity.

When the moisture adsorption in wt% is normalised over the porosity of the samples, then Lf1 has the highest moisture adsorption. In other words, the moisture adsorption is relatively higher in the pore network of Lf1, mainly related to the amount of subcapillary pores.

5.4.4 Water vapour diffusion

The diffusion of water vapour controls the second phase of drying of a wet porous rock until the moisture content is in equilibrium with the ambient relative humidity. The ease of water vapour diffusion is related to the gas permeability of the rock.

	μ
Lf1	25.84 ± 7.46
Lf2	19.56 ± 7.54
Lf3	12.59 ± 2.49

Table 5.6: Average water vapour resistance for each microfacies.

Method

The experiment is performed according to the wet cup principle, where the specimen is sealing to the open side of a cup containing an aqueous saturated solution, in this case pure H₂O (100 % RH). This assembly is placed in a climatic chamber, regulated at 25 °C and 50 % RH. The difference in partial vapour pressure between the test cup and the climatic chamber initiates a vapour flow through the stone sample, directed from cup to chamber. Periodic weighing of the assembly allows to determine the water vapour resistance from the linear part of the weight change (in steady state) according to equation 5.13 (EN ISO 12572, 2001).

$$\mu = \frac{A \cdot \Delta_p \cdot \delta_a}{G \cdot D} \quad (5.13)$$

With μ the water vapour resistance factor, A the surface of diffusion, Δ_p the water vapour pressure difference across the specimen, δ_a the water vapour permeability of air with respect to the partial vapour pressure, G the water vapour flow rate through the specimen and D the specimen thickness.

Results and discussion

The water vapour resistance factor is the lowest for Lf3 and the highest for Lf1 (Table 5.6). Lf3 has the highest porosity, the largest pores and a good pore connectivity. On the other hand, Lf1 has a lower porosity and the relative amount of subcapillary pores is more important. In these pores, capillary condensation can occur, leading to moisture adsorption and inhibiting the flow in the gas phase.

5.4.5 Gas permeability

Permeability is a rock property that defines how easily a fluid with specific viscosity flows through a rock under a pressure gradient. The key factors controlling permeability are thus porosity and the shape of the pore

	TP value	gas permeability (<i>mD</i>)
Lf1	12.027 ± 0.399	19.922 ± 20.945
Lf2	11.597 ± 0.512	87.65 ± 114.75
Lf3	10.482 ± 0.551	2651.0 ± 5026.6

Table 5.7: Average TP value and corresponding gas permeability for each microfacies.

network, i.e. pore throat sizes and connectivity. Notwithstanding the paucity of permeability data in weathering studies, the permeability and also the local variability in permeability can be an important parameter in the investigation of stone weathering (McKinley and Warke, 2007).

Method

Permeability was measured using a TinyPerm II gas permeameter of New England Research Inc. It allows non-destructive and local measurement of the permeability on the outer surface of a sample. A rubber nozzle with an inlet diameter of 9 mm and an outer diameter of 23 mm is placed on the surface and a vacuum is created. Atmospheric pressure in the rubber nozzle is restored by air flow through the sample and meanwhile a microcontroller measures the pressure change in function of time. The TinyPerm value (*TP*) is then a measure for air permeability *K* (mD) according to equation 5.14. More information can be found in (Filomena et al., 2014).

$$TP = -0.8206 \log(K) + 12.8737 \quad (5.14)$$

Results and Discussion

The gas permeability rises from 19.19 mD for Lf1, over 87.65 mD for Lf2 to 2651.0 mD for Lf3 (Table 5.7). More important is the large spread on the results. This indicates the variable nature of local permeability. Based on these values, only size of magnitude order conclusions can be drawn. The microfacies can be ranked by increasing permeability. The more porous stones are more permeable. In addition, the local variability on permeability increases with increasing permeability or porosity, as the more porous stones also have a higher textural variation on the scale of these permeability measurements.

5.4.6 Drying

Water contained within the pore network of building stones can leave the network by evaporation from the surface. When the rate of evaporation is larger than the rate of water absorption, the stone will dry. As several weathering processes occur in the presence of water, e.g. freeze-thaw decay, drying rate is an important property of building stones, figuring a stone is more vulnerable to decay in wet conditions or under cyclic wetting-drying.

Drying is a multistage process with two main phases characterized by a constant drying rate followed by a period of falling drying rate (Scherer, 1990; Hall and Hoff, 2002). The first phase is characterized by a rapid and linear (constant rate) decrease in water content. Water from a saturated porous rock evaporates from the surface, where the relative humidity will be 100 %. Capillary flow, now created by a gradient in water content, supplies water from the inner part of the rock towards the surface. In this regime, evaporation is controlled by ambient air conditions: humidity, air flow and temperature. As the drying proceeds, the mean water content will fall. After reaching the critical moisture content, the evaporation surface retreats into the stone and the drying process enters the second phase. As the evaporation takes place within the stone, the process is now controlled by the vapour diffusion resistance of the material.

Method

Six cylindrical samples of each microfacies were subjected to drying on all sides of the specimen. Initially, they were water saturation by total immersion (see section 5.4.1). Subsequently, they were left to dry in a climatic chamber at 25 °C at 85 % RH to ensure drying is slow enough with respect to the weight measuring intervals. Their weight was measured every 10 minutes for the first hour, every 30 minutes for the second hour, and then after 3.5, 5 and 6.5 hours after 1 day, 4 days and finally after 12 days. The results are presented as a decrease of water content in mg/g over time in hours. The constant drying rate is calculated by a linear regression over the first period.

Results and discussion

The two periods of drying can be distinguished in Figure 5.15 and the results are presented in Table 5.8. The constant drying rate of Lf1 and Lf2 are relatively similar, being -5.21 and -5.32 $\text{mg g}^{-1} \text{h}^{-1}$ respectively. The constant drying rate of Lf3 is somewhat higher, being -6.79 $\text{mg g}^{-1} \text{h}^{-1}$.

	Constant drying rate ($\text{mg g}^{-1}\text{h}^{-1}$)	critical moisture content (%)	time of constant drying period (h)
Lf1	-5.21 ± 0.54	70.24	1.5
Lf2	-5.32 ± 0.61	43.37	3.5
Lf3	-6.79 ± 0.90	40.31	6.5

Table 5.8: Average values for the drying characteristics of the different microfacies at 85 % RH and 25 °C. The critical moisture content is given in % of the initial water content.

Nevertheless, the period of constant drying rate is much longer for Lf3, which takes about 6.5 h, whilst Lf1 only stays for about 1.5 h in this period, and Lf2 for about 3.5 h. At this point, the critical water content of Lf1, Lf2 and Lf3 is $\pm 70\%$, 43% and 40% respectively. This means that they released respectively $\pm 30\%$, 57% and 60% of their initial water content in the faster first phase and that Lf1 dries the slowest. In terms of relative water saturation, Lf1 has reached a level of 36% of pore saturation, Lf2 26% and Lf3 25% .

During the second period of drying, the drying rate falls and the water content tends asymptotically to a relative water saturation of 7% for Lf1, 5% for Lf2 and 2% for Lf3 after 12 days. Lf1 has a higher vapour diffusion resistance, which inhibits the drying relative to that of Lf2 and Lf3. The residual water content can play a role in moisture related deterioration.

The drying rate can only be used relatively, to compare between the different microfacies. The true drying time in buildings will depend strongly on the environmental conditions such as temperature, humidity and wind, and on the depth of initial wetting.

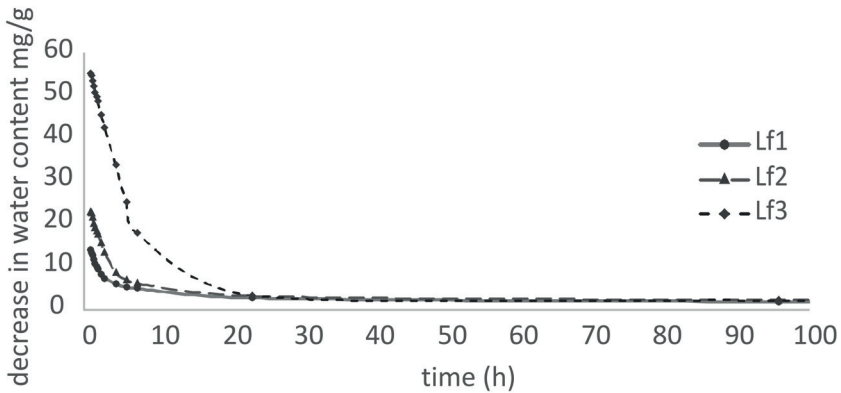


Figure 5.15: Decrease in water content in function of time for a representative sample for each microfacies, with the measurements indicated as bullet points. The graph is cut off at 100 h.

5.5 Strength properties and sound speed propagation

Strength properties could be determined for architectural purposes, to know if a stone is capable of withstanding stress imposed by the construction or internal stress induced by e.g. (re)crystallization. The strength mainly depends on the materials' composition and fabric and on the inheritance/legacy of historical stress.

5.5.1 Uniaxial compressive strength

The uniaxial compressive strength (*UCS*) was determined to compare the strength of the different microfacies. The true *UCS* is mainly depending on rock porosity, rock fabric and the water saturation of the rock (Török and Vasarhelyi, 2010). The measured *UCS* will also be influenced by sample shape and size. Shape refers to the length/diameter ratio of cylindrical samples, or an equivalent ratio for prisms. Size refers to the absolute size of a specimen, with a specific shape.

Method

Six specimen of each microfacies were tested at the Magnel Laboratory for Concrete Research (UGent) according to EN 1926 (2006). The cylindrical samples had a length/diameter or side ratio of 1:1, a nominal

	UCS (MPa)	TS (MPa)
Lf1	86.37 ± 18.2	10.38 ± 0.44
Lf2	27.45 ± 10.88	6.09 ± 1.19
Lf3	8.12 ± 3.47	3.04 ± 0.93

Table 5.9: Average values of uniaxial compressive strength and Brazilian tensile strength for the different microfacies.

diameter of 36.5 mm and a loading rate of 1 MPa/s. The load F was applied perpendicular to the bedding surface A and UCS (N/mm² or MPa) was calculated as:

$$UCS = \frac{F}{A} \quad (5.15)$$

Results and discussion

The three microfacies show distinct differences in UCS (Table 5.9), with high strength for Lf1, a low to medium strength for Lf2 and a low strength for Lf3. Figure 5.16 shows that the UCS values have an inverse exponential relationship with porosity. As such, Lf1 with the lowest porosity also has the highest UCS . The strength values rapidly increase when the porosity is lower than 10 vol.%. This is also related to the rock fabric. Lf1 contained the largest fraction of sand grains, with grain-supporting point contacts. When a compressive stress is applied, the pressure is distributed over the framework of sand grains. In the more porous samples, the porosity and larger clasts with an orientation act as a flaw and concentrate the stress in a specific direction. Examples of this are the moldic pores with a residual shell shape, the test of *Nummulites* and the larger rounded quartz grains which are weakly bound with the surrounding matrix and cement.

The results give a good idea of the UCS to be expected for different porosities and the relative differences. However, some drawbacks should be made in fully interpreting the strength of the rock. First, seen the heterogeneity typical to natural stone, testing more specimen would prove useful for a more adequate determination of the UCS . This is especially the case for stone with large textural features, which is the case for Lf3. In addition, the influence of anisotropy, i.e. bedding, was not assessed in this study, neither was the water content.

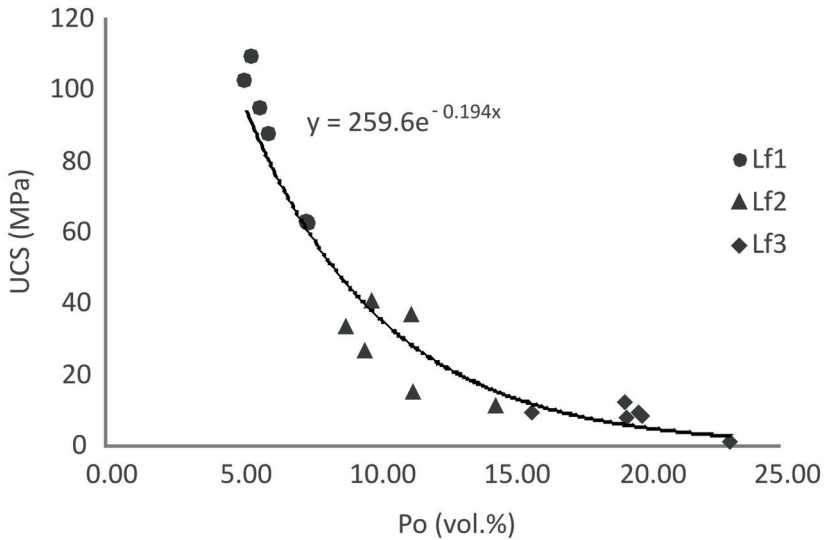


Figure 5.16: Values for the uniaxial compressive strength in relation to the total porosity.

5.5.2 Brazilian tensile strength

The tensile strength of a material reflects the maximum tensile stress a material with specific size can resist before failure. This parameter is not regularly used in construction, but it is essential for the resistance of internal stresses as created by e.g. ice or salt crystallization. The most usual test method for determining the tensile strength is the Brazilian test or indirect tensile strength test. In this procedure, a disc-shaped sample is subjected to an uniaxial compressive load exerted parallel to the circular cross section. The tensile stress is exerted perpendicular to the loading direction.

Method

Three samples of Lf1 and six samples of both Lf2 and Lf3 were subjected to a Brazilian tensile test. This test was preferred above the direct tensile strength test because it required less sample volume. The disc shaped samples had a diameter of approximately 36 mm and a thickness of approximately 15 mm. The load was applied perpendicular to the edges of the planes of anisotropy. The tensile strength is calculated according to equation 5.16:

$$BTS = \frac{2F}{dl\pi} \quad (5.16)$$

where BTS is the tensile strength (MPa) F is the loading force (N) at failure, d is the specimens' diameter (mm), l is the specimens' thickness (mm). The Brazilian tensile test and the true tensile strength by direct tensile testing, tearing apart a specimen, exhibit a ratio of 2:1.

Results and discussion

Lf1 has the highest Brazilian tensile strength with values around 10 MPa (Table 5.9). The tensile strength of Lf3 is much lower, around 3 MPa. This can be related to the higher porosity and to the rock fabric. As for UCS , the BTS is influenced by the orientation of larger anisotropic structures such as moldic porosity. TS of Lf2 is intermediate between both with values around 6 MPa. The spread however, on Lf2 and Lf3 can be relatively large, owing to the presence of the these structures, which can sometimes be larger than 1/10 of the sample size. The results for each microfacies are plotted (Fig. 5.17) with BTS in relation to the porosity of the specimen.

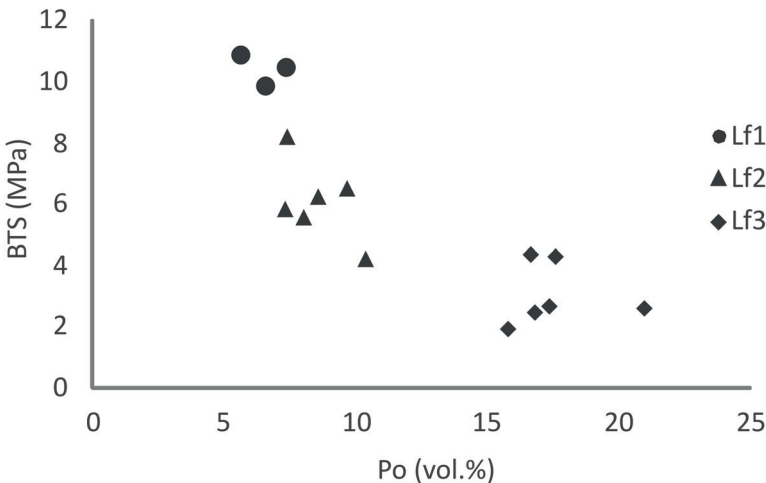


Figure 5.17: Values for the tensile strength in relation to the theoretical uniaxial compressive strength according to Figure 5.16.

5.5.3 Ultrasound velocity

The propagation of sound speed (US) through rock is a parameter which is relatively fast and easy measured. It is a function of mineral content and mineral density, porosity, moisture content and temperature. Relations between US and porosity or UCS have repeatedly been shown. It is frequently applied in the study of stone deterioration, both in laboratory as in on-site studies. US can also be used as reference for controlling batches of a specific material.

Method

The measurement was performed according to the direct method of ?. 55 kHz transducers were used, thus the preferable smallest dimension to avoid a reduced speed velocity is approximately 83 mm for samples having a US equal to 4500 m/s, 74 mm for samples having a US equal to 4000 m/s and 65 for samples having a US equal to 3500 m/s. US was measured on six cylindrical specimen of each microfacies on which also porosity by vacuum saturation and UCS was measured. The lateral dimension, however, was approximately 51 mm for Lf1 and Lf2 samples and 45 mm for Lf3 samples. Therefore, two additional prisms of each microfacies with a lateral diameter of 160 mm were measured to compare the values.

Results and discussion

The US values of the 160 mm samples show clear differences between Lf1, Lf2 and Lf3 (Table 5.10). Especially the US of Lf3 is much lower. This is mainly the result of the high porosity which slows down the sound speed. These values can be used as reference values for on-site identification of the microfacies.

It can be seen that the average US values of the six cylindrical specimen of each three microfacies are slightly lower than the US values for the 160 mm prisms (Table 5.10). Although the difference is small, it is possible that US was slightly reduced. Nevertheless, it allows to compare the results of US with the porosity and UCS . Figure 5.18 shows that the US increases more or less linear with decreasing porosity. From the relationship between porosity and UCS follows that if US correlates linear with porosity, it should not correlate linear with UCS (Fig. 5.19). US can thus be used as a reference to estimate the porosity of samples on-site.

	USV_{prism} (m/s)	$USV_{cylinder}$ (m/s)
Lf1	4348	4243 ± 99
Lf2	4098	3957 ± 115
Lf3	3317	3266 ± 72

Table 5.10: Average values of sound speed propagation for the prismatic and cylindrical samples of the different microfacies.

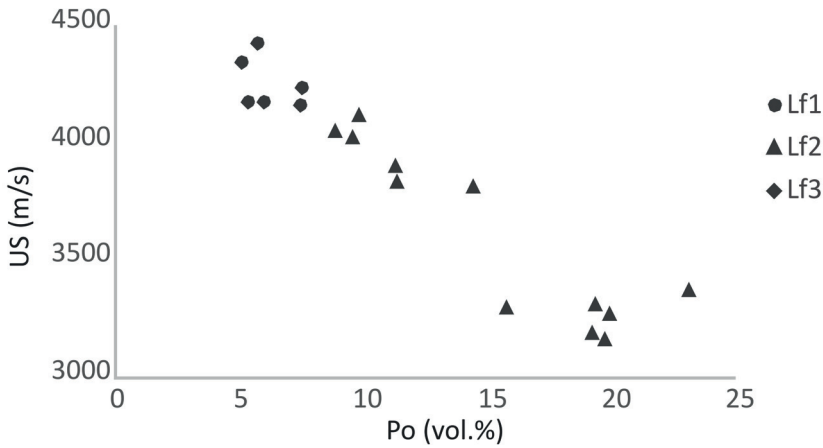


Figure 5.18: Values for the sound speed propagation in relation to the total porosity.

5.6 On-site methods for water absorption

On-site methods can be useful to assess the intrinsic properties of a material or to study the materials deterioration when the intrinsic properties are known. As such, it can be valuable to have reference values for specific methods, for the materials identification or its state. Assessing the water absorption on a surface is one of the most important studies for the conservation of stone in monuments. It allows also to test the effectiveness of conservation or restoration treatments if the measurement is non-destructive.

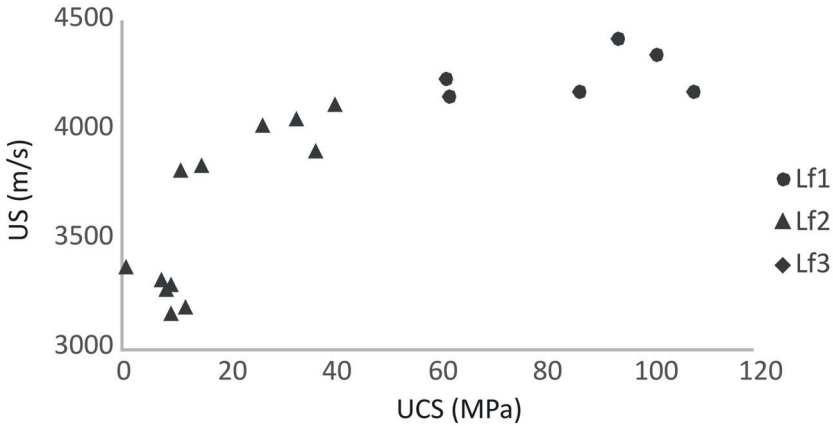


Figure 5.19: Values for the sound speed propagation in relation to the uniaxial compressive strength.

5.6.1 Karsten tube

The Karsten tube method is used to measure the water absorption behaviour of natural stone on-site (Leisen et al., 1996). The nature of the method exerts an extra pressure on the absorbing surface, i.e. by the weight of the water column. However, this pressure is lower than the capillary pressure and this will only have a significant effect for materials with very large pores and thus lower capillary pressures (Hendrickx, 2013); the effect is negligible for pores $< 10 \mu\text{m}$ (Snethlage and Wendler, 1989).

Method

A vertical tube containing 10 ml water was applied on in this case a vertical surface of each of the three microfacies. The tube was attached with removable plasticine and filled with water to the zero level at time zero. The water uptake is measured in ml after 90, 300, 600 and 900 seconds, which were converted to the corresponding mass after time i (m_i). The surface (A) was calculated from the true contact diameter by measuring the opening of the plasticine. A coefficient of water uptake by karsten tube (C_{Kt}) was calculated for the water uptake between 300 and 900 seconds according to equation 5.17.

$$C_{KT} = \frac{m_{900} - m_{300}}{A\sqrt{t_i}} \quad (5.17)$$

	C_{KT} $\text{g m}^{-2} \text{s}^{-1/2}$	C_{cs} $\text{g m}^{-2} \text{s}^{-1/2}$
Lf1	5.19	6.61
Lf2	71.64	20.13
Lf3	249.71	32.89

Table 5.11: Average values of water uptake by Karsten tube and contact sponge for the different microfacies.

Results and discussion

Table 5.11 shows the results for the water uptake by karsten tube and Figure 5.20 shows the water absorption over time. It can be seen that Lf3 is much more sorptive than Lf1. The water absorption of Lf2 is somewhat intermediate between both. This is also reflected by the coefficient of capillary water absorption determined by karsten tube. For Lf1, this resembles quite the coefficient of capillary uptake. This is because Lf1 has a low amount of pores $> 10 \mu\text{m}$. In addition, Lf has a very low C and the capillary front after 15 min of measurements will not have advanced deep in the material. C_{Kt} of Lf2 and Lf3, however, are much larger than their corresponding C. One reason for this is the presence of macrofossils in both samples (Hendrickx, 2013). The pressure created by the water column in the karsten tube could be sufficient to fill the larger macropores, whereas this is not the case in capillary rise as the capillary pressure in larger pores is not sufficient to overcome gravitational forces (Benavente et al., 2015). Moreover, in Lf3 where the difference is the most pronounced, the water front might have penetrated relatively deep inside the stone, because of the high C. With Karsten tube, however, the water penetration is in 3D, since the water will not only penetrate in depth but also sideways, whereas in capillary rise experiments the water penetration is in 2D. Therefore, the surface of water absorption will increase over time. In addition, well-connected macropores as in Lf3 could provoke gravitational leaking inside of the stone. For a correlation with the coefficient of capillarity, a correction should be applied for the volume of the water front and the water level in the tube should be kept constant throughout the test.

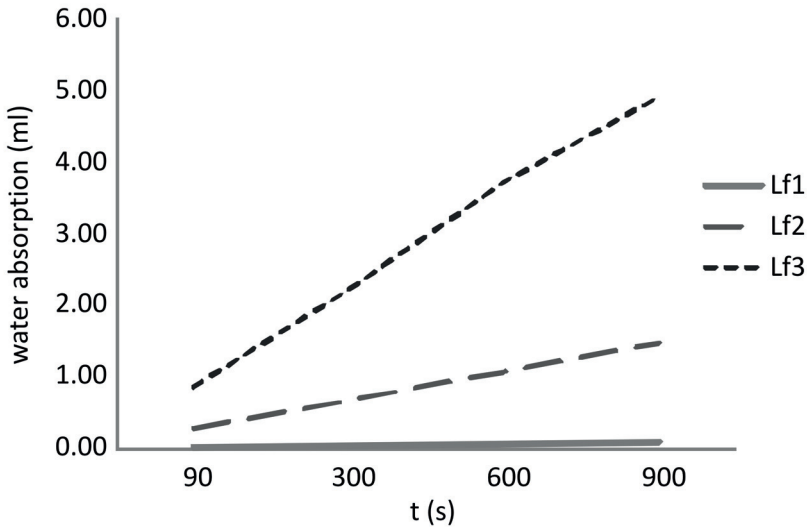


Figure 5.20: Average water absorption with Karsten tube in function of time for the different microfacies.

5.6.2 Contact sponge

The contact sponge method is an alternative for the measurement of water absorption of stones on-site. The method is precise for the initial water uptake and it measures the water absorption of the superficial layer of the stone (Vandevoorde et al., 2009). Nevertheless, Vandevoorde et al. (2009) showed a linear correlation between the capillary rise method and contact sponge method for non-weathered nor treated (consolidated, hydrophobed, ...) stones.

Method

A carefully non-excessive saturated contact sponge was pressed between a contact plate and a vertical stone surface of the different microfacies. After 90 seconds, the sponge was removed and the weight loss (Δm) was measured and interpreted as the volume of water absorbed by the stone. A coefficient of water absorption by contact sponge (C_{cs}) was calculated as the mass of the absorbed water per surface area (A) over the square root of time:

$$C_{cs} = \frac{\Delta m}{A\sqrt{t}} \quad (5.18)$$

Results and discussion

The water uptake of the different microfacies over a period of 90 s is shown in Table 5.11. As expected, Lf3 absorbs more water than Lf2 and Lf1. The coefficient of water absorption by contact sponge, however, shows a relative good correlation with C. This is because the volume of water absorbed is relatively low and the moment of measurement is very initial. Contact sponge cannot account for variability of structural damage deeper in the stone.

5.7 Salt weathering test

Salt crystallization is known to be a very effective weathering process, although a very complex one (e.g. Charola, 2000; Espinosa-Marzal and Scherer, 2010). Therefore, a laboratory salt crystallization test is often used as a proxy to estimate the durability of a specific stone (e.g. Ruedrich and Siegesmund, 2007; Beck and Al-Mukhtar, 2010; Akin and Ozsan, 2011; Vazquez et al., 2013). Physical weathering is provoked by the pressure exerted on the pore walls by growing salt crystals (Scherer, 1999). This crystallization pressure is related to the supersaturation of the salt solution. Therefore, sodium sulphate is more destructive than sodium chloride as it can obtain a higher degree of supersaturation (Steiger, 2005a). This is because sodium sulphate has both a hydrous and anhydrous phase, where the anhydrous phase can partially dissolve to increase the degree of saturation and act as nucleation site for the favourable rapid growth of the hydrous crystals (Shahidzadeh-Bonn et al., 2010). The crystallization pressure depends on the crystal size and therefore on the pore in which it is confined upon growing (Steiger, 2005b). On the other hand, damage occurs when the exerted stress exceeds the tensile strength of a rock.

Method

A salt crystallization test was performed on two cubic samples with edge length 40 mm of each microfacies according to EN 12370 (1999). The dry samples were immersed in a 14 wt% solution of sodium sulphate decahydrate ($\text{NaSO}_4 \cdot 10\text{H}_2\text{O}$) at 20 °C. After immersion, the samples were removed from the solution and dried in an oven where an initial high humidity was obtained by preconditioning the oven with a water dish. The drying temperature was increased from 20 °C to 105 °C in 12 h and

subsequently maintained at 105 °C for 8 h. Afterwards, the samples were left to cool for 2 h to attain 20 °C. This cycle (Fig. 5.21) was repeated 15 times and the weight was measured at the end of every cycle. After 15 cycles, the samples were immersed in water for 24 h and subsequently rinsed with water and dried at 105 °C until constant mass. This final mass was used to calculate the percentage weight loss after 15 cycles. The test allows relative comparison between the different microfacies and other (lime)stone described in literature. The test gives an indication of relative susceptibility to salt weathering, rather than an absolute assessment.

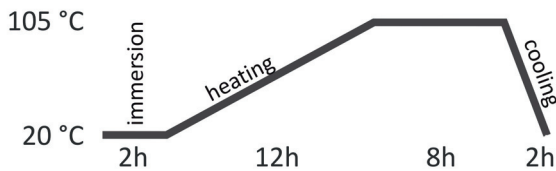


Figure 5.21: Visualization of a salt weathering cycle.

Results and discussion

Figure 5.22 shows the evolution of the normalized weight of the samples. Lf1 and Lf2 show the same behaviour, whilst Lf3 is more divergent. The samples initially gain in weight during the first 2 to 4 cycles, which is due to the imbibition of salt in the pore system. After this, Lf1 and Lf2 show only a very gently, almost negligible, decrease in weight over the remaining cycles, with a weight loss of less than 0.10 and 0.20 wt% respectively after 15 completed cycles. In contrast, the samples of Lf3 show a stronger weight loss after 15 cycles, 2.47 and 3.87 wt% (Fig. 5.23 and 5.24). The damage is expressed at the corners and somewhat at the edges, where pieces detach from the stone, often along the edges of macropores (Fig. 5.25).

Lf3 shows a pronounced efflorescence on the entire surface, with some larger salt clusters at the top edges of macropores. This reflects the fact that more salt is imbibed during the immersion as a result of a higher coefficient of capillarity and a higher porosity. Lf3 dries relatively fast, but because of a higher initial saturation, the drying process takes longer. Nevertheless, the critical moisture content is only 40 %, meaning that 60 % of the evaporation took place at the surface, near the larger pores, which corresponds to the larger salt clusters around larger pores. Sandstones with a high drying rate and a critical moisture content below 60 % tend to show sanding rather than scaling (Ruedrich and Siegesmund, 2007). Lf3 also shows the lowest

tensile strength, making them susceptible to lower crystallization pressure and thus to lower critical degrees of supersaturation with respect to Lf1 and Lf2.

Lf1 and Lf2 show a good resistance to the laboratory test of salt crystallization. In between the cycles, they show slight and dispersed efflorescence on the surface. Compared to Lf3, they have a lower coefficient of capillarity and a higher tensile strength. Lf1 has a critical moisture content of 70 %, suggesting that this type might be sensitive to scaling (Ruedrich and Siegesmund, 2007). This is because the evaporation front will retreat below the stone surface when only 30 % is evaporated, and salt might crystallize below the surface. However, no damage occurred after 15 cycles.

In absolute values, Lf2 has more weight loss than Lf1, but no damage is clearly visible. The higher weight loss could be related to a higher coefficient of capillarity and a lower tensile strength. The former results in a higher relative water and thus salt absorption for Lf2 with respect to Lf1. Considering a critical moisture content of 43 %, the expected damage would be sanding rather than scaling, as most crystallization would take place near the surface.

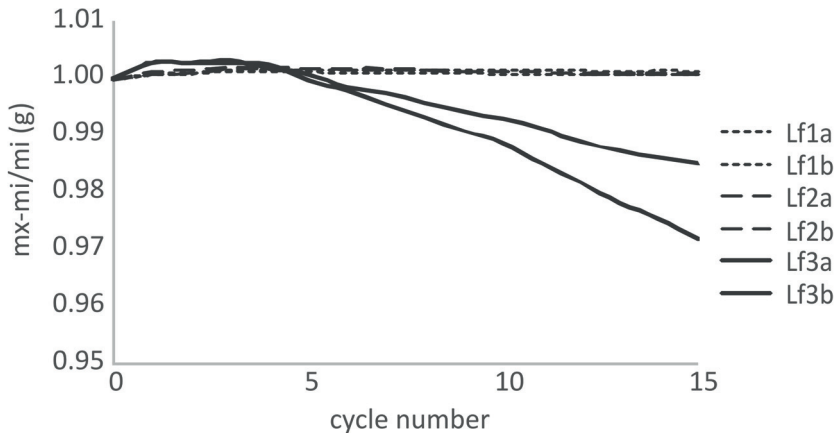


Figure 5.22: Normalized weight evolution during 15 cycles of the salt test for the different microfacies.

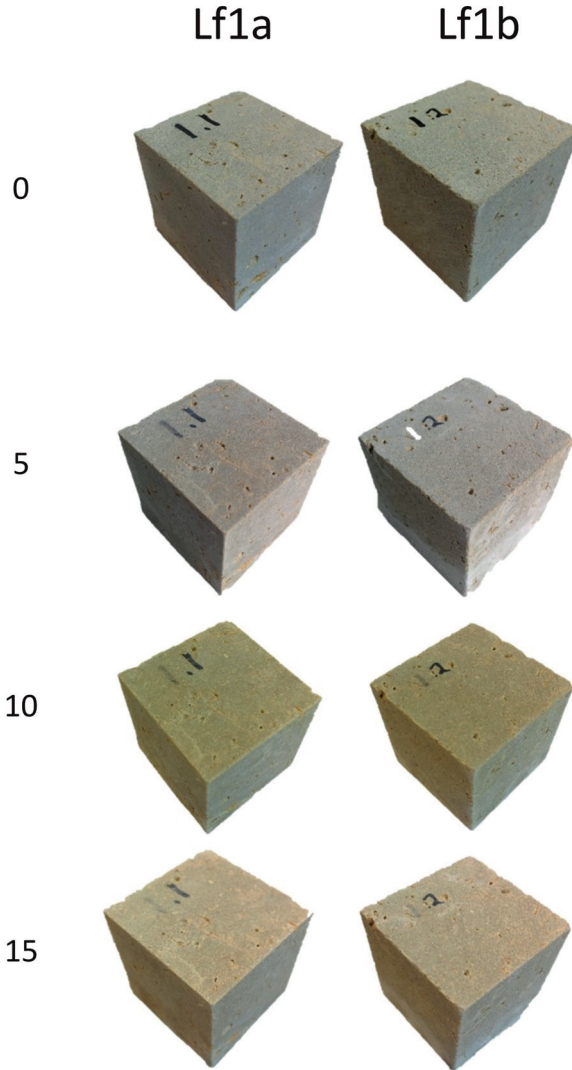


Figure 5.23: Visual evolution of the samples from Lf1 after 0, 5, 10 and 15 salt cycles.

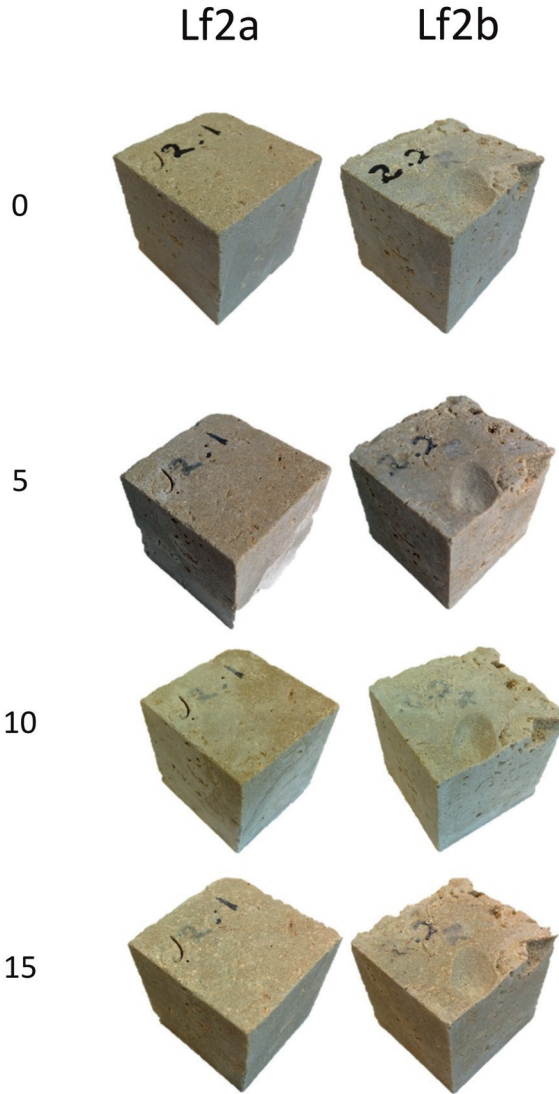


Figure 5.24: Visual evolution of the samples from Lf2 after 0, 5, 10 and 15 salt cycles.

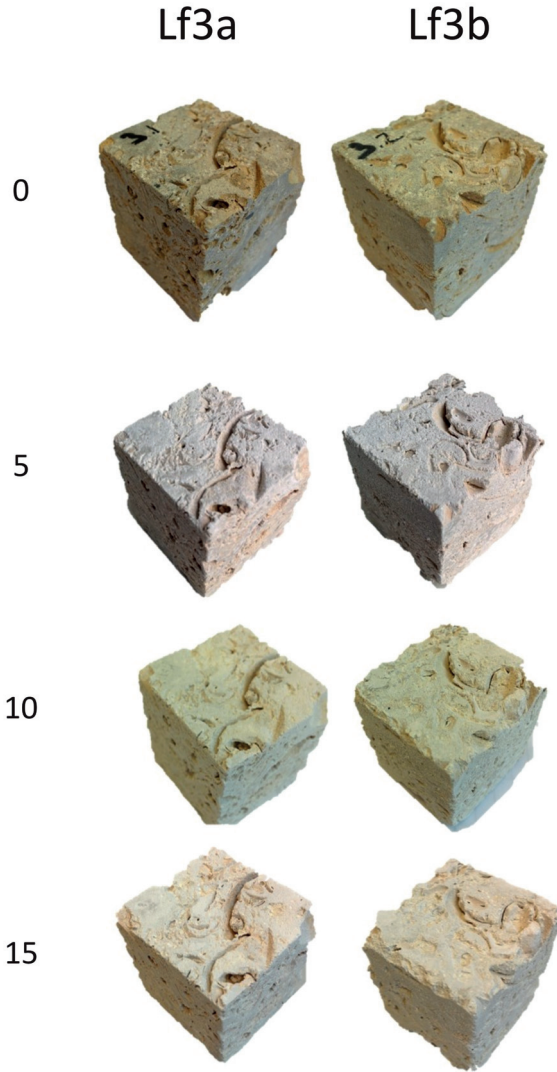


Figure 5.25: Visual evolution of the samples from Lf3 after 0, 5, 10 and 15 salt cycles.

5.8 Freeze-thaw weathering test

Freeze-thaw action can be a very effective process for stone weathering in cold and humid environments. Therefore several laboratory tests have been developed to test the performance of stones in relation to freeze-thaw cycling (e.g. Ingham, 2005). It is ice crystallization that finally induces damage in a stone (e.g. Scherer, 1999) (see also Chapter 7). In contrast to the crystallization of salts, not supersaturation, but supercooling is the driving factor.

Method

Freeze-thaw cycling was performed according to the European Standard EN 12371 (2010) on two prismatic samples (40 mm × 40 mm × 160 mm) of each microfacies, progressively immersed in tap water. The freeze-thaw cycles consist of 6 h freezing at a temperature of $-12\text{ }^{\circ}\text{C}$ followed by 6 h of thawing immersed in water at a temperature of $20\text{ }^{\circ}\text{C}$. The samples were weighted and visually inspected after 14, 56 and 100 cycles. In practice, the older Belgian standard is regularly applied to test the performance in use. This standard comprises unidirectional rather than omnidirectional freezing, and the preconditioning (degree of saturation) depends on the application (e.g. masonry, flooring, ...). However, the method of EN 12371 (2010) was chosen to compare the microfacies mutually, to be able to compare with other rocks in literature and for reasons of sample dimensions.

Results and discussion

Figure 5.26 shows the normalized weight evolution of the samples after 14, 56 and 100 freeze-thaw cycles. Lf1 and Lf2 show no significant weight loss. Similar to the salt weathering test, the samples of Lf3 do show a weight loss. The damage is illustrated in Figure 5.27. It mainly concerns the crumbling of the coarse bioclasts. The damage potential is related to the fast absorption of water and the fact that freezing is initiated immediately after saturating the samples. In addition, Lf3 has the lowest strength, making it the most vulnerable to stresses induced by ice crystallization.

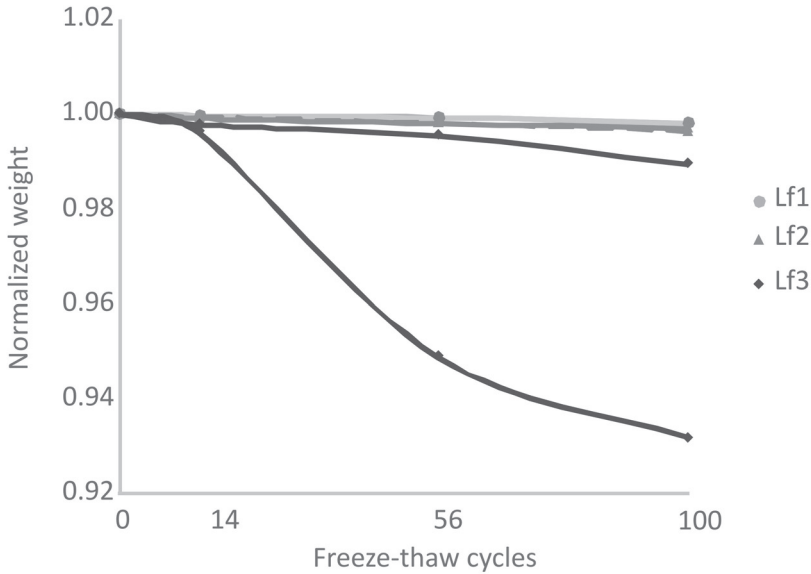


Figure 5.26: Normalized weight evolution after 14, 56 and 100 freeze-thaw cycles for two samples of each microfacies.

5.9 Comparison with technical sheet

The most recent results on the technical properties of Lede stone date from testing at Ghent University in 2012 (De Kock et al., 2015) and were presented in Table 3.2. The testing sample size was larger in most cases; cubes of 70 mm × 70 mm × 70 mm compared to 50 mm × 50 mm × 50 mm for the tests in this chapter. When comparing ρ , P_o , C and UCS , it can be said that the average specimen tested in 2012 has properties intermediate between Lf1 and Lf2. This will apply to a majority of the stone blocks from the stock pile in the quarry in Balegem. However, for a detailed indication of the stone properties of individual blocks, the VEC (Fig. 5.1) can be used to estimate the resembling type. From this, the corresponding properties can be compared to Lf1 (type 1–2), Lf2 (type 3–4–5) and Lf3 (type 6).

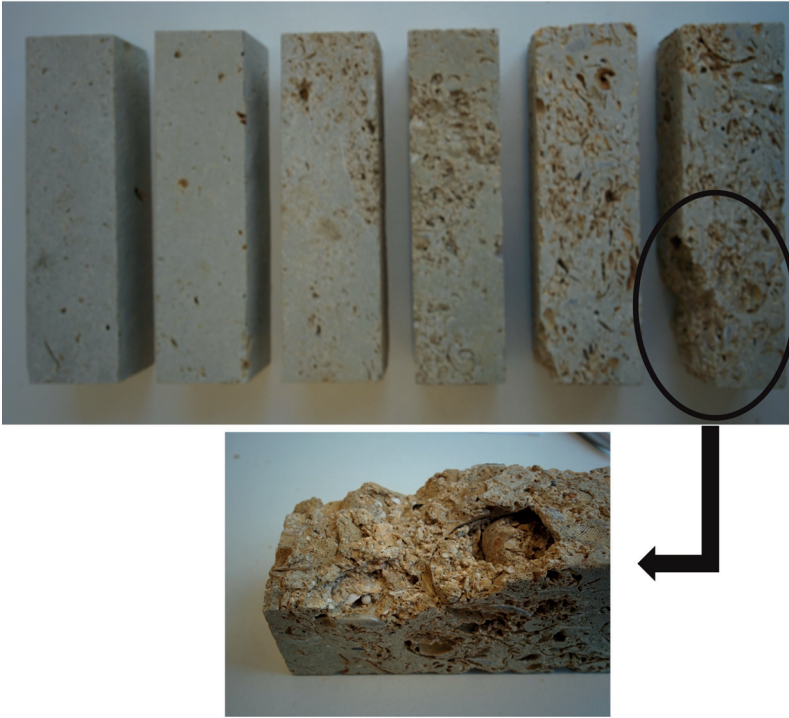


Figure 5.27: Photograph of the samples after 100 freeze-thaw cycles, with detail of the damage of sample 3.1 (bottom). From left to right: Lf1.1, Lf1.2; Lf2.1, Lf2.2, Lf3.1, Lf3.2.

5.10 Performance in use

Lede stone is mostly used as a freestone in all different elements of a façade; in basements, plinths, masonry, corner blocks, door and window frames, as well as in columns, buttresses, crockets finials and exceptionally as floor tiles and sills. All of these applications have specific structural requirements considering strength or wear. However, upon use, durability and resistance to the environmental factors will play an important role, with gradual or catastrophic processes leading to an inherent decline of the stone properties. To assess this, some preconditions for specific applications have been established in the past. Although it is known that stone decay results from a summation of different actors and inheritance, it is useful to test the intrinsic properties of the different

microfacies to the established preconditions.

For this assessment, a performance diagram for natural stones in the Seine climate, which is the climate of central to northern France (Centre d'assistance technique et de Documentation, 1980), is used as region adjacent to northern Belgium. The diagram is based on the porosity and saturation coefficient of a stone and it is arbitrarily divided in different zones related to the possible applications of stones with a specific combination of porosity and saturation coefficient (Fig. 5.28). Zone 1 groups stones with a combination low porosity and low saturation coefficient, which can be used in all applications. Zone 4 groups stones with high porosity and high saturation. It is based on the fact that a high water absorption in large volumes is not appropriate for applications exposing it to the strongest environmental conditions, such as for example a cricket. Zones 2 and 3 are intermediate between both. It should be pointed out that this diagram is usable to compare with the performance of other rocks which are established in this diagram, in terms of porosity and saturation. However, it does not account for other stone properties, for example drying or thermal dilatation, that also influence the performance and durability of stone.

Plotting the average values of Lf1 and Lf2 show that these types are potentially applicable in all outdoor environments. Lf3 is potentially applicable in most outdoor environments, except for flooring or for gargoyles, due to its a higher porosity.

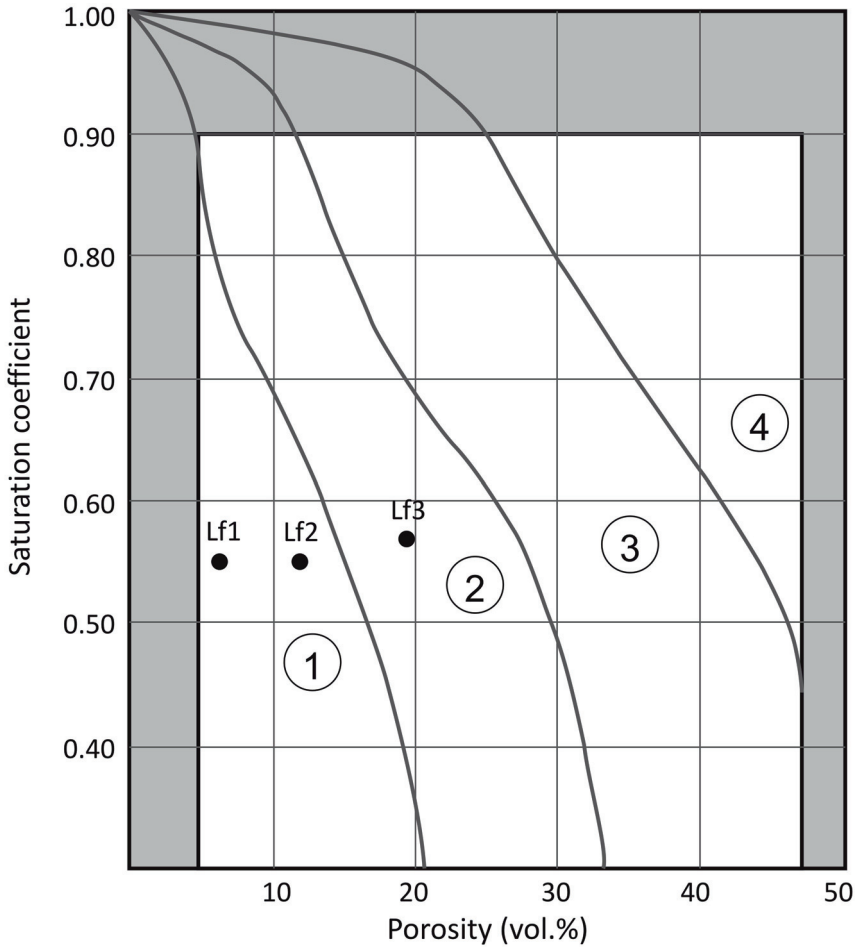


Figure 5.28: Performance diagram with plot of the different microfacies. Zone 1: all exterior applications; zone 2, all exterior applications except for flooring or gargoyles; zone 3 exterior except for very exposed parts; zone 4: only exterior masonry.

5.11 Discussion and Conclusion

The durability of building stones in architecture will depend both on their intrinsic properties and their environment. As for their intrinsic properties, the water transfer properties play an important role as most of the weathering processes involve the presence of water (Stück et al., 2013). Hence, rocks with a high porosity, a high coefficient of capillarity and a high coefficient of saturation are potentially more vulnerable to weathering. On the other hand, the process of drying is important to release water. Thus, stones with a high constant drying rate and a low critical moisture content are potentially less prone to weathering. These water transfer properties are mainly related to the pore network. Capillary pores will determine the speed of water absorption and the drying in the first stage of the constant rate period. Larger capillary pores have a higher velocity of capillary uptake, but also a higher rate of drying because they have a lower capillary pressure and a lower water retention. Smaller capillary pores will have a lower velocity of capillary uptake, but a higher water retention during drying. In pores with a radius larger than 1000 μm , the gravitational forces become more important than the capillary forces (Benavente et al., 2015), and therefore these pores do not easily saturate. Subcapillary pores will adsorb and desorb water in relation to the relative humidity. Moisture adsorption prohibits the water vapour diffusion and influences the critical moisture content. Stones with a high amount of subcapillary pores will more easily become damp and do not easily dry completely. Finally, the connectivity between all the different pores and pore sizes will define the final outcome of the water transfer properties. Rocks with a higher breakthrough radius will therefore tend to take up and release water more easily. In addition to the water transfer properties, also the rock strength and especially the tensile strength has an influence on the physical expression of stone weathering as this determines how much a stone can resist internal stress.

In this chapter, the natural variability of the Lede stone has been shown. This results from different microfacies, related to the initial depositional environment and subsequent lithification. It only illustrates the variability in one specific location, the Balegro quarry in Balegem. However, this is studied here in terms of petrophysical properties, not purely in geological setting. Therefore, it can be used as illustration for the technical properties of Lede stone from other resource areas. Although very interesting,

studying the regional geological variability was not within the scope of this work.

It is shown that the microfacies can vary from compact, low porous to fossiliferous, high porous stones, and that this can result in some striking physical differences. The compact microfacies, Lf1, has a relative low porosity, with a considerable amount of subcapillary pores. It has a bimodal distribution with a macropore population which is connected by a microporous capillary network. Therefore, it absorbs water very slow and in low amounts. Because of the microporous network, the drying rate is relatively slow, and capillary condensation in the subcapillary network inhibits water vapour diffusion. Thus, it has a relative high critical moisture content. Nevertheless, as the amount of macropores is relatively low and badly connected, the combination of macropores and micropores does not have a significant negative effect. Moreover, the strength properties are remarkably high for a (sandy) limestone. Hence, this microfacies can resist relatively high stress related to weathering. This behaviour is illustrated by the salt crystallization test, where the final loss of weight after 15 days was insignificant. It is mainly the result of a very low imbibition with salt water during the immersion phase, and the high strength for stresses that might develop beneath the surface.

The intermediate microfacies, Lf2, has a medium porosity, with a breakthrough radius in the micropore network, as in Lf1. Aside from these connections, several subordinate breakthrough radii exist within the mesopore network, connecting individual macropores to the outside. This macropore network is more important and larger in volume with respect to that of Lf1. As for this, the water absorption and also the vapour diffusion is higher than that of Lf1. And whilst the initial drying rate is comparable, the critical moisture content is lower for Lf2, since the subcapillary pore network is less important. With an increase in porosity, there is also a decrease in strength. In the salt crystallization test, the behaviour and performance is very similar to that of Lf1. The somewhat higher weight loss after 15 cycles can be attributed to the higher capillary water absorption resulting in higher salt imbibition in combination with the lower tensile strength.

The fossiliferous microfacies Lf3 has a high porosity. It has a very important volume fraction of macropores that are well connected by pore throats larger than the microporous network. The most important fraction is part of the capillary pore network. It is thus not surprising that this

microfacies shows a medium to sometimes high capillary absorption. In addition, it has much lower strength properties than Lf1 and Lf2. From this point of view, this microfacies might be the most vulnerable to weathering. However, associated with the well-connected micropore network is the ability to dry relatively fast and to have a low critical moisture content. Thus, a possibly higher weathering susceptibility only applies to settings where the wetting rate is higher than the evaporation rate or which involve salt in case of cyclic wetting and drying. This interpretation is supported by the salt crystallization test, where a low amount of weight loss after 15 cycles yet is significant compared to Lf1 and Lf2. The amount of salt efflorescence after drying illustrates the higher salt water absorption. This, combined with lower tensile strengths results in the observed weight loss for Lf3 after 15 cycles.

Overall, the properties of Lede stone and especially the relation with the thoroughly studied pore network have been characterized more profound compared to previous studies. Attention has been paid to the large heterogeneity which is possible under the denomination Balegem stone or Lede stone. This variability should not be considered as a negative point, but should in contrary be used to create a pleasant aesthetic amenity. In general, the Lede stone is expected to have a good performance and durability, which has been proven over centuries in historic monuments, and now is supplemented by the interpretations of this laboratory study. When Lede stone is adequately approached and used, its durability should be guaranteed. The Visual Estimation Chart might be a first aid help in the approach of Lede stone blocks, to link macroscopic observation in practice with the technical results obtained by this study. Nevertheless, regular stone testing is advisable for the confirmation of the properties in case of doubt, special applications of the stone or the application of treatments.

References

- A B Abell, K L Willis, and D A Lange. Mercury Intrusion Porosimetry and Image Analysis of Cement-Based Materials. *Journal of colloid and interface science*, 211(1):39–44, mar 1999. ISSN 1095-7103. doi: 10.1006/jcis.1998.5986.
- M Akin and A Ozsan. Evaluation of the long-term durability of yellow travertine using accelerated weathering tests. *Bulletin of Engineering Geology and the Environment*, 70(1):101–114, 2011. doi: 10.1007/s10064-010-0287-x.
- G F Andriani and N Walsh. Physical properties and textural parameters of calcarenitic rocks: qualitative and quantitative evaluations. *Engineering Geology*, 67(1-2):5–15, 2002. doi: Pii0013-7952(02)00106-010.1016/s0013-7952(02)00106-0.
- K Beck and M Al-Mukhtar. Evaluation of the compatibility of building limestones from salt crystallization experiments. *Geological Society, London, Special Publications*, 333(1):111–118, jan 2010. ISSN 0305-8719. doi: 10.1144/SP333.11.
- K Beck and M Al-Mukhtar. Cyclic wetting-drying ageing test and patina formation on tuffeau limestone. *Environmental Earth Sciences*, 71(5): 2361–2372, 2014. doi: 10.1007/s12665-013-2637-z.
- K Beck, M Al-Mukhtar, O Rozenbaum, and M Rautureau. Characterization, water transfer properties and deterioration in tuffeau: building material in the Loire valley - France. *Building and Environment*, 38(9-10):1151–1162, 2003. doi: 10.1016/s0360-1323(03)00074-x.
- K Beck, O Rozenbaum, M Al-Mukhtar, and A Plançon. Multi-scale characterisation of monument limestones. In *6th Internation Symposium on the Conservation of Monuments in the Mediterranean Basin*, page 6p, 2006.

- M Bednarik, B Moshhammer, M Heinrich, R Holzer, M Laho, J Rabeder, C Uhlir, and M Unterwurzacher. Engineering geological properties of Leitha Limestone from historical quarries in Burgenland and Styria, Austria. *Engineering Geology*, 176(0):66–78, 2014. doi: <http://dx.doi.org/10.1016/j.enggeo.2014.04.005>.
- D Benavente, N Cueto, J Martínez-Martínez, M A García del Cura, and J C Cañaveras. The influence of petrophysical properties on the salt weathering of porous building rocks. *Environmental Geology*, 52(2):215–224, mar 2007. ISSN 0943-0105. doi: 10.1007/s00254-006-0475-y.
- D Benavente, C Pla, N Cueto, S Galvañ, J Martínez-Martínez, M A García-del Cura, and S Ordóñez. Predicting water permeability in sedimentary rocks from capillary imbibition and pore structure. *Engineering Geology*, 195:301–311, sep 2015. ISSN 00137952. doi: 10.1016/j.enggeo.2015.06.003.
- V Boel. *Microstructuur van zelfverdichtend beton in relatie met gaspermeabiliteit en duurzaamheidsaspecten*. Phd dissertation, Ghent University, 2007. URL <https://biblio.ugent.be/publication/4271638>.
- M A Boone, T De Kock, T Bultreys, G De Schutter, P Vontobel, L Van Hoorebeke, and V Cnudde. 3D mapping of water in oolitic limestone at atmospheric and vacuum saturation using X-ray micro-CT differential imaging. *Materials Characterization*, 97(0):150–160, 2014. doi: <http://dx.doi.org/10.1016/j.matchar.2014.09.010>.
- L Brabant, J Vlassenbroeck, Y De Witte, V Cnudde, M N Boone, J Dewanckele, and L Van Hoorebeke. Three-Dimensional Analysis of High-Resolution X-Ray Computed Tomography Data with Morpho+. *Microscopy and Microanalysis*, 17(2):252–263, 2011. doi: 10.1017/s1431927610094389.
- C Camerman. *Les pierres naturelles de construction*. Imprimerie N.I.C.I., Gent, 1961.
- Centre d’assistance technique et de Documentation. *Les pierres de France : pierres calcaires roches marbrières granit grès*. Moniteur, Paris, 1980.
- A E Charola. Salts in the deterioration of porous materials: An overview.

- Journal of the American Institute for Conservation*, 39(3):327–343, 2000. doi: 10.2307/3179977.
- P W Choquette and L C Pray. Geological nomenclature and classification of porosity in sedimentary carbonates. *American Association of Petroleum Geologists Bulletin* 1, 54(2):207–250, 1970.
- V Cnudde, A Cwirzen, B Masschaele, and P Jacobs. Porosity and microstructure characterization of building stones and concretes. *Engineering Geology*, 103(3-4):76–83, 2009. doi: 10.1016/j.enggeo.2008.06.014.
- T De Kock, M Boone, J Dewanckele, M De Ceukelaire, and V Cnudde. Lede stone: a potential "Global Heritage Stone Resource" from Belgium. *Episodes*, 38(2):91–96, 2015.
- C Di Benedetto, P Cappelletti, M Favaro, S F Graziano, A Langella, D Calcaterra, and A Colella. Porosity as key factor in the durability of two historical building stones: Neapolitan Yellow Tuff and Vicenza Stone. *Engineering Geology*, 193:310–319, jul 2015. ISSN 00137952. doi: 10.1016/j.enggeo.2015.05.006.
- S Diamond. Mercury porosimetry. *Cement and Concrete Research*, 30(10): 1517–1525, oct 2000. ISSN 00088846. doi: 10.1016/S0008-8846(00)00370-7.
- EN 12370. Natural stone test methods - Determination of resistance to salt crystallisation, 1999.
- EN 12371. Natural stone test methods - Determination of frost resistance, 2010.
- EN 12440. Natural stone - Denomination criteria, 2008.
- EN 13755. Natural stone test methods - Determination of water absorption at atmospheric pressure, 2008.
- EN 1925. Natural stone test methods - Determination of water absorption coefficient by capillarity. Technical report, European Committee for Standardization, 1999.
- EN 1926. Natural stone test methods - Determination of uniaxial compressive strength, 2006.

- EN 1936. Natural stone test methods - Determination of real density and apparent density, and of total and open porosity, 2006.
- EN ISO 12572. Hygrothermal performance of building materials and products - Determination of water vapour transmission properties, 2001.
- R M Espinosa-Marzal and G W Scherer. Mechanisms of damage by salt. *Geological Society, London, Special Publications*, 331(1):61–77, jan 2010. ISSN 0305-8719. doi: 10.1144/SP331.5.
- C M Filomena, J Hornung, and H Stollhofen. Assessing accuracy of gas-driven permeability measurements: a comparative study of diverse Hassler-cell and probe permeameter devices. *Solid Earth*, 5(1):1–11, 2014. doi: 10.5194/se-5-1-2014.
- E Flügel. *Microfacies of Carbonate Rocks - Analysis, Interpretation and Application*. Springer, Berlin Heidelberg, 2nd edition, 2010. ISBN 978-3-642-03796-2.
- C Franzen and P W Mirwald. Moisture content of natural stone: static and dynamic equilibrium with atmospheric humidity. *Environmental Geology*, 46(3-4):391–401, 2004. doi: 10.1007/s00254-004-1040-1.
- G Fronteau, C Moreau, C Thomachot-Schneider, and V Barbin. Variability of some Lutetian building stones from the Paris Basin, from characterisation to conservation. *Engineering Geology*, 115(3-4):158–166, 2010. doi: 10.1016/j.enggeo.2009.08.001.
- H Giesche. Mercury Porosimetry: A General (Practical) Overview. *Particle & Particle Systems Characterization*, 23(1):9–19, 2006. doi: 10.1002/ppsc.200601009.
- B Graue, S Siegesmund, and B Middendorf. Quality assessment of replacement stones for the Cologne Cathedral: mineralogical and petrophysical requirements. *Environmental Earth Sciences*, 63(7-8): 1799–1822, 2011. doi: 10.1007/s12665-011-1077-x.
- C Hall and W D Hoff. *Water transport in Brick, Stone and Concrete*. Taylor & Francis, 2002.
- R Hendrickx. Using the Karsten tube to estimate water transport parameters of porous building materials. *Materials and Structures*, 46(8):1309–1320, aug 2013. ISSN 1359-5997. doi: 10.1617/s11527-012-9975-2.

- J P Ingham. Predicting the frost resistance of building stone. *Quarterly Journal of Engineering Geology and Hydrogeology*, 38:387–399, 2005. doi: 10.1144/1470-9236/04-068.
- S M Kidwell. The stratigraphy of shell concentrations. In P A Allison and D E G Briggs, editors, *Taphonomy: releasing the data locked in the fossil records*, volume 9, pages 211–290. Plenum, New York, 1991.
- H Leisen, E Plehwe-Leisen, and L von Sattler. Weathering and conservation of Apsara reliefs at Angkor Vat, Cambodia - project Angkor. In J. Riederer, editor, *Proceedings of the 8th international congress on deterioration and conservation of stone*, pages 1137–1146. Möller, Berlin, 1996.
- B Masschaele, M Dierick, D Van Loo, M N Boone, L Brabant, E Pauwels, Veerle Cnudde, and Luc Van Hoorebeke. HECTOR: A 240kV micro-CT setup optimized for research. *11th International Conference on X-Ray Microscopy (Xrm2012)*, 463, 2013. doi: Unsp01201210.1088/1742-6596/463/1/012012.
- J M McKinley and P A Warke. Controls on permeability: implications for stone weathering. *Geological Society, London, Special Publications*, 271:225–236, 2007.
- S Mosch. *Optimierung der Exploration, Gewinnung und Materialcharakterisierung von Naturwerksteinen*. PhD thesis, Göttingen, 2008.
- C Rodriguez-Navarro and E Sebastian. Role of particulate matter from vehicle exhaust on porous building stones (limestone) sulfation. *Science of the Total Environment*, 187(2):79–91, 1996. doi: 10.1016/0048-9697(96)05124-8.
- J Ruedrich and S Siegesmund. Salt and ice crystallisation in porous sandstones. *Environmental Geology*, 52(2):343–367, 2007. doi: 10.1007/s00254-006-0585-6.
- J Ruedrich, T Bartelsen, R Dohrmann, and S Siegesmund. Moisture expansion as a deterioration factor for sandstone used in buildings. *Environmental Earth Sciences*, 63(7-8):1545–1564, 2011. doi: 10.1007/s12665-010-0767-0.
- G W Scherer. Theory of drying. *Journal of the American Ceramic Society*, 73(1):3–14, 1990. doi: 10.1111/j.1151-2916.1990.tb05082.x.

- G W Scherer. Crystallization in pores. *Cement and Concrete Research*, 29 (8):1347–1358, 1999. doi: 10.1016/s0008-8846(99)00002-2.
- N Shahidzadeh-Bonn, J Desarnaud, F Bertrand, X Chateau, and D Bonn. Damage in porous media due to salt crystallization. *Physical Review E*, 81(6), 2010. doi: 06611010.1103/PhysRevE.81.066110.
- S Siegesmund and H Dürrast. Physical and Mechanical Properties of Rocks. In S Siegesmund and R Snethlage, editors, *Stone in Architecture - Properties, Durability*, chapter 3, page 552. Springer, Berlin Heidelberg, 4th edition, 2011.
- B J Smith, S McCabe, D McAllister, C Adamson, H A Viles, and J M Curran. A commentary on climate change, stone decay dynamics and the greening of natural stone buildings: new perspectives on deep wetting. *Environmental Earth Sciences*, 63(7-8):1691–1700, aug 2011. ISSN 1866-6280. doi: 10.1007/s12665-010-0766-1.
- R Snethlage and E Wendler. Der Wassereindringprüfer nach Karsten-Anwendung und Interpretation der Messwerte. *Bautenschutz Bausanierung*, 12(6):110–115, 1989.
- M Steiger. Crystal growth in porous materials - I: The crystallization pressure of large crystals. *Journal of Crystal Growth*, 282(3-4):455–469, 2005a. doi: 10.1016/j.jcrysgro.2005.05.007.
- M Steiger. Crystal growth in porous materials - II: Influence of crystal size on the crystallization pressure. *Journal of Crystal Growth*, 282(3-4): 470–481, 2005b. doi: 10.1016/j.jcrysgro.2005.05.008.
- H Stück, R Plagge, and S Siegesmund. Numerical modeling of moisture transport in sandstone: the influence of pore space, fabric and clay content. *Environmental Earth Sciences*, 69(4):1161–1187, 2013. doi: 10.1007/s12665-013-2405-0.
- A Török and B Vasarhelyi. The influence of fabric and water content on selected rock mechanical parameters of travertine, examples from Hungary. *Engineering Geology*, 115(3-4):237–245, 2010. doi: 10.1016/j.enggeo.2010.01.005.
- M Urosevic, E Sebastián Pardo, E Ruiz-Agudo, and C Cardell. Physical properties of carbonate rocks used as a modern and historic construction material in Eastern Andalusia, Spain. *Materiales de Construcción*, 61

- (301):93–114, mar 2011. ISSN 1988-3226. doi: 10.3989/mc.2010.53809.
- D Vandevoorde, M Pamplona, O Schalm, Y Vanhellefont, V Cnudde, and E Verhaeven. Contact sponge method: Performance of a promising tool for measuring the initial water absorption. *Journal of cultural Heritage*, 10:41–47, 2009.
- P Vazquez, F J Alonso, L Carrizo, E Molina, G Cultrone, M Blanco, and I Zamora. Evaluation of the petrophysical properties of sedimentary building stones in order to establish quality criteria. *Construction and Building Materials*, 41:868–878, 2013. doi: 10.1016/j.conbuildmat.2012.12.026.
- P Vazquez, B. Menendez, M F C Denecker, and C Thomachot-Schneider. Comparison between petrophysical properties, durability and use of two limestones of the Paris region. *Geological Society, London, Special Publications*, 416, mar 2015. ISSN 0305-8719. doi: 10.1144/SP416.15.
- J Vlassenbroeck, M Dierick, B Masschaele, V Cnudde, L Van Hoorebeke, and P Jacobs. Software tools for quantification of X-ray microtomography. *Nuclear Instruments & Methods in Physics Research Section a-Accelerators Spectrometers Detectors and Associated Equipment*, 580(1):442–445, 2007. doi: 10.1016/j.nima.2007.05.073.

6

Laminar black crusts on Lede stone

In the past decades, black crusts or gypsum crusts have been recognised as a main threat to Lede stone (see Section 3.4). In this chapter, the formation of a laminar black gypsum crust is studied by a characterization and additional weathering experiments. The sampling, measurements, analysis and interpretation in Section 6.2 were done by the author, in cooperation with Prof. Dr. Gilles Fronteau for microscopy, Dr. Geert Silversmit and Prof. Dr. Laszlo Vince for the μ XRF measurements, Dr. Fabrice Dagrain for the scratch test, Dr. Marijn Boone for the Tinyperm II measurements, Dr. Wesley De Boever for optimization of the SEM analysis and Jeroen Van Stappen for the stereoplot model. Sections 6.3 and 6.4 contain (explorative) weathering experiments designed in the light of the discussion in Section 6.2. Prof. Dr. Marcos Lánzon (UPCT, Cartagena, Spain) assisted in the glauconite experiments (section 6.4).

6.1 Introduction

Natural building stones are known to alter their surface properties when used and exposed to atmospheric conditions, as a result of the interaction between the stone and its environment. Many processes interfere with each other and the eventual alteration pattern can be complex and dynamic. Eventually, the interaction of different processes leads to different erosional or depositional alteration patterns (ICOMOS-ICS, 2008). Erosional weathering removes material from the stone by e.g. dissolution, exfoliation, flaking or scaling, while depositional weathering adds material to the stone's surface by e.g. efflorescence, encrustation, biocolonization. Both can be caused by chemical, physical and biological processes.

Of all types of alteration, gypsum crusts and more specifically black crusts on carbonate rocks are among the most studied. Black crusts are sulfate encrustations on building stones in polluted urban environments which mainly consist of gypsum crystals incorporating airborne dust and particulate matter (Camuffo et al., 1983). Several studies were assigned to the relation between black crust formation and urban pollution (Zappia et al., 1998; Ghedini et al., 2003; Grossi et al., 2003). Morphologically, these crusts can have a laminar or more framboidal or dendritic structure (Török and Rozgonyi, 2004), depending on the conditions under which they were formed. Their structure is strongly related to the microfabric of the host rock (Fronteau et al., 2010). In general, a gypsum crust consists of an outer opaque layer, a subsurface layer with gypsum crystallization and a deeper fractured zone irregularly passing into the sound stone (Maravelaki-Kalaitzaki and Biscontin, 1999). Black crusts develop on rain-sheltered surfaces due to dry or wet deposition of airborne SO₂ on stone with a carbonate phase or lime mortars in the presence of water and catalyzing air pollutants (Rodriguez-Navarro and Sebastian, 1996; Ausset et al., 1999; Siegesmund et al., 2007). On surfaces exposed to rain, black crusts will be washed off due to the moderate solubility of gypsum, if the rate of rain washing exceeds the rate of deposition. On more rain-protected surfaces, they have the potential to initially stabilize the stone surface (Török, 2003). Eventually, they can detach mechanically through contour scaling, where not only the crust, but also a layer of the disaggregated stone held by the crust is lost (Vergès-Belmin, 1994; Smith et al., 2003). Detachment of the crust can occur by other processes like

mechanical impact, crystallization of ice or salt behind the crust, hydration/dehydration or thermal stresses. After detachment, the process of gypsum crust formation can resume (Smith et al., 2003), although the conditions might be different due to the legacy of the previous crust forming episode.

6.2 Microstructure, composition and petrophysical properties of the laminar gypsum crust

Accurate classification of stone weathering and diagnosis of the stone conditions is the first step for stone conservation studies (Warke et al., 2003). Notwithstanding having fundamental knowledge on weathering forms, a preliminary case-study of the exact stone type and building environment is often appropriate. Therefore, several methods exist and are being developed for the effective characterization of building materials, both in the field and in the laboratory (Török and Prikryl, 2010). Although stone decay is observed and handled on the macroscale, it is the expression of microstructural changes in the pore space of the building material. This section therefore presents a microspatial structural and chemical characterization of a laminar black gypsum crust on the Lede stone. Such crusts have been studied previously (Larbi et al., 2003; Dreesen et al., 2006). It was stated that glauconite could play a triggering role in the sulphation process (Dreesen and Nielsen, 2009). The formation of gypsum crusts on Lede stone was recently studied on the micro-scale in laboratory conditions (Dewanckele et al., 2012, 2013). Here, current methods as thin section microscopy, SEM-BSE and EDX, which have typically been used for describing gypsum crusts (Weber et al., 2007; Török and Rozgonyi, 2004; Kim et al., 2013) are multidisciplinary combined with advanced methods such μ CT (Ketcham and Carlson, 2001; Cnudde and Boone, 2013), X-ray fluorescence micromapping (μ XRF) (Cnudde et al., 2009) and the scratch test (Richard et al., 2012).

6.2.1 Materials and methods

A weathered Lede stone was collected from the Late Gothic Sint-Salvator church in Wieze (Belgium) from the ventilated top of the tower where they were protected from direct rain impact (Fig. 6.1). In these conditions, a

thin black crust developed on the stone surface (Fig. 6.2). This crust was studied using different techniques, accordingly or complementary to Larbi et al. (2003); Dewanckele et al. (2012, 2013), to evaluate its decay and the implications on stone conservation.



Figure 6.1: Image of the Lede stone sample with gypsum crust from the Sint-Salvator church in Wieze.

The weathered sample was cut into sagittal sections for subsampling. The first section was impregnated with an EpoFix resin, stained with yellow fluorescent dye (EpoDye) for the preparation of subsamples for optical microscopy, SEM, and μ XRF. Optical microscopy was performed on a 30 μ m thin section using a Zeiss Axioscope A1 equipped with an Axiocam and EpoDye filter. Polished sections were prepared for SEM and μ XRF studies. A JEOL 5300-LV SEM was used for SEM-BSE imaging and EDX mapping. μ XRF spectra were recorded in vacuum with an EDAX-EAGLE III μ -probe at the X-ray Microspectroscopy and Imaging Group (Ghent University). An area with both crust and stone material was mapped with the following acquisition settings: 40 kV, 11 s live time per pixel, pixel resolution \pm 100 μ m, map dimensions 9100 μ m \times 5100 μ m. Two cylindrical subsamples with diameters of 8 and 1.8 mm were cored for μ CT scanning at the Centre for X-Ray Tomography of the Ghent University (UGCT) using the first custom built micro-CT setup at the facility (Masschaele et al., 2007). The 8 mm sample was scanned at a tube voltage of 120 kV and a tube current of 75 μ A, and a 1 mm Al filter was used for beam hardening reduction. For the 1.8 mm sample, the tube was operated at 80 kV and a tube current of 37.5 μ A. A spatial resolution of 12.48 μ m and 2.04 μ m was obtained for each sample respectively. The μ CT images were reconstructed with the Octopus reconstruction software

(Vlassenbroeck et al., 2007), 3D image analysis was performed with Octopus Analysis (formerly Morpho+) (Brabant et al., 2011) and the volumes were rendered using VGStudio MAX software.

The second section was not impregnated and used to perform the scratch test (Richard et al., 2012) to assess the microspatial variation in rock strength. Successive 100 μm deep cuts were made along the sample surface using a 94 μm wide cutter to generate a groove with a total depth up to 2750 μm . The resulting rock strength was expressed as unconfined compressive strength and the tomography image was matched with a photo of the stone section. Afterwards, six drilling tests were performed on the same sample, aligned in the same direction of the scratch test. The size of the specimen limited the number of measurements to six. The custom-built drilling system (Dagrain et al., 2013) used a 5 mm drill bit and measures both torque and weight on bit versus depth as an indicator of the variation in strength. The drill bit was operated at a Rotational speed of 250 RPM and Rate of Penetration of 50 $\mu\text{m}/\text{rotation}$.

Non-destructive gas permeability measurements were performed with a TinyPerm II probe permeameter (Filomena et al., 2014) on the same sample after the scratch test measurements. The measurements were performed in a grid on the sagittal section and the results were interpolated and plotted in Matlab. This plot was also matched with a photo of the stone section. However, measurement was somewhat problematic near the crustal surface because of stone instability and thus not the entire section could be covered by measurements. This area is left white within the resulting image.

Finally, samples of approximately 4 g were mechanically scratched from the surface to determine the organic matter content in the superficial black crust by measuring weight loss on ignition at 550 $^{\circ}\text{C}$ after preconditioning the samples at 110 $^{\circ}\text{C}$ (Heiri et al., 2001).

6.2.2 Results

2D Structure

Figure 6.3 shows thin section micrographs at different magnifications of the Lede stone from the Sint-Salvator church with a laminar gypsum crust on the left side. The porosity of the same field of view can be more easily observed in green on the fluorescence image (Fig. 6.3B). In general, the

crust exists of three layers: an opaque layer (zone 1), a subsurface layer with gypsum crystallization (zone 2), and a deeper fractured layer which passes into the sound stone (zone 3). This can be best observed in a higher magnification (Fig. 6.3C). The opaque layer is thin (tens of microns) and irregular. It consists of loosely bound opaque and iron rich particles, adherent to the surface. Loss on ignition was used to evaluate the organic matter in the crust. Indeed, this confirmed the presence of in average 1.03 wt% of organic matter. Underneath, there is a zone which is cemented by very fine gypsum crystals. Its thickness is variable, but mainly fluctuates around 500 μm . It encompasses autochthonous quartz grains and patches of calcite. Larger bioclasts such as *Nummulites variolarius* show a positive relief with respect to the rest of the unweathered stone. Specifically for these bioclasts, weathering starts with dissolution of the fibrous carbonate cement lining of the object, followed by partial dissolution of the calcite test (i.e. the body) layer per layer (Fig. 6.3D). It is remarkable that a substantial amount of the glauconite has a brown discolouration. This is especially true for glauconite grains within the gypsum crust or adjacent to the underlying fracture network. This discolouration is due to atmospheric weathering, releasing free iron that subsequently can precipitate as amorphous iron oxide, ferrihydrite or goethite.



Figure 6.2: Cross-section photograph of Lede stone with gypsum crust from the Sint-Salvator church in Wieze.

Looking at the porosity distribution on the fluorescence image of Figure 6.3B, a zone of lower porosity can be seen up to approximately 500 μm deep below the surface. This corresponds with the formerly described zone 2. Behind this low porosity zone, a number of surface-parallel

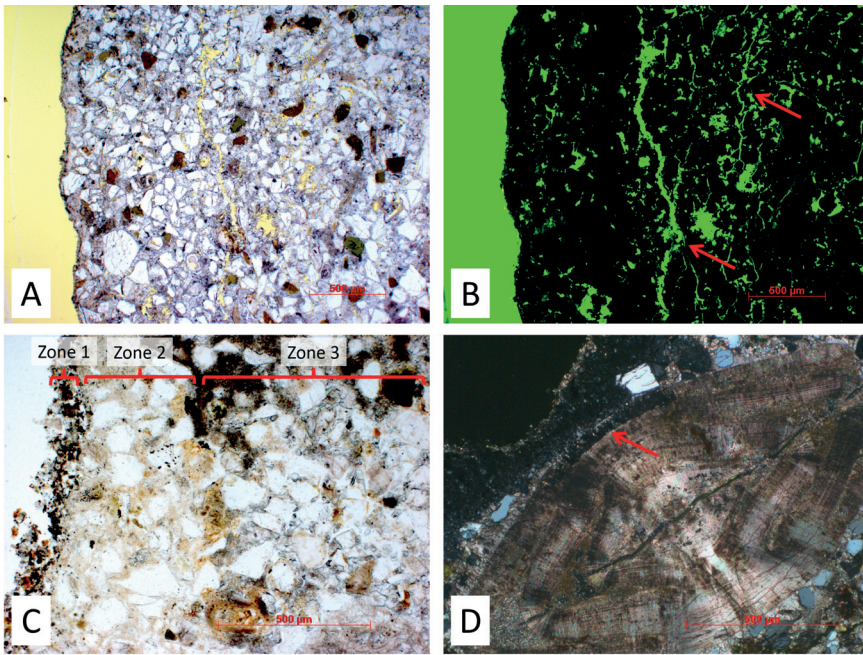


Figure 6.3: A) thin sections micrograph of gypsum crust; B) fluorescent image of the same view as A, illustrating the porosity and fractures in green; C) indication of opaque upper layer (zone 1), gypsum crystallization layer (zone 2) and sound stone with fractures (zone 3); D) *Nummulites variolarius* with partial dissolution of the outer shell, indicated by arrow. Scale bars are 500 μm .

fractures exist over a depth of several hundred of microns. The fracture network protrudes deeper inside the stone than the gypsum alteration does. However, under the SEM, gypsum crystals were sometimes found within these fractures. The fracture network is preferentially accommodated by some textural features such as the lining of coarse quartz grains and bioclasts. Small fractures initiate at the interface of the coarse well-rounded quartz grains and the surrounding cement or matrix. Fractures also form through the axial plane of the planispiral forams *N. variolarius* (Fig. 6.3D). The major fracture network develops where these features are aligned and smaller fractures are connected.

The same structure can also be observed on SEM-BSE images in Figure 6.4A. In the opaque layer of zone 1 (Fig. 6.43B), fly ash can be recognized both as smooth and rough spherical particles of 5 to 10 μm diameter. Airborne silt-sized quartz particles are also present. Zone 2 consists of

densely intertwined acicular gypsum crystals, within the micrometer scale. In zone 3, cracks can be observed, sometimes with gypsum crystallization inside.

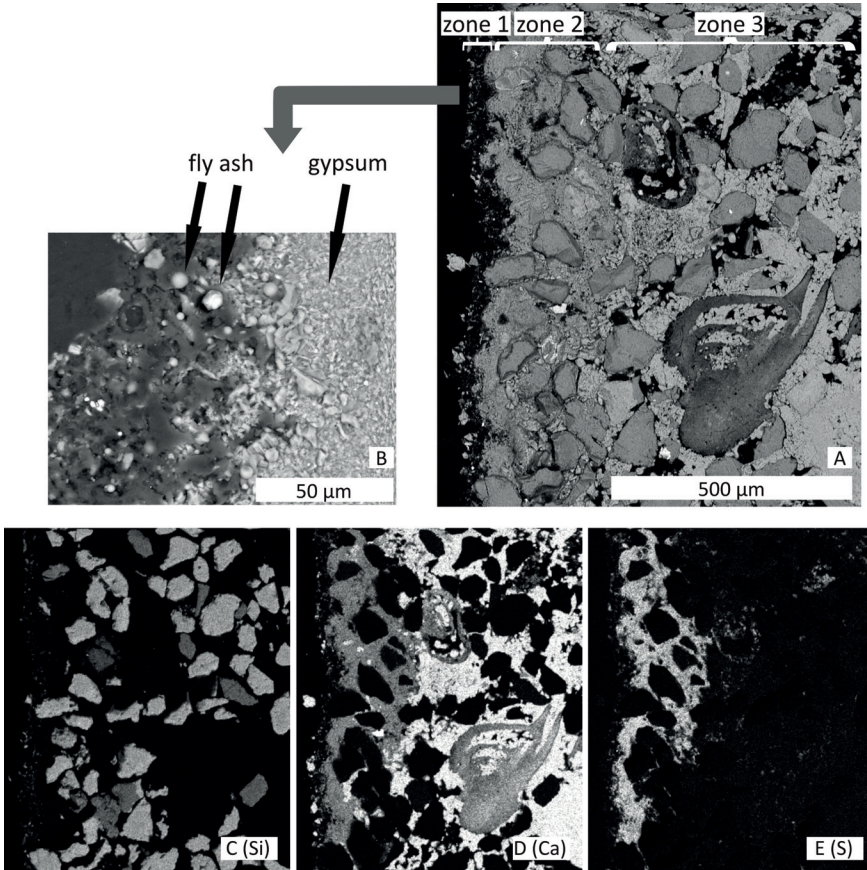


Figure 6.4: A) SEM-BSE image of gypsum crust oriented to the left with indication of zones 1, 2 and 3; B) detailed SEM-BSE image of the crust with particulate matter in the outer layer and intertwined gypsum crystals underneath; C-E) SEM-EDX mapping of Si, S, Ca with the same field of view as A.

2D Composition

SEM-EDX mapping and point spectrum measurement was performed to provide more chemical information on the decay pattern (Fig. 6.4C-E). The structure of the crust is reflected in the elemental maps. On the Si map (Fig. 6.4C), quartz and feldspar grains are visible. Feldspars could be recognized by spotting them in a K map, but can be differentiated here from

quartz by the number of counts for Si in the EDS images. Quartz grains are bright, feldspars are more grey. The Ca map (Fig. 6.4D) displays the calcite cement and matrix on the right side of the sample together with the Ca-tests of *Miliolina* forams. To the left, there is a Ca signal with lower number of counts. This correlates well to the S map (Fig. 6.4E) and corresponds to the gypsum crust as observed in thin section. Finally, the signal of P and Fe was too low to be detected in SEM-EDX mapping.

Laboratory μ XRF mapping shows the spatial occurrence of Al, Si, P, S, K, Ca, Fe and Zr in relative concentrations, with the crustal surface oriented to the left (Fig. 6.5). The hotspot areas for Si and Ca are opposite. Six main hotspots of Si can be recognized, representing the fraction of coarse well-rounded quartz grains. The Ca signal is low for these pixels. On the other hand, the Ca hotspots are related to bioclasts. Over the rest of the area, pixels show a combined Si and Ca signal. This is because of the sampling depth of μ XRF and the resolution ($\pm 100 \mu\text{m}$) which is too low to resolve very fine quartz fraction ($< 125 \mu\text{m}$) from the calcite matrix and cement. The hotspots in Al, K and Fe are related to feldspar grains (K, Al and possibly Ca), and glauconite (K, Al, Fe). The elemental maps show a clear elevation in P and S content in the crust compared to the bulk of the stone. The S relates to the gypsum crystallization in the outermost 500 μm of the sample, with irregular thickness and distribution. The P enrichment in the crust was not noticed in SEM-EDX spectra. Fe and K enrichments in the crust are less clear, and lack true hotspots. However, the relative concentration is higher for the crust than for the bulk of the sample, hotspots excluded.

3D structure

Finally, the sample was analyzed in 3D using μ CT. Figure 6.6 shows a sagittal μ CT slice through the cylindrical subsample of 1.8 mm, with the gypsum crust oriented to topwards. μ CT has the advantage of analyzing and rendering the sample in both 2D and 3D, providing a numerous stack of slices (several hundreds) which each represent a different section of the total 3D volume.

Figure 6.6 represents a 2D sagittal section through the 3D volume in an 8 bit greyscale image. Black represents pore, whilst the various grey values are material. At a specific X-ray energy, the lower the effective atomic number and density of a material, the darker it appears in the image, and vice versa. The dark grains are mainly quartz, sometimes feldspar or, a little brighter, glauconite. The lightest cement phase in the bottom of the sample

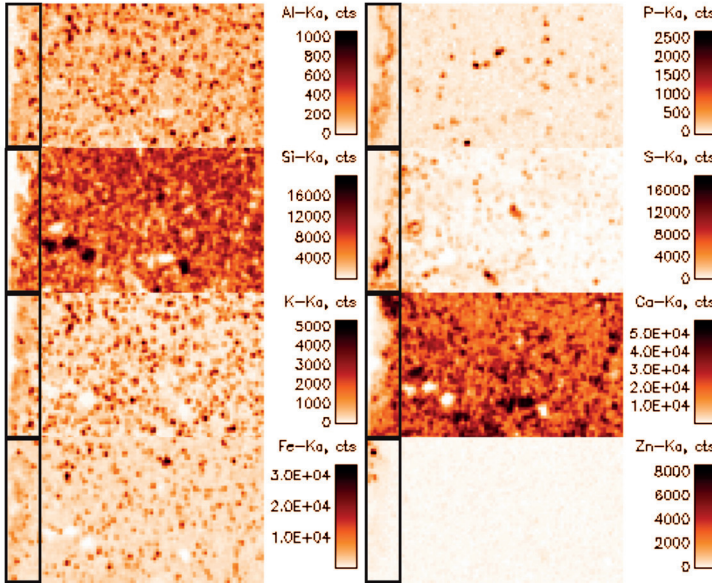


Figure 6.5: μ XRF mapping of cross section of $5.1 \text{ mm} \times 9.1 \text{ mm}$, crustal surface oriented on the left side and marked by rectangle, with relative concentrations of the elements Al, P, Si, K, Ca, Fe and Zn.

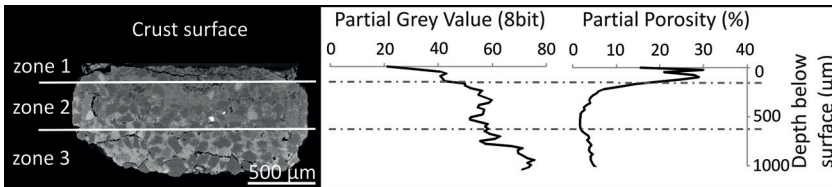


Figure 6.6: Sagittal slice obtained with μ CT and correlated Partial Grey Volume and Partial Porosity graphs of the total volume in function of depth beneath the crustal surface.

is calcite, whilst the darker cement on top is gypsum. The same three zones as observed in thin section can also be recognized in this sagittal slice. A frontal slice through the three zones is presented in Figure 6.7. They are marked as such on the image.

The Partial Grey Value (PGV) and Partial Porosity (PP) were calculated on the 3D volume from top to bottom. Whilst PP is dependent on the segmented porosity only, the PGV also reflects the average grey value of

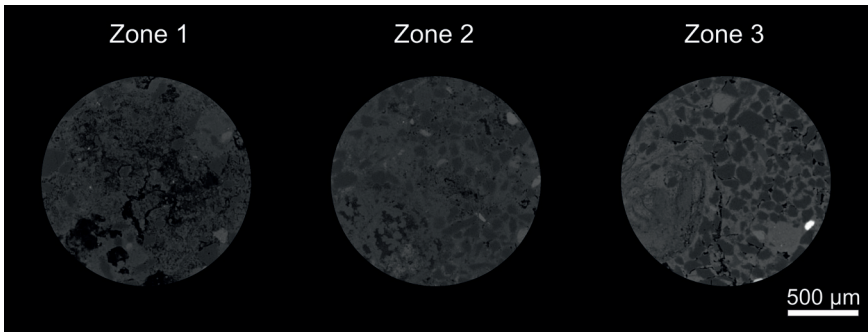


Figure 6.7: Frontal slices obtained by μ CT through each zone. Zone 1 consists of fine grained accretionary material. Zone 2 consists of dark grey quartz grains in a matrix with higher grey value (gypsum). Zone 3 consists of similar quartz grains in a lighter matrix (calcite) and fractures. Grains with higher grey value represent glauconite, calcite and accessory dense mineral phases; black zones are porosity.

the material. Thus PGV is dependent on the amount of porosity as well as the phases present. In both PGV and PP, the three zones are distinguishable when their values are plotted in function of depth beneath the crustal surface (Fig. 6.6). Based on this and the visual observations, the three zones are arbitrary marked on the image. Although they are separated by straight lines for simplification and correlation between the image and the graphs, it should be clear that the real boundary between each zone is irregular. It can be seen that zone 1, the opaque layer, is loosely bound, resulting in a very high PP and thus low PGV. The difference with the underlying zone 2 is remarkable. This zone has a much lower porosity with a minimum around 500 μ m below the surface. The PGV shows a plateau for this zone, allowing to delimit its extension. This plateau is caused by a uniform zone of low porosity consisting mainly out of quartz grains in a gypsum matrix. Underneath, zone 3 is differentiated by higher PGV and slightly higher porosity. Gypsum crystallization is almost nonexistent in this zone and calcite remains chemically unaffected. The average porosity of this zone is similar to normal values for similar fresh stone samples of the compact microfacies Lf1 (see Chapter 5). Peaks in porosity are both caused by natural variability within the fabric and the occurrence of small fractures. The preparation of longer cores, although imbedded in resin, was problematic. Most likely, this was the result of a larger crack being present at the irregular base of the sample seen in Figure 6.6.

Very specific features can be observed in some of the various slices. Zone 2 is less thick where larger bioclasts are present. The coarser bioclasts are known to stand in positive relief upon weathering. In this case, it can be seen that *N. variolarius* specimens are less prone to weathering than the surrounding calcite components, similar to the thin section observations. Nevertheless, weathering is protruding from the outer edge into the test layers along the perforate hyaline calcite. Where calcite is dissolved, gypsum subsequently precipitates. Also axial fractures are formed within these planispiral forams. Glauconite within the gypsum crystallization zone is intensely cracked and corroded, so that released parts could disintegrate completely.

The cracks were segmented in 3D, using a multiscale Hessian fracture filtering (Voorn et al., 2013) to select elongated features that belong to porosity. After this segmentation, the cracks were separated from the elongated primary pores by manual selection in Octopus Analysis. Once the cracks were isolated, they were separated into objects using the Octopus Analysis tool based on a watershed separation. The resulting objects were regarded as individual cracks, composing a crack network. It is possible to calculate the maximum opening (MO), i.e. diameter of the largest sphere that fits within the object, and the object orientation in 3D. Figure 6.8 displays the 3D rendering of the cylindrical samples and the location of the fractures within the transparent volume.

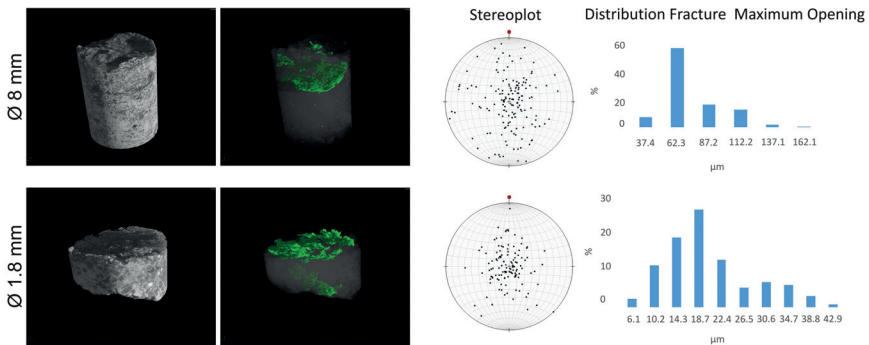


Figure 6.8: 3D rendering of μ CT samples (left) represented as a semi-transparent volume, while fractures are depicted in green (right); stereoplot of fracture orientation and distribution of the fracture size based on Maximum Opening (right).

In the 1.8 mm cylinder, many fractures exist very near to the surface. They are found within the opaque layer and on the boundary with the zone below. Also, the smaller cracks at the bottom, which were observed in Figure 6.6, are clearly connected to the border, when rendered in 3D. They are most likely part of a larger crack network, which caused the sample to crack during coring. Thus, the bottom surface can be seen as a larger crack, but could not be analyzed quantitatively. The segmented fractures have a MO which is distributed around 20 μm . The fractures are mainly oriented (sub-)parallel to the stone surface (Fig. 6.8).

In the 8 mm sample, smaller cracks are also present near the surface, but the largest fracture network runs approximately 2.5 mm below the surface. The pole of the fracture is plotted on stereographic projections. A plot in the centre of the projection thus represents an object with its long axis oriented parallel to the stone surface (i.e. crustal surface). The majority of the fractures plot around the centre and thus run (sub-)parallel to the stone surface (Fig. 6.8). Some fractures, however, clearly have an inclined orientation. These second generation of fractures form the connection steps between the first generation, individual and sub-parallel fractures. The MO of these fractures is distributed around 60 μm , but can grow larger than 100 μm , which is quite substantial on the scale of observations. As only objects with MO three times the spatial resolution were included in the analysis, the small fractures as observed in the 1.8 mm sample were not included in the analysis of the 8 mm sample. It is thus the intention to combine the information of both separate analysis.

Petrophysical properties

Understanding the petrophysical properties of weathering forms is important to estimate stone surface stability and to decide on interventions and stone treatments. Here, this was addressed by measuring confined compressive strength and gas permeability. The stone section on which the analysis was performed is given in Figure 6.9. The scratch test was performed in the outer 27.5 mm of the stone surface (Fig. 6.9B). Red and yellow represent the strongest parts of the rock, with compressive strengths up to 150 MPa, which are not unusual for this type of rock. The dark to light blue represents strengths from tens of MPa to around 50 MPa. There is an important decreasing gradient in strength in the outer few centimeters, as a result of the superficial stone decay. Drilling resistance profiles (Fig. 6.10) show more detail of this weaker zone. Drops in weight on bit illustrate the passage through weaker zones while peaks are stronger

zones. The larger drops at 8 mm depth in drilling resistance profile 6 and at 2 mm depth at drilling resistance profile 1 are the result of major fractures. The decayed zone is the thinnest in drilling resistance 4, where the stone strength increases at a depth of 5 mm. It can be correlated to the position where the scratch test reaches its highest strength values. This means that initial rock strength corresponds to an average weight on bit of around 20 N, whilst lower weights are measured in the decayed zone, as is most clear in profiles 1, 3 and 5. The measurements again show that the decayed part has an irregular thickness. After performing the scratch test, part of the crust (top left in Fig. 6.9A) broke off during the cutting of the sample, preparing it for gas permeability measurements. This crack correlates with an area of weakness observable in the scratch test tomography and to the drop in weight on bit at a depth of 8 mm in profile 6. Therefore, unfortunately, gas permeability measurements could not be obtained for the entire cross section. In addition, permeability very near to the crustal surface was too high to obtain representative measurements with this method. However, the mapping does show some interesting features (Fig. 6.9C). The core of the sample demonstrates relatively low gas permeability, scaled in blue, with values ranging from 98 to 240 mD. Within this bulk, there is a zone of slightly higher permeability represented in light blue. This could be due to variation within the stone fabric. Towards the remainder of the crust, permeability starts to increase strongly up to 679 mD, with highest permeability correlating to a thick zone of relative weakness observed in the scratch test tomography.

6.2.3 Discussion

Black crusts drastically change the aesthetic appearance of architecture and sculptures by a black discolouration and a modification of surface finishing and details. Furthermore, they are only a dominant visual expression of several interacting decay processes combining crystallization, dissolution, cracking and bio-colonization, leading to heavy damages on the stone surface such as scaling and flaking. The relation between the morphology of the laminar black gypsum crust and the stone's microstructure can be revealed by combining several spatial characterization techniques that identify different structural and compositional elements in the crust and the stone underneath. This allows to study the weathering process and to understand the impact on surface stability and strength.

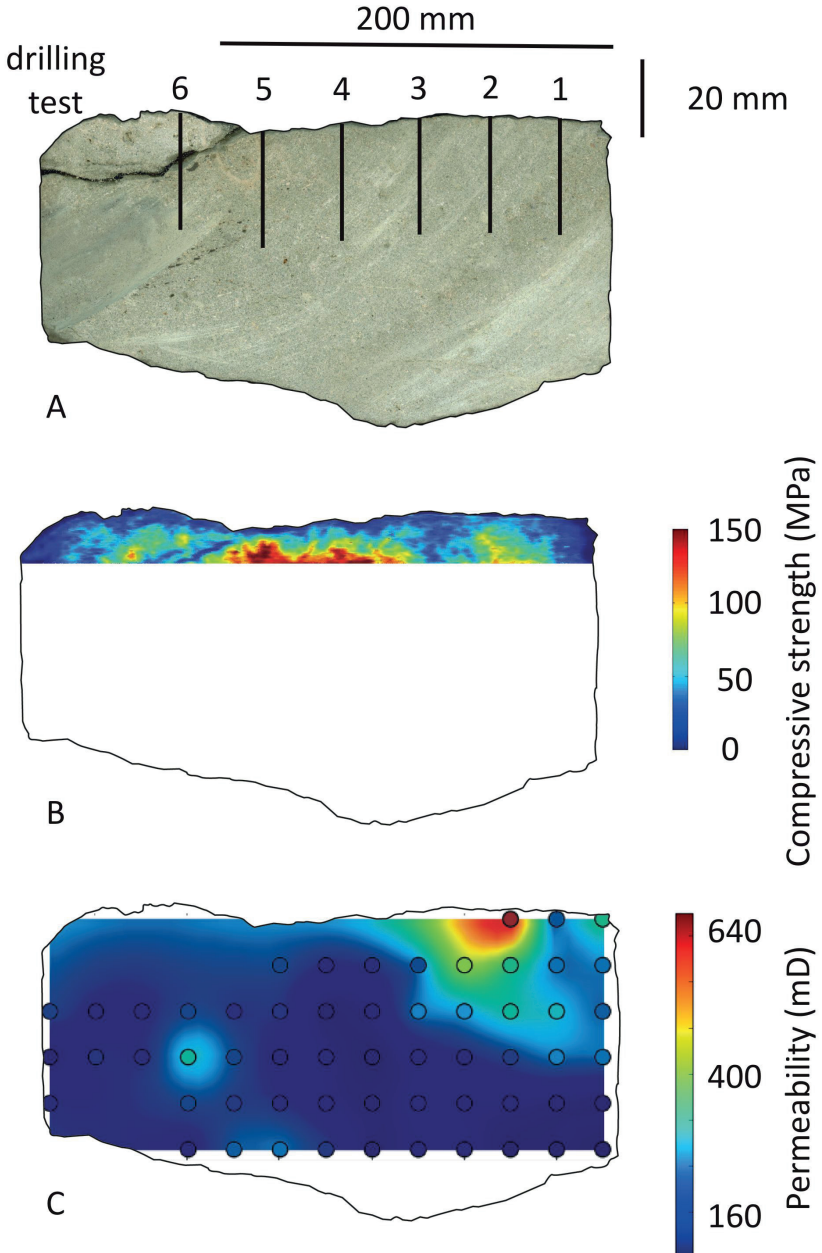


Figure 6.9: A) sagittal sample for scratch test and gas permeability measurements with position of drilling test; B) scratch test tomography fitted to sample outline; C) gas permeability mapping fitted to sample outline.

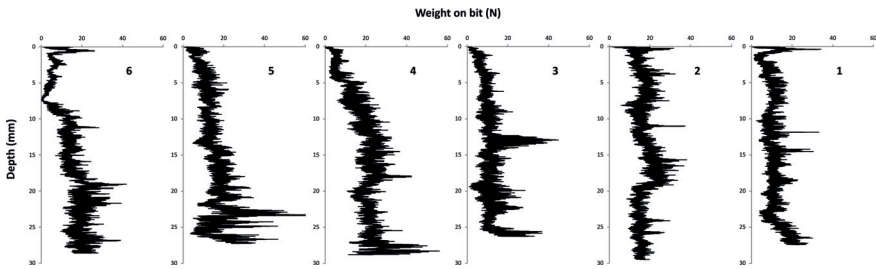


Figure 6.10: Depth logs of the drilling strength measurements. Average weight on bit around 20 N corresponds to average initial rock strength, while lower average weight on bit corresponds to the decayed zone near the surface. The decayed zone is thinnest in profile 4 (± 5 mm) and thickest in profile 1 and 3 (± 25 mm).

The large drop in weight on bit at 8 mm depth in profile 6 correlates to the fracture observed in Fig. 6.9A and B.

Microstructure

The observed layered structure of the black crust is consistent with the observations of Maravelaki-Kalaitzaki and Biscontin (1999). There is a clear contribution of particulate matter and other airborne dust on the surface of the crust, which can best be studied under the SEM microscope. μ CT images, on the other hand illustrate the nature of these particles; irregularly adherent to the outer surface on which they are deposited. Gypsum alteration, however, occurs underneath this zone where calcite crystals are dissolved by sulphurous acid solutions and provide Ca^{2+} ions. This process preferentially exploits finer crystal phases as these have higher specific surface (Fronteau et al., 2010; Dewanckele et al., 2013). Therefore, calcite dissolution is mainly restricted to the finer calcite matrix and cement. Gypsum does not necessarily crystallize on locations where calcite was dissolved. In moist rocks, the pore fluids enriched in atmospheric sulphur and autochthonous calcium will migrate through the pore system towards the exterior in case of drying or towards the interior in case of wetting. Salts, and thus gypsum, crystallize by heterogeneous nucleation out of a supersaturated solution (Steiger, 2005). In rocks, there are sufficient nuclei available, yet still phases with high specific surface have higher chance to act as nucleus (Dewanckele et al., 2013). On the other hand, crystals form in supersaturated solutions, which can be obtained by drying. When crystallization is induced by drying, gypsum will accumulate at the evaporation front, near the surface and subsurface of the stone (Charola et al., 2007). This explains the occurrence of the gypsum layer, zone 2, near the stone surface with an irregular thickness of

approximately 500 μm , very similar to the observations made by (Beck and Al-Mukhtar, 2010) on tuffeau limestone. It can be assumed that this zone grows by crystallization of gypsum at the interface with the stone. For the same reason, gypsum crystallization can be observed at fracture surfaces deeper within the stone. Beck and Al-Mukhtar (2010) made similar observations on tuffeau limestone, where they measured a thickness of 0.5 mm for the real gypsum crust, but a thickness of 20 mm for the altered stone.

Cracks

μCT facilitated the 3D characterization of the orientation and maximum opening of the crack network. Most are oriented (sub-)parallel to the surface. The cracks can grow to more than 100 μm wide, several millimeters below the surface, initiating the detachment of the crust by scaling as observed by Smith et al. (2003). The fractures originate near the rounded coarse quartz grains, where initial circumgranular porosity is present. Thus, the presence of these grains can be seen as a flaw. They are further facilitated by the axial plane of *N. variolarius* and by the easily weathered glauconite grains. Dewanckele et al. (2012) observed the initiation of micro-cracks due to the sulphation process underneath the gypsum crust. Dreesen et al. (2006) found such (sub-)parallel cracks in Lede stone at depths of 5 to 25 mm and designated them as frost cracks. Cracks at depths of 5 to 25 mm are in accordance with the observations of the scratch test and the drilling test, which is reflected by a decrease in strength. The thickness of the weaker layer is variable, but reaches more than 27.5 mm near the stone edges. This exceeds by far the average thickness of 500 μm of the gypsum alteration zone, but rather corresponds to the zone where cracks are present. This cracking might be enhanced or facilitated by progressive discrimination between the deeper stone and the crystallization zone, where porosity is altered and water flow might be redirected parallel to the surface (Beck et al., 2003). In turn, these cracks increase the permeability and reduce rock strength. This will have a positive feedback on both the partial dissolution of carbonates within the deeper altered rock and the further propagation of micro-cracks induced by gypsum crystallization pressure. It will also affect the local water saturation which influences freeze-thaw weathering. Such increase in permeability is confirmed by the gas permeability mapping, which suggests an increased permeability near the stone surface. However, only a small part near the stone surface could be accurately measured and more tests on permeability variation within the decayed zone should be done on

other samples.

Glauconite

The glauconite grains in the decayed zone show physical disintegration and a brownish discolouration. This could be the result of acid-induced release of Al, Fe and Mg from the crystal lattice (Hassan and Baioumy, 2006) when glauconite comes in contact with sulphurous pore waters, a process enhanced by cracking-increased permeability. This results in wedge-like splitting, which facilitates initiating cracks and further physical disintegration. In contrast to the suggestion of Dreesen and Nielsen (2009), there is no evidence here of glauconite acting as favourable nucleation site for gypsum crystallization. The released iron can precipitate locally, causing the brownish discolouration of the grains or it can participate to the relative iron enrichment in the crust observed by μ XRF mapping. This process then contributes to the patina formation (see 3.3). Fobe (1990) suggested that glauconite not necessarily contributes to the formation of a patina. However, μ XRF mapping revealed a K enrichment at the surface. This K-enrichment can possibly be used as a tracer for glauconite weathering and element mobilization, as where the exchangeable cations such as K^+ can easily be replaced by e.g. H^+ from acidic solutions. If the K-enrichment in the crust reflects this process, this infers the mobilization of weathered glauconite elements, such as iron, and their participation in the crust.

Phosphorous

Finally, a phosphorous enrichment in the crust was observed in the μ XRF sample, but not in the SEM-EDX samples. Designation of phosphorous phases in crusts on building materials can be troublesome (Alves, 2013). Different authors have described the potential role of historical treatments (de Buergo and Gonzalez, 2003), organic contributions (Hosono et al., 2006) or atmospheric pollution (Xu et al., 2010) on phosphates present on building stone surfaces. Here, the information is insufficient to determine the origin of the phosphorous unambiguously. However, given the sample was provided from the tower, bird droppings are the most probably source. This would also explain its presence in the μ XRF mapping and its absence in SEM-EDX images, as bird droppings vary locally.

6.3 Acid weathering: evolution of the stone with black crust

Most studies on black crust focus on the characterization to identify the contributing sources and the sulphation process (e.g. Camuffo et al., 1983; Siegesmund et al., 2007; Fronteau et al., 2010; Török et al., 2011) or on laboratory experiments exposing fresh stones to atmospheric simulating environments (e.g. Sabbioni et al., 1996; Rodriguez-Navarro and Sebastian, 1996; Dewanckele et al., 2012). This section will explore how stone with a laminar gypsum crust evolves under an acidic environment.

6.3.1 Materials and Methods

A cylindrical sample with a diameter of 6 mm was cored from the same stone which was used for the characterization of the laminar gypsum crust (Fig. 6.2, see 6.2.1). It was mounted on a sample holder with the same diameter and sleeved with a heat-shrink tubing so that only the crust was exposed on top (Fig. 6.11A). Similar to Dewanckele et al. (2012), the sample was subjected for 21 days to an acid environment according to EN 13919. First, the sample was wetted and placed in the atmosphere of a closed 50 liter container, containing a solution of 150 ml H₂O and 500 ml 5–6% H₂SO₃. After 21 days, the sample was removed from the container, rinsed with water and left to dry in a custom designed climatic cell whilst the sample was scanned with μ CT using HECTOR (Masschaele et al., 2013) (Fig. 6.11B). The conditioning of the sample in the climatic cell was controlled by a humidity generator (GenRH - Surface Measurement Systems Ltd.) (Fig. 6.11C). The sample was scanned with μ CT before the test and during drying at the end of the test. To allow a direct comparison of the μ CT images before and after the test, scanning, reconstruction and analysis were performed with the same parameters for all scans. The X-ray tube was operated at 120 kV and 10 W and equipped with an 1 mm Al filter. 2401 projections of 1 s were taken over 360 °. The resulting voxel size was 4.99 μ m or 9.88 μ m for rebinned (factor 2) images. The scans were registered using Dataviewer software from Bruker MicroCT and analysis was performed with Octopus Analysis (Brabant et al., 2011) using the same parameters for both scans.

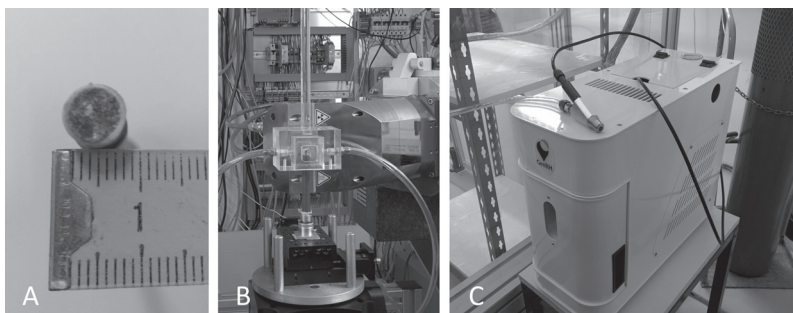


Figure 6.11: A) 6 mm diameter sample for acid weathering experiment sleeved with heat-shrink tubing; B) climatic cell set-up on HECTOR; C) GenRH humidity generator.

6.3.2 Results

Figure 6.12 shows a sagittal cross-section of the sample with μ CT before (initial state) and after the test (final state), with the exposed crust on the top. The sample has undergone dimensional changes, prohibiting an easy registration of the scans. As the dimensional changes, which include a rotation and translation of the grains, are more pronounced in the top part, the bottom part of the scans were used to register both volumes. The obtained transformation parameters were then applied to register the entire volume of the final state to the initial state. Subsequently, both volumes were cylindrically cropped to eliminate the irregularity of the lateral edges and the heat-shrink tubing in the analysis.

Figure 6.13 shows the 8-bit grey value histogram of the initial and final state. The voxels that represent porosity have grey values of 30–40, quartz and feldspar grains have grey values of 85–105, gypsum has grey values of 105–115 and calcite has grey values of 115–130. Voxels on the interface between two phases have an average value depending on the relative weight of each phase in the voxel (partial volume effect). The histogram of the initial state shows a peak in the quartz interval and a positive skew for the grey values related to calcite. In the final state, after 21 days of acid weathering, this positive skewness has decreased and the peak has increased. This indicates a relative decrease of calcite compared to the initial state. The increase in the peak can be interpreted as a result of different effects, firstly the increase in gypsum, and secondly to an increase in the surface/volume ratio of the porosity (i.e. different kind of

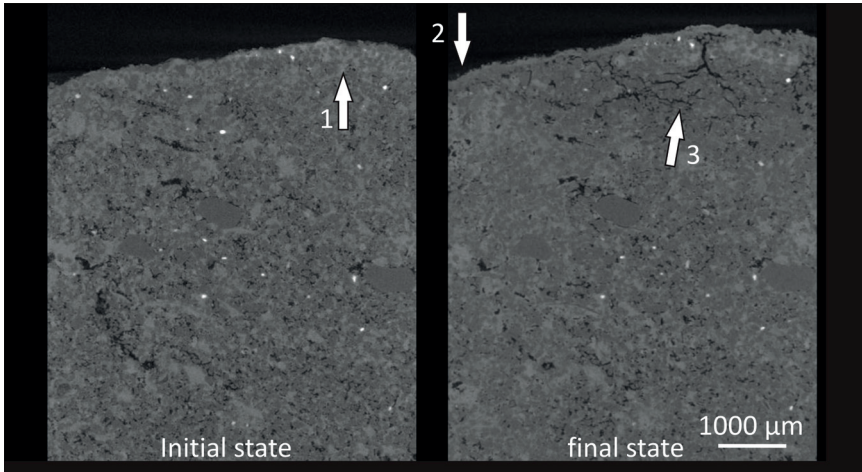


Figure 6.12: Sagittal cross section of μ CT with the crust on top of the initial state (left) and the final state (right). Arrow 1 indicates the depth of the original gypsum crust. Arrow 2 indicates superficial gypsum crystallization crust after 21 days acid exposure. Arrow 3 indicates a zone with a development of cracks. Relative grey scale given in the histogram of Fig. 6.13.

porosity) which results in an increase of partial volume effect around the carbonate and gypsum phase.

On Figure 6.12, it can be seen that the volume of the final state has increased at the top of the sample. This can also be observed when plotting the amount of voxels that represent the sample in function of depth for both the initial and final state 6.14. This graph can also be seen as a representation of the largest volumetric cross section of the sample with the top directed to the left. It shows that the volume has expanded $\pm 200 \mu\text{m}$ in the topwards direction.

Figure 6.12 also gives a visual impression of the changes within the sample. In the final state, three differences are remarkable compared to the initial state. First, a new compact and thin crust developed on top of the initial crust. Secondly, a zone with intensive cracking developed just beneath the initial crust. And finally, the bulk of the sample is less porous. This is shown in Figure 6.15 where the partial porosity is plotted in function of depth beneath the crust. The initial state can be interpreted the same way as in 6.2.2. However, because of the lower resolution, zone 1 and 2 cannot be distinguished clearly. Rather, only the transition of zone 1 and 2 to zone 3 is visible at around $750 \mu\text{m}$ depth. The partial porosity has changed

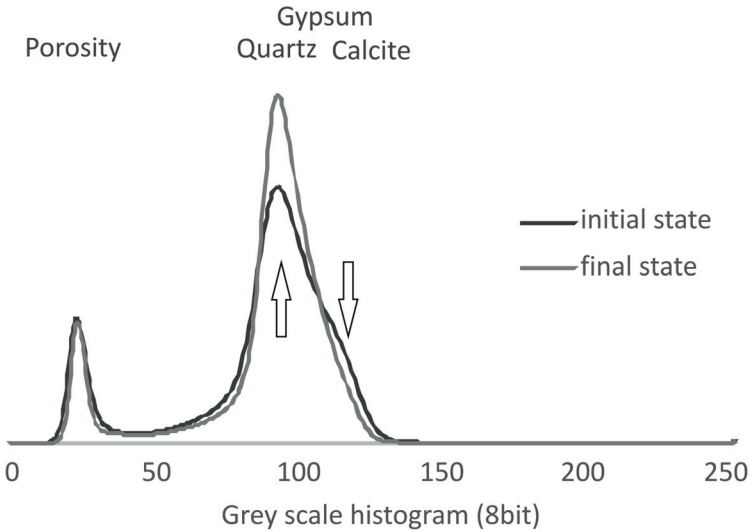


Figure 6.13: Histogram of the grey values (relating to the attenuation) obtained with μ CT of the initial state and final state. First peak represents porosity, second peak represents the bulk with quartz for the lower grey values, calcite for the higher and gypsum in between both.

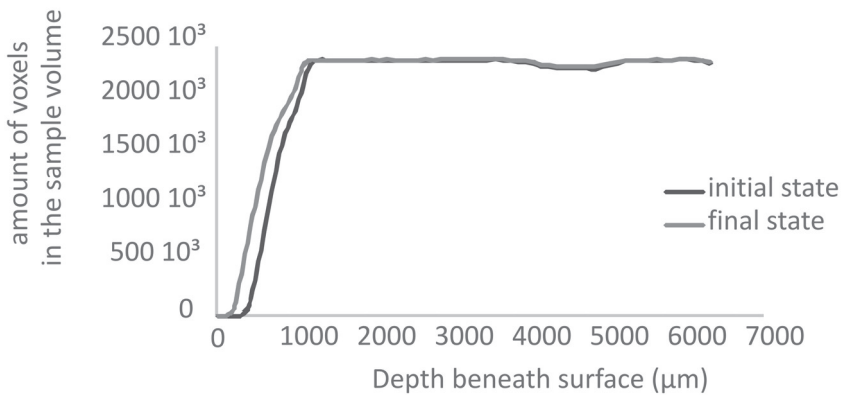


Figure 6.14: Plot of voxel volume in function of depth for the initial and final state.

drastically in the final state. Whilst the porosity of the top part increased almost 5 times, the porosity in the deeper parts decreased by a factor 2.

The increase in porosity can be attributed to dissolution and the

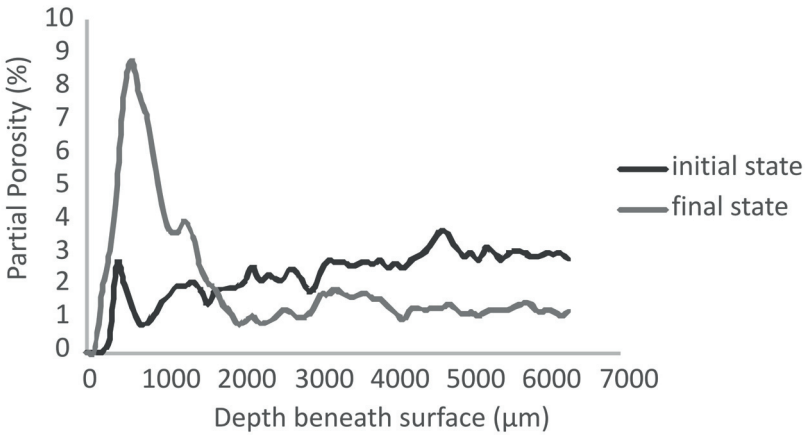


Figure 6.15: Plot of the partial porosity in function of depth for the initial and final state. The partial porosity in the final state increased in the top part and decreased deeper in the sample.

development of cracks in a zone up to 1500 μm depth (Fig. 6.12). These cracks form a network subparallel (horizontal) and oblique (vertical) to the surface. They mainly develop in the zone just below the initial gypsum crust. On the other hand, the decrease in porosity in the deeper parts of the stone can mainly be attributed to precipitation in the pore network. To illustrate this, Figure 6.16 shows a detail of the top part of the sample (top) together with a zonal model (bottom). Here it can be seen that a newly crystallized crust covers the entire top of the sample. Underneath, the initial gypsum crust remains largely unaffected, except for some cracks accommodating the underlying cracked zone and connecting it to the outside. As these cracks are covered with the new crystallization, they developed pre- or contemporary to the crystallization on the top.

Figure 6.17 shows a slice through the top, with the original crust on the initial state image (top) and the evolution of this crust in the final state (bottom). The crust clearly increased in volume. The tracking of dense particles near the border of the original crust can be used to evaluate the growth direction of the crust. Doing so, it can be seen that the gypsum crust has grown in two directions. In some locations, the crust grew outwards, as a result of crystallization on the top (also visible in Fig. 6.16). Other grains indicate the inwards progression of the crust, as they become incorporated in the gypsum crust in the final state. Over the entire sample, the crust grew inwards, by dissolution of the calcite cement and the precipitation of

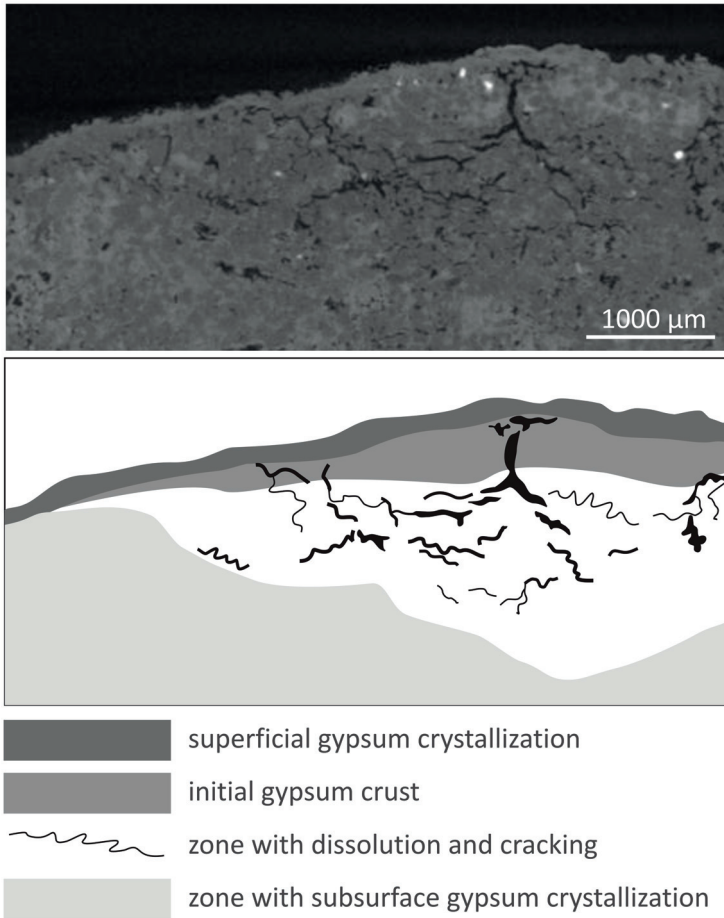


Figure 6.16: Detail of Figure 6.12 showing the top of the sample in the final state together with a zonal model. A superficial gypsum crystallization can be observed, with the development of a crack network underneath.

gypsum. Underneath this superficial crystallization, the crack network is visible in plan view (subparallel to the crustal surface). Here, the crack network tends to form a more polygonal network. The cracks observed here, mainly correspond to the vertical cracks in Fig. 6.16.

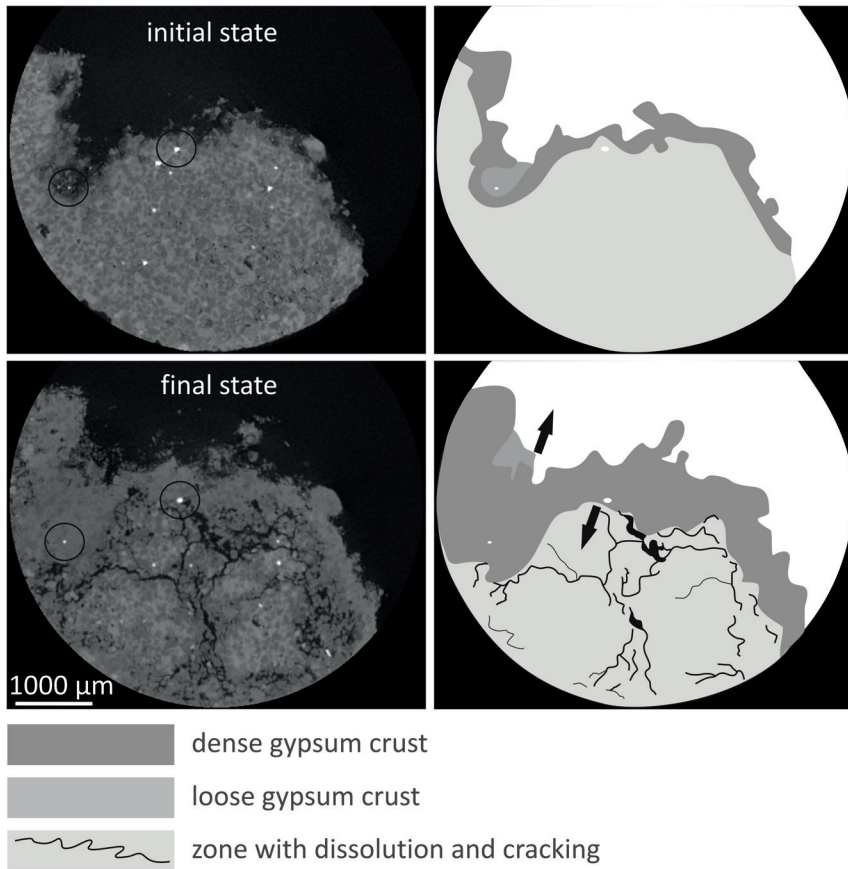


Figure 6.17: Slice through the crust of the initial and final state together with a zonal model. Arrows indicate the growth direction of the crust, which is observed by tracking the encircled dense grains on top (left) and beneath (right) the original crust. Both become incorporated in the final crust, illustrating crystallization on top and below the original crust. The view on the crack network is subparallel to the surface. Two dense grains used for tracking are encircled.

6.3.3 Discussion

From the cross sections and the plots of the voxel volume of interest and partial porosity, it can be seen that the sample has undergone some dimensional changes as a result of local dissolution and precipitation. The histogram suggests that calcite has been dissolved and that probably gypsum precipitated. The plots indicate an outwards extension of the sample.

The dissolution of calcite took mainly place in the zone underneath the original gypsum crust. Crystallization, on the other hand, took place in the pore network of the deeper stone and on the top of the sample. Here, it crystallized both on top of the older crust, as well as underneath, thereby including non-reactive grains of the stone in the crust.

Very striking is the development of cracks underneath the original and newly formed crust. This zone is situated close to the surface, between two parts where crystallization occurred: the top crust and the deeper stone. As such, the development of these cracks could be related either to differential length changes induced by gypsum crystallization, either by drying induced tension. Differential length change can be caused by crystallization of gypsum at the top and in the deeper parts of the stone. Crystallization causing an accretion at the surface, could induce tensile stresses in the substrate. Later crystallization in the deeper parts of the stone could induce shear stresses at the base of the overlying layer, which was already cracked. Alternatively, during the period of falling drying rate, the largest pores empty first which can cause local stress (Scherer, 1990). In unweathered conditions, this is insufficient to crack Lede stone. However, it is not clear how much this cracked zone was weakened by dissolution during the experiment.

It is not unlikely that the same process is responsible for the cracks observed in section 6.2 (e.g. Fig. 6.8), though on a different scale and with different intensities. Dreesen et al. (2006) attributed similar cracks in Lede stone to frost action. However, given the good frost resistance as shown by the technical tests (see section 3.6 and 5.8) and the observations in this experiment which did not involve freeze-thaw cycling, also the sulphation process itself could be responsible for cracking. Yet, if sulphation initiates the formation of this crack network, this will have a positive feedback on other processes such as freeze-thaw weathering which can enhance the initiated cracking.

6.4 Glaucinite weathering: explorative experiments

In 6.2 it was observed that the glauconite grains near the surface of the sample show brown weathering. From the μ XRF images, it was suggested that the K and Fe enrichment at the surface could possibly be related to the weathering of glauconite. In this section, some explorative tests were

performed to study the weathering of glauconite and the potential release of Fe.

6.4.1 Materials and methods

Glauconite was sampled from the Kattendijk Formation sands, which are very rich in glauconite with an average size between 300–600 μm . The sands were passed three times through a magnetic separator to separate the glauconite from the other, mainly quartz, minerals. Four 200 mg subsamples were exposed to 10 weathering cycles at the SAIT laboratory at UPCT (Cartagena, Spain) during a research stay. The first subsample was immersed in 10 ml distilled H_2O at room temperature. The second subsample was subjected to 10 cycles of heating to 65 $^\circ\text{C}$ for 3h in 10ml distilled H_2O , using a condensor to prevent evaporation. After each cycle, the sample was left to cool to room temperature, decanted and refilled with fresh distilled H_2O . The third subsample was subjected to 10 cycles of heating in air at 85 $^\circ\text{C}$ in 10 ml distilled H_2O , left to evaporate freely. After each cycle, the sample was cooled to room temperature and immersed again. The fourth subsample was exposed to an immersion for 3h in an aqueous 10 % H_2SO_4 solution. After each cycle, the sample was washed, decanted and left to dry at room temperature. After 1, 5 and 10 cycles, samples of the aqueous solutions were taken to measure the amount of Fe using an ICP-MS Agilent 7500ce equipped with an Integrated Autosampler (I-AS). The samples were introduced into a Scott spray chamber using a MicroMist glass concentric nebulizer and then into a Fassel type torch. An octopole reaction system (ORS) using He as collision gas was employed to remove polyatomic interferences. The sample temperature was maintained at 2 $^\circ\text{C}$ and the radio frequency power was set to 1500 W.

6.4.2 Results and discussion

Figure 6.18 shows the results of the iron concentration measured by ICP-MS. The sulphuric acid solution is very effective in leaching Fe from the glauconite. Heat cycles in pure water are far less. The heating tests in neutral water show that most of the eventually released iron is extracted after the first cycle. Almost negligible amounts of iron are extracted after 5 or 10 cycles. Water temperature plays a role in the extraction of iron, as

the amount of iron extracted increases with temperature. Heating in water has different potential in extracting Fe from glauconite with increasing temperature, but once the potential Fe ions are extracted, heat cycling with pure water is very ineffective to extract iron, as glauconite preserves its structure up to 800 °C (Mashlan et al., 2012).

The sulphuric acid solution is almost 100 times more effective than heating in pure water. Moreover, the extraction remains significant after 5 and 10 cycles. This indicates the continuing structural breakdown of the glauconite, which allows continued extraction of iron from the freshly exposed parts. The leaching of Fe^{2+} by a H_2SO_4 solution was already observed by Hassan and Baioumy (2006). Hence, the process of sulphation might have enhanced glauconite weathering and the mobilization of Fe from glauconite to contribute to the patina formation. This does not exclude other sources of Fe to contribute to the patina formation, e.g. Fe-rich calcite cement.

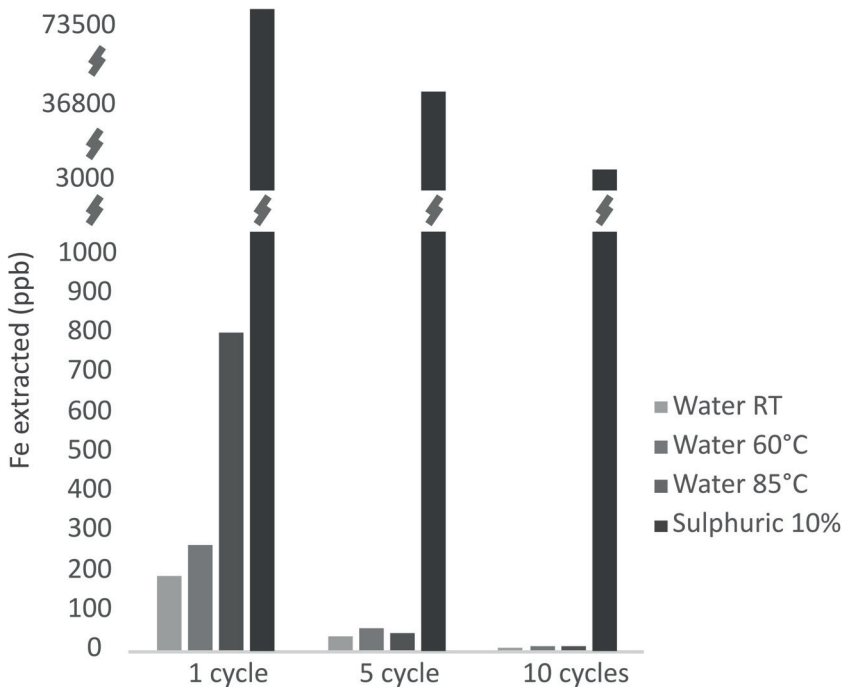


Figure 6.18: Leached Fe in ppb after 1, 5 and 10 cycles of wetting 200 mg of glauconite at room temperature, heating in water to 60 °C, heating in air to 85 °C and immersion in an aqueous 10 % H_2SO_4 solution.

6.5 Conclusion

The combination of several techniques allows a microspatial characterization of the gypsum crust. Optical microscopy and SEM are powerful investigation tools for the study of stone weathering. μ XRF can provide additional information on the spatial distribution and the relative concentration of different elements and was in this case particularly helpful to identify a weak enrichment of Fe in the crustal surface, whilst μ CT allows for 3D structural characterization, such as crustal thickness, and the orientation and opening of cracks. Scaling of the gypsum crust is caused by a crack network parallel to the surface which extends several millimeters in depth below the superficial gypsum crystallization. The scratch test provides a spatial characterization of surface strength and illustrates that superficial strength can be reduced more than 27.5 mm below the stone surface. This is the result of preferential dissolution of the calcite matrix and cement and the development of a crack network facilitated by elongated features such as circumgranular porosity or the axial plane of planar fossils. As evidenced by the acid weathering experiments, the origin of those cracks can possibly be assigned to the sulphation process, rather than freeze-thaw action. Such cracks eventually lead to the flaking or scaling of the crust. With decreasing SO₂ emissions over the last decades (Dreesen et al., 2012), this implies a positive outlook on the future weathering and deterioration of Lede stone in monuments.

References

- C Alves. Scanning Electron Microscopy Studies of Neoformations on Stony Materials of Modern Building Works. *Microscopy and Microanalysis*, FirstView:1–7, 2013. doi: doi:10.1017/S1431927613012701.
- P Ausset, M Del Monte, and R A Lefèvre. Embryonic sulphated black crusts on carbonate rocks in atmospheric simulation chamber and in the field: role of carbonaceous fly-ash. *Atmospheric Environment*, 33(10):1525–1534, 1999. doi: [http://dx.doi.org/10.1016/S1352-2310\(98\)00399-9](http://dx.doi.org/10.1016/S1352-2310(98)00399-9).
- K Beck and M Al-Mukhtar. Weathering effects in an urban environment: a case study of tuffeau, a French porous limestone. *Geological Society of Special Publications*, 331:103–111, 2010.
- K Beck, M Al-Mukhtar, O Rozenbaum, and M Rautureau. Characterization, water transfer properties and deterioration in tuffeau: building material in the Loire valley - France. *Building and Environment*, 38(9-10):1151–1162, 2003. doi: 10.1016/s0360-1323(03)00074-x.
- L Brabant, J Vlassenbroeck, Y De Witte, V Cnudde, M N Boone, J Dewanckele, and L Van Hoorebeke. Three-Dimensional Analysis of High-Resolution X-Ray Computed Tomography Data with Morpho+. *Microscopy and Microanalysis*, 17(2):252–263, 2011. doi: 10.1017/s1431927610094389.
- D Camuffo, M Delmonte, and C Sabbioni. Origin and growth mechanisms of the sulfated crusts on urban limestone. *Water Air and Soil Pollution*, 19(4):351–359, 1983.
- A Elena Charola, Josef Pühringer, and Michael Steiger. Gypsum: a review of its role in the deterioration of building materials. *Environmental*

- Geology*, 52(2):339–352, mar 2007. ISSN 0943-0105. doi: 10.1007/s00254-006-0566-9.
- V Cnudde and M N Boone. High-resolution X-ray computed tomography in geosciences: A review of the current technology and applications. *Earth-Science Reviews*, 123:1–17, 2013. doi: 10.1016/j.earscirev.2013.04.003.
- V Cnudde, G Silversmit, M Boone, J Dewanckele, B De Samber, T Schoonjans, D Van Loo, Y De Witte, M Elburg, L Vincze, L Van Hoorebeke, and P Jacobs. Multi-disciplinary characterisation of a sandstone surface crust. *Science of the Total Environment*, 407(20): 5417–5427, 2009. doi: 10.1016/j.scitotenv.2009.06.040.
- F Dagrain, J C Scaillet, S Modestou, and I Ioannou. Evaluation of the effectiveness of masonry consolidation treatments based on scratching tomography. *American journal of civil engineering and architecture*, 7: 556–574, 2013.
- M A de Buergo and R F Gonzalez. Protective patinas applied on stony facades of historical buildings in the past. *Construction and Building Materials*, 17(2):83–89, 2003.
- J Dewanckele, T De Kock, M A Boone, V Cnudde, L Brabant, M N Boone, G Fronteau, L Van Hoorebeke, and P Jacobs. 4D imaging and quantification of pore structure modifications inside natural building stones by means of high resolution X-ray CT. *Science of the Total Environment*, 416:436–448, 2012. doi: 10.1016/j.scitotenv.2011.11.018.
- J Dewanckele, M A Boone, T De Kock, W De Boever, L Brabant, M N Boone, G Fronteau, J Dils, L Van Hoorebeke, P Jacobs, and V Cnudde. Holistic approach of pre-existing flaws on the decay of two limestones. *Science of the Total Environment*, 447:403–414, 2013. doi: 10.1016/j.scitotenv.2012.12.094.
- R Dreesen and P Nielsen. On the triggering role of glauconite in the sulphate attack of sandy limestones, based on a study of historical building stones in Flanders, Belgium. In *12th Euroseminar on Microscopy Applied to Building Materials*, pages 13–19, Dortmund, 2009. Technische Universität Dortmund.
- R Dreesen, P Nielsen, and D Lagrou. *Provenance, durability and damage analysis of natural building stones by means of petrographical*

- techniques*. 2006. ISBN 978-1-4020-5076-3. doi: 10.1007/978-1-4020-5077-0{_}29.
- R Dreesen, V Cnudde, M Duser, M De Ceukelare, D Bossiroy, E Groessens, J Elsen, T De Kock, and J Dewanckele. In het voetspoor van Camerman: de opmars van de Franse steen in België. In R P J Van Hees, H De Clercq, and Quist W J, editors, *Stenen van binnen, stenen van buiten: natuursteen in de jonge bouwkunst*, pages 33–63, Delft, 2012. Delftdigitalpress.
- C M Filomena, J Hornung, and H Stollhofen. Assessing accuracy of gas-driven permeability measurements: a comparative study of diverse Hassler-cell and probe permeameter devices. *Solid Earth*, 5(1):1–11, 2014. doi: 10.5194/se-5-1-2014.
- B Fobe. Voorkomen, samenstelling en gebruik van de Balegemse steen. *Bulletin de la Société belge de Géologie*, 99(2):167–170, 1990.
- G Fronteau, C Thomachot-Schneider, E Chopin, V Barbin, D Mouze, and A Pascal. Black-crust growth and interaction with underlying limestone microfacies, 2010.
- N Ghedini, C Sabbioni, and M Pantani. Thermal analysis in cultural heritage safeguard: an application. *Thermochimica Acta*, 406(12):105–113, 2003. doi: [http://dx.doi.org/10.1016/S0040-6031\(03\)00224-7](http://dx.doi.org/10.1016/S0040-6031(03)00224-7).
- C M Grossi, R M Esbert, F Diaz-Pache, and F J Alonso. Soiling of building stones in urban environments. *Building and Environment*, 38(1):147–159, 2003. doi: Pii0360-1323(02)00017-310.1016/s0360-1323(02)00017-3.
- Mervat S Hassan and Hassan M Baioumy. Structural and chemical alteration of glauconite under progressive acid treatment. *Clays and Clay Minerals*, 54(4):491–499, 2006. doi: 10.1346/ccmn.2006.0540410.
- O Heiri, A F Lotter, and G Lemcke. Loss on ignition as a method for estimating organic and carbonate content in sediments: reproducibility and comparability of results. *Journal of Paleolimnology*, 25(1):101–110, 2001.
- T Hosono, E Uchida, C Suda, A Ueno, and T Nakagawa. Salt weathering of sandstone at the Angkor monuments, Cambodia: identification of the origins of salts using sulfur and strontium isotopes. *Journal of*

- Archaeological Science*, 33(11):1541–1551, 2006. ISSN 03054403. doi: 10.1016/j.jas.2006.01.018.
- ICOMOS-ICS. Illustrated glossary on stone deterioration pattern, 2008. URL http://international.icomos.org/publications/monuments{_}and{_}sites/15/pdf/Monuments{_}and{_}Sites{_}15{_}ISCS{_}Glossary{_}Stone.pdf.
- R A Ketcham and W D Carlson. Acquisition, optimization and interpretation of X-ray computed tomographic imagery: applications to the geosciences. *Computers & Geosciences*, 27(4):381–400, 2001. doi: 10.1016/s0098-3004(00)00116-3.
- J Kim, C H Lee, R H Kim, and E Je Shin. Characterization of White and Black Deposits on the Surface of Korean Stone Cultural Heritages. *Microscopy and Microanalysis*, 19(SupplementS5):167–171, 2013. doi: 10.1017/S1431927613012580.
- J A Larbi, R P J van Hees, and S Naldini. Microscopic study of weathering of white Flemish stone from the monumental Church of Our Lady in Breda, The Netherlands. *Heron*, 48(3):13, 2003.
- P Maravelaki-Kalaitzaki and G Biscontin. Origin, characteristics and morphology of weathering crusts on Istria stone in Venice. *Atmospheric Environment*, 33(11):1699–1709, 1999. doi: [http://dx.doi.org/10.1016/S1352-2310\(98\)00263-5](http://dx.doi.org/10.1016/S1352-2310(98)00263-5).
- M Mashlan, P Martinec, J Kaslik, E Kovarova, and J Scucka. Mossbauer Study of Transformation of Fe Cations during Thermal Treatment of Glauconite in Air. In J Tucek and L Machala, editors, *Mossbauer Spectroscopy in Materials Science - 2012*, volume 1489, pages 169–173. Amer Inst Physics, Melville, 2012. ISBN 0094-243X 978-0-7354-1101-2. doi: 10.1063/1.4759486. URL [GotoISI://WOS:000311909900020](http://www.isinet.org/WOS:000311909900020).
- B Masschaele, M Dierick, D Van Loo, M N Boone, L Brabant, E Pauwels, Veerle Cnudde, and Luc Van Hoorebeke. HECTOR: A 240kV micro-CT setup optimized for research. *11th International Conference on X-Ray Microscopy (Xrm2012)*, 463, 2013. doi: [Unsp01201210.1088/1742-6596/463/1/012012](https://doi.org/10.1016/j.xrm.2012.11.012).
- B C Masschaele, V Cnudde, M Dierick, P Jacobs, L Van Hoorebeke,

- and J Vlassenbroeck. UGCT: New x-ray radiography and tomography facility. *Nuclear Instruments & Methods in Physics Research Section a-Accelerators Spectrometers Detectors and Associated Equipment*, 580 (1):266–269, 2007. doi: 10.1016/j.nima.2007.05.099.
- T Richard, F Dagrain, E Poyol, and E Detournay. Rock strength determination from scratch tests. *Engineering Geology*, 147:91–100, 2012. doi: 10.1016/j.enggeo.2012.07.011.
- C Rodriguez-Navarro and E Sebastian. Role of particulate matter from vehicle exhaust on porous building stones (limestone) sulfation. *Science of the Total Environment*, 187(2):79–91, 1996. doi: 10.1016/0048-9697(96)05124-8.
- C Sabbioni, G Zappia, and G Gobbi. Carbonaceous particles and stone damage in a laboratory exposure system. *Journal of Geophysical Research: Atmospheres*, 101(D14):19621–19627, 1996. doi: 10.1029/95jd03755.
- G W Scherer. Theory of drying. *Journal of the American Ceramic Society*, 73(1):3–14, 1990. doi: 10.1111/j.1151-2916.1990.tb05082.x.
- S Siegesmund, A Torok, A Hupers, C Muller, and W Klemm. Mineralogical, geochemical and microfabric evidences of gypsum crusts: a case study from Budapest. *Environmental Geology*, 52(2):369–381, 2007. doi: 10.1007/s00254-006-0588-3.
- B J Smith, A Török, J J McAlister, and Y Megarry. Observations on the factors influencing stability of building stones following contour scaling: a case study of oolitic limestones from Budapest, Hungary. *Building and Environment*, 38(9-10):1173–1183, 2003. doi: 10.1016/s0360-1323(03)00076-3.
- M Steiger. Crystal growth in porous materials - I: The crystallization pressure of large crystals. *Journal of Crystal Growth*, 282(3-4):455–469, 2005. doi: 10.1016/j.jcrysgr.2005.05.007.
- Á Török. Surface strength and mineralogy of weathering crusts on limestone buildings in Budapest. *Building and Environment*, 38 (910):1185–1192, 2003. doi: [http://dx.doi.org/10.1016/S0360-1323\(03\)00072-6](http://dx.doi.org/10.1016/S0360-1323(03)00072-6).
- Á Török and R Prikryl. Current methods and future trends in testing, durability analyses and provenance studies of natural stones used in

- historical monuments. *Engineering Geology*, 115(3-4):139–142, 2010. doi: 10.1016/j.enggeo.2010.07.003.
- Á Török and N Rozgonyi. Morphology and mineralogy of weathering crusts on highly porous oolitic limestones, a case study from Budapest. *Environmental Geology*, 46(3):333–349, 2004. doi: 10.1007/s00254-004-1036-x.
- Á Török, T Licha, K Simon, and S Siegesmund. Urban and rural limestone weathering; the contribution of dust to black crust formation. *Environmental Earth Sciences*, 63(4):675–693, 2011. doi: 10.1007/s12665-010-0737-6.
- V Vergès-Belmin. Pseudomorphism of gypsum after calcite, a new textural feature accounting for the marble sulphation mechanism. *Atmospheric Environment*, 28:295–304, 1994.
- J Vlassenbroeck, M Dierick, B Masschaele, V Cnudde, L Van Hoorebeke, and P Jacobs. Software tools for quantification of X-ray microtomography. *Nuclear Instruments & Methods in Physics Research Section a-Accelerators Spectrometers Detectors and Associated Equipment*, 580(1):442–445, 2007. doi: 10.1016/j.nima.2007.05.073.
- M Voorn, U Exner, and A Rath. Multiscale Hessian fracture filtering for the enhancement and segmentation of narrow fractures in 3D image data. *Computers & Geosciences*, 57:44–53, 2013. doi: 10.1016/j.cageo.2013.03.006.
- P A Warke, J M Curran, A V Turkington, and B J Smith. Condition assessment for building stone conservation: a staging system approach. *Building and Environment*, 38(9-10):1113–1123, 2003. doi: 10.1016/s0360-1323(03)00085-4.
- J Weber, S Beseler, and K Sterflinger. Thin-section microscopy of decayed crystalline marble from the garden sculptures of Schoenbrunn Palace in Vienna. *Materials Characterization*, 58(11-12):1042–1051, 2007. doi: 10.1016/j.matchar.2007.04.014.
- F G Xu, J Tang, and S X Gao. Characterization and origin of weathering crusts on Kylin carved-stone, Kylin countryside, Nanjing - A case study. *Journal of Cultural Heritage*, 11(2):228–232, 2010. doi: 10.1016/j.culher.2009.11.006.

G Zappia, C Sabbioni, C Riontino, G Gobbi, and O Favoni. Exposure tests of building materials in urban atmosphere. *Science of the Total Environment*, 224(1-3):235–244, 1998. doi: 10.1016/s0048-9697(98)00359-3.

7

A pore-scale study of freeze-thaw processes in Lede stone and Noyant limestone

Frost action is an effective weathering process for porous media in cold and humid environments. Even in the warm-temperated humid climate of Belgium, there are annually sufficient rainy and frost days for frost action to take place (see section 3.4). As such, historical natural stones have been subjected to numerous freeze-thaw cycles and will be subjected to more in the future. Although Lede stone has a good performance (section 3.4), some damage can occur due to frost cycling (section 5.8). This chapter explores the pore-scale processes that occur when water crystallizes to ice inside the pore network of building stones. It is partly based on De Kock et al. (2015), where Dr. Marijn Boone and Dr. Derluyn assisted in data acquisition and processing, Thomas De Schryver designed the custom μ CT freezing stage, Jeroen Van Stappen in the fracture analysis, Dr. Bert Masschaele in the hardware and software developments and Prof. Dr. Geert De Schutter provided lab facilities for stone characterization.

7.1 Introduction

Freeze-thaw cycling can affect the properties of porous building materials such as rock (e.g. Matsuoka and Murton, 2008) and concrete (e.g. Pigeon et al., 1996). It is currently accepted that ice crystallization pressure is responsible for damage and crack growth in soil, rock and concrete (Everett, 1961; Walder and Hallet, 1985, 1986; Scherer, 1999; Steiger, 2005a,b). Here, pore water is constrained within the pore network and crystallization occurs through heterogeneous nucleation when the temperature drops below the freezing point. The pressure under which water is contained in the pores results in a reduction of the freezing point as a function of decreasing pore size. Hence, water can be supercooled within the pore network at temperatures below 0 °C. Assuming a spherical crystal with radius equal to a given pore radius, the depressed freezing point can be calculated by equation 7.1 (Camuffo, 1998) and the corresponding crystallization pressure of this crystal is given by equation 7.2 (Scherer, 1999).

$$T_f = -273 \frac{2\gamma}{r\rho L} \quad (7.1)$$

$$P_{cr} = \frac{-2\gamma \cos\theta}{r} \quad (7.2)$$

where γ is the surface tension at the ice-water interface, r is the radius of the spherical ice crystal, ρ is the ice density, L the latent heat of fusion and θ the contact angle between the crystal and the pore wall. In laboratory, the rate of cooling, which creates a temperature gradient, as well as sample size, which relates to the probability of having a good nucleation site, affect the freezing temperature (Ruedrich and Siegesmund, 2007; Valenza and Scherer, 2006).

The crystallization pressure exerted by a growing ice crystal under confined conditions in contact with a supercooled liquid is determined by the entropy of the system, the molar volume of ice, the freezing temperature and the temperature of the supercooled liquid film. Based on a thermodynamic approach, Everett (1961) illustrated that crystallization will start in the larger pores, because of a more favorable chemical potential for larger ice crystals. The pressure will build up when the crystal grows against the constraints of a pore wall, from which it is

separated by a supercooled liquid nano-film. Eventually, damage will occur when the resulting stress exceeds the rock strength, i.e. when the stress field is large enough to affect a strength-controlling flaw (Scherer, 1999). In the example of sedimentary rocks as used in this study, such flaws can be features related to the depositional environment and rock texture (Nicholson and Nicholson, 2000). Applying poromechanics, the crystallization-induced macroscopic stress σ is related to the crystallization pressure P_{cr} according to equation 7.3 and failure occurs when equation 7.4 is fulfilled (Coussy, 2006; Espinosa-Marzal et al., 2011).

$$\sigma \approx bS_c P_{cr} \quad (7.3)$$

$$\sigma > \frac{\sigma_z}{\sqrt{3(1-2\nu)}} \quad (7.4)$$

where b is the Biot coefficient, S_c the ice crystal saturation degree (i.e. the volume fraction of ice crystals in the pores), σ_z the tensile strength and ν the Poisson's ratio. In addition to temperature, the water saturation of the pore network plays an important role in freeze-thaw weathering (Chen et al., 2004). Higher saturation implies a higher risk for damage or residual strain (Ruedrich and Siegesmund, 2007), as with a higher degree of saturation, a larger volume fraction of the body will be exposed to crystallization pressure.

The prediction of the frost susceptibility of a rock in a certain climate, however, stays a delicate topic. In addition, climate change can have a future impact on the intensity of freeze-thaw weathering (Grossi et al., 2007). Materials which have proven to be durable in certain regions, might respond differently and less durable when imported into other climatic regions (Cnudde et al., 2013). Laboratory freeze-thaw testing always seems advisable for building materials. Nevertheless, the correlation between laboratory tests and natural environments is far from easy (Ingham, 2005). The outcome of laboratory tests should be interpreted with care (Martinez-Martinez et al., 2013). More than an absolute conclusion, the outcome is to be compared with stones whose historical performance is well known in both laboratory and natural environments.

7.2 Pore-scale freeze-thaw experiments with EMCT on Noyant limestone

In the last decade μ CT has been explored or suggested as a tool to achieve quantitative information on the microstructural deformation caused by freeze-thaw cycles (Ruiz de Argandona et al., 1999; McAllister et al., 2013). Indeed, recent advances in laboratory μ CT open new perspectives in the pore-scale study of materials (Cnudde and Boone, 2013), processes (Wildenschild and Sheppard, 2013; Boone et al., 2014b) and decay (Dewanckele et al., 2012; Derluyn et al., 2014). Dewanckele et al. (2013) studied the frost damage on a limestone at the micro-scale by employing μ CT on a sample subjected to a laboratory scaled freeze-thaw test. The main advantage of laboratory μ CT is its non-destructive, 3D nature, allowing to monitor the spatial impact of processes on the microstructure of the material. However, a drawback for studying dynamic processes is that the data acquisition is considered static, because the total duration of a scan is typically in the order of (an) hour(s). Recent developments on the environmental μ CT (EMCT) at Ghent University (Dierick et al., 2014), however, overcome this limitation reducing the data acquisition speed below one minute (Bultreys et al., 2015). The EMCT was used to study the pore-scale dynamics related to ice crystallization under in-situ freeze-thaw cycles. This is done by performing time-lapse freeze-thaw series as well as dynamic imaging of the freezing process using the EMCT. Because of the good resistance of Lede stone to laboratory freeze-thaw weathering, an alternative stone -Noyant limestone- was used for the fundamental study of ambient freeze-thaw weathering with μ CT.

7.2.1 Material

Noyant limestone is a miliolid limestone from the Eocene Calcaire Grossier Formation in the Paris Basin (France), quarried in Noyant/Septmonts. This bioclastic rock with a wackestone to packstone texture is mainly composed of marine organisms, mainly *Miliolina* forams, within a micrite matrix. It contains low amounts of fine quartz grains and glauconite. The presence of the *Orbitolites complanatus*, a discoidal planispiral benthic foram, is remarkable for later results in this experiment. In cross section, this foram has a diameter of several millimeters, and its test contains chambers which are pores with a size of

20–60 μm . The rock has a high porosity of approximately 35 vol.%. Data of the pore size distribution was recovered from mercury intrusion porosimetry measurements from a previous study (Dewanckele et al., 2013). 90 % of the pores have radii below 8.1 μm with a frequency maximum at 1.3 μm . The 10 % largest pores show a frequency maximum around a pore radius of 102.7 μm . These are interconnected by the 90 % of smaller pores. The major fraction of porosity thus lies within the range of capillary pores (0.1–1000 μm). This rock was chosen for this study from a pragmatic view; it has a lot of capillary pores, a bimodal pore size range, a low strength. Although it has a higher porosity than Lede stone, it has some comparable textural components, such as similar foraminiferal assemblage and micrite.

7.2.2 Methods

The EMCT is a gantry-based system capable of acquiring μCT scans in the order of one minute. Hence, the sample remains stationary during the scan, so that any structural change to the sample due to dynamic processes occurring at a time scale smaller than one minute are considered to be negligible. For single scans, the Hamamatsu L9181-2 X-ray tube was operated at 65 kV and a power of 13 W and 1401 projections were taken over 360 $^\circ$ with an exposure time of 100 ms with the Teledyne Dalsa Xineos-1313 high-speed flat-panel detector. A 20.4 μm voxel resolution is obtained after reconstruction with XRE reconstruction software (www.xre.be).

An added advantage of the gantry-based EMCT system is the possibility to incorporate in situ devices to condition the sample's environment or state, e.g. humidity, stress, strain, temperature, etc., with no restriction to external wiring, which would normally be wound up during the sample's rotational movement in any other conventional μCT scanner. In this case the EMCT was upgraded with a custom-made freezing stage (Fig. 7.1) which can control and monitor a sample's temperature with an accuracy of ± 0.3 $^\circ\text{C}$ (De Schryver et al., 2014). The actively cooled volume, which measures 30 mm from top to bottom and 14 mm in diameter, is encapsulated by aluminum to ensure a uniform temperature distribution (down to -20 $^\circ\text{C}$). This aluminum encapsulation also filters out the low energy X-rays that would normally be attenuated by the sample itself and cause beam hardening artefacts in the CT reconstructions. The cylindrical

samples have a diameter of 9 mm and are not confined within the 14 mm diameter cooling volume. A temperature sensor is placed in contact with the bottom of the sample. Furthermore, finite element simulations were performed with QuickField to model dynamic heat transfer throughout the complete freezing stage assembly including the sample. According to these simulations the temperature difference between the center and the edge of the sample should not exceed more than 0.2 °C at the time the temperature reaches -9.7 °C.



Figure 7.1: Photo of the custom designed cooling stage for μ CT (De Schryver et al., 2014).

The dynamics of both the capillary water uptake and the freezing process were monitored at the EMCT through a continuous scanning protocol. During freezing, 14400 projections with a 100 ms exposure time were taken over a total period of 24 minutes, while the gantry was rotating and while operating the X-ray tube at a tube voltage of 65 kV and a power of 14.3 W. In total, 18 scans of each 800 projections were performed, resulting in a reconstructed voxel size of 20.4 μ m. The 3D CT images were matched with the DataViewer software package (Bruker microCT), which is based on a 3D attenuation rigid body registration algorithm.

Cylindrical samples of 9 mm diameter were capillary imbibed and sealed in Al-foil to maintain wet conditions throughout the experiment. Overnight, the samples were conditioned by capillary imbibition. The

duration of freeze-thaw cycles was shortened to facilitate scanner operations. Two types of cycles were performed, one with cooling to $-5\text{ }^{\circ}\text{C}$ and one with cooling to $-15\text{ }^{\circ}\text{C}$ (Fig. 7.2). The cycles were looped every 3h, with freezing temperatures set for 2h, followed by 1h of thawing at $20\text{ }^{\circ}\text{C}$. The cell is cooled at a rate of $\pm 2.5\text{ }^{\circ}\text{C}/\text{min}$. A time-lapse scan was performed at 1 h (freezing) and 2.5 h (thawing) after the start of each loop. Continuous scanning was performed during the cooling stage.

The capillary water uptake was analyzed by calculating the average gray value of the consecutive slices from bottom to top in 16 different time steps. As the settings of the experiment remained constant, the increase in gray value reflects increasing water saturation. This is valid for all 16 time steps, with the exception of time step 7 where aberrant values might have been caused by fluctuations in X-ray intensity during the scan. The image analysis of the freeze-thaw experiment was done with Avizo 3D software. Fractures at the edge of resolution were segmented using a Multiscale Hessian fracture filtering plugin for Fiji (Voorn et al., 2013).

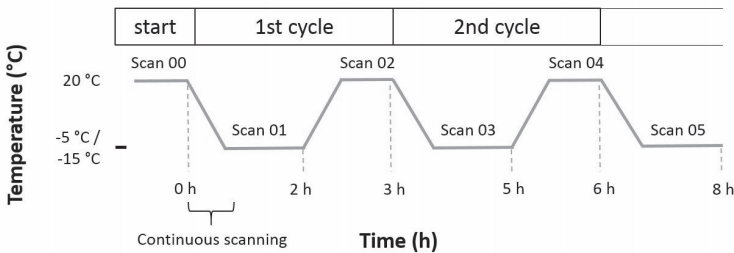


Figure 7.2: Visual representation of the freeze-thaw cycles and the moments of scanning.

Scanning Electron Microscopy (SEM) images were obtained with a FEI Quanta 200F on gold-coated samples. Total porosity (P_o) and bulk density (ρ) were determined according to the European standard (EN) 1936 (1999) using hydrostatic weighing. Samples, sized $50\text{ mm} \times 50\text{ mm} \times 50\text{ mm}$, were saturated with distilled water at a 98.66 kPa vacuum. Water absorption by total immersion (W) was obtained by progressive immersion within a total of 48 h and the saturation coefficient (S) was calculated as the ratio of total water content under atmospheric versus vacuum condition. Capillary water absorption was measured according to EN 1925 (1999) on cubic samples of $50\text{ mm} \times 50\text{ mm} \times 50\text{ mm}$ by putting them on supports in demineralized water. The capillary coefficient

(C) corresponds to the slope for amount of water uptake as a function of surface and the square root of time. The higher the coefficient, the larger the amount of initial water uptake for a given time period. The Barret-Joyner-Halenda (BJH) pore size distribution < 40 nm was measured with nitrogen adsorption using a Micromeritics TriStar 3000. Samples were prepared overnight at $40\text{ }^{\circ}\text{C}$ in a Micromeritics VacPrep 061.

The unconfined uniaxial compressive strength (UCS), the flexural strength (R_{tf}) and the Brazilian tensile strength (BTS) were measured with a Walter-Bai Digi Con 2000 at the Magnel Laboratory for Concrete research (Ghent University). Samples of $40 \times 40 \times 160$ mm were loaded in the center until rupture to determine R_{tf} . From the resulting halves, $40 \text{ mm} \times 40 \text{ mm} \times 40 \text{ mm}$ samples were subjected to UCS measurements with the same device. UCS was also measured on samples that underwent a specific number of freeze-thaw cycles (N_c). BTS was measured on 40 mm diameter cores by applying a loading force diametrically across the circular cross section. Ultrasound velocity (US) was measured according to EN 14579 (2004) using 55 KHz transducers.

7.2.3 Petrophysical properties

The properties of Noyant limestone are listed in Table 7.1. The BJH pore size distribution shows a peak around 4 nm. Based on SEM observations (Fig. 7.3), these nanometric pores are expected within the test of the forams. The pore sizes measured by nitrogen adsorption are only a fraction of the total pore network, which has a primary distribution around $1.3\text{ }\mu\text{m}$, related to interparticular porosity of the lime mud matrix. The fraction of largest pores $> 8.1\text{ }\mu\text{m}$ are related to test chambers of the forams.

The rock is highly absorbing, with a capillary coefficient of $83.3\text{ g m}^{-2}\text{ s}^{-1/2}$. This is not surprising as the major fraction of pore sizes lies within the range of capillary pores. The high absorption rate illustrates the good connectivity between the larger capillary pores. 71% of the pore space is saturated with water after progressive immersion of 48 h. The remaining 29% of the pore space remains unsaturated because of the combined presence of trapped air and relatively small pores ($< 1\text{ }\mu\text{m}$) in which the capillary rise is slower and which thereby block the access to some of the larger pores. Special attention is given to the presence of O .

ρ	$1739 \pm 12 \text{ kg/m}^3$
P_o	$34.81 \pm 0.53 \text{ vol.}\%$
Modal pore radius 1	$1.3 \text{ }\mu\text{m}$
Modal pore radius 2	$102.7 \text{ }\mu\text{m}$
10 % intrusion pore radius	$8.1 \text{ }\mu\text{m}$
W	$15.45 \pm 0.38 \text{ wt}\%$
S	0.071 ± 0.01
C	$83.3 \pm 5.7 \text{ g m}^{-2} \text{ s}^{-1/2}$
US	$2571 \pm 21 \text{ m/s}$
UCS	$13.3 \pm 1.0 \text{ MPa}$
R_{tf}	$2.6 \pm 0.20 \text{ MPa}$
BTS	$0.916 \pm 0.107 \text{ MPa}$

Table 7.1: Results for bulk density, effective porosity, atmospheric absorption, saturation degree, capillary coefficient, ultrasound velocity, uniaxial compressive strength, flexural strength, Brazilian tensile strength of Noyant limestone for a minimum of six samples with exception of MIP measured on one sample.

complanatus, whose discoid test with internal pores results in the alignment of capillary pores in the plane of this forams test.

The UCS (13.3 MPa), R_{tf} (2.6 MPa) and BTS (0.92 MPa) show values of low strength rocks. Especially tensile strength is important, as crystallization pressure exerts a tensile stress to the pore walls.

7.2.4 Capillary water absorption with μCT

The sample has a high capillary water uptake, which was investigated at the pore-scale using μCT . Figure 7.4 shows the height of the water front as a function of time, which is reflected by the progressive elevation of gray level with slice height in function of time. Moreover, also the continuous saturation can be seen to increase in gray value for a specific slice as a function of time. The water distribution in the rock is visualized for every time step by differential imaging (Boone et al., 2014a). This shows that the water front is not flat, but that the water follows preferential flow paths. These preferential flow path are located within the forams *O. complanatus*. The pores of its test chambers are larger than the surrounding pores within the matrix, resulting in a larger capillary suction velocity. In addition, these pores are aligned and appear to be well connected.

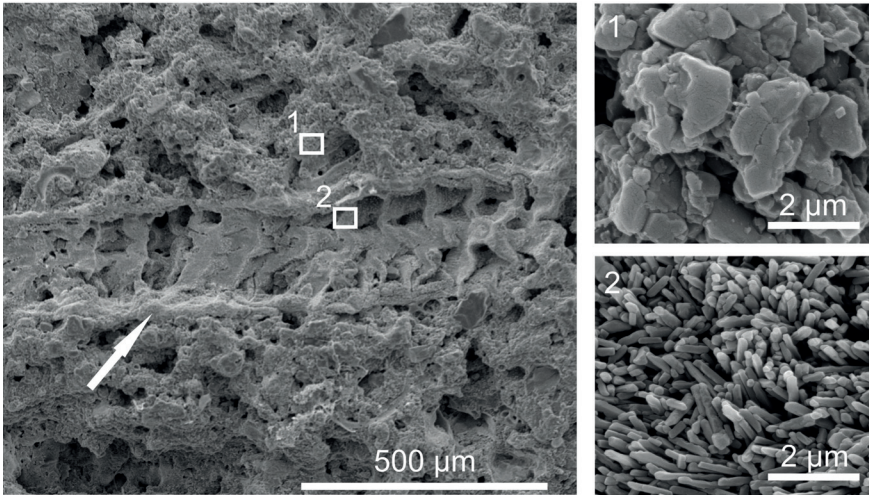


Figure 7.3: SEM images of *O. complanatus* foram indicated by the arrow with large cavities, surrounded by a microporous lime mud matrix (close up 1). The test of the foram consists of calcite microcrystals (close up 2) and is nanoporous.

7.2.5 Pore-scale freeze-thaw cycling

Freeze-thaw cycling with freezing temperatures down to $-15\text{ }^{\circ}\text{C}$ results in the development of fractures throughout the completion of 18 scans, i.e. 9 cycles (Fig. 7.5). Two things can be noted visually: (i) the number of fractures increases with the number of cycles and (ii) the volume of the fractures is substantially higher during freezing periods compared to the subsequent thawing periods, when the fractures even close during the first stages.

The fractures are segmented and analyzed with the same parameters so that they can directly be compared. The only exception on this, is the initial fracture in scan 3, where the partial volume effect plays a large role in the outcome of the segmentation. Therefore, lower grey-scale threshold values had to be applied during image analysis. The total fracture size (not its opening) is measured by their equivalent diameter (ED). This parameter represents the diameter of a sphere with the same total volume as the measured object, in this case the segmented fracture. The evolution of the (ED) of the above discussed fracture for 17 successive scans is given in Figure 7.6.

The first fracture appears during the second cycle (scan 3), and grows

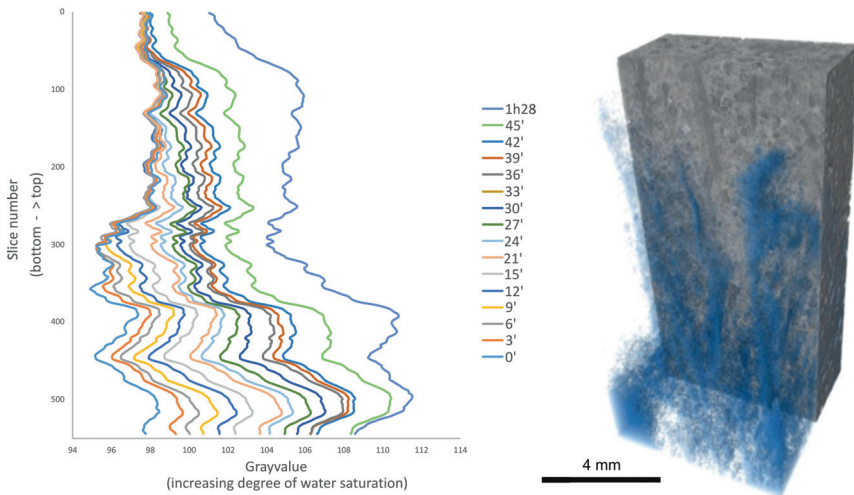


Figure 7.4: Left: graph with temporal evolution (in minutes, indicated in legend) of the partial grey value (ordinate) during capillary uptake. The increase in gray value is the result of water progressively saturating the pore system in time and height. Right: visualization of water uptake through preferential flow paths within the rock; the rock rendering has been partially cut, showing the location of water in blue at a specific time.

during subsequent freezing periods (scan 5 and 7). It must be noted that the fracture might have initiated in the first cycle, being too small to detect, i.e. much smaller than the voxel size. During the first thawing periods (scan 4, 6 and 8), the fracture closes. After the 5th freezing period (scan 9), the fracture reaches a critical volume what results in residual strain. During subsequent thawing, there is only partial closure of the fracture, dividing it in two smaller fracture planes, represented by the dashed lines in Figure 7.6. During the 6th cooling stage (scan 11), these residual fractures rejoin and the total fracture grows with the appearance of two new fracture volumes. In the subsequent cycles, these two fracture planes show the same dynamics of the major fractures: growing in volume during freezing periods and (partial) closing during thawing. In the 8th cooling stage (scan 15), the aperture grows above the Hessian detection limit (Voorn et al., 2013) and this volume connects to the largest fracture plane. The fractures have a specific relation with the rock texture. Namely, the initial fracture plane is strongly aligned with the test of the foram *O. complanatus*. Also at the top of the sample, the fracture develops in association with this foram (Fig.7.5).

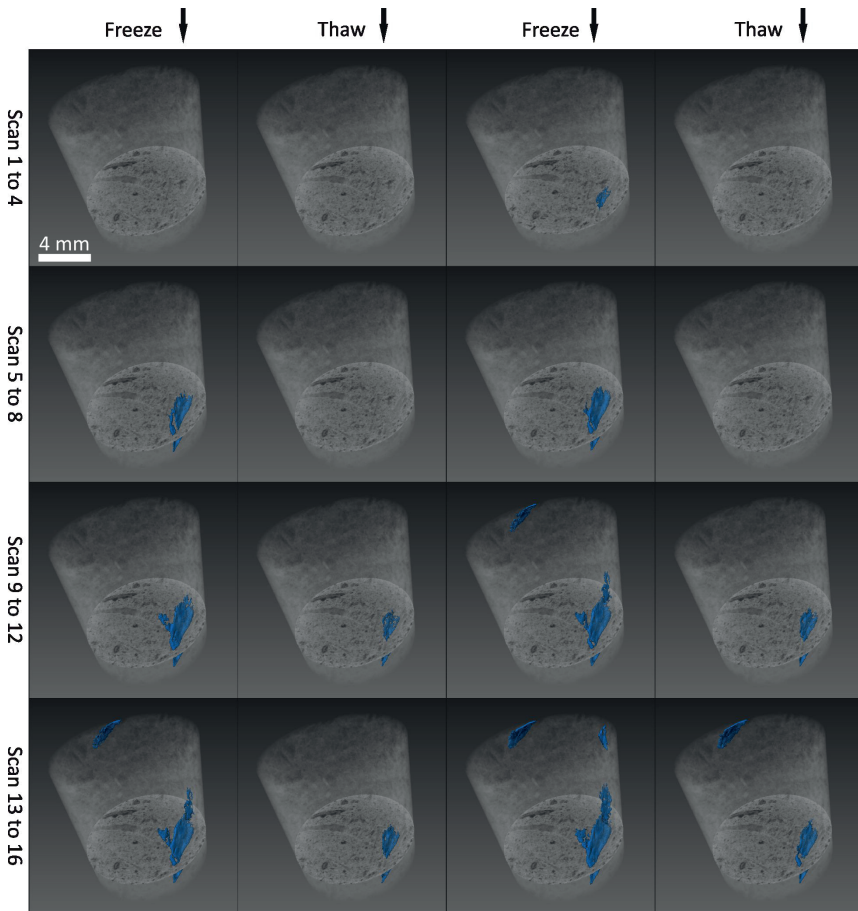


Figure 7.5: Chronological renderings of the scans: sample volume transparent, 2D slice in gray-scale and fracture volume in blue showing the opening and closing of the fractures during subsequent freeze-thaw cycles. The first fracture can be segmented in scan 3, which was performed during the freezing period of the 2nd cycle. Its growth and the development of new fractures is visible in subsequent freezing periods.

With the same number of cycles, no clear damage occurs when the samples are subjected to freezing temperatures of -5°C . The nature of this strong difference with freezing to -15°C can be deduced from Figure 7.7. This graph displays the readout temperature of the sensor placed in contact with the rock sample in function of time. For both freezing temperatures, the graph shows a cooling stage, with an undershoot at the set freezing temperature, followed by a stable trend where the freezing

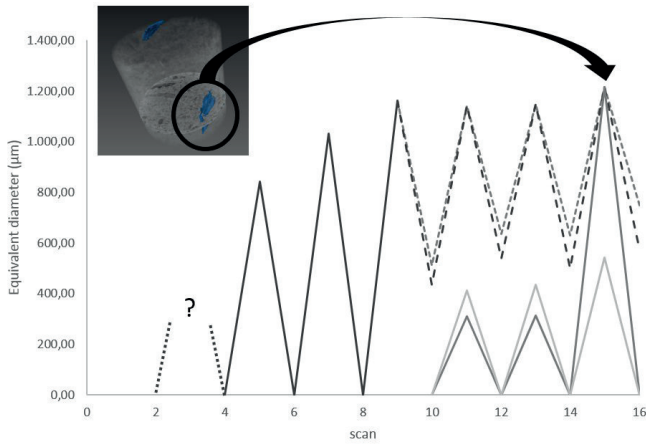


Figure 7.6: Equivalent diameter of objects in the lower fracture zone for a given scan. Even scan numbers represent the thawing stage, odd scan numbers the freezing stage. Different lines represent co-existing fracture planes, separated by apertures below the Hessian detection limit or by partial closure. The fracture opens and grows during freezing stages and (partially) closes during subsequent thawing stages. The initiating fracture in scan 3 was analyzed with different parameters.

temperature is maintained. In graph b, which represents the cooling to $-15\text{ }^{\circ}\text{C}$, the cooling stage is interrupted by an exothermal peak, considered here as a proxy for ice crystallization, which initiates at a cooling temperature of $-9.7\text{ }^{\circ}\text{C}$. Such an exotherm is absent when cooling to $-5\text{ }^{\circ}\text{C}$.

In addition to the time-lapse scans during consecutive freeze-thaw cycles, continuous scanning during the cooling stage has the significant advantage that the sample can be visualized at any chosen period in time, i.e. the period needed to obtain 360° projections. In this case, this period amounted 80 seconds. This allows rendering and analyzing the rock 80 seconds before and 80 seconds after the observation of the exotherm. As illustration, Figure 7.7 displays two slices of this situation during the freezing stage of the 9th cycle; which is the freezing stage just prior to the acquisition of scan 17, subsequent to the scans displayed in Figure 7.5. The latter figure illustrates the presence of a dynamic fracture at the start of the cooling stage prior to scan 17. Together with the occurrence of the exothermal peak, there is an opening of the fracture, illustrated in the slices of Figure 7.7, which is also

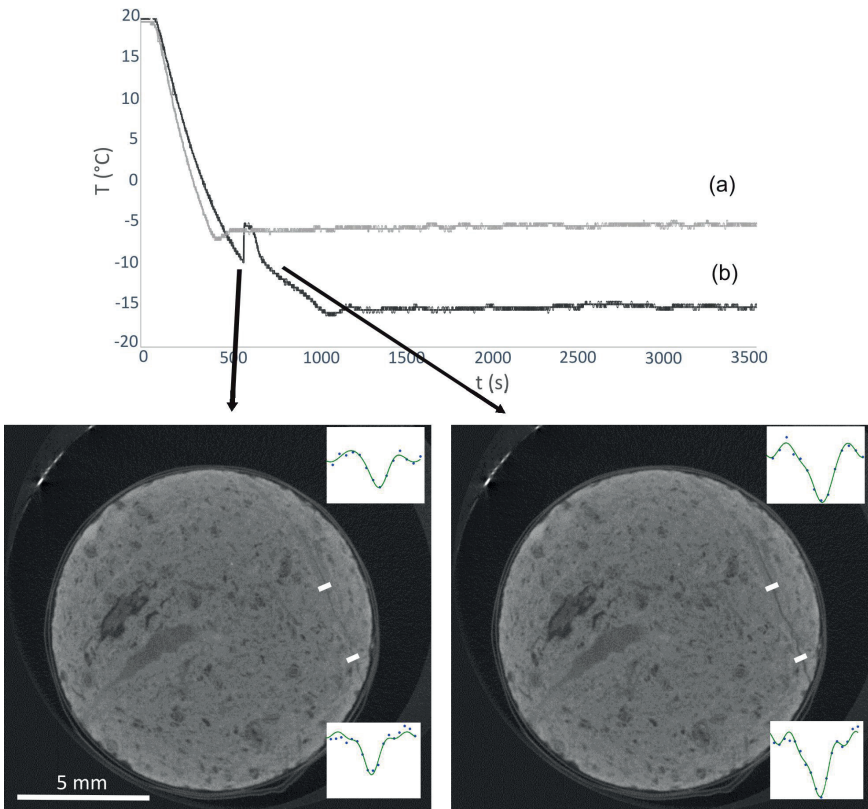


Figure 7.7: Readout of the temperature sensor in function of time, with set point -5°C (a) and -15°C (b). A small undershoot is visible after reaching the set point temperature. Note the sudden increase in (b) at $t = 547$ s after the start of the cooling stage, caused by the release of latent heat upon ice crystallization at a temperature of -9.7°C . This is not observed in (a), suggesting no crystallization takes place and the water is only supercooled within the pores. Below, the reference slice is reconstructed for the situation just before and just after crystallization, showing the opening of the existing fracture. Graphical insets of FWHM have the same scale.

apparent from the Full Width Half Maximum (FWHM) (Mazumder et al., 2006; Ketcham et al., 2010) values extracted from the transversal crack profiles. Before the occurrence of the exothermal peak, the FWHM of the fracture measures $57.4 \pm 13.4 \mu\text{m}$ in the center and $67.2 \pm 20.1 \mu\text{m}$ near the samples edge. After the exothermal peak, the FWHM measures $69.2 \pm 11.3 \mu\text{m}$ and $82.6 \pm 19.8 \mu\text{m}$ respectively. Hence, the fracture dynamics observed in Figure 7.5 coincide with the exothermal peak and they occur at

a sudden moment in time.

7.2.6 Discussion

Experimental section

Hall and André (2003) already stated the importance of studying processes on the micro-scale to understand macro-scale behavior. The experimental setup in the EMCT is designed to study the damage observed in macro-scale laboratory freeze-thaw experiments at the pore-scale level with μ CT. Therefore the samples were downsized to be compatible with the design of the μ CT system. A lower sample size allows for a higher resolution, but this compromises the representative volume of the sample with respect to its texture and the freeze-thaw conditions. It was opted to use samples of 9 mm diameter. At its lower limits, this is almost tenfold the size of the largest capillary pores, which provides a representative capillary pore network within the sample. At the upper size limit, the total diameter of sample plus encapsulation and isolation permits a maximal resolution close to 20 μ m, related to the scanner setup. The experiment is cyclic with reference to EN 12371 (2010) and no pre-existing cracks were induced or present in the sample. The freezing temperatures were chosen at -5 °C and -15 °C following the temperature range of Walder and Hallet (1985). Because of the restricted sample size, the sample can be regarded as a closed system, with limited water available. The samples were capillary saturated with water, meaning that approximately 71 % of the pore space was filled. This is relevant for natural systems which contain water by capillary rise. The freezing is omnidirectional, which means that at any point within the rock, the freezing front propagates inwards from several (the nearest) surfaces, resulting in a low modeled temperature difference within the sample. Hence, the water is forced to freeze in situ, with water exchange being limited between adjacent smaller and larger pores.

In this study, the ice crystallization exotherm was recorded at a temperature of -9.7 °C. This proves the presence of water that actually froze and crystallized to ice. Ruedrich and Siegesmund (2007) measured temperatures of -4 °C to -7 °C for ice crystallization in porous, capillary water-saturated rocks in laboratory tests; Hall (2006) illustrated freezing temperatures of -3 °C to -5.9 °C in field measurements. The cooling in this experiment was fast, being 2.5 °C/min, but the temperature difference

in the sample is estimated to be less than 0.2 °C. According to Sun and Scherer (2010), ice forms at lower temperatures in smaller samples because the probability of having a good nucleation surface decreases with sample volume. No exotherm was recorded when cooling to -5 °C and maintaining this temperature, indicating that the water remained supercooled because it lacks a nucleation site.

Continuous scanning shows that the fracture dynamics coincide with the occurrence of the exotherm. Therefore this decay is related to the moment of ice crystallization and is thus the expression of freeze-thaw decay and not of any synergetic weathering. This process is called ice wedging; the ice crystals push the fracture surfaces apart in equilibrium with the curvature of the water/ice interface at the mouth of adjacent pores (Valenza and Scherer, 2006). This occurs when the mode I stress intensity due to undercooling exceeds the fracture toughness. It is also important to note that the dynamics of fracturing are strictly related to the moment of ice crystallization. No further changes were observed during the entire period when the freezing temperature was maintained. Of course, this experiment is considered as a closed system with no water available from a reservoir external to the freezing site, so when all the water is consumed during crystallization, the pressure build-up stops. The fracturing is most pronounced along the plane of *O. complanatus* tests, which acted as preferential water uptake paths during capillary rise. Therefore, the water saturation is relatively high in the volume fraction of the rock surrounding these forams, exposing it to a higher probability of crystallization.

Future experimental work could be the integration of strain measurements. This is restricted by the current design of the specific freezing stage used and in general by measurement resolution, as strain is expected within a magnitude of $1-10^2$ $\mu\text{m}/\text{m}$, whereas the samples for μCT are constrained in size for optimal scanning resolution. This can be resolved by using long cylinders for strain measurement with small diameters for scanning a specific part.

Theoretical section

Using equation 7.1 with $\gamma = 0.033 \text{ N m}^{-1}$; $\rho = 917 \text{ kg m}^{-3}$; $L = 333550 \text{ J kg}^{-1}$, a freezing temperature of $-9.7 \text{ }^\circ\text{C}$ corresponds to crystallization in pores with a radius of 6 nm or a pore size of 12 nm. In reality, this is a lower value based on the surface tension at the ice-water interface, whereas similarly an upper pore radius of 20.1 nm can be calculated from the surface tension of the ice-vapor interface (0.109 N m^{-1}) (Camuffo, 1998). With the modeled low temperature differences within the sample ($< 0.2 \text{ }^\circ\text{C}$) and the presence of nanometric pores measured with nitrogen adsorption, these values are assumed to be relevant for the entire volume of the sample. This indicates that crystallization did not start within the larger pores, which is more favorable according to equilibrium thermodynamics (Everett, 1961), but within the nanometric pores under transient conditions.

The crystallization pressure can be calculated according to equation 7.2; for both radii $P_{cr} = 10.9 \text{ MPa}$. According to equation 7.3 and 7.4, the critical crystal fraction leading to failure can be calculated for these crystallization pressures. Assuming that the Brazilian tensile strength relates to the true tensile strength in a 2:1 ratio (Siegesmund and Dürrast, 2011) and that Poisson's ratio $\nu = 0.25$, the macroscopic stress σ needed to exceed the failure strain energy according to equation 7.4 is 0.374 MPa . To obtain this resulting stress with the above derived crystallization pressure, a local crystal fraction of 4.3 % is required, assuming a value of 0.8 for the Biot coefficient. This crystal fraction corresponds to 1.5 % of the total stone volume.

The fracturing is most pronounced along the plane of *O. complanatus* test. The fracture develops along the test's edge, where the nanoporous test is connected to the larger test chambers and the microporous network within the surrounding matrix. According to the above calculations, failure occurs when the water is forced to crystallize in the nanometric pores of the test and results in failure when the local crystal fraction accounts for 4.3 % of the pore network. This seems plausible, considering the volume of the foram tests and the relative high degree of water saturation within these parts of the sample ($> 71 \%$, of the pore space). Therefore, the tests of *O. complanatus* act as a primary flaw, as was already observed in previous work (Dewanckele et al., 2013). Another remark is that fractures are located on the outer edge of the foram, with respect to the sample dimensions; thus in the direction pointing towards the freezing front. This is an interesting detail to investigate in the future, as it might be indicative

for locating crystal nucleation.

The dynamic behaviour of fractures is in support of the ice crystallization theory (Scherer, 1999; Steiger, 2005a,b). Surely, fractures form along the flaw when ice is forced to crystallize within similar pores of a specific size. When temperature is raised, the crystallization pressure will be released and indeed, the fracture closes as is observed in Figure 7.5. During the next freezing stage, the pressure build-up re-opens the fracture to close again upon thawing until fatigue results in residual strain after multiple cycles.

The macro-scale freeze-thaw decay is an expression of these pore-scale dynamics. The increase in the capillary coefficient and compressive strength reflects the initiation of fractures which have been clearly demonstrated in 7.5. Water imbibition at atmospheric pressure is sufficient for further freeze-thaw cycling to initiate fractures, which propagate through the rock, leading to cracks and eventually resulting in material loss.

7.3 Freezing induced dilatation of Lede stone

Not only temperature exotherms (Hall, 2006) but also the dilatation of the material (Ruedrich and Siegesmund, 2007) can be used as a proxy for ice crystallization. Ruedrich and Siegesmund (2007); Ruedrich et al. (2011) show that different phases exist in the freezing of water contained within a stone. These phases could be contraction or expansion, related to the thermal dilatation of stone, water, ice, a combination of stone plus water or ice, and to the crystallization of ice. To study the process of ice crystallization in Lede stone, a dilatometric setup was designed in the laboratory.

7.3.1 Material and methods

Three cylindrical subsamples of 20 mm diameter and 50 mm length were drilled from the different microfacies of Ledestone as studied in Chapter 5 (Lf1, Lf2 and Lf3; Fig. 5.2). The samples all had the sample orientation as the tests in Chapter 5, which was perpendicular to their bedding. The experiments at different water saturation degree were performed on the same samples. For 0 % saturation, the samples were oven-dried at 40 °C.

For atmospheric saturation, the samples were oven-dried at 40 °C and subsequently imbibed in water for 48 h. For 100 % saturation, the samples were oven-dried at 40 °C and subsequently imbibed in water under vacuum. To avoid a change in water content and to avoid thermal isolation, the samples were sealed in Al-foil, except at the contact points with the dilatometric setup. The tests were performed in order of saturation, to minimize the potential effect of weathering on the subsequent test. In essence, this means that the first test was performed at 0 % saturation and the last test was performed at 100 % saturation, assuming the potential decay at 0 % saturation and atmospheric saturation is negligible with respect to the potential decay at 100 % saturation. At this point, the samples had undergone only 2 frost cycles, which is assumed to be too low to induce effective damage, based on former experiments.

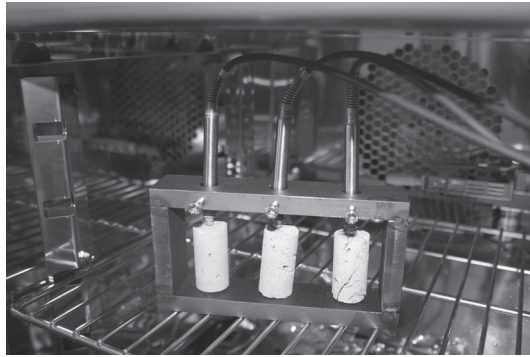


Figure 7.8: Custom dilatometric setup in invar, with an indication of the sample position.

A dilatometric setup was designed to measure the length changes during freeze-thaw cycles in a climatic chamber (Fig. 7.8). This consists of a designed frame in invar (Fe-Ni alloy), to avoid thermal dilatation, with 3 sample positions. The length change was measured by linear variable differential transformer (LVDT) sensors by Solartron Metrology. The length changes were measured by subtracting absolute positions, in millimeter up to 10^{-6} . The samples were kept in place by a pin at the bottom and the LVDT at the top. Length changes are presented as absolute values, but interpreted relatively.

The samples were subjected to one freeze-thaw cycle for each degree of saturation. A freeze-thaw cycle is composed by 2h of cooling from +20 °C to -12°C, maintenance of -12°C for 0.5 h, 2 h of heating from -12°C

to +20 °C and finally a maintenance for 1 h at +20 °C. This implies a cooling and heating rate of (+/-)0.26 °C/min. The temperature was measured in the climatic chamber and by a temperature sensor adjusted at the central sample, below the Al-foil (Lf2). The results are plotted against the reference of the chamber's temperature. The moment of ice crystallization was deduced from the time stamp in the dilatometric measurements, and the temperature of ice crystallization was taken from the sample sensor at the given time stamp. The temperature measurements are considered as absolute values, used in the calculations of section 7.3.3.

7.3.2 Results

The length change behaviour for Lf1, Lf2 and Lf3 at the different saturation conditions is presented in Figure 7.10. The simultaneous temperature measurement of the sensor attached to Lf2 is given in Figure 7.9. Both graphs have the chamber temperature in abscissa as reference, to correlate the sample temperature with the length change of the samples.

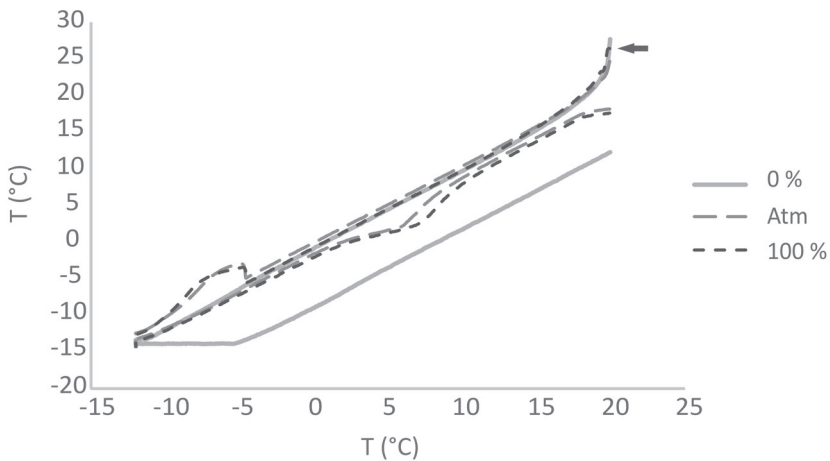


Figure 7.9: Temperature evolution of the Lf2 sample (ordinate) for 0 %, atmospheric and 100 % water saturation in relation to the chamber temperature (abscissa) during a freeze-thaw cycle. The start point is indicated by the black arrow.

The evolution of the specimen temperature in relation to the chamber temperature indicates that there is a fast initial cooling, that tapers off

towards the chamber temperature. This is a laboratory effect as the samples at room temperature adjust to the (decreasing) temperature in the climatic chamber. Soon, the samples are in equilibrium with the ambient chamber temperature. This is independent of the saturation degree, as they show the same trend. In equilibrium, the decreasing sample temperature keeps pace with the decreasing chamber temperature. For the sample at 0 % saturation, this is a linear trend until the lowest ambient temperature of $-12\text{ }^{\circ}\text{C}$. At this point, the sample shows an undershoot in temperature, without further consequences and where it stays during the period of constant temperature at $-12\text{ }^{\circ}\text{C}$. During the heating phase, the sample shows an initial delay with respect to the chamber temperature. The sample starts to heat at chamber temperatures of $-5\text{ }^{\circ}\text{C}$. Subsequently, it shows continuous and linear heating, delayed with respect to the chamber temperature. It will attain $+19\text{ }^{\circ}\text{C}$ approximately 30 min after the ambient temperature attained $+20\text{ }^{\circ}\text{C}$.

The sample shows different curves for atmospheric water saturation and 100 % water saturation, which mutually are alike. In the initial cooling phase, the curve is similar to that of the sample with 0 % saturation, but they behave different underneath $0\text{ }^{\circ}\text{C}$. The linear cooling phase is suddenly interrupted by an exothermal peak at $-4.68\text{ }^{\circ}\text{C}$ for both the atmospheric and 100 % water saturated samples. After the occurrence of this peak, the sample starts to cool again. In this phase, the gradient of cooling increases gradually until the minimum temperature. During heating, the sample temperature shows a linear heating, without a delay. At a temperature of $0\text{ }^{\circ}\text{C}$, both samples show decreased heating, whilst the chamber temperature rises to $+5\text{ }^{\circ}\text{C}$. Subsequently, the rate of sample heating increases and tapers off to become linear again.

The length change of the samples in relation to the chamber temperature (Fig. 7.10) shows different shapes for different degrees of water saturation, but a similar shape for different samples with the same water saturation, though having different amplitudes. This means that the degree of saturation plays an important role in the processes that take place.

For Lf1, Lf2 and Lf3, the length change at 0 % water saturation is very similar, in rate and in amplitude. The length change shows a high correlation with the temperature change. During cooling, the sample shows a linear contraction to a maximum at $-12\text{ }^{\circ}\text{C}$. During the heating stage, the sample shows a delayed response, similar to the delay in temperature increase. The moment the temperature of the sample starts to

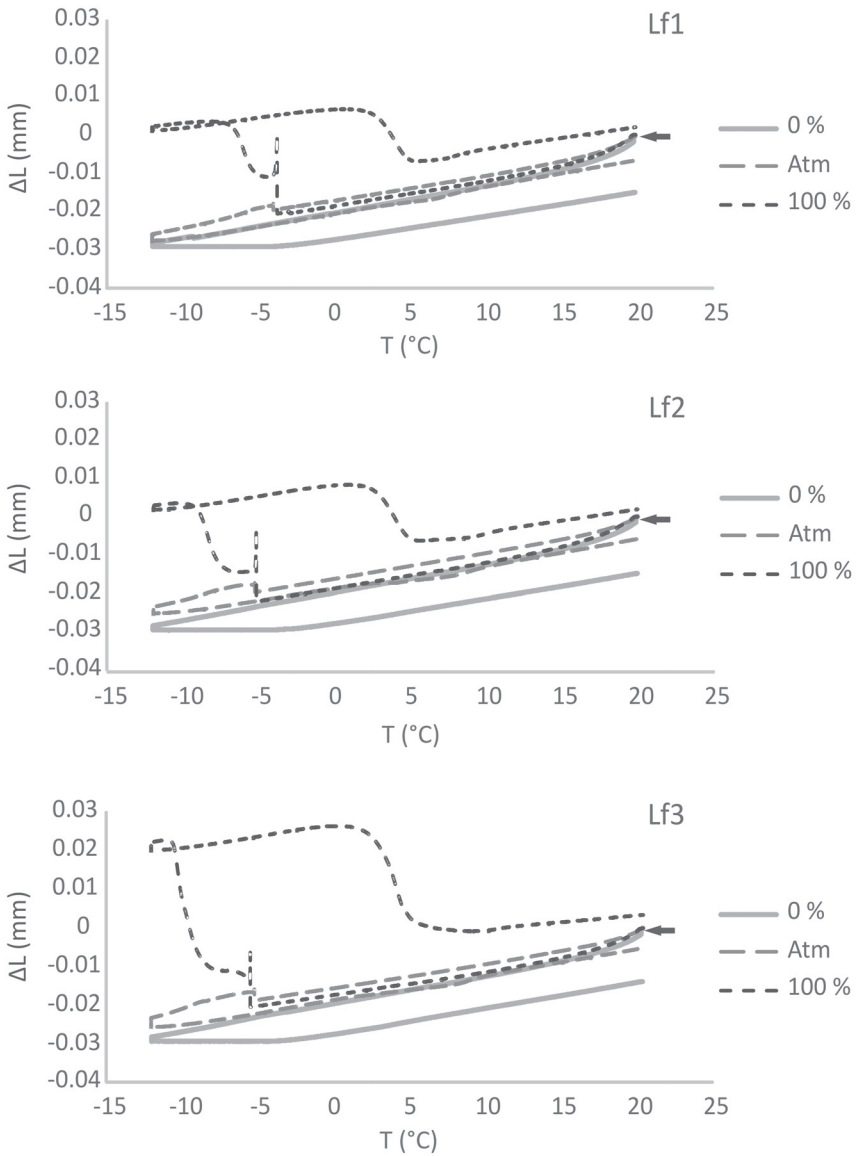


Figure 7.10: Length change (ordinate) of Lf1 (top), Lf2 (middle) and Lf3 (bottom) for 0 %, atmospheric and 100 % water saturation in relation to the chamber temperature (abscissa) during a freeze-thaw cycle. The starting point is indicated by the black arrow.

rise, the sample starts to expand linearly together with increasing sample temperature. Thus, the dry samples show linear contraction during cooling and linear expansion during heating. The sample temperature during heating shows a delay with respect to the chamber temperature. When the sample temperature equilibrates with the chamber temperature at 20 °C, the sample returns to its original length (not depicted in Fig. 7.10).

At atmospheric water saturation, the linear contraction of Lf1, Lf2 and Lf3 during cooling is interrupted by a sudden expansion at -3.33 °C for Lf1 and -4.68 °C for Lf2 and Lf3. The expansion of Lf1 shows the lowest amplitude and the expansion of Lf3 shows the highest. After this expansion, the stones start to shrink again until they reach their shortest length during the maintenance of -12 °C in the chamber. In the heating phase, the samples show an immediate response by expanding. Around 0 °C, the samples show a temporal decrease in expansion rate.

At 100 % water saturation, a sudden expansion during cooling takes place at approximately the same temperatures compared to that of the atmospheric water saturation. However, the amplitude is much larger for all microfacies. This expansion is very instantly, with an instant length decrease after the expansion peak. However, the samples do not return to their length just before the occurrence of this expansion peak. Rather, they show a residual expansion with respect to the moment before this expansion. Subsequently, the samples show a gradual expansion during further cooling. After reaching a maximum, which amplitude is much higher for Lf3 compared to Lf1 and Lf2, the samples show a linear shrink during further cooling to its minimum temperature. During heating, the samples linearly expand with rising temperature. Around 0 °C, they show a temporal high shrink, to linearly expand further during the heating to +20 °C.

7.3.3 Discussion

Experimental section

The length change of Lf1, Lf2 and Lf3 at 0 % saturation can be used as reference for the length changes at atmospheric and 100 % saturation. Any differences at the latter will be related to the presence of water in the pore network. The length change of the samples at 0 % saturation will be a combined effect of the length change of the setup, although this was maximally reduced, and mainly the length change of the dry material. The linear shrink during cooling and the linear expansion during heating reflect the thermal expansion coefficient of the material(s). The delay in expansion during heating is related to the delay in heating of the specimen itself. This effect is less or not pronounced when the pore system is water saturated.

The temperature exotherm, observed for an atmospheric and 100 % water saturation is used as a proxy for ice crystallization. As such, a T_f of -3.33 °C for Lf1 and -4.68 °C for Lf2 and Lf3 could be captured. At this point, ice crystallization takes place in the sample. Together with the occurrence of this exotherm, the length change shows a sudden expansion. Thus, ice crystallization within the sample causes a positive dilatation due to the growth of ice crystals within the pore network. The relative amplitude of this expansion is $Lf3 > Lf2 > Lf1$. Lf3 has a higher water absorption as a result of a higher porosity, and the amplitude seems to correlate with the amount of water/ice within the sample. After this initial ice crystallization, the initial phase of recommencing temperature decrease coincides with an increasing rate of shrinkage. At this moment, there is ongoing crystallization, but at a decreasing rate. Finally, the decrease in temperature tapers off linearly to its minimum and the samples shrink accordingly. This is now a combined effect of the contraction of stone and ice (Ruedrich and Siegesmund, 2007).

At 100 % water saturation, the amplitude of the expansion at the moment of the exotherm is much larger. This indicates the effect of larger saturation; the higher water content has a higher volumetric potential for ice crystals. The instant peak in expansion could indicate that the formed ice crystals immediately re-equilibrate due to pressure solution and precipitation at the unconfined crystal faces (Scherer, 1999). The ongoing expansion after this first peak shows that ice crystallization continues until all water is exhausted. At this point, a limited shrinkage reflects the

thermal contraction of the material and ice with decreasing temperature.

During heating, the samples show linear expansion with increasing temperature, related to the thermal expansion coefficient of ice and stone and similar to the dry samples. Around 0 °C, both the atmospheric and 100 % water saturated samples show an interruption of the linear expansion. The atmospheric saturated samples show a temporal decrease of expansion rate, whilst the 100 % water saturated samples show a strong shrinkage. This is the result of the melting of ice. The pressure exerted by the ice crystals on the pore walls disappears. The strong shrinkage of the 100 % saturated samples around 0 °C shows that this crystallization pressure is very significant, but mainly in the completely saturated rock. The effect for Lede stone is less pronounced in atmospheric saturated samples.

The potential for freeze-thaw deterioration increases with increasing degree of water saturation. Also, the potential is much larger for Lf3 than for Lf1 or Lf2, because of the higher amplitudes of length change. This is the result of a higher water absorption, related to a higher porosity.

Theoretical section

Similar to the calculations in 7.2.6, the pore radius where crystallization takes place, and the corresponding crystallization pressure, could be calculated for Lf1, Lf2 and Lf3. According to equation 7.1 and 7.2, the lower pore radius for Lf1 is 18 nm, and for both Lf2 and Lf3 13 nm and the corresponding crystallization pressure is 3.73 MPa for Lf1 and 5.24 MPa for Lf2 and Lf3. With the tensile strength measured in section 5.5.2, the macroscopic stress needed to induce failure (Eq. 7.4) is 4.24 MPa for Lf1, 2.49 MPa for Lf2 and 1.24 MPa for Lf3. With the former calculated crystallization pressure, a crystal fraction of 283 % for Lf1, 118 % for Lf2 and 59 % for Lf3 is required to fulfill the precondition for failure, corresponding to respectively 17.9 %, 13.0 % and 11.6 % of the stone volume.

Putting the latter in perspective, this means that Lf1 and Lf2 are frost resistant, as the crystal fraction can never obtain values that are sufficient to induce instant failure. This is because the pore volume is not large enough (see section 5.3), even when it is completely saturated. The only way that failure can be induced is crystallization in smaller pores, hence at lower temperatures or by changing the materials intrinsic properties for example by fatigue.

These calculations, however, show that failure under these experimental

conditions can occur in Lf3. Moreover, failure could be induced at water saturation degrees that correspond to the atmospheric water saturation (see 5.4.1). Indeed, such observations are made in the laboratory freeze-thaw experiment (see 5.8), where the samples were saturated by immersion under atmospheric conditions. Lf3 showed freeze-thaw damage, whilst Lf1 and Lf2 remained intact.

A further point of discussion is that the pore radius where crystallization takes place is larger for Lf1 compared to Lf2 and Lf3, whilst in section 5.3 it was shown that the pore network of Lf2 and Lf3 consists of larger pores, connected by larger pore throats. This is an observation that certainly needs to be further explored in the future. A possible theory is that crystallization starts at higher temperatures in the larger pores in equilibrium conditions (Everett, 1961), which are large enough to accommodate the ice crystals and that length change takes place when ice is forced to bulge into the smaller surrounding pores. As Lf2 and Lf3 have a larger volume of macropores, this could take place at lower freezing temperatures. The moment that ice is forced into the smaller pores should more or less represent the moment when most water in the pores crystallize to ice, as it is also at this moment the temperature exotherm is observed.

7.4 Discussion and conclusion

Noyant limestone was an ideal sample to explore the potentials of continuous μ CT in the study of the freeze-thaw process in stone under ambient conditions. This was illustrated by the experimental results that shows the rapid initiation of cracks and by the theoretical results that indicate the low threshold for failure in combination with the rapid capillary water uptake and relatively high saturation degree of this rock. This experiment supports the ice crystallization theory as the mechanism responsible for failure within the stone.

The susceptibility of Lede stone to laboratory freeze-thaw experiments was proven to be relative low. When no damage occurs, the time of scanning outweighs which would take months, the amount of data produced, the costs and the analysis time outweighs the advantage of continuous μ CT. Therefore, Lf3 is potentially the most interesting sample, being it for a long-term study which could not be performed in the time frame of this

work, but which certainly has future potential.

The dilatometric study of Lede stone during freeze-thaw cycling allowed to have insights on the freeze-thaw processes within the stone. From the μ CT experiments with Noyant limestone, it was clear that any exotherm relates to the crystallization of ice and that any damage was the result. Such a temperature exotherm was also observed in the experiments with Lede stone and allowed to estimate the crystallization temperature. Here, it coincides with an expansion peak, which is not observed during the cooling of dry stone. Therefore, this expansion is caused by the crystallization of ice. The amplitude of this expansion seems to be related to the total porosity as well as to the water saturation degree. Higher amplitudes were observed in the most porous rock at higher saturation, hence these are the most vulnerable to freeze-thaw decay.

Nevertheless, the theoretical approach indicates that the theoretical susceptibility is relatively low. The theoretical frost resistance of Lf1 is larger than that of Lf2, which in turn is larger than that of Lf3. Moreover, only Lf3 shows a theoretical potential damage. However, the preconditions are a relative high ice crystal fraction upon freezing. This can only be obtained by high saturations, in the magnitude of complete imbibition under atmospheric pressure. This is indeed observed in laboratory-scale freeze-thaw cycling, where Lf1 and Lf2 are frost resistant and Lf3 shows frost susceptibility. Here, the samples are completely water imbibed at atmospheric pressure. In real-time conditions, Lf3 has proven to have a high initial drying rate, and macropores will drain easily. Therefore, freeze-thaw events should follow immediately after intense wetting of the stone. Whilst Lf1 and Lf2 have no applicable limitations in terms of frost susceptibility, the use of Lf3 might be discouraged for outdoor flooring, water draining elements or architectural work that is omnidirectional exposed to direct rain impact, such as crockets, finials and parapets.

References

- M A Boone, T De Kock, T Bultreys, G De Schutter, P Vontobel, L Van Hoorebeke, and V Cnudde. 3D mapping of water in oolitic limestone at atmospheric and vacuum saturation using X-ray micro-CT differential imaging. *Materials Characterization*, 97(0):150–160, 2014a. doi: <http://dx.doi.org/10.1016/j.matchar.2014.09.010>.
- M A Boone, P Nielsen, T De Kock, M N Boone, M Quaghebeur, and V Cnudde. Monitoring of Stainless-Steel Slag Carbonation Using X-ray Computed Microtomography. *Environmental Science & Technology*, 48(1):674–680, 2014b. doi: 10.1021/es402767q.
- T Bultreys, M A Boone, M N Boone, T De Schryver, B Masschaele, L Van Hoorebeke, and V Cnudde. Fast laboratory-based micro-computed tomography for pore-scale research: Illustrative experiments and perspectives on the future. *Advances in Water Resources*, in press, may 2015. ISSN 03091708. doi: 10.1016/j.advwatres.2015.05.012.
- D Camuffo. *Developments in atmospheric science 23 - Microclimate for cultural heritage*. Elsevier Science Bv, Amsterdam, 1998.
- T C Chen, M R Yeung, and N Mori. Effect of water saturation on deterioration of welded tuff due to freeze-thaw action. *Cold Regions Science and Technology*, 38(2-3):127–136, 2004. doi: 10.1016/j.coldregions.2003.10.001.
- V Cnudde and M N Boone. High-resolution X-ray computed tomography in geosciences: A review of the current technology and applications. *Earth-Science Reviews*, 123:1–17, 2013. doi: 10.1016/j.earscirev.2013.04.003.
- V Cnudde, J Dewanckele, T De Kock, M A Boone, J M Baele, P Crombe, and E Robinson. Preliminary structural and chemical study of two quartzite varieties from the same geological formation: a first step in the

- sourcing of quartzites utilized during the Mesolithic in northwest Europe. *Geologica Belgica*, 16(1-2):27–34, 2013.
- O Coussy. Deformation and stress from in-pore drying-induced crystallization of salt. *Journal of the Mechanics and Physics of Solids*, 54(8):1517–1547, 2006. doi: 10.1016/j.jmps.2006.03.002.
- T De Kock, M A Boone, T De Schryver, J Van Stappen, H Derluyn, B Masschaele, G De Schutter, and V Cnudde. A Pore-Scale Study of Fracture Dynamics in Rock Using X-ray Micro-CT Under Ambient Freeze-Thaw Cycling. *Environmental Science & Technology*, 49(5): 2867–2874, 2015. doi: 10.1021/es505738d.
- T De Schryver, M Boone, T De Kock, B Masschaele, M Dierick, and L Van Hoorebeke. A compact, low cost cooling stage for X-ray micro-CT setups. In *Industrial Computed Tomography, 5th Conference, Abstracts*, page 1p, Wels, 2014.
- H Derluyn, J Dewanckele, M N Boone, V Cnudde, D Derome, and J Carmeliet. Crystallization of hydrated and anhydrous salts in porous limestone resolved by synchrotron X-ray microtomography. *Nuclear Instruments & Methods in Physics Research Section B-Beam Interactions with Materials and Atoms*, 324:102–112, 2014. doi: 10.1016/j.nimb.2013.08.065.
- J Dewanckele, T De Kock, M A Boone, V Cnudde, L Brabant, M N Boone, G Fronteau, L Van Hoorebeke, and P Jacobs. 4D imaging and quantification of pore structure modifications inside natural building stones by means of high resolution X-ray CT. *Science of the Total Environment*, 416:436–448, 2012. doi: 10.1016/j.scitotenv.2011.11.018.
- J Dewanckele, M A Boone, T De Kock, W De Boever, L Brabant, M N Boone, G Fronteau, J Dils, L Van Hoorebeke, P Jacobs, and V Cnudde. Holistic approach of pre-existing flaws on the decay of two limestones. *Science of the Total Environment*, 447:403–414, 2013. doi: 10.1016/j.scitotenv.2012.12.094.
- M Dierick, D Van Loo, B Masschaele, J Van den Bulcke, J Van Acker, V Cnudde, and L Van Hoorebeke. Recent micro-CT scanner developments at UGCT. *Nuclear Instruments & Methods in Physics Research Section B-Beam Interactions with Materials and Atoms*, 324: 35–40, 2014. doi: 10.1016/j.nimb.2013.10.051.

- EN 12371. Natural stone test methods - Determination of frost resistance, 2010.
- R M Espinosa-Marzal, A Hamilton, M McNall, K Whitaker, and G W Scherer. The chemomechanics of crystallization during rewetting of limestone impregnated with sodium sulfate. *Journal of Materials Research*, 26(12):1472–1481, 2011. doi: doi:10.1557/jmr.2011.137.
- D H Everett. The thermodynamics of frost damage to porous solids. *Transactions of the Faraday Society*, 57(9):1541–&, 1961. doi: 10.1039/tf9615701541.
- C M Grossi, P Brimblecombe, and I Harris. Predicting long term freezethaw risks on Europe built heritage and archaeological sites in a changing climate. *Science of the Total Environment*, 377(23):273–281, 2007. doi: <http://dx.doi.org/10.1016/j.scitotenv.2007.02.014>.
- K Hall. Monitoring of thermal conditions in building stone with particular reference to freeze-thaw events. In S K Koukoulis, editor, *Fracture and Failure of Natural Building Stones: Application in the Restoration of Ancient Monuments*, pages 373–394. Springer, Dordrecht, 2006.
- K Hall and M F André. Rock thermal data at the grain scale: applicability to granular disintegration in cold environments. *Earth Surface Processes and Landforms*, 28(8):823–836, 2003. doi: 10.1002/esp.494.
- J P Ingham. Predicting the frost resistance of building stone. *Quarterly Journal of Engineering Geology and Hydrogeology*, 38:387–399, 2005. doi: 10.1144/1470-9236/04-068.
- R A Ketcham, D T Slottke, and J M Sharp. Three-dimensional measurement of fractures in heterogeneous materials using high-resolution X-ray computed tomography. *Geosphere*, 6(5):499–514, 2010. doi: 10.1130/ges00552.1.
- J Martinez-Martinez, D Benavente, M Gomez-Heras, L Marco-Castano, and M A Garcia-del Cura. Non-linear decay of building stones during freeze-thaw weathering processes. *Construction and Building Materials*, 38:443–454, 2013. doi: 10.1016/j.conbuildmat.2012.07.059.
- N Matsuoka and J Murton. Frost weathering: Recent advances and future directions. *Permafrost and Periglacial Processes*, 19(2):195–210, 2008. doi: 10.1002/ppp.620.

- S Mazumder, K H A A Wolf, K Elewaut, and R Ephraim. Application of X-ray computed tomography for analyzing cleat spacing and cleat aperture in coal samples. *International Journal of Coal Geology*, 68(34):205–222, 2006. doi: <http://dx.doi.org/10.1016/j.coal.2006.02.005>.
- D McAllister, S McCabe, B J Smith, S Srinivasan, and P A Warke. Low temperature conditions in building sandstone: the role of extreme events in temperate environments. *European Journal of Environmental and Civil Engineering*, 17(2):99–112, 2013. doi: 10.1080/19648189.2012.751225.
- D T Nicholson and F H Nicholson. Physical deterioration of sedimentary rocks subjected to experimental freeze-thaw weathering. *Earth Surface Processes and Landforms*, 25(12):1295–1307, 2000. doi: 10.1002/1096-9837(200011)25:12<1295::aid-esp138>3.0.co;2-e.
- M Pigeon, J Marchand, and R Pleau. Frost resistant concrete. *Construction and Building Materials*, 10(5):339–348, 1996. doi: 10.1016/0950-0618(95)00067-4.
- J Ruedrich and S Siegesmund. Salt and ice crystallisation in porous sandstones. *Environmental Geology*, 52(2):343–367, 2007. doi: 10.1007/s00254-006-0585-6.
- J Ruedrich, D Kirchner, and S Siegesmund. Physical weathering of building stones induced by freeze-thaw action: a laboratory long-term study. *Environmental Earth Sciences*, 63(7-8):1573–1586, 2011. doi: 10.1007/s12665-010-0826-6.
- V G Ruiz de Argandona, L Calleja, A Rodriguez-Rey, L Miguel Suarez del Rio, and C Celorio. X-ray Computed Tomography study of the influence of consolidants on the hydric properties of sandstones for stone conservation studies. *Engineering Geology*, 103(3-4):69–75, 1999. doi: 10.1016/j.enggeo.2008.06.008.
- G W Scherer. Crystallization in pores. *Cement and Concrete Research*, 29(8):1347–1358, 1999. doi: 10.1016/s0008-8846(99)00002-2.
- S Siegesmund and H Dürrast. Physical and Mechanical Properties of Rocks. In S Siegesmund and R Snethlage, editors, *Stone in Architecture - Properties, Durability*, chapter 3, page 552. Springer, Berlin Heidelberg, 4th edition, 2011.
- M Steiger. Crystal growth in porous materials - I: The crystallization

- pressure of large crystals. *Journal of Crystal Growth*, 282(3-4):455–469, 2005a. doi: 10.1016/j.jcrysgro.2005.05.007.
- M Steiger. Crystal growth in porous materials - II: Influence of crystal size on the crystallization pressure. *Journal of Crystal Growth*, 282(3-4): 470–481, 2005b. doi: 10.1016/j.jcrysgro.2005.05.008.
- Z Sun and G W Scherer. Effect of air voids on salt scaling and internal freezing. *Cement and Concrete Research*, 40(2):260–270, 2010. doi: 10.1016/j.cemconres.2009.09.027.
- J J Valenza and G W Scherer. Mechanism for salt scaling. *Journal of the American Ceramic Society*, 89(4):1161–1179, 2006. doi: 10.1111/j.1551-2916.2006.00913.x.
- M Voorn, U Exner, and A Rath. Multiscale Hessian fracture filtering for the enhancement and segmentation of narrow fractures in 3D image data. *Computers & Geosciences*, 57:44–53, 2013. doi: 10.1016/j.cageo.2013.03.006.
- J Walder and B Hallet. A theoretical model of the fracture of rock during freezing. *Geological Society of America Bulletin*, 96(3):336–346, 1985. doi: 10.1130/0016-7606(1985)96<336:atmotf>2.0.co;2.
- J S Walder and B Hallet. The physical basis of frost weathering - toward a more fundamental and unified perspective. *Arctic and Alpine Research*, 18(1):27–32, 1986. doi: 10.2307/1551211.
- D Wildenschild and A P Sheppard. X-ray imaging and analysis techniques for quantifying pore-scale structure and processes in subsurface porous medium systems. *Advances in Water Resources*, 51:217–246, 2013. doi: 10.1016/j.advwatres.2012.07.018.

8

Replacement stones for Lede stone

At the end of the 19th century and the beginning of the 20th century, a combination of critical factors compromised the use of Lede stone in buildings. On one hand, exploitation of Lede stone was ceasing (see Section 3.2), while on the other hand sulphation and the formation of black crusts on Lede stone in buildings was an emerging problem (see Section 3.4). This led to the use of other stones at the expense of damaged Lede stone during restorations. Natural stone replacement (see Section 1.2) is often based on the appreciation of the state of a natural stone (see Chapter 4). However, natural stone replacements are not always appreciated and the perception of ageing is important for blending into the architecture. This chapter explores the replacement of Lede stone specifically and discusses the preconditions for replacement stones. It is partly based on De Kock et al. (2014) where the co-authors contributed to the discussion. Section 8.1 gives an overview of used replacement stones in northwestern Belgium, by observations at different monuments. This is followed by Section 8.2, where a case-study of the St Bavo cathedral tower in Ghent is presented, to illustrate the use of different replacement stones in a timeframe and to evaluate the decision-making factors of their use. Section 8.3 gives an overview of the geological background and properties of the the different replacement stones covered in Section 8.1

and 8.2, with a discussion on the different aspects of compatibility.

8.1 Historical replacement of Lede stone in northwestern Belgium

The diversity of stone types used in the historical replacement of Lede stone is extensive and varied over time. Quist (2011) exhaustively illustrated this situation in The Netherlands. He summarized the materials used to replace Lede stone and Brussels stone in illustrative Dutch historical monuments to figure out the arguments on which the choices for these materials were based, and how these arguments changed through time. He identified more than 25 different stone types from France, Germany and the UK, with lithologies ranging from arenites and carbonates to magmatic intrusive and extrusive rocks, which were used in replacement series in four monuments in the period from 1871 to 2010. In particular the white French limestones were also used in Belgium. On the other hand, the use of German sandstones, such as Bentheimer and Udelfanger, German limestones, such as Muschelkalk, different magmatic stones such as tuffs, basalts and trachyte and the British Portland limestone are common practice in The Netherlands, but not typically in northwestern Belgium.

8.1.1 19th and early 20th century

In the 19th century, Brussels stone and more specifically Gobertange stone was used as replacement stone for Lede stone (Nijs, 1990; Duser et al., 2009; Cnudde et al., 2009). Examples can be found in buildings such as the Meat Hall, the Clothmakers' Hall and the Caermers monastery in Ghent and the Chapel Church and Our Blessed Lady of the Sablon Church in Brussels. As discussed in Chapter 2 this stone is geologically closely related to Lede stone, and has a similar, own historical value.

In the second half of the 19th and in the 20th century, the use of French limestone steadily increased in Belgium. Accordingly, they were also involved in restoration works, progressively replacing both Lede stone and older replacement stones. Camerman (1961) reported the use and diversity of imported limestone in the first half of the 20th century. His publications

and excursion guides are still reference works for this period (Dreesen et al., 2012). In the second half of the 19th and the first half of the 20th century, Savonnières and Euville limestone were the most important replacement stones. During the 20th century, the use of Massangis (or Vaurion) increased and became the predominant replacement stone (De Witte, 1990). Savonnières was for example used as replacement stone in the St Martinus Basilica in Halle (Fig. 8.1); Euville can be found in the Our Blessed Lady of the Sablon Church in Brussels and Massangis was used in the crockets and pinnacles of the Chapel Church in Brussels or in the St Martinus Basilica in Halle (Fig. 8.1). Similar examples in Belgium are numerous, and it is not surprising that Savonnières, Euville and Massangis limestone have always been available in large quantities, up to this date. This probably explains their dominance amongst the foreign white limestones.

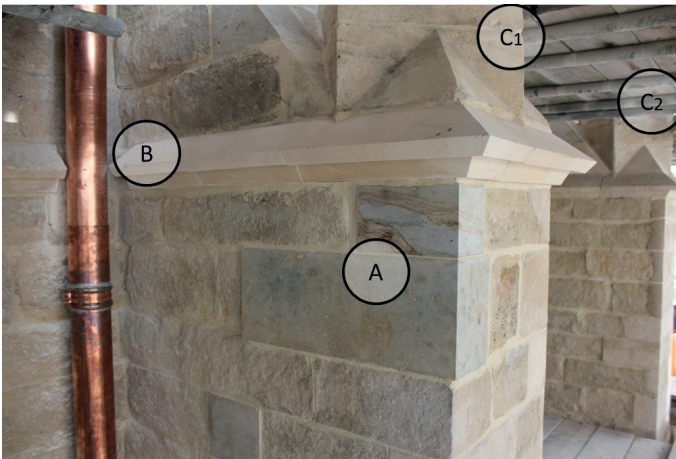


Figure 8.1: Replacement of Lede stone at St Martinus Basilica in Halle. A) Use of new Lede stone to replace Lede stone; B) the use of Massangis to replace Massangis that formerly replaced Lede stone; C1) old replacement of Lede stone in Savonnières; C2) replacement of Savonnières that formerly replaced Lede stone by Savonnières.

Less obvious is the use of other French limestones, which excavations have ceased during the 20th century. Morley, St Joire and Reffroy stones were also used as replacement material around the second half of the 19th and in the 20th century. Morley stone was used as Lede stone replacement in the Church of St John the Baptist at the Béguinage in Brussels. St Joire/Reffroy was used in the St Jacobs Church and St Bavo's cathedral in Ghent.

The use of resources from time-equivalent Cenozoic deposits from the neighbouring Paris Basin has been argued as an option (Dusar et al., 2009). The proximity of these resources also limits the ecological footprint of transport, which fits in the recent aim for sustainability. Traditional examples are St Pierre-Aigle and St Maximin from the Calcaire Grossier which are also used in the Netherlands (Quist, 2011). However, the use of these stones as replacement stone has never been put through persistently.

Larochette stone from the Grand Duchy of Luxembourg, was probably also applied in smaller scale restorations. Some examples are the St Antonius Abt church in Borsbeke, the St Martinus Church in Oombergen and the St Amandus Church in Schendelbeke, although in the latter it is possible that the original stone was Ypresian stone.

8.1.2 Late 20th and 21th century

By the end of the 20th century, Lede stone was consistently replaced by Massangis varieties in such that this was called massangitis by Breda (2005). The use of Massangis became so obvious that it turned into an awareness. The question rose whether other materials could be justifiable as replacement stones for specific cases. In addition to the on-going use of Massangis, new materials were used in restoration and the replacement of the Lede stone, some of them relatively unknown. Recent examples of such stones used in Ghent are Azul Bateig and San Louis, both from Spain. While San Louis was used as Lede stone replacement in the Caermers monastery in Ghent (Fig. 8.2) and the St Martinus Church in Edelare, Azul Bateig was used to replace Lede stone in the Emile Braun school in Ghent. In the latter however, the stones were painted in order to restore the authenticity of the building. Another example is the Coulmier-le-Sec limestone (France), which was used as replacement stone in the St Ludgerus Church in Zele (Belgium).



Figure 8.2: Wall dormers in the Caermers monastery in Ghent. Left: the bottom of the water dormer is retained in Brussels stone (masonry) and Lede stone (corners), whilst the top of the wall dormer is replaced with Gobertange stone (masonry) and San Louis (corners). Right: wall dormer originally in Lede stone which is now completely replaced by San Louis.

8.2 The tower of St Bavo's cathedral in Ghent as textbook example

The St Bavo's Cathedral tower in Ghent, Belgium, is currently under restoration. Over a period of 73 years, this tower was built during the 15th–16th century in Eocene white stone. Restorations over the last two centuries introduced different Jurassic limestones from the Paris Basin. The documentation of these interventions, however, is very poor for the period antedating the 20th century and documentation on the original construction is not traceable. Nevertheless, the use of the different stones in their historical context forms a typical example of the historical mindset on the use of white stone, representative for Ghent and by extension northwestern Belgium.

8.2.1 Ghent and St Bavo's Cathedral

The city of Ghent developed in a riverine environment, where the rivers Scheldt and Lys confluence. It is built on elevations of Late Glacial aeolian sands (Van Nieuland et al., 2013) and a Cenozoic outlier called *Blandijnberg* composed of alternating clay and sand sequences. In

postclassical and modern history, Ghent was an important cultural and economic centre. This is reflected in the many historic buildings Ghent is rich of, built over several centuries. St Nicholas' Church, the Belfry and St Bavo's Cathedral still dominate the skyline of the historical centre by forming the famous three-tower row. Of all three, the tower of St Bavo's is the only one in white stone, referring to light, porous limestone. The others are in dark, compact, Palaeozoic Belgian limestone. The construction of the 89.23 m high St Bavo's tower started in 1462 and finished in 1535 (Dhanens, 1965). It is an excellent example of Brabantine Gothic architecture (De Smidt and Dhanens, 1980). The tower is composed of five vertical sections. The lower four are based on a square ground plan with simple buttresses. The upper section is an octagonal shaped and narrower lantern, separated by open parapets and flanked on four sides by smaller octagonal towers. These flanking towers have a stone pinnacle with crockets. The top of the lantern is crowned with a stone base for the spire, which was finished in 1535 but has now disappeared.

The Cathedral and its artwork suffered from the Iconoclastic Fury in 1566 and 1578 and a fire after a thunderstorm in 1602 (Delbecq, 1774). It was this storm that destroyed the wooden spire on the tower and only few ambiguous illustrations of its presence remain. In addition, three of the four pinnacles on the flanking towers were destroyed, only to be rebuilt in the 19th century.

Neither the tower's construction nor the interventions prior to 1950 are well documented. Yet, it is important to know the used materials, and understand why and when they were used; both to understand their value and their historical performance as well as to find suitable replacements for deteriorated stones. Dhanens (1965) mentions different donations of both money and stones for the construction in the 15th century. However, no transcripts on the construction were found in the archives of the province, the city or the churchwardens. The oldest documents on restoration of the church and tower were found in the church archives (Van Bockstaele et al., 2014) and date back to a campaign in 1811 led by architect De Broe. It mentions the use of new white stone for the tower, but it does not specify which type and where they were used. In between 1860–1866, the pinnacles of the flanking towers were reconstructed, followed by a larger restoration of the tower in 1875. After recurring falling debris, an ad hoc intervention in 1952 precluded a thorough restoration in 1958 and the following years. After a small campaign in

1985, the recent restoration of 2013–2017 again treats the whole tower.

An interesting footnote regarding its preservation is a critical decision of the churchwardens back in 1940. With the plea that the German army declared that they fired at the cathedral of Reims in the First World War because the French used it as an observation post, the churchwardens of St Bavo's denied up to six times access to the Belgian army at the start of World War II. Indeed, the Cathedral of Our Lady of Reims in France was severely damaged in the First World War, which has ongoing implications. St Bavo's Cathedral was spared, and the importance of this decision might be unrecognized. It was the application of article 3 of the Venice Charter (ICOMOS, 1966) *avant la lettre*.

8.2.2 White stones and historical reconstruction

St Bavo's Cathedral tower is a textbook example for the historical use of white stone in Ghent, and by expansion the rest of northwestern Belgium. Today, six different white stone types can be found in the tower (Fig. 8.3). Two of them come from the Belgian Cenozoic deposits and are considered as original building materials or as authentic replacement stones: Brussels stone and Lede stone. The other four come from the Mesozoic Paris Basin in France (see also Fig. 8.9): Reffroy stone, Euville stone, Savonnières stone and Massangis stone. These were used as replacement stones during previous restorations over the last two centuries. Two stones were nominated as replacement stones, but were finally discarded: Larochette stone from the Mesozoic Paris Basin in the Grand Duchy of Luxembourg and St Maxim from the Cenozoic Paris Basin near Paris (see also Fig. 8.9).

Lede stone and Brussels stone (Diegem variety) are two of the most popular historical building materials in northern Belgium. Despite the lack of historical documentation on the construction of the tower these stones are considered as the original building material. Fortunately, according to other studies, quarry accounts from Dilbeek near Brussels mention the supply of Lede stone for St Bavo's Cathedral in the period that the tower was built (Van Liedekerke and Verhasselt, 1998). If Lede stone was imported from the area of Brussels, it is not surprising that Brussels stone, excavated between the Senne and Dyle, was also supplied. When both stone types were used together, it was current practice to use Brussels stone for masonry and Lede stone for corner blocks and framework, as is the case in the Cathedral's tower. Both rock types have comparable

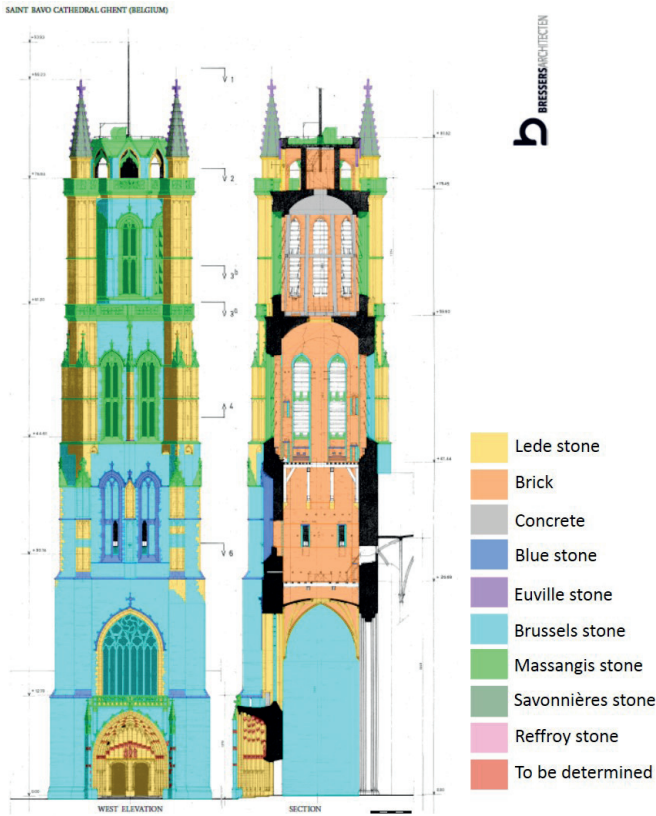


Figure 8.3: Lithological map indicated on plan in frontal view (left) and in a sagittal section (right) of the St Bavo tower (property of Architectenbureau Bressers bvba).

petrophysical properties, but the dimensions of Brussels stone are more restricted in height. Today, some Gobertange variants of Brussels stone can be found in between the Diegem variants. They are easily distinguishable by the presence of intense burrowing, but also by the fact that their edges are much sharper. This reflects their origin as recent replacement stones. As such, their emplacement might go back as far as the 1811 restoration by De Broe, but not as far as being original stones. The eastern façade is ambiguous on this matter. Several levels are built entirely in Gobertange stone, window frames included, with relative sharp edges and fine joints. It is unclear whether or not this is the original stone or a restoration with complete stone replacement. One such window frame is also made up in Gobertange on the west façade, which was likely a

replacement. Also, some Gobertange stones catch the eye in a photograph which should antedate 1885, when the houses in front of the Cathedral were removed (Fig. 8.4). On this picture, they look rather clean. It is the question if they were emplaced during the restoration of 1811 or rather the restoration of 1875.

Euville stone is present in the frontal façade, where it seems to serve as a substitute for Lede stone. These blocks catch the eye in a photograph which should antedate 1885, when the houses in front of the Cathedral were removed (Fig. 8.4). Thus, it is likely that they were emplaced during the restoration of 1875, as substitute for Lede stone.

Savonnères stone is dominantly present in the pinnacles and as finial of the four flanking towers, which were reconstructed in 1860–1866. However, one finial and some crockets were shaped in Euville stone.

Reffroy stone is probably present in the plints on the main level. This is very similar to the situation in St Jacobs Church, where it was also used for the window frames. The use of Reffroy is typically around the turn of the 20th century. Possibly, they were also emplaced during the restoration of 1875. In addition, some lanterns and statues in the portal are made in oolitic limestone. This stone is yet to be identified by microscopy, but could potentially be Reffroy stone.

The restoration of 1958 is more thoroughly documented. Contractors who subscribed for the public tender had to propose their view on the use of four possible replacement stones: St Maximin, Larochette, Massangis and Balegem (i.e. Lede stone, mostly recuperation material from other wharfs). The contractors proposed the volumes they would use from each stone, with unit price and the resulting total. Not all contractors could supply volumes of Lede stone or all of the other stone and the assignment was due to be a question of budget. Either way, it is interesting that St Maximin and Larochette stone were proposed as alternative material. Ever since, St Maximin stone has been suggested as a possible replacement stone for Lede stone. Not only is there a certain geological affinity as time-equivalent Lutetian deposit of the Paris Basin, but also the ochre colour is interesting to match the age patina of Lede stone. Yet, very few times was this rock selected as a Lede stone replacement over the last century. As in the case of the Cathedral's tower, the selection of replacement material at other monuments would be in favour of Massangis. Also Larochette stone develops an orange-grey patina. It was

used in Ghent for constructions such as the old Post office and St Michael's bridge in the first part of the 20th century; the expertise was available. Carl Camerman, mining engineer at the Geological Survey of Belgium, even wrote a positive advice for this restoration on the properties and use of Larochette. In the end St Maximin nor Larochette were used. Instead, the choice was in favor of Massangis, and this stone would dominate the restoration of white stone in the second half of the 20th century.

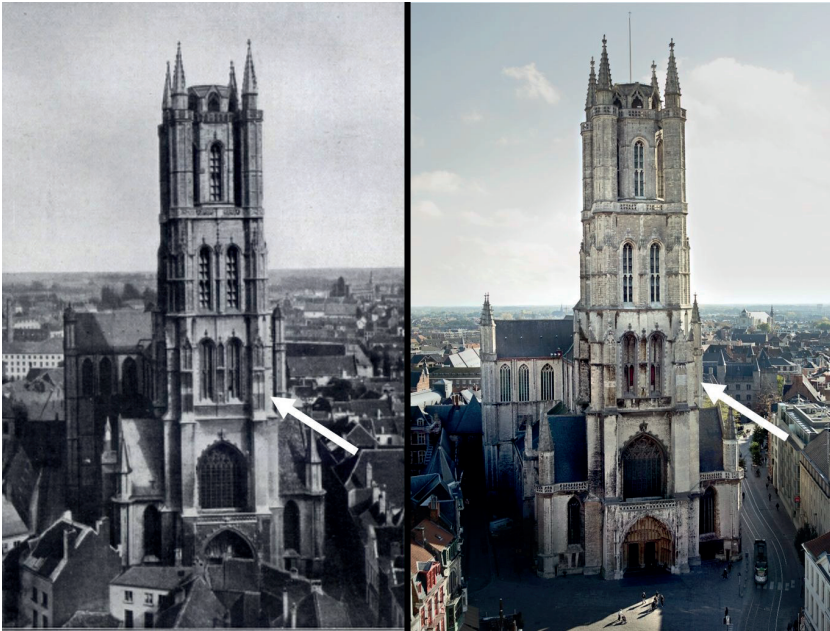


Figure 8.4: Frontal view of the tower, pictures taken in between 1866–1885 (left; Ghent University Library, topographical collection, BRKZ.TOPO.558.A.02) and in 2011 (right; photo Visit Gent). Arrow points out Gobertange stone, which were already present by the time the left photograph was taken. These are also indicated on Fig. 8.3.

8.2.3 Decision-making factors

The geological setting of Ghent did not allow for near-site excavation of natural stone. The nearest historic exploitations of Lede stone (see Section 3.2) were located a little less than 20 km away in a beeline, in the region of Oosterzele and Vlierzele. Nevertheless Lede stone was (also?) bought

from a quarry in Dilbeek, located almost 50 km away, near Brussels. This implies transport first northwards over the Senne river, than westwards over the Dyle river and eventually back south over the Scheldt. Yet still, this is among the most proximal locations of natural stone resources, definitely with respect to white stone. The origin of the stone was mostly determined by geology, but already influenced by socio-economic factors, being supply and availability.

Euville and Savonnières stone appear for the first time in northern Belgium halfway the 19th century. Soon they were to become very popular building materials for new constructions and restorations, and they are very easy to handle and to shape. Because of this, the selection of Savonnières stone for the reconstruction of the pinnacles was obvious. It is likely that the use of Euville as crocket or finial indicates later replacement (20th century?), perhaps already of Savonnières stone.

The choice for Massangis stone in 1958 was more intricate. Compared to the other alternatives, St Maximin and Larochette, one might say that from an aesthetic point of view, Massangis was the least choice. Although this vision is a very subjective criterion. On the other hand, looking at the petrophysical properties which were known at that time, Massangis leans most closely to Lede stone. However, none of these two considerations have played a true role in the decision making process. Initially, in 1956 the restoration was assigned to the company Bruxelman. They had performed the ad hoc intervention in 1952 and proposed to use Larochette and Lede stone for the upcoming restoration. However, in 1957 this decision was overruled by the Ministry of Justice and the Ministry of Public works and Reconstruction, whose opinion was to assign the works to the lowest bidder, which was the company Vlaminck who proposed the use of Massangis. The absolute difference was small: 11 338 041 Belgium Francs vs. 11 530 909. Moreover, Bruxelman proposed the combined use of Larochette and Lede stone, whereas Vlaminck proposed to integrally use Massangis. The final decision was purely made on budgetary reasons. The implications, however, might have been larger than one would expect. This would prelude four decades where Massangis was the most dominant replacement material for Belgian white stones.

Today, during the restoration of 2013–2017, the natural stones are replaced, only if necessary, by the exact same material. The original material is preserved as much as possible, and if needed repaired by Dutchmen interventions, replaced with recuperated stones or replaced with

new stones from the quarry. One exception are the crockets and finial on the flanking towers, of which most existed in Savonnières and some in Euville: based on the stone's performance these will all be replaced in Euville (Fig. 8.3).

8.3 Compatibility of traditional and new replacement stones

Few guidelines on the requirements of replacement stones have been published. Quist (2011) concluded that the choice of replacement stone was barely restricted by specific demands. To counteract this, he proposed the use of a list of performance, which pinpoints the main criteria in the initial phase of restoration. This list is based on the different aspects of compatibility: historical, aesthetical and technical compatibility.

Historical compatibility comprises material continuity. The aim is to use the same material which was used originally or the same replacement material if the replacement contributes to the historic aspect of the building. Aesthetical compatibility contains the appearance of the stone, or how the replacement stone resembles the original in fresh and aged colour, in texture, in size and in finishing. Technical compatibility relates to the mineralogical composition, the porosity, the environment and the durability of the stone.

According to Sneath and Pfanner (2013) the properties and ageing colour of replacement stones should be in the same range of the original. Therefore, he listed texture, mineralogical composition, cement, porosity, pore size distribution, capillary absorption, saturation coefficient, water vapour diffusion resistance, compressive strength and modulus of elasticity. Basically, this infers that the material properties of replacement stones should match the properties of the specific Lede stone as listed in Chapter 5, depending on the best matching Lede stone type, mindful of the historical compatibility.

The historical compatibility creates a special situation for Lede stone. Not only the material itself should warrant for the continuity, also the architectural combination of materials should be respected. Lede stone was often used together with Brussels stone. Stone replacement should also take this into consideration, as it is not uncommon that Lede stone

and Brussels stone were used in a specific architectural combination. Therefore, the aesthetic compatibility of a replacement stone should not only aim to match the appearance of Lede stone, but also to preserve the different aspect towards Brussels stone (i.e. size, texture and colour).

The final assessment on the different aspects of compatibility, i.e. what aspect is the most important, depends on the situation. In the context of monuments; historical compatibility should always be fulfilled, as long as the availability of the appropriate materials allows it. The balance between aesthetical and technical compatibility is more subjective. In case of total replacement, aesthetical compatibility might be the most important, on the precondition that the materials' performance is suited for the application. In case of partial replacement, technical compatibility becomes important in order to prevent accelerated decay of the original material.

This section gives an overview of different replacement stones which are used (Section 8.1) or which have a potential to replace Lede stone. Section 8.3.1 provides some geological background and a petrographical description based on the samples acquired by the author. Section 8.3.2 gives an overview of the basic petrophysical properties measured on these samples. The different aspects of compatibility of these stones are discussed in Section 8.3.3.

8.3.1 Description of replacement stones

The properties of Lede stone have already been discussed in Chapter 3 and 5. Nevertheless, Figure 8.5 gives a random macroscopical and microscopical view for comparison with the replacement stones listed below. The source locations of all stones is given in Figure 8.9.

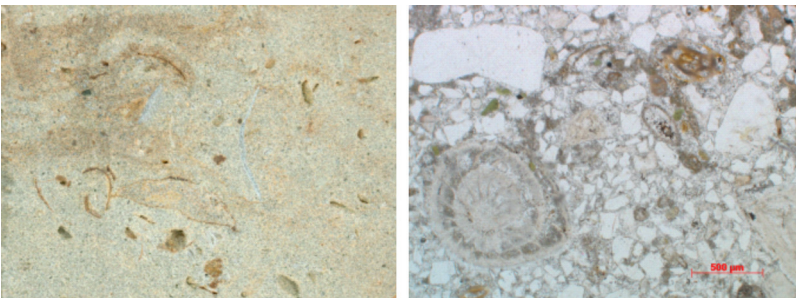


Figure 8.5: Macroscopical and microscopical photograph of Lede stone.

Brussels stone (Fig. 8.6A) was already discussed in Chapter 2. It has a laminated texture which is the result of an alternation between a mudstone to wackestone texture and pack- to grainstone texture. This is very pronounced in its macroscopic appearance. Some facies have intense bioturbation with burrows. This is for example the case for the intensive exploited Gobertange stone. These burrows are about a centimetre thick and several centimetres long and the infilling has a more dark, larger grained texture of packstone to grainstone. The quartz content is below 50 % and shows an average sorting, a subangular texture and is mainly confined in the range of 100 to 300 μm . The packstone to grainstone textures contain up to 5 % glauconite, while bioclasts are a less dominant component of the rock. These comprise mainly forams, e.g. *Milliolina*. *Nummulites laevigatus* is typical for these deposits, but not always observed. Other bioclastic components are bivalves and echinoderms. A micrite matrix is dominant with zonal sparite cement. Silicifications occur throughout the matrix and silicified echinoderms and forams can be present. The porosity is dominated by the intergranular space. A significant difference with the Ledestone comprises the thickness of the banks and consequently the size of the blocks which is typically smaller than the Lede stone. In addition, sedimentary structures such as lamination or burrows can be more pronounced while a great fossil diversity is absent. Another remarkable difference is the colour of both rock types. As mentioned earlier, Lede stone has a slight light yellow to greenish colour, while a fresh block of Gobertange stone is pale white to light grey. Brussels stone and Lede stone are often co-existing in historical monuments nowadays, often in a fixed arrangement, as both are the result of combined original use or replacement. When found in combination, Brussels stone is dominant in ashlar, while Lede stone is used for corner blocks and door and window frames, or as horizontal lines interbedded in the Brussels stone masonry.

Euville stone (Fig. 8.6B) is a well-sorted crinoidal limestone from Commercy and its surrounding towns in the Meuse Department in northern France, about 40 km northeast of Savonnières-en-Perthois (Lathuiliere et al., 2003). It belongs to the Lorraine Fm (Oxfordian, Upper-Jurassic). The fabric is made by an accumulation of coarse crinoidal ossicles in submarine dunes. Accessory bivalves and echinoderm spines can be found. The crinoids are bound by a syntaxial cement with a high intergranular porosity. This gives the stone a homogeneous, granular aspect with a white-grey colour. Macroscopically, the stone has a

homogeneous, coarse-grained aspect, often with a shiny aspect due to the calcite cleavage of the crinoids. The formation of black crusts and sugaring is a typical weathering aspect.

Savonnières stone (Fig. 8.6C) is an oolitic limestone from the northeast of the Paris Basin: Savonnières-en-Perthois in the French Meuse Department (Fronte, 2000). It stratigraphically belongs to the Oolithe Vacuaire (Tithonian, Upper-Jurassic). Savonnières is a grainstone composed of vacuolar ooids with a relict concentric texture. These are lined by an isopachous dog tooth sparite cement, which only partly fills the intergranular space. These ooids were deposited in cross-bedded layers. Macroscopically, this cross-bedding is often reflected by the soiling of these vacuolar ooids. Lumachelle layers with concentrated molds of bivalve shells occur within this stone. They break up the macroscopic homogeneity of this stone. The dominant porosity for this rock is intragranular with a relict intergranular porosity.

Massangis stone (Fig. 8.6D) is a Burgundian limestone from the Yonne Department in France (Dessandier et al., 2006). It is extracted from the Oolithe Blanche Formation (Bathonian, Middle-Jurassic). Several varieties of the Massangis exist, which are classified based on colour (and porosity/hardness) ranging from *roche clair* to *roche jaune* with some varieties in between. This colour reflects a different microstructure. The most common replacement stones are the Massangis *jaune* and Massangis *jaune clair*. These are bioclastic oolitic grainstones. The fabric is condensed grain supported with sutured contacts between the calcite ooid grain boundaries. Rhombic dolomite crystals are present at grain contacts and penetrate into the ooids without inheritance of the ooid texture. Bioclasts consist of echinoderm fragments, shell fragments and corals. The latter two have a calcite edge, but dolomitic internal structure. The cement is a combination of blocky euhedral dolomite crystals and smaller sub- to anhedral mixed dolomite and calcite crystals. The dominant porosity is moldic dolomite porosity, with locally some intraparticle porosity associated with ooids. The ageing colour varies from grey to yellow.

San Louis stone (Fig. 8.7A) is probably a variety of the Spanish commercial Arenisca Floresta stone, which belongs to the Catalanian Tàrraga limestone in Spain (personal communication Dr. Marius Vendrell), which is an Oligocene terrestrial limestone. It has a brown colour and a homogeneous macroscopic texture. San Louis is a grainstone

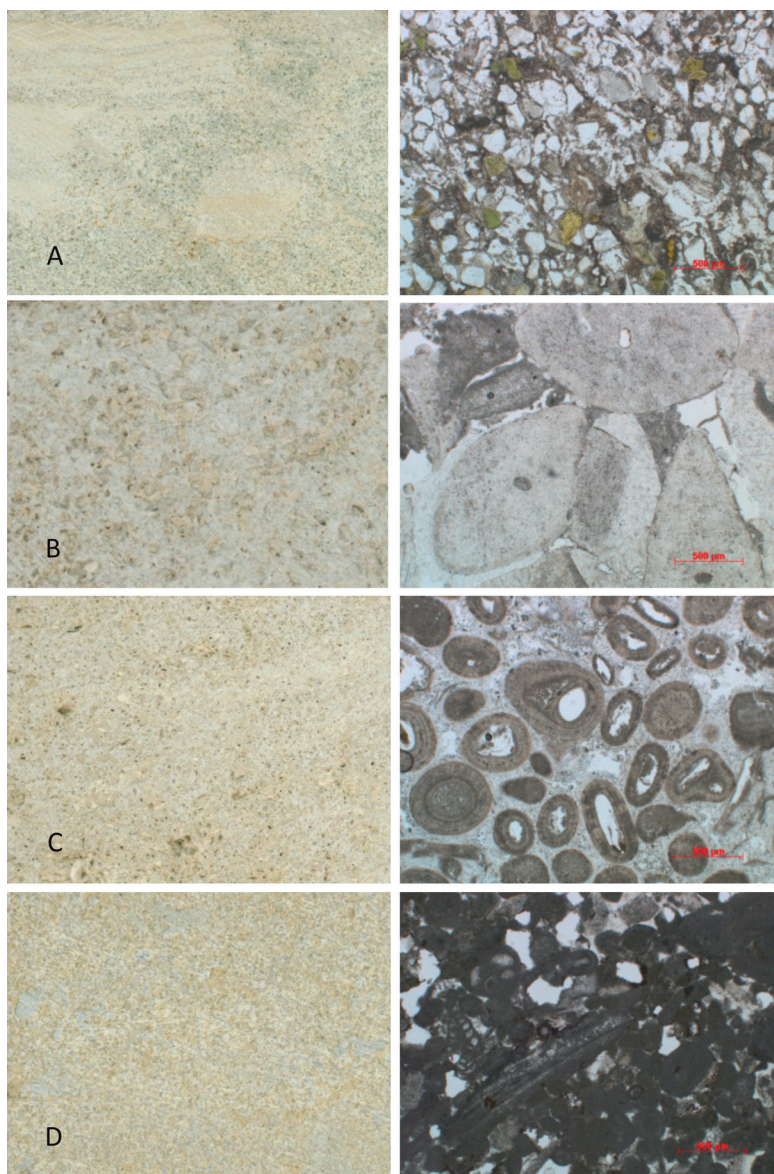


Figure 8.6: Macroscopical and microscopical photograph of A: Brussels stone; B: Euville stone; C: Savonnières stone; D: Massangis roche jaune.

with subhedral to euhedral dolomite with some interbedded micrite calcite grains. The fabric is grain supported without a matrix. Therefore, the dominant porosity is intergranular. An amount smaller than 3 % of fine

sand sized quartz grains occurs randomly throughout the rock.

Azul Bateig stone (Fig. 8.7B) is quarried in the region of Novelda in Alicante (Spain) and is a blue-grey arenaceous limestone with fossil structures. Azul Bateig is a bioclastic packstone with a subordinate quartz and glauconite fraction cemented by granular microsparite with local silicification in molds. Bioclasts consist mainly of forams, echinoderms, bivalves, bryzoa, sponge spicula and rhodophytes. The porosity is both intragranular and intergranular.

Coulmier-le-Sec limestone (Fig. 8.7C) is quarried in the French Côte d'Or Department, Burgundy, from the Middle-Jurassic Oolithe Blanche Formation (Dessandier et al., 2006). Coulmier-le-sec dorée is a bioclastic oolitic grainstone. Ooids and bioclasts are partially to complete micrized. Dominant bioclasts are shells, bivalves, and some forams. The texture is well compacted, with grain contacts and a granular to blocky intergranular calcite cement. Moldic porosity sometimes reveals diamond shaped molds, related to dedolomitization. Iron oxy-hydroxide stains are associated with this moldic porosity.

Reffroy and St Joire stone (Fig. 8.7D) come from the Ornain valley in the Meuse Department (France) and are bioclastic limestones from the Oolithe de Bure (Tithonian, Upper-Jurassic) (Centre d'assistance technique et de Documentation, 1980). They are yellow-grey pseudo-oolitic limestones, bounded by a microsparite cement. The ooids are mainly formed as a cortex on bioclasts.

St Pierre-Aigle stone (Fig. 8.8A) is a laminated packstone from the Eocene Calcaire Grossier in the Aisne Department in France (Centre d'assistance technique et de Documentation, 1980). It is composed of pellets and bioclasts and a subordinate very fine sand sized subrounded quartz fraction. The dominant bioclasts are forams, mainly Miliolina such as *Quinqueloculina* and molds of Cerithiidae gastropods. The cement is intergranular microsparite and the porosity is moldic macroporosity, intergranular and intragranular meso- and microporosity.

St Maximin stone (Fig. 8.8B) is a creamy white to buff-coloured bioclastic packstone to grainstone from the Eocene Calcaire Grossier in the Oise Department in France (Centre d'assistance technique et de Documentation, 1980). Forams are the main bioclasts; amongst them the *Miliolina Quinqueloculina sp.*, *Triloculina sp.* and *Orbitolites complanatus* and also *Textulariina* and *Rotaliina*. Other bioclasts are

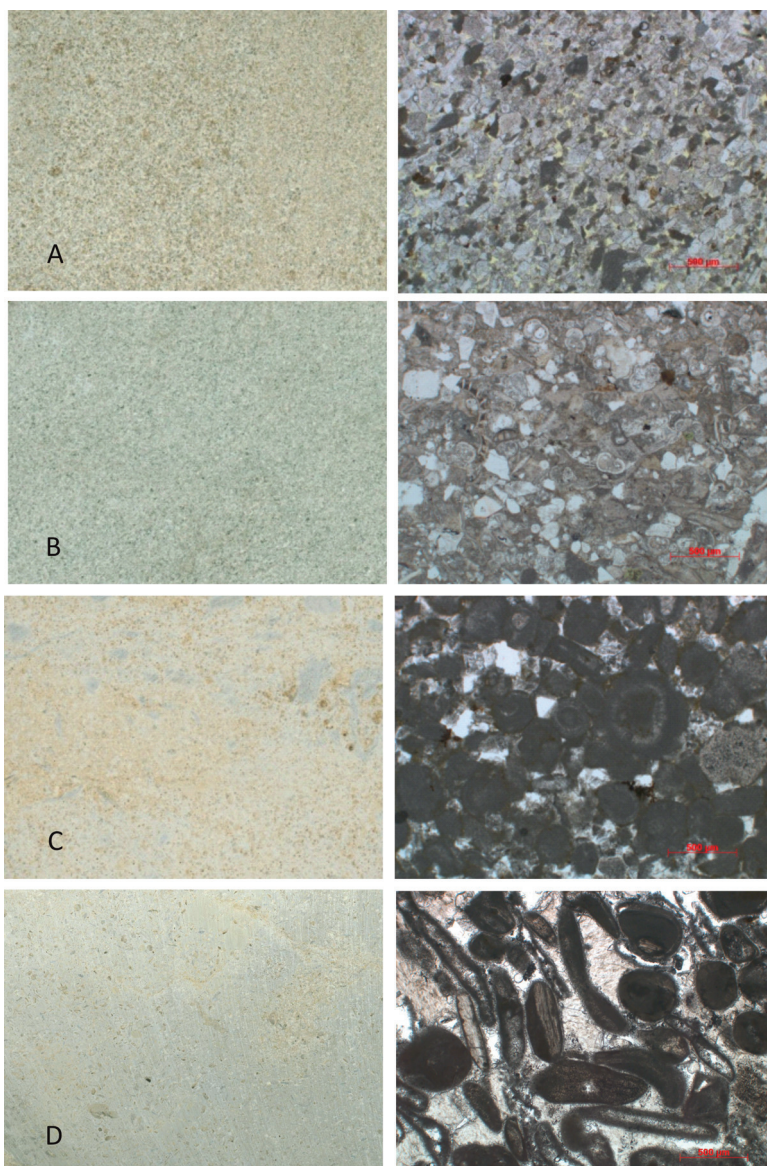


Figure 8.7: Macroscopical and microscopical photograph of A: San Louis stone; B: Azul Bateig stone; C: Coulmier-le-Sec stone; D: Reffroy stone.

echinoderms, red and green algae and bivalves. A fine sand detritic quartz fractions reaches up to 5 %. The granular cement fills part of the inter- and intragranular space, with a remaining high primary porosity. Some

variants are commercially available; the *liais* variant is less porous than the *roche franche* variant, but is also more homogeneous and contains less macroporosity. The *roche franche* variant seems the best fit with Lede stone.

Portland stone (Fig. 8.8C) is an oolitic limestone with (moldic) bioclasts from the Portland Stone Beds (Tithonian, Upper-Jurassic) that outcrop in the Isle of Portland (Dorset, UK) (Hughes et al., 2013). Typically, Portland is a white to creamy oolitic packstone with varying abundance of shelly bioclasts and a micrite matrix. Several variants exist, and while the fine grained variants are too homogeneous and white compared to Lede stone, the Jordans Roach variant contains large shell fragments and molds of turreted gastropods, what could be more interesting.

Larochette or Ernzen stone (Fig. 8.8D) (Hettangian-Sinemurian, Lower-Jurassic) from Luxembourg (Cameran, 1961) mostly connects to the Paris Basin, but is influenced by the Eifel Depression bringing in sandy sediments and forming major sandstone bodies. It consists of mainly very fine to fine quartz grains bounded by a varying amount of Fe-rich calcite cement. Bioclastic fragments can occur throughout the stone. Carbonate rich variants show an ochre patina, whilst carbonate poor variants are white to yellow. Mostly it has a homogeneous texture, but sedimentary structures can occur.

8.3.2 Petrophysical properties of replacement stones

The properties of Lede stone were retrieved from Chapter 5, with the exception of flexural strength, which was tested on a compact Lede stone (Lf1) according to the procedure below. The open porosity and density were measured using the triple weight method by water impregnation under vacuum. After drying, the same samples were imbibed with water under atmospheric conditions by progressive immersion. The saturation coefficient was calculated by the ratio of water imbibition under atmospheric conditions versus vacuum conditions. The capillary absorption was measured on cubic samples with sides of 50 mm and the coefficient was calculated by the regression of the first slope. The ultrasonic velocity was measured by direct transmission with 55 kHz transducers on prisms of $40 \times 40 \times 160 \text{ mm}^3$ in the longest direction. The flexural strength was measured on these samples with a Digi Con 2000 device, by means of an increasing three-point bending load with a span of

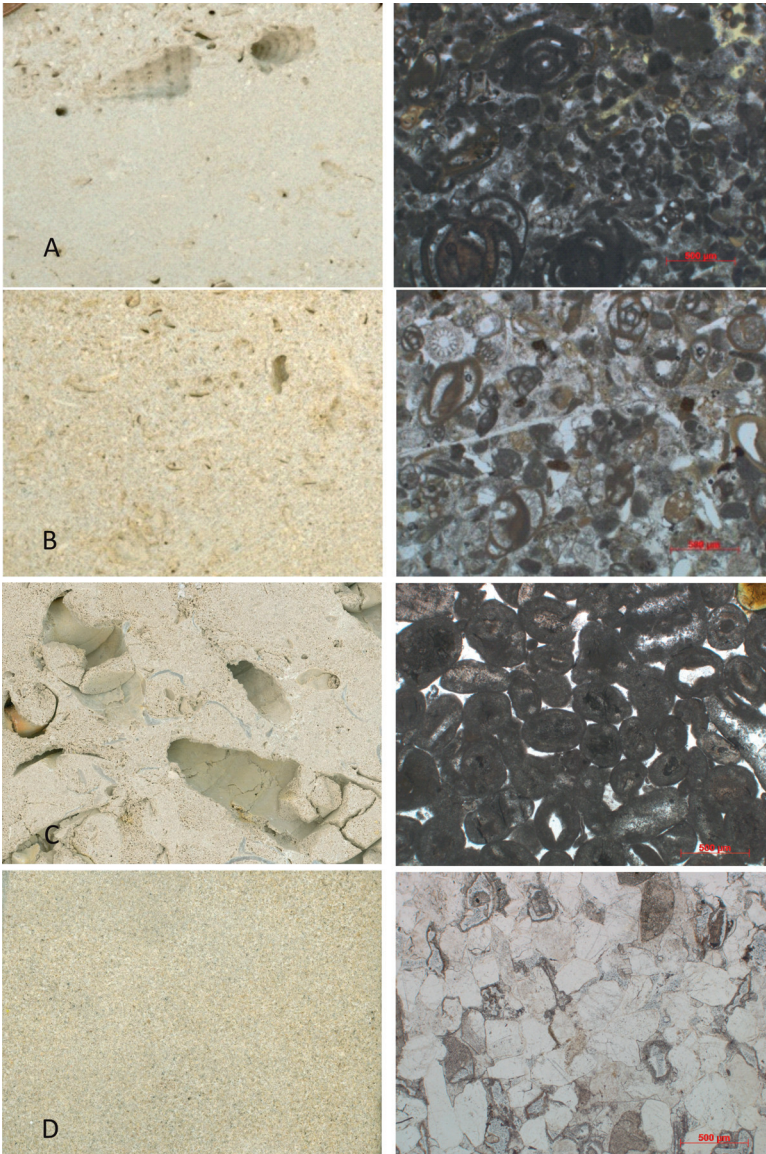


Figure 8.8: Macroscopical and microscopical photograph of A: St Pierre-Aigle stone; B: St Maximin stone; C: Portland stone; D: Larochette stone.

10 cm until rupture. Uniaxial compressive strength was measured by the same device on the retrieved halves of the bending test by increasing compressive load on a $40 \times 40 \text{ mm}^2$ platform. The results are summarized



Figure 8.9: Source locations of the different replacement stones mentioned in Section 8.3.1.

in Table 8.1 and Figure 8.10. The obtained results were completed with data from publications, technical sheets or oral communication, as indicated in Table 8.1.

Table 8.1 and Figure 8.10 show why the replacement of Lede stone has led to the use of many different stones in Belgium and The Netherlands, and why this replacement has been a point of discussion from Van Nieuckerken in 1904 until today. The stones presented in this table and figure have been selected based on either their geological affinity, composition, appearance

and supply potential or a combination of the previous. Nevertheless, their properties can differ significantly from those of the Lede stone. The results show that the porosity of the compact and intermediate Lede stone is quite low compared to the other limestones, with the exception of Brussels stone, and that the strength is relatively high. This is a result of the partially grain-supporting quartz fraction, and the high amount of matrix or cement. In addition and related to the former, also the coefficient of capillary absorption is relatively low.

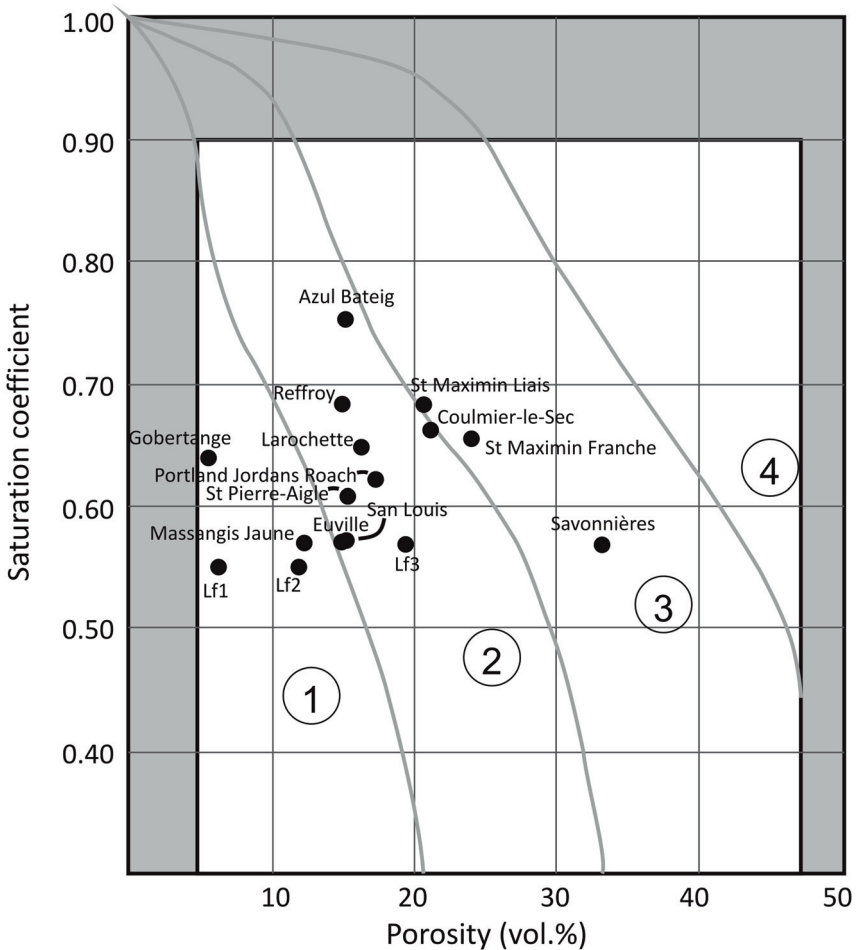


Figure 8.10: Performance diagram (see Figure 5.28) with a plot of the replacement stones based on the properties of Table 8.1.

Table 8.1: The properties of Lede stone (see Chapter 5) and different discussed replacement stones for Lede stone. The properties were measured by the author except where otherwise indicated.

Commercial name	Density kg/m ³	Open porosity vol. %	Saturation coefficient	Capillary coefficient g m ⁻² s ^{-1/2}	Ultrasound velocity m/s	Compressive strength MPa	Flexural strength MPa
Lede stone (Lf1)	2531 ± 26	6.30 ± 0.95	0.54 ± 0.02	4.73 ± 0.37	4348	86	15.6
Lede stone (Lf2)	2416 ± 46	10.95 ± 1.82	0.55 ± 0.02	15.76 ± 8.62	4098	27	
Lede stone (Lf3)	2184 ± 57	19.57 ± 2.13	0.58 ± 0.03	33.55 ± 19.76	3317	8	
Gobertange	2485 ± 18	5.54 ± 0.54	0.64 ¹	5.03 ± 2.88	4587	93.9	12.5
Euville	2297 ± 20	14.57 ± 7.60	0.58 ± 0.01	60–100 ²	3209	32.8	4.8
Savonnières	1816 ± 26	33.04 ± 1.00	0.57 ± 0.03	100–160 ²	3117	14.8	2.7
Massangis ^{Jaime}	2400 ± 48	11.12 ± 2.23	0.58 ¹	25–35 ²	4488	66.3	11.9
San Louis	2310 ± 30	15.54 ± 3.11	0.58 ± 0.12	139.20 ± 1.00	3995	66.0	11.5
Azul Bateig	2250 ± 5	15.72 ± 0.13	0.76 ± 0.00	24.90 ± 72	3571	53	10.4
Coulmier-le-Sec	2119 ± 22	21.61 ± 0.81	0.68 ± 0.01	91.96 ± 7.18	3960	38.6	6.1
St Pierre-Aigle	2262 ± 35	15.11 ± 3.02	0.61 ± 0.12	19.05 ± 1.84	4203	50.1	12.2
St Maximin ^{Franche}	2026 ± 22	24.82 ± 0.92	0.67 ± 0.04	65.23 ± 4.70	3620	32.5	7.0
Portland ^{Jordans Roach}	2195	17.43	0.62		44.2	3.9	
Larochette ⁴	2180	16.6	0.65 ⁵	87.2–91.4		50.9	1.4
Reffroy ⁷	2200–2350	13–18	0.68–0.72 ⁵			30–50	

Data completed from: ¹ Dusar et al. (2009); ² technical data Rocamat; ³ technical data Albion stone company; ⁴ technical data carrières Feldt;

⁵ calculated from technical sheet; ⁶ oral communication Jolien Delepiere; ⁷ Camerman (1957).

8.3.3 Discussion

It are mostly pure limestones that have been used as replacement stones. Only Brussels stone and Larochette stone are limestones with a significant detrital quartz population. On the other hand, Bentheimer stone is pure sandstone and the lack of carbonate and bioclasts is a serious disadvantage for its use as replacement stone for Lede stone, in terms of technical compatibility. Moreover, its homogeneous texture, its dark discolouration and the lack of carbonate in its weathering processes result in a poor aesthetical compatibility.

Brussels stone and Larochette stone have the best mineralogical compatibility. However, the Gobertange variant is striking different in its texture (the presence of burrows), colour (white-grey) and size (small), whilst the Diegem variant is no longer excavated. Equally important is the fact that it has a similar historical value in the built cultural heritage. Therefore, replacement of Lede stone by Gobertange diminishes the historical variability which might not be advisable. Larochette stone is very homogeneous, which results in a limited aesthetical compatibility.

Amongst the limestones, Mesozoic oolites are the most abundant. Euville is an exception, being a crinoidal limestone. Its homogenous, coarse grained texture, its colour and its weathering upon ageing are relatively different from that of Lede stone. Reffroy and St Joire are more compact, yellow to grey and bioclastic limestones, which correspond much better to Lede stone than the crinoidal or oolitic limestones. The historical choice for these stones can be justified, but today they are no longer available. Savonnières is the most pure oolitic limestone. It is very porous and relatively homogeneous with the exception of regular cross-bedded structures. It is easily workable, but texturally it has no affinity with Lede stone. Massangis jaune is the most used replacement stone, which certainly has to do with economic factors and availability, but its yellow colour is often better suited compared to most other oolitic limestones. Moreover, although the bioclast fraction is totally different from that of Lede stone, the presence of macrofossils grants somewhat textural amenity, which also applies for Lede stone. The same goes for Coulmier-le-Sec, but this stone is more porous. Portland stone is whiter than Massangis jaune and therefore it seems aesthetically less suited. Especially when Lede stone is used in combination with Brussels stone, Portland is not a good replacement for Lede stone as its colour will relate

more to that of Brussels stone. However, a specific variant of Portland could be interesting when it concerns fossiliferous Lede stone (Lf3). Portland Jordans Roach contains an accumulation of grey shelly material and large turreted gastropod molds. This grants the stone a high textural variability and amenity, which can be found in the fossiliferous Lede stone. Moreover, the presence of these shells and molds breaks the white colour, which is certainly an advantage.

Resources from the Calcaire Grossier, St Pierre-Aigle and St Maximin, have the advantage that they are not oolitic limestones. Moreover, they contain a fossil fauna which relates to that of Lede stone. As Portland Jordans Roach, St Pierre-Aigle also contains turreted gastropod molds. This could be adequate for the replacement of fossiliferous Lede stone. St Maximin is more fine grained, but contains an important foram fauna and it is more brownish. This could be an advantage for an aesthetical match with more compact Lede stone, compared to the aforementioned limestones.

Finally, San Louis has a low geological affinity with Lede stone and is dolomitic. The colour, on the other hand, is an advantage. It is however not clear how this stone will age over time in the Belgian climate. Azul Bateig is probably the best match of the aforementioned stones for fresh Lede stone which is yellowish to greenish grey. There is some geological affinity in the fossil fauna and Azul Bateig also contains some glauconite. As for San Louis, however, it is not yet known how the stone will age in the Belgian climate.

Based on the technical properties, none except the Brussels stone fulfill the requirements listed by Snethlage and Pfanner (2013). Brussels stone has the best technical compatibility, but the use of Gobertange should be avoided for aesthetical and historical compatibility. From the other investigated stones, Massangis jaune has the most technical compatibility with the compact and the intermediate Lede stone. It is followed by Reffroy, San Louis and Azul Bateig. Together with the aesthetical characteristics, the recent use of San Louis and Azul Bateig can be justified. However, the saturation coefficient of Azul Bateig is relatively high and more tests about its durability and water transport behaviour is advisable. Especially the resistance to freeze-thaw cycling needs to be investigated, as the stone is sourced in a region with less to none wet freeze-thaw cycles. While Azul Bateig resembles best the fresh coloured Lede stone, the brown colour of San Louis could be seen as more fitting

for the yellow to brown patina of aged Lede stone. This is especially an advantage when Lede stone is used in an architectural combination with the more white Brussels stone as in the wall dormers of the Caermers monastery in Ghent (Fig. 8.2). Unfortunately, the capillary water absorption is high and the stone risks to be more damp in the Belgian climate than Lede stone. This is another issue which needs to be explored more thoroughly in the future, by evaluating the sites where it has been used today.

In terms of technical compatibility, the use of other stones to replace compact and medium porous Lede stone does not seem advisable. However, St Pierre-Aigle and St Maximin have a relative better aesthetical and compositional compatibility to Lede stone compared to the oolitic and crinoidal limestones. When used in a relatively protected environment, such as masonry, and especially when entire units need to be replaced, the use of one of both could be beneficial.

For the range of intermediate to fossiliferous Lede stone, it can be seen that Portland Jordans Roach and St Pierre-Aigle show a relatively good technical compatibility. Together with the aesthetic compatibility, the use of one these rocks for these porous types of Lede stone seems a good option.

It should be noted that Lede stone is quarried by Balegro in Balegem. Although it is good to deal with these resources in a conscious way, their availability implies that the potential use of Lede stone itself should premise all other decisions.

8.4 Conclusion

Over the last two centuries, Lede stone has been replaced by a diversity of alternative stones. The selection of an appropriate replacement stone was not purely on historical, aesthetical or technical compatibility, it was also strongly influenced by socio-economic factors, such as the availability and the price of the stones. Nevertheless, the awareness for aesthetical and technical compatibility has contributed to the discussion and quest for adequate replacement stones over the last century. For example, Van Nieukerken studied possible replacement stones in 1904, Camerman gave advise on the qualities of replacement stones in in 1958, and Breda discussed the massive use of Massangis jaune in 2005. The latter was the

most common replacement stone in northwestern Belgium, but new alternatives such as Azul Bateig and San Louis have been suggested and applied over the last decade.

When replacing Lede stone, a careful analysis should be made of the original stone. Is it compact, or porous and fossiliferous? And what is the architectural context? Is it part of an integral construction of Lede stone, or is it used in combination with other materials such as Brussels stone? For restorations where historical compatibility is the most important, the use of Lede stone should be preferred. In this context, also Massangis jaune (or jaune clair) can be used when older replacements were done in Massangis. In situations where aesthetical compatibility is the most important, St Pierre-Aigle, St Maximin or Portland Jordans Roach could be considered if the use of Lede stone is not an option. Also Azul Bateig and San Louis are potentially beneficial, although water absorption behaviour should be further assessed. In Chapter 4 it was shown that the ageing of the stones is an important aspect in the appreciation and thus the aesthetical compatibility. Therefore, the aspect of ageing should be taken into account and the ageing of Azul Bateig and San Louis in the Belgian climate should be evaluated. In restorations where aesthetical compatibility is important, it might be considered to pay attention to the stone finishing, as straight blocks do not give this ageing aspect. When a technical compatibility is the most critical aspect, Lede stone or alternatively Massangis jaune are the most feasible options for compact to intermediate Lede stone. For intermediate to fossiliferous Lede stone, St Pierre Aigle or Portland Jordans Roach might be considered. Nevertheless, this indicates the need for a thorough study of the natural stone in upcoming restorations.

References

- K Breda. De 'carrière' van een architect. In *ICOMOS contact*, volume 18, pages 20–24, Leuven, 2005.
- C Camerman. *Les pierres naturelles de construction*. Imprimerie N.I.C.I., Gent, 1961.
- Centre d'assistance technique et de Documentation. *Les pierres de France : pierres calcaires roches marbrières granit grès*. Moniteur, Paris, 1980.
- V Cnudde, J Dewanckele, M De Ceukelaire, G Everaert, P Jacobs, and M C Laleman. *Gent...Steengoed!* Academia Press, Ghent, 2009.
- T De Kock, J Dewanckele, M. Boone, G De Schutter, P Jacobs, and V Cnudde. Replacement stones for Lede stone in Belgian historical monuments. *Geological Society, London, Special Publications*, 391(1): 31–46, mar 2014. ISSN 0305-8719. doi: 10.1144/SP391.9.
- F De Smidt and E Dhanens. *De Sint-Baafskathedraal te Gent*. Lannoo, Tielt, 1980.
- E De Witte. Natuursteen in de monumentenzorg: vervangen of conserveren? *Bulletin de la Société belge de Géologie*, 99(2):197–205, 1990.
- J B Delbecq. *Eenige bijzonderheden van Ghendt tesaemen gebragt tot myn geheugenisse*. 1774.
- D Dessandier, G Ambroise, and A Longet. Mémento des pierres ornementales & de construction de la région Bourgogne. Technical report, BRGM, 2006.
- E Dhanens. *Sint-Baafskathedraal Gent*. Provinciebestuur Oost-Vlaanderen, Gent, 1965.

- R Dreesen, V Cnudde, M Dusar, M De Ceukelare, D Bossiroy, E Groessens, J Elsen, T De Kock, and J Dewanckele. In het voetspoor van Camerman: de opmars van de Franse steen in België. In R P J Van Hees, H De Clercq, and Quist W J, editors, *Stenen van binnen, stenen van buiten: natuursteen in de jonge bouwkunst*, pages 33–63, Delft, 2012. Delftdigitalpress.
- M Dusar, R Dreesen, and A De Naeyer. *Natuursteen in Vlaanderen - Versteend verleden*. Kluwer-Wolters Belgie nv, Mechelen, 2009.
- Fronte. L'Oolithe Vacuolaire: caractéristiques, mise en oeuvre et altération. *Bull. Inf. Bass. Paris*, 37(3):34–39, 2000.
- T Hughes, G K Lott, M J Poultney, and B J Cooper. Portland Stone: A nomination for "Global Heritage Stone Resource" from the United Kingdom. *Episodes*, 36(3):221–226, 2013.
- ICOMOS. The Venice Charter - International Charter for the conservation and Restoration of Monuments and sites. Approved by the 2nd International Congress of Architects and Technicians of Historic Monuments. Technical report, Venice, 1964, 1966.
- B Lathuiliere, C Carpernier, G Andre, G Dagallier, M Durand, M Hanzo, V Huault, D Harmand, C Hibsich, J Le Roux, F Malartre, B Martin-Garin, and L Nori. Production caronatéée dans le Jurassique de Lorraine, 2003.
- R Nijs. Tertiaire kalksteen en Franse witte steen als natuurlijke bouwsteen voor onze historische monumenten. *Bulletin de la Société belge de Géologie*, 99(2):115–121, 1990.
- W J Quist. *Vervanging van witte Belgische steen: Materiaalkeuze bij restauratie*. PhD thesis, TU Delft, Delft, 2011.
- R Snethlage and M Pfanner. *Leitfaden Steinkonservierung*. Fraunhofer IRB Verlag, Stuttgart, 2013.
- G Van Bockstaele, J Van Bockstaele, and M Van Bockstaele. *Inventaris van de kerkarchieven van Gent - Deel I: St.-Baafskathedraal, St.-Michiels-en St.-Niklaasparochie*. Oost-Vlaams Verbond van de Kringen voor Geschiedenis, Zottegem, 2014.
- M Van Liedekerke and M Verhasselt. *Steenrijk Dilbeek*, 1998.
- J Van Nieuland, D Vandenberghe, F Gelaude, and P Van den Haute. Absolute dating of aeolian sediments in relationship to the development

of the city of Ghent: first results. *Mediterranean Archaeology & Archaeometry*, 13(3):25–35, 2013.

9

The identification and characterization of white limestone in the 12th century tower of Dudzele: a reflection

A good knowledge base on natural stone in monuments is crucial for an adequate and successful restoration. First of all, the identification of the stone type is important for the historical context of the monument. Secondly, it permits to consider the same stone type as replacement stone, if necessary. Or, if the particular stone is no longer available, to evaluate possible replacement stones based on the properties of the original. In addition, a description of the damage can indicate the prevailing weathering agents, something to incorporate in the long term strategy for the preservation of the monument. As such, each of the previous chapters aims to contribute to some of these specific considerations. Together, they contribute to the general knowledge of Lede stone in our historical monuments and they can be used for further approaches in conservation. Although Lede stone was often replaced, sometimes it appears to have been used as a replacement stone itself. In this chapter, the principles of natural stone restoration elaborated in the previous chapters are extended to a situation with another unknown stone type, which was in turn replaced

by Lede stone. This chapter is based on De Kock et al. (2015), where Dr. Wesley De Boever assisted in the survey and Dr. Jan Dewanckele and Dr. Marijn Boone in the sampling.

9.1 Introduction

The ruins of the medieval tower of Dudzele (Province of West-Flanders, Belgium; Fig. 9.1) are the only remnants that nowadays testify of the former Romanesque pilgrimage church erected in stone from the 12th century onwards. Durable construction materials like stone allow to investigate remains of nine centuries of history at this location. In fact, natural building stones are of great importance for the built heritage (e.g. ICOMOS, 1966; Prikryl and Török, 2010; Smith et al., 2010; Cassar et al., 2014). Their present-day value is considered crucial as they reflect the historical use of natural resources, historical trade ways and architectural development of a region. However, their present-day condition may largely differ from the original one as a result of stress factors acting on the stone over time (McCabe et al., 2010). For safety, functionality and both aesthetic and historical considerations it is important to conserve natural stone within historical buildings. In order to respect the building's authenticity and character, it is therefore necessary to decipher the stone's origin, its current condition and the environmental changes to which the stone was exposed over time. The onset of each respectful and durable restoration project thus typically requires a preliminary case-study of the material's identity and condition.

Currently, public access to the medieval tower ruins of Dudzele is prohibited because of hazardous falling debris. The new restoration project aims to restore the building's stability and functionality whilst preserving the original building material as appropriate as possible. Unfortunately, not all materials used were documented or archived. Therefore, our research aims are to determine the unknown origin and to assess the deterioration and performance of the stones and establish criteria for replacement stones. As most of the stones could be identified macroscopically as Fieldstone, Römer tuff, Lede stone and Luxembourg sandstone, special attention was paid to a buff-coloured limestone with a packstone texture composing the lower façade.



Figure 9.1: Tower ruin in Dudzele as seen from the northwest. The lower façade is mainly built with buff-coloured limestone, the upper masonry with Fieldstone and parts in brick.

Historic environmental and anthropological significance

Dudzele is located in the Belgian polders, approximately 7 km from the North Sea coast. In the 12th century, the Zwin inlet extended more inland in the direction of Dudzele (Fig. 9.2). The Zwin's natural tidal channels and artificial waterways provided the area with excellent transport routes to which cities as Bruges (Belgium), Damme (Belgium) and Sluis (The Netherlands) owed their medieval wealth (Charlier, 2011). In the period between 1150–1161 A.D., the town of Dudzele started the construction of a major Romanesque church (Wintein, 1967). Later expansions with chapels reflect the maintenance and ongoing use of this religious building during the 14th and 16th century. However, from the second part of the

16th century onwards, socio-economical instabilities jeopardized and threatened its further development. A religiously inspired revolution associated with the Protestant iconoclasm of 1566 stripped multiple churches from their rich decoration and religious wealth. During the following Eighty Years' War, the church was looted and vandalized in 1583. It never regained its old glory and was only partially repaired using bricks instead of natural stone. In addition to these anthropological threats, the climatic changes brought along by the Little Ice Age could have induced an additional environmental stress to the stone. In 1673 the crossing tower finally collapsed, probably as a result of environmental and anthropological stress combined with inadequate maintenance. It was then decided to construct a new church, partly on the older fundamentals. In the beginning of the 18th century another part of the remains collapsed. Most of the original church has now fallen into ruins with the exception of the tower still present today. This remaining tower is the southern one of two, which were originally flanking the main westerly entrance (Fig. 9.1 and 9.3). Above these a new bell tower was built in brick. Although poorly documented, this tower ruin was restored in the early 1900's and again in 1972. A new restoration is planned for 2016.

9.2 Methods

The natural building stones were identified based on macroscopic determination (with the naked eye). Stones which could not immediately be identified were sampled for further microscopic study. A historical background check was performed to list the main construction and destruction phases. A cartography of the lower façade limestone was made by visual observation (Fig. 9.3 and 9.4). The buff-coloured limestone in this façade was subdivided in three categories based on the following criteria: volume intact (category A); visible deterioration with visible fissures or cracks, meteorological weathering and partial loss of volume (category B); strong retreat of surface with high loss of volume and sanding (category C).

A Zeiss Axioscope with AxioCam was used for optical microscopy on 30 μm thin sections. SEM-EDX was carried out on polished sections with a JEOL II SEM. X-ray diffraction (XRD) patterns were collected with a Philips X'PERT system and interpreted using X'PERT HighScore

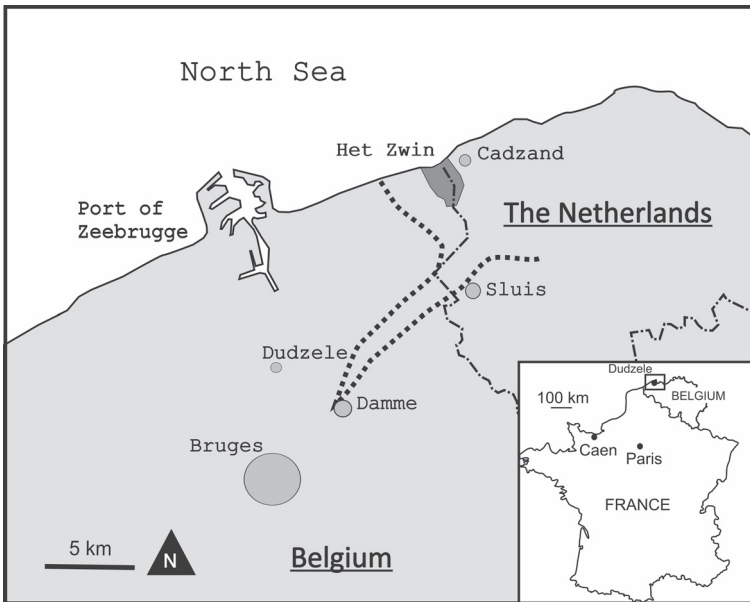


Figure 9.2: Location map of Dudzele with respect to Bruges, the North Sea and The Zwin. The present-day extent of The Zwin is shaded, while its extent in the 12th century (adapted from Wintein (1967)) is represented by the dashed line.

Software. μ CT was performed at the UGCT using a custom-built set-up (Masschaele et al., 2007). The X-ray tube was operated at a power of 9 Watt and a voltage of 100 keV. The sample diameter was 2 mm and the obtained voxel resolution is 3.69 μ m. Octopus software (Vlassenbroeck et al., 2007) was used for reconstructing the images and Octopus Analysis software for 3D image analysis (Brabant et al., 2011).

Physical properties were determined in the lab after cutting the samples to cubes of 50 mm \times 50 mm \times 50 mm. Open porosity (P_o) and apparent density (ρ) were determined according to European standard EN 1936 (2006). The coefficient of capillary absorption (C) was determined using EN 1925 (1999). Sound speed propagation (US) was measured using 14579 (2004) with 55 KHz transducers on the large samples before cutting into cubes. Uniaxial compressive strength (UCS) was determined according to EN 1926 (2006).

Accelerated weathering tests were used to assess the stone's performance. Frost susceptibility was tested on 11 samples in an adapted Weiss climate chamber during 48 freeze-thaw cycles (N_c) according to the technological

test EN 12371 (2010) using compressive strength as characterization method. Salt weathering was determined according to EN 12370 (1999) using $\text{Na}_2\text{SO}_4 \cdot 10\text{H}_2\text{O}$ as attacking salt, performing 15 cycles of imbibition and subsequent drying at 105 °C. The heating experiment for the fire simulation was performed on 12 samples with dimensions of approximately 10 mm × 10 mm × 20 mm. Six times two samples were heated for three hours in a muffle oven at six different temperatures respectively (150 °C, 300 °C, 450 °C, 600 °C, 750 °C en 900 °C), similar to Gillhuber et al. (2010).

9.3 Materials

Based on the results of the cartography observation of the ashlar masonry, a category A block was removed from the wall for further analysis as its properties were considered the best possible match with the original stones. The block was cut into 27 cubes with dimensions of 50 mm × 50 mm × 50 mm to be used for physical and accelerated weathering tests. From the remaining volume, subsamples were retrieved to determine texture and composition with special attention for sampling both crust and bulk. Salt samples for XRD were obtained from efflorescence material after performing capillary absorption.

Fresh quarried blocks of Caen stone *ferme* and *demi-ferme* were delivered by Pierre Paris from the Cintheaux quarry in France. Caen stone is quarried as a building material from the upper layers of Calcaire de Caen Formation, middle Bathonian platform carbonates which crop out in the surroundings of Caen in northwestern France. They have been exploited and exported overseas from the 11th century onwards and production sites have existed at several locations. Today they are quarried in the Cintheaux quarry, located approximately 15 km SSE of Caen, as two commercial varieties: Caen *ferme*, a denser, and Caen *demi-ferme*, a softer variety. The technical properties of these rocks are listed in Table 9.1.

9.4 Results and discussion

9.4.1 Stone and architecture

The restoration of historical monuments constructed in natural building stones requires the exact determination of the different stone types and in particular the knowledge of their composition and physical properties. Most of the stone types used in the tower ruins of Dudzele could be determined visually based on previous documentation about historic building materials in northern Belgium and The Netherlands whilst their composition and physical properties are well known from literature (e.g. Gullentops and Wouters, 1996; Cnudde et al., 2009; Dусar et al., 2009). Green sandstone is used as rubble masonry for massive and high walls. This stone type originates from nearby Eocene outcrops and is locally named as Fieldstone. Fieldstone outcrops in northwestern Belgium are found from the North Sea coast to the south of Ghent, but it has shown to be very hard to locate the exact quarry site for artifacts and local building stones. This glauconite rich sandstone is very resistant to weathering. Also Römer tuff, a volcanoclastic rock, is recognized in small quantities. This stone is widely used in Dutch Romanesque architecture (Nijland, 2015) and to a lesser extent in northwestern Belgium (e.g. Debonne and Dreesen, 2015).

In the present study, two stone types could not be identified by macroscopic observations only: a buff-coloured limestone and a white chalk. Moreover, it was not clear whether these are original stones or subsequent replacement material. Thin sections were therefore prepared in order to identify the nature of these two stone types. The buff-coloured limestone was used in the lower part of the façade. This stone type does not belong to the regular local building stones in northwestern Belgium. It was probably imported for its architectural function, to serve as freestone (i.e. fine-grained, easily shapeable building stone) at the western entrance of the church. This smooth finished masonry contrasts with the ascending rubble wall of the tower built in the local Fieldstone. This buff-coloured limestone shows different weathering patterns; locally, they have been replaced by both Lede stone (Belgium) and Ernzen or Larochette (Luxembourg) sandstone (Grand Duchy of Luxembourg).

The white chalk, a stone type often denominated as *tuffeau*, occurs as dimension stone in arcs and engaged columns, often in combination with

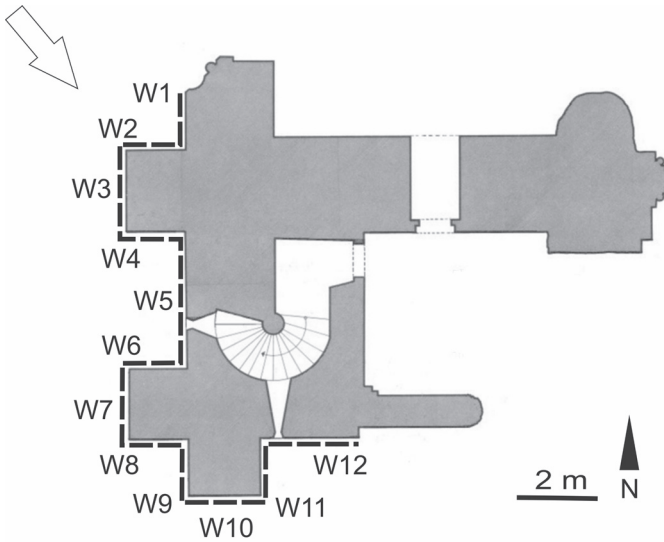


Figure 9.3: Floor plan of the tower ruins. Dashed lines indicate where the lower ashlar masonry is composed out of buff-coloured limestone and where cartography was performed.

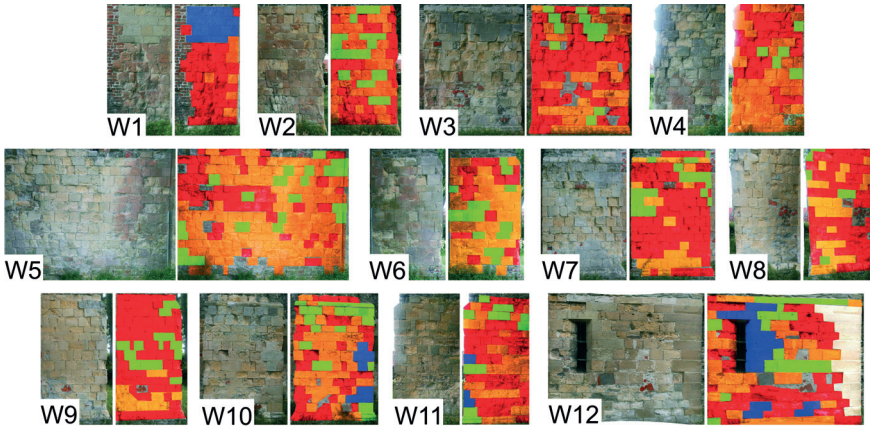


Figure 9.4: Cartography of the different walls as indicated on Figure 9.3, with three colours for the buff-coloured limestone. Intact stones (category A) are coloured in green; stones with cracks or partial loss of volume (category B) in orange; stones with surface retreat (category C) in red. Replacement stones are given in blue (Lede stone) and white (Luxembourg sandstone).

the buff-coloured limestone. Literature documents the old, nowadays disappeared, crossing tower to be constructed out of white stones (Wintein, 1967). Possibly, this concerns either the buff-coloured limestone or the white chalk.

9.4.2 Identifying the buff-coloured limestone

The buff-coloured limestone (Fig. 9.5) can be classified as a bioclastic pelloidal packstone (Dunham, 1962) or a biopelmicrite (Folk, 1959). Its homogeneous structure shows no clear bedding. Its main components consist of faecal pellets and bioclasts (Fig. 9.6A). The ratio of pellets to bioclasts varies amongst the samples but in general the amount of pellets is larger than that of the bioclasts. Echinoderm fragments and forams make up the bioclast fraction. A minor amount of silt sized quartz is present in the bulk. Ooids have not been observed. The texture is grain-supported, with intergranular micrite or minor amounts of syntaxial sparite. XRD patterns confirm the presence of calcite and quartz, but do not reveal significant peaks of other minerals. However, small amounts of pyrite can be observed in SEM-BSI pictures (Fig. 9.7). In addition, SEM-EDX also reveals silicification to occur in the interparticular pore space. This phase is greenish in thin sections, indicating the presence of traces of iron in its reduced form (Fig. 9.6B). In accordance to petrographic descriptions (Palmer, 2008a), this buff-coloured limestone can possibly be identified as Caen stone.

There is no historical use of Caen stone documented in northern Belgium. However, it is known that Caen stone was exported along the Channel and the North Sea to be used in northern parts of France and England since the 11th century (Dugué et al., 2010). Thus during construction of the Dudzele Romanesque church, Caen stone was exported towards the north over the Channel. Because of its vicinity to the North Sea and the Zwin tidal inlets, the import of Caen stone for the Dudzele crossing tower construction definitely seems possible. Nevertheless, similar facies can be found in the Jurassic deposits of the Boulonnais area (France) (oral communication Prof. Gilles Fronteau) and although Caen stone makes a good match with the buff-coloured limestone from Dudzele, it could not be excluded that the resources came from the Boulonnais area.

The good match of the buff-coloured limestone with Caen stone can be confirmed by corroborating research results for the physical properties

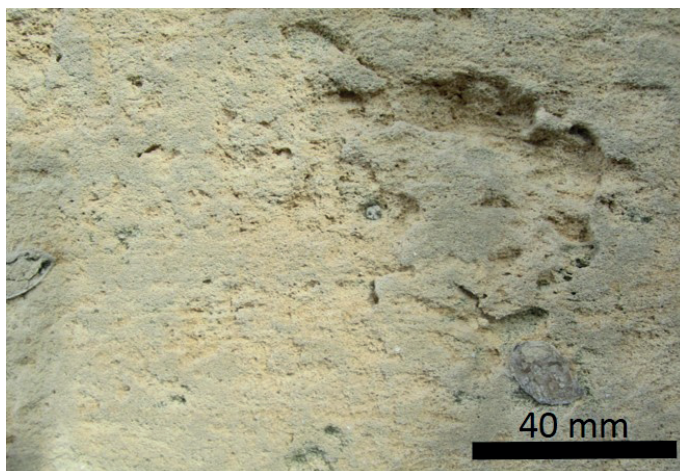


Figure 9.5: Macroscopic image of the buff-coloured limestone from Dudzele, identified as Caen stone.

with reference values. Moreover, based on these properties, an appropriate replacement stone could be selected. The results of the physical tests are listed in Table 9.1. The Caen stone from Dudzele has an intermediate (13.91–18.79 vol.%) porosity. The porosity is highly comparable with the Caen stone *ferme* variety. As tests were performed on a category A stone (Figure 9.4, Table 9.2), it is plausible that these intact stones represent Caen stone *ferme* that have been mingled within the wall with more weathered Caen stone *demi-ferme* varieties, which are represented by category B and C stones (Fig. 9.4, Table 9.2). The latter are more porous, softer and have a lower compressive strength, mainly due to the dominating presence of pellets over crinoids (Palmer, 2008b), a feature also observed in several of our thin sections of samples across the façade.

The capillary rise test caused a salt (halite and gypsum; see Section 9.4.3 and Table 9.3) efflorescence at the surface. This can explain the lower coefficient of capillary absorption of the Dudzele samples ($30.09 \text{ g m}^{-2} \text{ s}^{-1/2}$) compared with the reference values of Caen stone *ferme*. The presence of water soluble ions in the pore system due to several wet-dry cycles and exogenous ion supply probably over the centuries caused a pore-clogging effect, resulting in a lower capillary absorption of the stones from Dudzele. The values of US and UCS are comparable to reference values of Caen stone *ferme* (Table 9.1). Ultrasound velocity is strongly influenced by mineral composition, rock fabric, the pore space

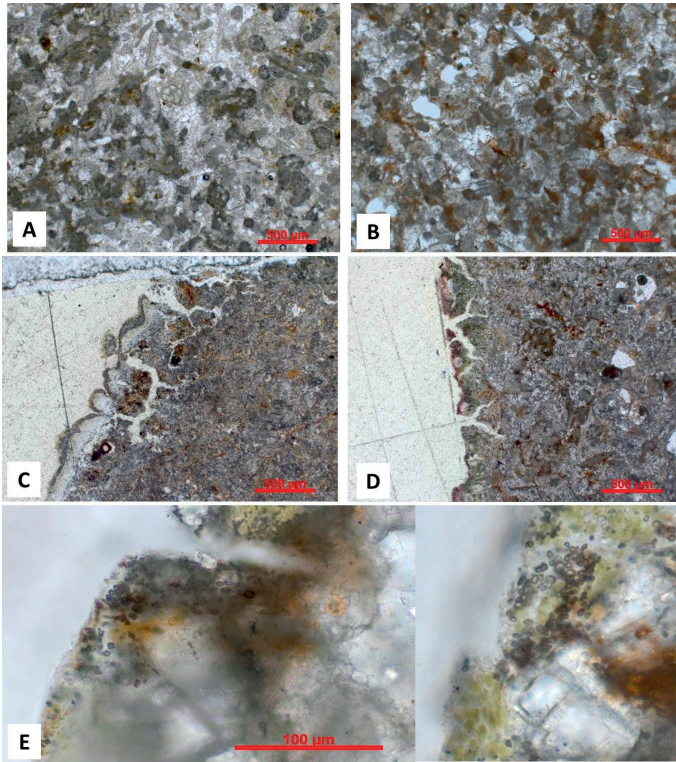


Figure 9.6: A) Thin section micrographs of buff-coloured limestone illustrating the packstone texture with dominant pelloidal components; B) discolouration in the crust section; C and D) growth of saxicolous lichens; E) detail of lichens with individual cells.

and the pore content such as fluids. As the stones were dry, the influence of pore fluids can be excluded, but salt present in the pore network could still influence the results. The values of US are 5.06 % lower than reference values of Caen stone *ferme*. This could be caused by natural heterogeneity of the source rock. However, as evidenced above, the Caen stone from Dudzele and the fresh quarried Caen stone *ferme* have similar mineralogy, fabric and open porosity. The lower ultrasound velocity of Caen stone from Dudzele might be caused by the presence of (micro-)fissures within the rock. This seems to overrule the presence of salts in the pore network, which could increase US by pore clogging.

With exception of the capillary absorption because of the before mentioned pore clogging, the petrophysical values of the Caen stone *ferme* thus fall

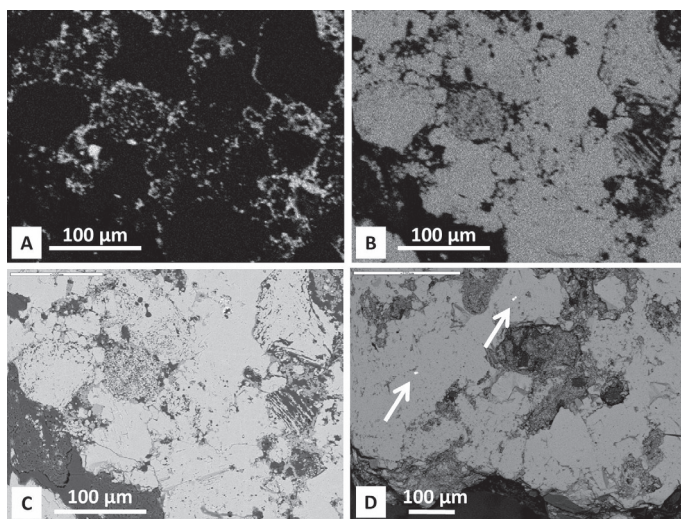


Figure 9.7: SEM-EDX images with A) Si-map; B) Ca-map; C) SEM-BSI image of mapped area; D) SEM-BSI image with pyrite particles indicated by arrows.

	ρ kg/m ³	P _o vol.%	C g m ⁻² s ^{-1/2}	US m/s	UCS MPa
Dudzele stone	2212 ± 71	16.4 ± 2.0	30.09 ± 6.58	3304 ± 43.3	43.3 ± 14.2
Caen stone <i>ferme</i>	2280	16.1	48.8/52.0	3480/3612	40.1
Caen stone <i>demi-ferme</i>	2050	24.4	106.2/117.6	2915/2970	25.9

Table 9.1: Physical properties of buff-coloured limestone samples from the tower ruin of Dudzele (tested) and Caen stone (technical information of the Cintheaux quarry).

within a 80–120 % range of those of the Dudzele stones, suggesting the use of Caen stone from the Cintheaux quarry as replacement stone (Snethlage and Pfanner, 2013).

9.4.3 Deterioration and performance

Different deterioration patterns involve forms of cracking, detachment, material loss, discolouration, deposit and biological colonization according to the ICOMOS-ICS (2008) (Fig. 9.8). Close analysis of the

cartography images reveals that the majority of stones underwent structural damage as most stones show partial or severe loss of volume. The percentage of each class as described in the sections 9.2 and 9.3 is displayed in Table 9.2. There exists no clear relation between the percentage of intact stones and the orientation of the wall, nor a constant ratio of intact to weathered stones, which convincingly illustrates the importance of individual stone quality.



Figure 9.8: Macroscopic view (field of view approximately $1.5 \times 1.5 \text{ m}^2$) of lower ashlar masonry of buff-coloured limestone with fissures and cracks, spalling, sanding, alveolization, soiling and red discolouration with large scaling.

The main structural damage is showcased by fissures and cracks and eventually surface retreat by spalling and sanding. Cracking and spalling often occurs below a reddish discoloured crust. This red discolouration penetrates up to 5 mm deep in the stone. It probably resulted of the 1585 fire, comparable to the red discolouration observed by iron oxy-hydroxide containing limestones at temperatures of 250–300 °C (Chakrabarti et al., 1996). Laboratory experiments were performed to visually confirm this observation on both buff-coloured stone samples from Dudzele and intact Caen stone *ferme* samples from the Cintheaux quarry. Both stone types showed similar changes. Samples heated at 300 °C underwent a distinct colour change from buff to red. This reddish discolouration is also visible in samples heated at 450 °C, but less pronounced. Samples heated at 600 °C, 750 °C and 900 °C did not show this red discolouration. However, at room temperatures, the latter started to break down by cracking after more than 24 h, eventually leading to a complete disintegration after several weeks. This cracking is in accordance with Chakrabarti et al. (1996) and Hajpál and Török (2004) who observed a similar deterioration phenomenon due to portlandite formation after CaO was formed as a result of CaCO_3 breakdown at temperatures above 750 °C. In thin sections

Area	% A	% B	% C	Orientation
Wall1	0	17	83	W
Wall2	22	42	35	N
Wall3	10	33	56	W
Wall4	6	58	35	S
Wall5	13	62	25	W
Wall6	19	58	23	N
Wall7	14	20	66	W
Wall8	5	30	65	S
Wall9	17	14	69	W
Wall10	20	46	34	S
Wall11	15	33	52	E
Wall12	18	35	47	S

Table 9.2: Percentage of categories A (intact stone), B (cracks, partial loss of volume) and C (strong surface retreat) blocks and orientation of the wall as can be seen in Figure 9.4.

of in-situ samples, it can be observed that the greenish silicification from the bulk is discoloured to red in the crust (Fig. 9.6B), which illustrates the oxidation of iron. However, neither XRD nor SEM-EDX measurements showed distinct differences between crust and bulk, implying that probably only traces of iron elements are involved rather than iron crystal phases. The effect and intensity of the fire is indicated by the thickness of this crust, representing the outer 5 mm of the stone volume. As already suggested by Chakrabarti et al. (1996), small fire damage does not markedly change the intrinsic stone strength and leaves the stability of the walls unaffected. Probably other parts of the former church suffered much more from the fire, thus decreasing their load bearing capacity which could have, partly, given rise to the collapses of 1673 and in the 18th century.

Soiling and biological colonization by crustose saxicolous lichens are present on more stable surfaces. These lichens can be present on buff-coloured limestones as well as on reddish-discoloured ones as can be observed in thin sections where they are associated with local orange discolouration (Fig. 9.6C-E), which are possibly be caused by the formation of oxalates. The growth of such lichens is accompanied by a surface rupture up to 500 μm depth. μCT revealed no further structural

damage underneath these lichens (Fig. 9.9).

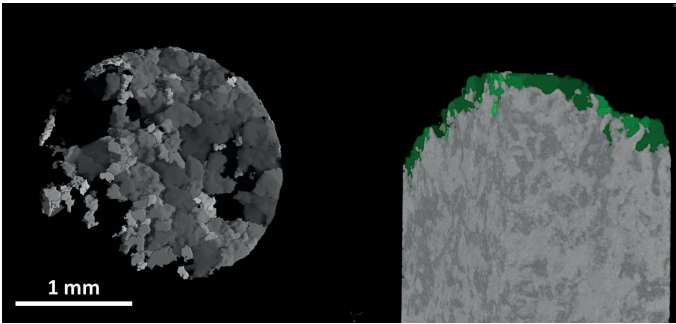


Figure 9.9: μ CT rendering of the crust with lichens (scale bar for both images). Left: top view with puzzle pattern of lichens. Right: sagittal section through stone with lichens in green showing limited lichen penetration.

Another morphology of surface retreat is alveolization, which develops on individual stones. Alveolization or honeycomb weathering is commonly attributed to salt action in combination with wind action, case-hardening agents or biofilms (Rodriguez-Navarro et al., 1999; McBride and Picard, 2004; Mustoe, 2010). The capillary uptake test clearly demonstrated the occurrence of salts inside the stones (Fig. 9.10). Thin sections reveal the possible presence of biofilms on the stone, whilst the reddish discolouration can be responsible for surface induration. The efflorescing salts from the capillary uptake were sampled for XRD analysis (Table 9.3). Sulphates and chlorides were present in the stone as gypsum and halite, but no pronounced gypsum crust was observed using optical microscopy, SEM-EDX or μ CT measurements. The sulphates and chlorides occur within the pore space underneath the surface. Although Dudzele is located in a rural area, it is only 10 km separated from the industrial sea port of Zeebrugge. The origin of the sulphates could thus be internal (oxidation of pyrite) as well as external (industrial atmospheric sulphur). The chloride might have originated from natural sea spray or could be introduced anthropogenically by using sea sand as joint mortar aggregate.

Samples from the tower ruins of Dudzele were subjected to laboratory induced freeze-thaw and salt weathering tests in order to examine their present-day performance. Freeze-thaw and salt weathering are potential agents for stone decay in Dudzele which can induce cracking and subsequent loss of volume. Belgium enjoys a temperate climate with temperatures in the coastal area approximately 1 °C higher during winter

Mineralogy	Semi-quantitative amount (%)
$\text{CaSO}_4 \cdot 2\text{H}_2\text{O}$	69
NaCl	17
CaCO_3	11
SiO_2	2

Table 9.3: XRD analysis of salt efflorescence after capillary rise tests.

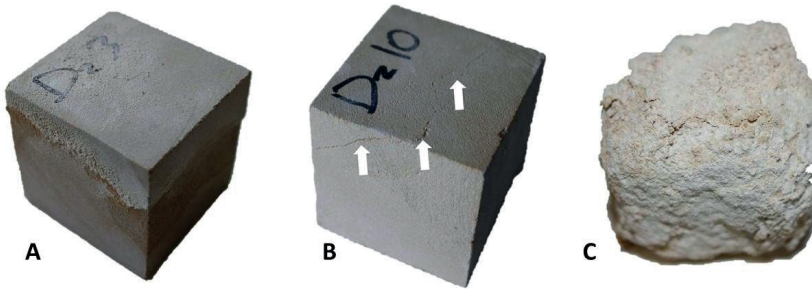


Figure 9.10: A) Salt efflorescence after capillary rise tests; B) sample with the most severe damage after freeze-thaw tests; C) decay pattern after salt weathering tests; all samples retrieved from the tower ruin of Dudzele.

with respect to central Belgium as a result of the climate mild Gulf Stream. In central Belgium, the temperature dropped 74 times below $0\text{ }^{\circ}\text{C}$ during the year 2010. Of course only a part of these negative temperature excursions are under wet conditions.

Only one out of ten samples was clearly damaged after 48 freeze-thaw cycles, while two other showed minor damage and seven remained intact. The weight loss was negligible for all samples (Table 9.4) as was the change in *UCS* compared to intact samples. The most damaged sample had a millimeter scaled fissure throughout its volume, but the sample did not fall apart in pieces (Fig. 9.10B). Overall, the results demonstrated the stone's good freeze-thaw resistance, even after being used for a longer time, thereby not losing its loading capacity. However, fissures and cracks can lead to scaling as observed in the tower wall. The fissure in the damaged sample is probably the result of pre-existing fissures, caused by weathering or load in the tower.

The stone samples show more susceptibility to salt weathering (Fig. 9.10C, Table 9.4). Granular disintegration and scaling is most effective during the

	weight loss (wt%)			Damage
	Min.	Max.	Average	
Salt weathering	16.06	47.47	26.43	Granular disintegration and scaling
Freeze-thaw weathering	0.27	0.75	0.46	Intact or occasional fissures height

Table 9.4: Results of laboratory induced freeze-thaw and salt weathering tests on the samples from the tower ruin of Dudzele.

immersion phase. In addition to the samples from Dudzele, fresh samples of Caen stone *ferme* and *demi-ferme* were also subjected to the same test, in order to compare the performance of the stone in Dudzele with fresh Caen stone. The dry weight of each samples was measured after each cycle of immersion and subsequent drying. The average normalized weights are presented in Figure 9.11. Caen stone *demi-ferme* is the most susceptible to this weathering test. This is not surprisingly, as this rock has the highest porosity and capillary water absorption coefficient. On the other hand, it was expected that the samples from Dudzele would behave similar to the Caen stone *ferme*, because of the petrophysical similarities. However, the samples from Dudzele seem to be more resistant to the salt weathering test. This can be explained by their lower capillary water absorption coefficient, which was probably related to the presence of NaCl in their pore system. It thus seems that the decay during this accelerated salt weathering test using $\text{NaSO}_4 \cdot 10\text{H}_2\text{O}$ was slowed down by the physical presence of NaCl, blocking the pore space and preventing the uptake of $\text{NaSO}_4 \cdot 10\text{H}_2\text{O}$.

The observed salt weathering in the tower is probably caused by sodium chloride, given the absence of sodium sulphate in the XRD measurements. However, for accelerated laboratory experiments, sodium sulphate (far more destructive than sodium chloride (e.g. Beck and Al-Mukhtar, 2010)) is used because it can achieve sufficient degrees of supersaturation and thus crystallization pressure (Steiger, 2005). The test performed is to study the performance of the stone in relation to salt weathering, but the damage obtained in laboratory environment is much more severe than decay in situ. Nevertheless, the performance of stones from Dudzele in this test are not worse (if not better) than fresh samples from Caen stone. Moreover, given the salt load at Dudzele, it is advisable to use Caen stone *ferme* over *demi-ferme*, based on the results of Figure 9.11.

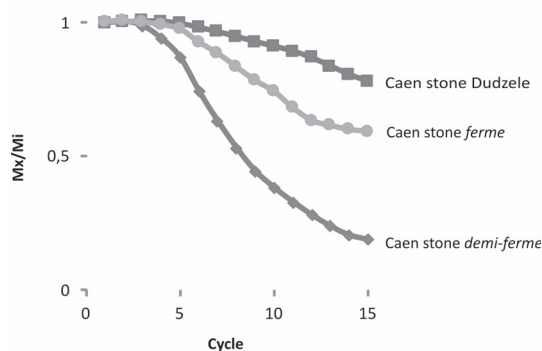


Figure 9.11: Average normalized dry weights of samples in function of the salt weathering cycles. The samples from the tower ruin of Dudzele show the least susceptibility to salt weathering.

9.5 Conclusion

The occurrence of Caen stone, or possibly a similar stone facies from the Boulonnais, in the Dudzele tower ruins illustrates the use of this stone across international borders. The coastal setting of Dudzele must have played an important role in the choice for this stone, favouring an easily accessible waterway transport route. Hence, this information contributes to the historical value of the tower ruin. The identification of Caen stone in Dudzele can be a reference to identify other Caen stone in similar settings. For example, shortly after the identification of Caen stone in Dudzele, Caen stone was also identified in Damme after personal communication (Debonne and Dreesen, 2015).

In addition to the stone's aesthetic compatibility, the study of its petrophysical properties clarified that the current exploitation site of Caen stone in Cintheaux (France) can provide adequate replacement stones within the range of physical compatibility; the use of Caen stone *ferme* variety is proposed. The Caen stone shows deterioration phenomena with respect to different weathering agents which left a distinct fingerprint, although its performance also depends on the individual stone quality. Despite various devastating historical events and environmental changes, the Caen stone in the actually remaining part of the tower ruins proved to possess a good durability over time. The stone still demonstrates a good performance in freeze-thaw weathering tests. The stone is more susceptible to accelerated salt weathering. XRD measurements indicated

the presence of gypsum and halite. Therefore, they are assumed to be the most destructive agents, causing the observed weathering such as sanding and alveolization in the lower façade of the tower ruin.

These results also show that the identification of the stone type, its properties and the weathering phenomena can help adequately in the restoration of the monument. First of all, it helps to select and approve the best replacement stone. Moreover, it shows that deterioration is gradual and that the stone shows a good performance in this environment. With respect to the tower's appearance, it could be discussed that only stones with large structural damage (cracks and fractures) should be replaced. Alveolization, on the other hand is not necessarily threatening for the stone's integrity. In contrary, this, together with the reddish discolouration of some stones, reflects the historical inheritance, and it shows the age and authenticity of the tower ruin. Therefore, it is valuable to preserve this appearance. Moreover, in chapter 4 it is shown that ageing is appreciated. A total restoration could therefore result in a decreased appreciation of the tower ruin. On the other hand, it can be questioned whether the historical replacements of Caen stone in Lede stone and Luxembourg sandstone have any historical or architectural importance. They seem to have their origin in the lack of adequate identification of Caen stone, which again underlines the importance of stone identification.

References

- EN 14579. Natural stone test methods - Determination of sound speed propagation, 2004.
- K Beck and M Al-Mukhtar. Evaluation of the compatibility of building limestones from salt crystallization experiments. *Geological Society, London, Special Publications*, 333(1):111–118, jan 2010. ISSN 0305-8719. doi: 10.1144/SP333.11.
- L Brabant, J Vlassenbroeck, Y De Witte, V Cnudde, M N Boone, J Dewanckele, and L Van Hoorebeke. Three-Dimensional Analysis of High-Resolution X-Ray Computed Tomography Data with Morpho+. *Microscopy and Microanalysis*, 17(2):252–263, 2011. doi: 10.1017/s1431927610094389.
- J Cassar, M G Winter, B R Marker, N R G Walton, D C Entwisle, E N Bromhead, and J W N Smith. Introduction to stone in historic buildings: characterization and performance. *Geological Society, London, Special Publications*, 391(1):1–5, mar 2014. ISSN 0305-8719. doi: 10.1144/SP391.10.
- B Chakrabarti, T Yates, and A Lewry. Effect of fire damage on natural stonework in buildings. *Construction and Building Materials*, 10(7): 539–544, 1996. doi: 10.1016/0950-0618(95)00076-3.
- R H Charlier. The Zwin: From Golden Inlet to Nature Reserve. *Journal of Coastal Research*, 27(4):746–756, 2011. doi: 10.2112/10a-00003.1.
- V Cnudde, J Dewanckele, M De Ceukelaire, G Everaert, P Jacobs, and M C Laleman. *Gent...Steengoed!* Academia Press, Ghent, 2009.
- T De Kock, W De Boever, J Dewanckele, M A Boone, P Jacobs, and V Cnudde. Characterization, performance and replacement stone compatibility of building stone in the 12th century tower of Dudzele

- (Belgium). *Engineering Geology*, 184(0):43–51, 2015. doi: <http://dx.doi.org/10.1016/j.enggeo.2014.10.026>.
- V Debonne and R Dreesen. Stenen immigranten in de Zwinstreek. Natuursteen in de Onze-Lieve-Vrouwhemelvaartkerk in Damme. *Relicta*, 12:149–190, 2015.
- O Dugué, L Dujardin, P Leroux, and X Savary. *La Pierre de Caen - Des dinosaures aux cathédrales*. Corlet, Imprimeur, S.A., Condé-sur-Noireau, 2010.
- R J Dunham. Classification of carbonate rocks according to depositional texture. . In W E Ham, editor, *Classification of carbonate rocks*, volume Memoir. 1, pages 108–121. American Association of Petroleum Geologists, 1962.
- M Duser, R Dreesen, and A De Naeyer. *Natuursteen in Vlaanderen - Versteend verleden*. Kluwer-Wolters Belgie nv, Mechelen, 2009.
- EN 12370. Natural stone test methods - Determination of resistance to salt crystallisation, 1999.
- EN 12371. Natural stone test methods - Determination of frost resistance, 2010.
- EN 1925. Natural stone test methods - Determination of water absorption coefficient by capillarity. Technical report, European Committee for Standardization, 1999.
- EN 1926. Natural stone test methods - Determination of uniaxial compressive strength, 2006.
- EN 1936. Natural stone test methods - Determination of real density and apparent density, and of total and open porosity, 2006.
- R L Folk. Practical petrographic classification of limestones. *American Association of Petroleum Geologists Bulletin*, 43:1–38, 1959.
- S Gillhuber, G Lehrberger, and J Göske. Fire damage of trachyte: investigations of the Teplá monastery building stones. In R Prikryl and Á Török, editors, *Natural Stone Resources for Historical Monuments*, volume 333, pages 73–80. Geological Society, London, 2010.
- F Gullentops and L Wouters. *Delfstoffen in Vlaanderen*. Vlaams Energieagentschap, 1996.

- M Hajpál and Á Török. Mineralogical and colour changes of quartz sandstones by heat. *Environmental Geology*, 46(3-4):311–322, 2004. doi: 10.1007/s00254-004-1034-z.
- ICOMOS. The Venice Charter - International Charter for the conservation and Restoration of Monuments and sites. Approved by the 2nd International Congress of Architects and Technicians of Historic Monuments. Technical report, Venice, 1964, 1966.
- ICOMOS-ICS. Illustrated glossary on stone deterioration pattern, 2008. URL http://international.icomos.org/publications/monuments{_}and{_}sites/15/pdf/Monuments{_}and{_}Sites{_}15{_}ISCS{_}Glossary{_}Stone.pdf.
- B C Masschaele, V Cnudde, M Dierick, P Jacobs, L Van Hoorebeke, and J Vlassenbroeck. UGCT: New x-ray radiography and tomography facility. *Nuclear Instruments & Methods in Physics Research Section a-Accelerators Spectrometers Detectors and Associated Equipment*, 580(1):266–269, 2007. doi: 10.1016/j.nima.2007.05.099.
- E F McBride and M D Picard. Origin of honeycombs and related weathering forms in Oligocene Macigno Sandstone, Tuscan coast near Livorno, Italy. *Earth Surface Processes and Landforms*, 29(6):713–735, 2004. doi: 10.1002/esp.1065.
- S McCabe, B J Smith, P A Warke, and Geological Society. A legacy of mistreatment: conceptualizing the decay of medieval sandstones in NE Ireland. In R Prikryl and Á Török, editors, *Natural Stone Resources for Historical Monuments*, volume 333, pages 87–100, London, 2010. Geological Society.
- G E Mustoe. Biogenic origin of coastal honeycomb weathering. *Earth Surface Processes and Landforms*, 35(4):424–434, 2010. doi: 10.1002/esp.1931.
- T G Nijland. Tufsteen uit de Eifel. *Gea*, 48(4):97–107, 2015.
- T Palmer. Understanding the Weathering Behaviour of Caen Stone. *Journal of Architectural Conservation*, 14(3):43–54, 2008a.
- T J Palmer. Limestone Petrography and durability in English Jurassic Freestones. In P Doyle, editor, *England's Heritage in Stone. A Publication of the English Stone Forum*, pages 66–78. 2008b.

- R Prikryl and Á Török. Natural stones for monuments: their availability for restoration and evaluation. *Geological Society, London, Special Publications*, 333(1):1–9, jan 2010. ISSN 0305-8719. doi: 10.1144/SP333.1.
- C Rodriguez-Navarro, E Doehne, and E Sebastian. Origins of honeycomb weathering: The role of salts and wind. *Geological Society of America Bulletin*, 111(8):1250–1255, aug 1999. ISSN 00167606. doi: 10.1130/0016-7606(1999)111<1250:OOHWTR>2.3.CO;2.
- B J Smith, M Gomez-Heras, H Viles, J Cassar, and (eds). *Limestone in the Built Environment: Present-Day Challenges for the Preservation of the Past*, volume 331. Geological Society, London, 2010.
- R Snethlage and M Pfanner. *Leitfaden Steinkonservierung*. Fraunhofer IRB Verlag, Stuttgart, 2013.
- M Steiger. Crystal growth in porous materials - I: The crystallization pressure of large crystals. *Journal of Crystal Growth*, 282(3-4):455–469, 2005. doi: 10.1016/j.jcrysgro.2005.05.007.
- J Vlassenbroeck, M Dierick, B Masschaele, V Cnudde, L Van Hoorebeke, and P Jacobs. Software tools for quantification of X-ray microtomography. *Nuclear Instruments & Methods in Physics Research Section a-Accelerators Spectrometers Detectors and Associated Equipment*, 580(1):442–445, 2007. doi: 10.1016/j.nima.2007.05.073.
- W Wintein. *De ontwikkeling van Dudzele - Historisch-geografische Schets van een Poldergemeente*, volume 9-1. Oostkerke : Kring voor heemkunde en geschiedenis "Sint Guthago", n.d., Brugge, 1967.

10

Conclusions and future outlook

Centuries of its application in constructions have led to an extensive amount of Lede stone in the cultural heritage in northwestern Belgium and in the surrounding areas such as The Netherlands. Lede stone is not found as massive deposits, but as stone horizons of limited size within the unconsolidated sediments of the Eocene Lede Formation. As a consequence, it was quarried at several locations where it outcropped, ranging from the Scheldt-Dender interfluvium southeast of Ghent, over the region of Aalst to the region of Brussels, at both sides of the Senne river. Because of its abundance in the cultural heritage, it has several times been the subject of smaller and larger studies; for its resources (Mortier, 1898; Camerman, 1955; Nijs, 1980; Fobe, 1990), its properties and weathering (Van Nieukerken, 1904; Camerman, 1951; Larbi et al., 2003; Dreesen et al., 2006; Dreesen and Nielsen, 2009; Dewanckele et al., 2012, 2013) and its replacement (De Witte, 1990; Quist et al., 2013).

The fact that it was quarried at several locations raises the question if there is a regional variability in appearance or in properties. At the moment, no such mapping has been performed. Historical studies were able to map the historic production and distribution (De Smet et al., 2003; Hurx, 2012). However, so far it is not possible to determine the provenance based on the

stone's analysis itself. This is hampered by the fact that many production sites are exhausted and outcrops have disappeared. The regional provenancing of Lede stone in buildings, however, could be a challenge for future studies.

In industry, but also in historic studies, Lede stone is always considered as one stone type, covered under the name Lede stone (referring to its geological affinity) or Balegem stone (referring to the Natural stone denomination criteria of NBN EN 12440 (2008)). For many commercial stones, however, building stones from the same resource are often specified by their specific differences. Obvious examples are Portland or Massangis, where many varieties exist, based on their appearance and/or properties. But also geological equivalent limestones such as St Maximin or St Pierre Aigle are commercialized under different varieties. Also for Lede stone, a significant natural variability can be seen, ranging from compact, low porous stones, over medium porous to high porous and fossiliferous varieties. This is not specifically related to its regional variability, but rather to changes in microfacies within the deposits in the same location. Therefore, the question rises how large the natural variability is, and how this controls its petrophysical properties, its mechanical properties and its durability. The consequence of Lede stone being considered as one stone type is that often one value or a range of values is given for a certain property. The difference in properties and the impact on durability of low porous, medium porous and high porous Lede stone has never been investigated thoroughly.

The natural variability of Lede stone can be observed at Balegro quarry in Balegem, where Lede stone is still produced today. This was illustrated in chapter 5. Stone samples from Balegro were divided in six types with increasing visible porosity. This porosity was estimated by image analysis and was summarized together with a macroscopic description in a visual estimation chart (VEC). This VEC can be used by professionals, to estimate the porosity of the Lede stone they are dealing with. The different types were grouped into low porous (type 1–2), medium porous (type 3–4–5) and highly porous (type 6). The properties of these groups were investigated more thoroughly. Once a Lede stone type is determined with the VEC, reference values of its properties can be found in the different sections of chapter 5.

The low porous variants have a very low capillary water absorption, because the major fraction of the pore network is situated in the lower

capillary and subcapillary pores and the total porosity is relatively low. On the other hand, these micropores tend to retain water during drying and therefore have a high critical moisture content. The highly porous variant has a well-connected macropore network, resulting in a high capillary suction, but also in a high drying rate and a low water retention or low critical moisture content during drying. The stones with medium porosity have a pore network which consists of macropores, connected by smaller pores. Therefore, the capillary water absorption and the water vapour permeability are somewhat higher than that of the low porous stones. The drying rate, however, is determined by the micropore network and is comparable to that of the low porous stones, but the critical moisture content is lower due to the presence of macropores.

All three varieties of Lede stone perform relatively well in durability tests. From the interpretation of their properties and weathering tests, it could be concluded that only the very porous Lede stones, which are not frequently used, should be applied with knowledge. As they absorb water faster than the less porous Lede stone, they should not be exposed to environments which are continuously wet, or where salts or freezing coincide with cyclic wetting, such as freestone work, flooring or pavements. In façades, they can perform properly. This can also be observed in the many historic buildings, where Lede stone has withstand climatic environments and inherited stresses for centuries. This does not mean that all Lede stone remains intact. Over the last two centuries, it has suffered from the increase in SO_2 emissions (Camerman, 1951; Larbi et al., 2003; Dreesen et al., 2006). The fact that these emissions are significantly reduced over the last decades gives a positive perspective for the life time estimations of Lede stone, although the effect of increasing NO_x levels, which can enhance SO_2 action, on Lede stone is not yet investigated. The formation of black crusts is already well understood for a longer time. Chapter 6 illustrates the effect of the formation of a laminar gypsum crust on the properties of Lede stone. It was observed that there is both a chemical and physical alteration. It is likely that SO_2 -action also enhances the weathering of glauconite, which can contribute to the formation of an iron-rich patina. Moreover, the cracks that are associated with the occurrence of black crusts are plausibly genetically related. These modify the water absorption and desorption behaviour and can subsequently influence the frost susceptibility of the stone. In fresh conditions, the frost resistance of Lede stone should be good, as was illustrated in chapter 7. The low and medium porous variants have relatively slow water uptake.

They should be wet for hours to saturate. Even when saturated, their high strength allows them to withstand the crystallization pressures in the larger pores. The formation of microcracks by the action of SO_2 , however, can increase the absorption rate and thus the frost susceptibility. The highly porous Lede stone saturates more easily and has a lower strength, allowing lower stresses to induce damage. The large macropores, however, allow a certain accommodation of ice crystals so that the dimensional changes of the high porous Lede stone is only significantly different to that of the less porous rocks when it is completely imbibed by water under vacuum. Further research in this pore-scale behaviour during the action of frost can reveal more details about its frost susceptibility in relation to the degree of wetting. As illustrated by the experiments in chapter 6 and 7, dynamic pore-scale experiments have a high potential to investigate the fundamental processes acting in or on natural stone.

Deterioration eventually leads to restoration and stone treatments or replacement. In this case, the natural variability of Lede stone has consequences for the restoration strategy, which were discussed in chapter 8. The natural variability is one of the amenity factors of this rock and is an authentic part of our cultural heritage. Replacing them by a more homogeneous stone creates a loss of aesthetical and historical value. This reveals the intrinsic difficulty of finding a suitable replacement stone for Lede stone. After more than a century, this question has not yet been resolved. In northwestern Belgium, mostly French limestones have been used as replacement. Today, new alternatives are sometimes proposed, although it must be emphasized that Lede stone is still available at the Balegro quarry in Balegem. For other replacement stones, it stays difficult to match both aesthetically and technically. Important aesthetical preconditions include the size, colour and texture to differentiate with other historical limestones such as Brussels stone. The petrophysical and strength properties depend on the type of Lede stone which is replaced, but many limestones have a higher porosity and a lower strength than Lede stone. Finally, also the ageing aspect is very important, as shown in chapter 4. This can be mimicked by the shape and finishing of the newly applied blocks, e.g. by not cutting straight edges, if the architecture aims at such situation. It is however, also important that the ageing of the stone itself resembles that of Lede stone. One aspect herein is its composition, bounding and texture; i.e. having a calcite cement, a detritic fraction and a similar pore size distribution. Another is the (low) presence of some glauconite or Fe-rich calcite to acquire an iron-oxide patina upon ageing.

This patina is certainly of feature of interest. Future research could include a detailed study of the components contributing to its formation and how this patina modifies the water absorption behaviour and further weathering of the stone (e.g. Thomachot-Schneider et al., 2008; Beck and Al-Mukhtar, 2014).

The technical requirements for replacement stones can be formulated based on properties of Lede stone. However, the application of any preservation treatments was not investigated here. Such studies can not be done without a decent knowledge of the stone properties themselves. Therefore, the study of such treatments on (weathered) Lede stone, with traditional but also innovative methods, is a logical next step for contributing to the safeguarding of our cultural heritage.

References

- K Beck and M Al-Mukhtar. Cyclic wetting-drying ageing test and patina formation on tuffeau limestone. *Environmental Earth Sciences*, 71(5): 2361–2372, 2014. doi: 10.1007/s12665-013-2637-z.
- C Camerman. Les pierres de taille calcaires. Leur comportement sous l'action des fumées. *Annales des travaux publics de Belgique*, 52:509–532, 1951.
- C Camerman. Le sous-sol de Bruxelles et ses anciennes carrières souterraines. *Annales des travaux publics de Belgique*, 2-3:5–28, 1955.
- L De Smet, P Devos, W Eeckhout, and R Nijs. *Balegemse steen - vier aspecten*. Provinciebestuur Oost-Vlaanderen, Gent, 2003. doi: D/2003/1933/4.
- E De Witte. Natuursteen in de monumentenzorg: vervangen of conserveren? *Bulletin de la Société belge de Géologie*, 99(2):197–205, 1990.
- J Dewanckele, T De Kock, M A Boone, V Cnudde, L Brabant, M N Boone, G Fronteau, L Van Hoorebeke, and P Jacobs. 4D imaging and quantification of pore structure modifications inside natural building stones by means of high resolution X-ray CT. *Science of the Total Environment*, 416:436–448, 2012. doi: 10.1016/j.scitotenv.2011.11.018.
- J Dewanckele, M A Boone, T De Kock, W De Boever, L Brabant, M N Boone, G Fronteau, J Dils, L Van Hoorebeke, P Jacobs, and V Cnudde. Holistic approach of pre-existing flaws on the decay of two limestones. *Science of the Total Environment*, 447:403–414, 2013. doi: 10.1016/j.scitotenv.2012.12.094.
- R Dreesen and P Nielsen. On the triggering role of glauconite in the sulphate attack of sandy limestones, based on a study of historical building stones in Flanders, Belgium. In *12th Euroseminar on*

- Microscopy Applied to Building Materials*, pages 13–19, Dortmund, 2009. Technische Universität Dortmund.
- R Dreesen, P Nielsen, and D Lagrou. *Provenance, durability and damage analysis of natural building stones by means of petrographical techniques*. 2006. ISBN 978-1-4020-5076-3. doi: 10.1007/978-1-4020-5077-0{-}29.
- EN 12440. Natural stone - Denomination criteria, 2008.
- B Fobe. Voorkomen, samenstelling en gebruik van de Balegemse steen. *Bulletin de la Société belge de Géologie*, 99(2):167–170, 1990.
- M Hurx. *Architect en aannemer - De opkomst van de bouwmarkt in de Nederlanden 1350-1530*. Vantilt, Nijmegen, 2012.
- J A Larbi, R P J van Hees, and S Naldini. Microscopic study of weathering of white Flemish stone from the monumental Church of Our Lady in Breda, The Netherlands. *Heron*, 48(3):13, 2003.
- S Mortier. Communications sur les recherches faites dans les anciennes carrières de Baelegem., 1898.
- R Nijs. Identificatie van Balegemse steen door middel van de korrelgrootteverdeling van de zandfractie. *Vlaanderens Erfgoed*, 55:8–13, 1980.
- W J Quist, T G Nijland, and R P J van Hees. Replacement of Eocene white sandy limestone in historical buildings: over 100 years of practice in the Netherlands. *Quarterly Journal of Engineering Geology and Hydrogeology*, 46(4):431–438, 2013. doi: 10.1144/qjegh2013-023.
- C Thomachot-Schneider, M Gommeaux, and G Fronteau. Modifications of the porous network of sandstone accompanying the formation of black varnish. *Environmental Geology*, 56(3-4):571–582, 2008. doi: 10.1007/s00254-008-1443-5.
- J J Van Nieukerken. Verslag over het onderzoek ingesteld naar de kwaliteit van eenige natuurlijke steensoort, ten behoeve van de Restauratie van de Groote of Onze Lieve Vrouwe Kerk te Breda. Technical report, 's Gravenhage, 1904.



 PROGRESS
Pore-scale Processes in Geomaterials

ISBN 978-9-4619737-9-5
University Press

